

FRICION STIR SPOT WELDING: ENGINEERING ANALYSIS AND DESIGN

By

Chase Davison Cox

Dissertation

Submitted to the Faculty of the  
Graduate School of Vanderbilt University

In partial fulfillment of the requirements

for the degree of

DOCTOR OF PHILOSOPHY

in

Mechanical Engineering

May, 2014

Nashville, TN

Approved:

Dr. Alvin M. Strauss

Dr. George E. Cook

Dr. David R. DeLapp

Dr. Greg Walker

Dr. Jason Valentine

*For my wife and daughter*

## ACKNOWLEDGMENTS

I would like to thank Professor Alvin M. Strauss and Professor George E. Cook for their support and guidance during my graduate career. I would also like to thank Dr. David R. DeLapp, Professor Greg Walker, and Professor Jason Valentine for serving on my PhD committee and for their numerous contributions to my education and research. I would like to thank John Fellenstein and Bob Patchin in the machine shop for their assistance. I would also like to thank my fellow graduate students, both past and present, in the Vanderbilt Welding Automation Laboratory for their help and support. I would like to thank the Tennessee Space Grant Consortium for their financial support.

Lastly, I'd like to thank my family for their support.

## Table of Contents

	Page
DEDICATION .....	ii
ACKNOWLEDGMENTS .....	iii
LIST OF FIGURES .....	vii
LIST OF TABLES .....	xv
Chapter	
I. INTRODUCTION .....	1
Background .....	1
Overview of Work .....	3
II. FRICTION STIR SPOT WELDING .....	7
The Friction Stir Spot Welding Process .....	7
Advantages of FSSW .....	8
Friction Stir Spot Welding Terminology .....	9
Process Parameters .....	13
Tool Design .....	16
Material Flow .....	23
Defects and Failure Modes .....	26
Notable FSSW Variations .....	29
III. FSSW MODELING AND SIMULATION .....	31
Introduction .....	31
Analytic (Process) Models .....	32
<i>Heat Generation</i> .....	32
<i>Weld Torque</i> .....	42
<i>Axial Force</i> .....	46
<i>Thermal Boundary Conditions</i> .....	49
<i>Material Flow</i> .....	52
Computational Modeling Studies .....	60
IV. EFFECT OF PIN LENGTH AND ROTATION RATE ON THE TENSILE STRENGTH OF A FRICTION STIR SPOT-WELDED AL ALLOY: A CONTRIBUTION TO AUTOMATED PRODUCTION .....	69
Abstract .....	69
Introduction .....	70
Experimental .....	72
Results .....	75
<i>Effect of Pin Length and Rotation Rate on Static Weld Strength</i> .....	75

<i>Failure Analysis</i> .....	77
<i>Weld Zone Imaging</i> .....	83
Discussion .....	86
Conclusions .....	93
<b>V. THE APPLICATION OF A PINLESS TOOL IN FRICTION STIR SPOT WELDING: AN EXPERIMENTAL AND NUMERICAL STUDY</b> .....	95
Abstract .....	95
Introduction .....	96
Experimental .....	98
Results .....	102
<i>Joint Strength</i> .....	103
<i>Spindle Torque</i> .....	107
<i>Temperature</i> .....	110
<i>Failure Analysis</i> .....	113
<i>Macrosection Analysis</i> .....	114
Numerical Simulation .....	116
Discussion .....	123
Conclusions .....	127
<b>VI. A METHOD FOR DOUBLE-SIDED FRICTION STIR SPOT WELDING</b> .....	128
Abstract .....	128
Introduction .....	129
Numerical Model .....	132
<i>Design</i> .....	132
<i>Thermal Model</i> .....	133
<i>Material Flow Model</i> .....	137
<i>Results</i> .....	140
Experimental .....	141
<i>Rotating Anvil Design</i> .....	141
<i>Using the RAFSSW Process</i> .....	148
Experimental Results .....	150
<i>Macrosection Analysis</i> .....	150
<i>Mechanical Strength</i> .....	151
<i>Process Forces</i> .....	153
Conclusions .....	155
<b>VII. ENERGY INPUT DURING FRICTION STIR SPOT WELDING</b> .....	157
Abstract .....	157
Introduction .....	157
Experimental .....	159
Results .....	161
<i>Axial Force</i> .....	163
<i>Spindle Torque</i> .....	164

<i>Spot Weld Energy</i> .....	164
<i>Tensile Shear Strength</i> .....	167
Discussion.....	168
Conclusions.....	172
VIII. ROTATING ANVIL APPLICATIONS FOR FRICTION STIR SPOT WELDING	
.....	173
Abstract.....	173
Introduction.....	174
Experimental.....	176
Results and Discussion .....	176
<i>Force Control</i> .....	176
<i>Non-Matched Rotation Rates</i> .....	183
<i>Triple-Lap Joint Welding</i> .....	189
<i>Al-Steel-Al With Through Hole</i> .....	195
<i>Spot Stich Welding</i> .....	205
Conclusions.....	207
IX. DISCUSSION OF RESULTS .....	209
Overview.....	209
Tool Geometry .....	209
Spot Welding Parameters.....	210
Rotating Anvil.....	211
Numerical Modeling.....	212
X. RECOMMENDATIONS FOR FUTURE WORK .....	213
Friction Stir Spot Welding.....	213
Tool Rotation Feedback.....	213
FSSW Tool Turn Limit.....	213
FSSW of Butt Joints.....	214
FSSW with Sealant .....	215
FSSW with “Energy” Control.....	215
XI. CONCLUSIONS .....	217
REFERENCES .....	218
APPENDIX.....	227
A. Design of A Pinless FSSW Tool.....	227
B. Patent Application for Double Sided Friction Stir Spot Welding Method .....	233

## LIST OF FIGURES

Figure 1: The friction stir spot welding process. ....	7
Figure 2: Advantages of FSW/FSSW [Mishra] .....	8
Figure 3: An FSSW tool with the shoulder and pin identified .....	9
Figure 4: Cross-section view of an FSSW spot weld [Arul] .....	11
Figure 5: Joint configurations for FSSW .....	12
Figure 6: The FSSW cycle .....	15
Figure 7: FSSW tool profile and pin size (d): (a) straight cylindrical, (b) tapered cylindrical, (c) threaded cylindrical, (d) square, (e) triangular and (f) hexagonal. [Bilici] .....	17
Figure 8: Schematic illustration of FSSW tool geometries (a) cylindrical pin shape (threads not shown in illustration) and (b) triangular pin shape [Badarinarayan 142-48].	18
Figure 9: Macro images of a) long step spiral pin (CP) and b) off-center hemisphere pin (OC) [Yuan] .....	18
Figure 10: Lap-shear separation load as a function of shoulder penetration depth [Yuan] .....	19
Figure 11: Effect of FSSW pin length (x-axis) and anvil insulation on 6111 aluminum alloy tensile shear strength (y-axis) [Bakavos 2009] .....	20
Figure 12: Schematic of FSSW tool shoulder geometries a) concave, (b) flat, (c) convex [Badarinarayan 814-23] .....	21
Figure 13: Different FSSW shoulder features shown before and after twenty welds: (a) featureless tool, (b) the short flute wiper tool (ii), (c) the long flute wiper tool (iii), (d) the fluted scroll tool (iv), and (e) the proud wiper tool (v) [Bakavos 2011] .....	22
Figure 14: Schematic illustration of material flow with a pinless tool [Tozaki 2010] .....	24
Figure 15: Material flow observed during FSSW. (a-d) cross section views of the weld formation sequence, (e) plan view below top surface of weld for 0 and 0.5 seconds of dwell time [Bakavos 2011]. .....	25
Figure 16: The hooking defect observed in a FSSW spot weld [Badarinarayan 142-148] .....	27
Figure 17: Relationship between generated heat and process parameters during FSSW [Mijajlovic] .....	33
Figure 18: Experimental apparatus for measuring momentum of friction and axial force [Mijajlovic]. .....	36
Figure 19: Variations of (a) fractional slip and (b) the friction coefficient [Nandan 2006] .....	38

Figure 20: Definition of contact condition, velocity/shear relationship, and contact state variable [Schmidt].....	40
Figure 21: Spatial variation of heat generation (watts) along the tool/workpiece interface for a) the shoulder b) the pin bottom [Nandan 2007] .....	41
Figure 22: Simplified geometry of the Nunes Rotating Plug model during FSW [Nunes 2011] .....	43
Figure 23: Estimated and experimental torque values for FSW of a) AA2524 and b) Ti-6Al-4V [Arora] .....	45
Figure 24: Computed axial force using Equation 3.20 (Data from Nunes RP et al.) .....	47
Figure 25: Idealization of weld metal flow around a FSW tool during the plunge stage [Nunes 2012].....	47
Figure 26: Free body diagram for flow elements around the FSW tool [Nunes 2012] ....	49
Figure 27: Schematic diagram of the pinless FSSW system considered in the model for thermal boundary conditions [Nandan 2006] .....	50
Figure 28: Three incompressible flow fields of FSW. a) rigid body rotation b) uniform translation c) ring vortex [Schneider] .....	53
Figure 29: a) schematic of the velocity field domain. b) flow field from well-tested viscoplastic flow code c) flow field from analytic expression [Arora].....	54
Figure 30: Flow stress data for Al 6061 and curve fitting values: $R^2 = 0.996$ [Tello] .....	57
Figure 31: Computed contours of viscosity. The contour labels represent logarithm to the base 10 of viscosity in Pa·s [Nandan 2007].....	58
Figure 32: Variation of viscosity with shear rate according to the Carreau model [Fluent] .....	59
Figure 33: Comparison between experimental and numerical results a) weld cross section b) contour graph of dynamic viscosity [Atharifar] .....	60
Figure 34: Mesh representation for FSSW tool, workpiece, and anvil. b) Boundary Conditions [Awang].....	61
Figure 35: Deformation and temperature distribution [Awang] .....	62
Figure 36: Temperature vs. radial distance from the center of the tool [Awang].....	62
Figure 37: Location of thermocouples imbedded in the workpiece (butt joint) [Song] ...	64
Figure 38: Temperature contours during the a) plunge stage, and b) the extraction stage of FSW [Song] .....	65
Figure 39: a) FSSW geometry used for CFD Simulation b) mesh scheme for cylindrical pin c) close up view of mesh scheme [Kim].....	66
Figure 40: Temperature distribution during FSSW for a cylindrical pin (left) and triangular pin (right) at t = a) 0.01 sec b) 1.0 sec c) 2.0 sec [Kim].....	67
Figure 41: Material flow during FSSW for a cylindrical pin (left) and triangular pin (right) at t = a) 1.94 sec b) 1.95 sec c) 1.96 sec .....	68



Figure 42 The Friction Stir Spot Welding Process. A-C: represents the traditional FSSW process using a tool with a pin. The resulting keyhole defect is illustrated. D-F: represents the FSSW process using a pinless tool. The lack of the keyhole defect is illustrated. ....	71
Figure 43: Clamp orientation relative to the spot welds for each sample. This clamp prevented the top plate from pulling away from the bottom plate during the spot welding process. The holes in the top plate were created off center for alignment purposes with the FSW machine.....	73
Figure 44: Lap tensile specimen. ....	74
Figure 45: Effect of pin length and rotation rate on static joint strength of spot welds....	75
Figure 46: FSSW Failure Modes for 750 RPM .....	77
Figure 47: FSSW Failure Modes for 1250 RPM .....	78
Figure 48: FSSW Failure Modes for 1500 RPM .....	79
Figure 49: FSSW Failure Modes for 2000 RPM .....	80
Figure 50: Comparison of failure mode to weld strength. Only 2 welds in the experiment were classified as a mode (i) failure while 12 (60%) of the welds were classified as a mode (ii). The mode (ii) type failures exhibited the highest joint strength when compared to the other failure modes. The remaining welds were classified as mode (iii) failures...	82
Figure 51: Macrosection images of cross-sections of welds. (a) 750 rpm/pinless, (b) 750 rpm/0.010” pin, (c) 750 rpm/0.032” pin, (d) 750 rpm/0.036” pin, (e) 750 rpm 0.038” pin .....	83
Figure 52: Images of bond interface modes and notable failures. (a) A compiled image for the cross section of the pinless tool at 2000 rpm. Bond (i and iii) account for 100% of the interface for this weld. (b) The combination of 750 rpm and a pinless tool resulted in a well formed stir zone with good metallurgical bonding. (c) The 0.032” pin length at 2000 rpm resulted in a weld exhibiting bond (i). (d) The 0.032” pin length at 750 rpm resulted in a good metallurgical bond. A small amount of bond (iii) was observed at the right edge of the interface between the plates. (e) The 0.038” pin length at 2000 rpm resulted in a weld exhibiting bond (i). (f) The 0.038” pin length at 750 rpm resulted in a good metallurgical bond. ....	85
Figure 53: Comparison of theoretical heat generated by the FSSW tools used at the various rotation rates and their resulting average tensile strength. $Q'/Q^*$ represents the normalized theoretical heat input calculated for each rotation rate used. $Q'$ is the individual calculated value for each tool and rotation rate combination and $Q^*$ is the maximum calculated value. The average tensile values represented as $TS'/TS^*$ were calculated by averaging each of the measured tensile strengths for a given rotation rate for all pin lengths used. $TS'$ and $TS^*$ represent the individual average tensile strength for a given rotation rate and the maximum average tensile strength respectively. ....	88
Figure 54: Comparison of velocity field at various depths (0.02, 0.04, 0.06 and 0.08) created beneath the shoulder during FSSW. Two rotation rates were considered; 750 and 2000 rpm. A pinless and non-zero pin design were considered. $V'$ represents the	

magnitude of the 3 dimensional velocity field for a given parameter set (u, v, w, r, z). The velocity is calculated such that r = radius of shoulder or pin. V\* represents the maximum calculated value..... 91

Figure 55: Graphical representation of the observed pin length effect on joint strength. Region “A” represents the velocity field created by the shoulder. Region “B” represents the velocity field created by two different pin lengths. It can be seen that in the case of the longer pin length, the total velocity field is increased by the pin bottom’s contribution. Region “C” represents the resultant velocity field..... 92

Figure 56: The Friction Stir Spot Welding Process. A-C: represents the traditional FSSW process using a tool with a pin. The resulting keyhole defect is illustrated. D-F: represents the FSSW process using a pinless tool. The lack of the keyhole defect is illustrated. .... 97

Figure 57: Spot weld sample geometry ..... 99

Figure 58: Instrumented Anvil. Thermocouples are located 1/16<sup>th</sup> of an inch beneath the surface of the anvil beneath the weld zone. .... 100

Figure 59: FSSW tool with scrolling ..... 101

Figure 60: Contour plots of shear load of spot welds vs. all parameters. The label of each access can be seen in the title of each subplot (y-label \* x-label) ..... 104

Figure 61: Contour plots of spindle torque. The label of each access can be seen in the title of each subplot (y-label \* x-label)..... 108

Figure 62: Comparison of experimental, empirical, and analytic torque values ..... 110

Figure 63: Contour plots of the peak temperature measured via the thermocouples. The label of each access can be seen in the title of each subplot (y-label \* x-label)..... 111

Figure 64: Temperature versus dwell time. The welding tool makes contact at 5 seconds. .... 112

Figure 65: Temperature versus rotation rate. Tool contact at 7 seconds. .... 112

Figure 66: A shear specimen exhibiting the weld pullout mode. a) The top of the bottom plate. The weld nugget remains in the bottom plate. b) The top of the top plate. c) The bottom of the bottom plate. d) The bottom of the top plate..... 113

Figure 67: Macrosections of spot welds. Hold parameters: 2 sec dwell, 0.006 in plunge depth, 0.5 ipm plunge rate. a) 750 rpm b) 1000 rpm c) 1250 rpm d) 1500 rpm e) 1750 rpm ..... 114

Figure 68: Geometry mesh for FSSW simulation..... 117

Figure 69: Maximum temperature value at a point located at the bottom-center of the workpiece during welding (1250 RPM, 6 Sec Dwell) for experimental measurement and the values predicted by simulation..... 118

Figure 70: Development of temperature field within the workpiece during an FSSW spot weld. 1250 rpm, 4 sec dwell. Temperatures are reported in K. The y-axis has units of 10<sup>-4</sup> meters. The x-axis has units of meters. .... 119

Figure 71: Cross section view of velocity magnitude contour from CFD model for a tool rotation speed of 750 RPM ..... 121

Figure 72: Cross section view of velocity magnitude contour from CFD model for a tool rotation speed of 1250 RPM .....	121
Figure 73: Cross section view of velocity magnitude contour from CFD model for a tool rotation speed of 1750 RPM .....	122
Figure 74: Regression graphs for a) Shear failure load b) Torque c) Temperature .....	123
Figure 75: Strength of the spot welds vs. the number of rotations made by the weld zone during the weld. ....	124
Figure 76: Dependence of gas consumption on the weight of an automobile [Prangnell] .....	129
Figure 77: The Friction Stir Spot Welding Process. A-C: represents the traditional FSSW process using a tool with a pin. The resulting keyhole defect is illustrated. D-F: represents the FSSW process using a pinless tool. The lack of the keyhole defect is illustrated ....	131
Figure 78: Thermal boundary conditions and mesh used for the workpiece in the FSSW simulation.....	135
Figure 79: Temperature field within the workpiece during FSSW with a rotating anvil for 1 mm and 2 mm thick workpieces. Temperatures are reported in °K.....	136
Figure 80: Cross section view of the velocity contours and arrow surface of the RAFSSW process when joining a) 1 mm and b) 2 mm thick workpieces of Al 6061 T6. A rotation rate of 1000 rpm is used. The contour is taken at the end of the 3 second dwell period, immediately before the tool is retracted.....	139
Figure 81: The VUWAL FSW Machine.....	142
Figure 82: CAD drawing of the preliminary RAFSSW device design.....	144
Figure 83: The RAFSSW Device. The motor can be seen mounted in front of the welding machine. During welding the worktable and rotating anvil would raise causing the belt to slip.....	146
Figure 84: Plot of accelerometer data from the sample stage during welding with (red line) and without (blue line) the stabilization arm. ....	147
Figure 85: The RAFSSW device. The FSSW tool receives power from the main spindle of the FSW machine. The rotating anvil assembly, stabilization arm and 7.5 HP motor are all mounted to the stage of the FSW machine. The vertical actuation of the RAFSSW device is achieved through a simple combination of the vertical drive of the FSW machine and the floating stage.....	148
Figure 86: The welding tool and rotating anvil. A spherically tapered (convex) shoulder with scrolling and a 10.2 mm flat ground into the end. ....	149
Figure 87: Macrosection image of spot welds made using the RAFSSW process. Spot weld created at a) 750 rpm (welding tool and anvil) and a 0.5 second dwell phase and b) 1500 rpm and a 0.5 dwell time. A hooking defect can be seen on the left and right side of the 1500 rpm spot weld macrosection. ....	150

Figure 88: Comparison of joint strengths between spot welds made using the RAFSSW process using 750 and 1500 rpm and two different dwell times in 1 mm thick Al 6061 plate.....	152
Figure 89: Comparison of joint strengths between spot welds made using the RAFSSW process using 750 and 1500 rpm and two different dwell times in 2 mm thick Al 6061 plate.....	153
Figure 90: Comparison of welding forces between the traditional FSSW and RAFSSW processes created in the 1 mm (0.04”) thick plate. Axial forces created in 2 mm (0.08”) and 3 mm (0.125”) using the RAFSSW are also presented.....	154
Figure 91: Pinless FSSW tool with a spherically tapered shoulder.....	160
Figure 92: Open-loop position control system used for this experiment. The rotation rate, dwell time, plunge depth, plunge and extraction rates are inputs. The plunge depth and dwell time are the limits in this system. The resulting axial force and spindle torque are monitored during welding.....	161
Figure 93: Axial force during FSSW for different numbers of tool turns. The average axial force is 10.1 kN ± 0.5 kN. For this experiment, an open-loop position control scheme was used. Error bars represent standard deviation.....	163
Figure 94: Spindle torque (Nm) and energy (J) during spot welding. 1200 RPM, 0.5 sec dwell, 10 tool turns. ....	166
Figure 95: Total spot welding energy generated during FSSW. Error bars represent standard deviation. ....	167
Figure 96: Spot Weld Strength. Error bars represent standard deviation. ....	168
Figure 97: Spot Weld Tensile Shear Strength vs. Spot Welding Energy. Error bars represent standard deviation. ....	170
Figure 98: Proposed FSSW open-loop control system with energy monitoring. Like with traditional position control, the rotation rate, plunge depth, plunge and extraction rate are still input into the system. Instead of inputting a dwell time, total weld energy is specified. The plunge depth and total weld energy are now the limits on the system. Once the specified weld energy is generated, the welding tool would retract. ....	171
Figure 99: Axial force during RAFSSW with position control. The desired plunge depth is 0.008 inch. The maximum axial force of RA1 is 6080 N, of RA8 is 6710 N, and of RA18 is 7140 N. ....	178
Figure 100: Vertical position of welding stage during a friction stir spot weld (rotating anvil) without force control. RA1 overshoot the desired plunge depth by 0.0018 in (23%), RA8 by 0.0022 in (28%), and RA18 by 0.0018 in (23%) .....	179
Figure 101: Z-Force vs. Plunge Depth. An increase in the plunge depth resulted in a linear increase in the axial force acting on the welding frame. The weld data for this plot is from the experiments performed in Chapter IV.....	180

Figure 102: Axial force during RAFSSW with force control. The cut-off force is 4250 N. The maximum axial force of RAFC5 is 4645 N, of RAFC8 is 4581 N, and of RAFC9 is 4843 N. RAFC5 exceeded the cut-off force by 9%, RAFC8 by 8%, and RAFC9 14%.	181
Figure 103: Vertical position of welding stage during a friction stir spot weld (rotating anvil) with force control.....	182
Figure 104: Tensile shear strength of spot welds made using non-matched rotation rates between the FSSW tool and rotating anvil. The rotation rate of the FSSW tool for all cases was 1200 rpm. The rotating anvil had rotation rates of 1200 (0 rpm difference), 1500 (300 rpm difference), and 1800 (600 rpm difference). .....	184
Figure 105: Total spot weld energy of spot welds made using non-matched rotation rates between the FSSW tool and rotating anvil. The rotation rate of the FSSW tool for all cases was 1200 rpm. The rotating anvil had rotation rates of 1200 (0 rpm difference), 1500 (300 rpm difference), and 1800 (600 rpm difference). .....	185
Figure 106: Tensile shear strength (kgf) vs. total spot weld energy (kJ). Increase in weld energy results in a decrease in joint strength. ....	186
Figure 107: Numerical simulation results of the double-sided FSSW process showing the temperature contours within the workpiece during welding using non-matched rotation rates. ....	187
Figure 108: Acura’s “3D Lock Seam” technology created to join Al-Steel-Al in a triple-lap joint configuration.....	190
Figure 109: Triple-lap joint configuration used for the Al-Al-Al and Al-Steel-Al spot welds. ....	191
Figure 110: Macrosection of an Al-Al-Al triple lap spot weld made using RAFSSW. .	192
Figure 111: Interlocking of the top and bottom plate with the thicker middle plate of an Al-Al-Al triple-lap joint made using the RAFSSW process. ....	192
Figure 112: Al-Steel-Al triple lap spot weld with RAFSSW .....	193
Figure 113: No mixing or mechanical interlocking was observed for the Al-Steel-Al RAFSSW joint. ....	194
Figure 114: Cross section of an aluminum to steel FSSW spot weld using a tool that penetrates into the steel sheet [Bozzi].....	196
Figure 115: Aluminum plastically deformed into the threaded hole. a) top view of extruded weld zone material b) side view of threads c) side view with a standard nut attached to the threads.....	197
Figure 116: The proposed through hole method. A 0.125 inch hole is punched in the steel directly in line with the RAFSSW weld zone. The size, location, and orientation may be altered.....	198
Figure 117: % Volume of the available material to be extruded into the through hole according to the selected diameter of the through hole. ....	199
Figure 118: Tensile shear strength of spot welds made using the through hole with the RAFSSW process. Three cases are presented; no hole, center hole, and an offset hole.	

The dwell time and control force for each case are listed above (or within) their respective case. For all cases the welding tool and anvil had a rotation rate of 1200 rpm.

.....	201
Figure 119: Al-Steel-Al with a through hole. 1200 rpm, 1 sec, 4250 N control force. The extruded material has not completely filled the volume of the through hole. No weld joint is formed. ....	201
Figure 120: Al-Steel-Al with a through hole. 1200 rpm, 1 sec, 8000 N control force. The extruded material from the top and bottom sheet has not completely filled the volume of the through hole. A weld joint was formed within the through hole however. ....	203
Figure 121: Al-Steel-Al with through hole. 1200 rpm, 5 sec, 8000 N control force. The extruded material from the top and bottom sheets has completely filled the volume of the through hole. There is no observable joint line.....	204
Figure 122: The Friction Stir Spot Stitch welding process. d is the spacing between each FSSW spot weld.....	206
Figure 123: A series of overlapping spot welds created using the RAFSSW process. ..	207
Figure 124: Estimated torque vs. experimental torque for various plunge depths. ....	232

## LIST OF TABLES

Table 1: FSSW tool dimensions and material.....	72
Table 2: Chemical composition (% weight) of Al 6061-T6 .....	99
Table 3: Mechanical properties of Al 6061-T6.....	99
Table 4: Experimental factors and levels.....	102
Table 5: Experimental design for FSSW using a pinless tool .....	103
Table 6: Regression coefficients for shear load, spindle torque and temperature .....	106
Table 7: Temperature dependent material properties .....	120
Table 8: Temperature dependent material properties of Al 6061 T6.....	138
Table 9: Experimental Welding Parameters .....	159
Table 10: Experimental spot welding results.....	162
Table 11: Experimental results for the non-matched rotation rates for the FSSW tool and rotating anvil. ....	183

## CHAPTER I

### INTRODUCTION

#### Background

Friction stir welding (FSW) was invented by Wayne Thomas at The Welding Institute (UK) in 1991. As a solid-state joining process capable of joining light-weight metals with lower melting points, FSW quickly received the attention of many researchers around the world. In 1996, NASA began to investigate the use of Al-Li 2195 in the manufacture of the external fuel tanks in an effort to reduce the cost of shuttle launches. The difficulties in joining this alloy with traditional fusion techniques drove NASA engineers to explore FSW as a possible alternative. In 2005, just nine years later, NASA successfully took the FSW process from the laboratory to the manufacturing floor when external tank 134 took flight [Romine]. NASA's success with the process demonstrates the need and willingness of manufacturers to adopt new technologies in an effort to reduce cost and improve efficiency.

While FSW has been the focus of a great deal of research for more than two decades, friction stir spot welding (FSSW) didn't become a serious topic of interest until the early 2000's. The initial development of FSSW was performed by Sumitomo Light Metal Industries, LTD., Mazda, Kawasaki Heavy Industries, LTD., and Norsk Hydro. In 2003, Mazda implemented FSSW in the assembly of the rear door panel of their RX-8, the first noted application of the process [Mishra]. This quick three year turnaround compared to the NASA example above speaks to the level of understanding of the



FSSW processes garnered by the welding community in the first decade of its existence.

In FSSW, the joint is created by plunging a rotating tool into a weldment until the tool's shoulder reaches a desired penetration depth. It will remain at this depth for a specified length of time, at which point the tool is retracted. Unlike fusion welding, FSSW does not melt the parent material, require consumables such as filler rod, shielding gas, or welding sticks, and uses 99% less energy to create the weld [Feldman]. For these reasons FSSW can be considered a "green technology". The FSSW process can be characterized by three main parameters: rotation rate, plunge depth, and dwell time. Compared to the multitude of parameters involved in resistance spot welding, FSSW presents the operator with a simpler, more controllable process. Using technologies like self-piercing rivets affords manufacturers some of the same advantages of FSSW but adds to the overall complexity and weight of the design and increases the overhead for production.

One identified drawback of this process is that the tooling leaves a keyhole (the size of its dynamic volume – the volume created by rotating the tool's geometry) in the weld during retraction that requires removal via either post-processing or costly, highly specialized tool design. As such, pinless tool designs have been identified in the literature as a low-cost alternative in this situation. However, there exists very little information on the topic of the application of a pinless tool for FSSW and it is the purpose of this work to expand upon the understanding of the process through numerical simulation and experimentation.

## Overview of Work

Chapters II and III presents a review of previously published research on the topic of friction stir spot welding. Chapter II considers experimental investigations (methods and results) while Chapter III focuses on analytic and numerical models and their results. These chapters form the basis for the motivation of this dissertation.

Chapter IV covers the initial efforts on FSSW with a pinless tool. This work helped in understanding the role the pin and shoulder play in FSSW. It is accepted that for joining a specific thickness of plate there exists an optimal pin length and that the use of a longer pin will result in a lesser quality weld. It has also been shown that a pinless tool can be used to create spot welds that are approximately 90% as strong as those created with a pin of optimal length. However, the addition of a pin of any length greater than zero and less than the optimal length will result in a proportional increase in weld strength [Bakavos]. This claim is supported by interpolating the resulting weld strengths created with a pinless tool and a tool with a pin of nearly optimal length. In this work, sub-optimal pin lengths (pin lengths that do not penetrate the bottom sheet) were tested and it was found that the inclusion of such a pin is detrimental to weld quality. The results of an analytic model of the material flow during spot welding found that, for thin sheet, the shoulder largely contributes to the shape and size stir zone of the spot weld. It was found that unless the pin is long enough to contribute to the effective size of the stir zone it will only leave a keyhole in the spot weld, reducing the load carrying capacity.

Chapter V continues the investigation of the use of pinless tools for FSSW. A new spot welding tool was developed with a spherically tapered and scrolled shoulder.

Experiments determined that, in addition to providing additional stirring in some instances, the inclusion of a pin added to the overall stability of the process. Using the traditional pinless tool required the need for rigid clamping due to the tool “chattering” during the initial plunge phase of spot welding. The spherically tapered shouldered improved the stability and the tolerance of the FSSW process. This new tool was then used in a large experimental study to investigate the effect the rotation, plunge, and extraction rates and the dwell time had on weld quality. The plunge rate had been previously identified in the literature as the most important parameter for FSSW. The results found the plunge rate to be almost negligible when compared to rotation rate, dwell time, and plunge depth. By comparing the experiments with the data presented in the literature one is led to conclude that welding with parameters that result in lower heat inputs resulted in higher quality welds i.e. low rotation rates and short dwell times. The data that supported the claim on the importance of plunge rate was actually found to be largely dependent on pin length and as a result, plunge rate. The use of a pin requires a slower plunge rate which can significantly increase the heat input into the weld during the plunge stage. By eliminating the pin it is possible to drastically reduce the cycle time of the process by eliminating the need for a lengthy plunge phase.

A transient CFD model was created for the pinless FSSW tool to understand the material flow and heat transfer during welding. The model was found to be in good agreement with experimental temperature measurements made during welding. It was found that the majority of the material within the weld zone rotates at a much lower rate (< 5%) than the FSSW tool. Combining the results of the CFD model with the experimental data it was determined that the highest weld quality was achieved when the

weld zone completed approximately one complete rotation during welding. “Over-stirring” the spot weld was found to negatively affect weld quality.

Chapter VI introduces the idea of using a rotating anvil for FSSW and presents an in-depth look into the process. The objective was to improve the weld quality by increasing the size of the stir zone and to increase the thickness of plate that could be joined with a pinless tool. A transient CFD model was created to help understand how the addition of a rotating anvil would affect the material flow in the stir zone and to aid in tool design and parameter selection. A device was designed and built so that a rotating anvil could be tested using the existing FSW machine at Vanderbilt. After several iterations the process was successfully able to create quality spot welds reliably. In addition to being able to weld material up to 0.125 inches thick (both workpieces are 0.125 inches thick for a total joint thickness of 0.25 inches), the initial objective of the device, it was also found to improve the strength of the welds made in thinner plate. The rotating anvil also helped to reduce the axial load experienced during welding and lowered the cycle times of the process. The rotating anvil is a promising technology that is already beginning to garner the interest of the FSW community for its applications in automotive and aerospace manufacturing.

Chapter VII investigates the effect tool rotations have on the quality of the spot weld. To achieve this goal, different combinations of rotation rate and dwell time were investigated. A linear relationship was found to exist between the number of tool rotations completed during the spot weld and the resulting tensile shear strength. Spot welds that only completed 10 rotations were 177% stronger than those created at 50 tool rotations. Further investigation revealed that the energy generated during the welding

operation had strong linear relationship to the tensile shear strength. A modified open-loop position control system is proposed that could monitor and limit the energy generated during friction stir spot welding by adjusting the dwell time.

Chapter VIII explores several novel applications of the rotating anvil for FSSW including triple-lap joints and a “stitch” welding method. First, the operation of the welding process is improved by implementing an open-loop *force* control system. Selecting axial force as the input variable resulted in a more repeatable process and improved the cycle time. Additionally, Non-matched rotation rates between the welding tool and anvil are also investigated.

## CHAPTER II

### FRICITION STIR SPOT WELDING

#### The Friction Stir Spot Welding Process

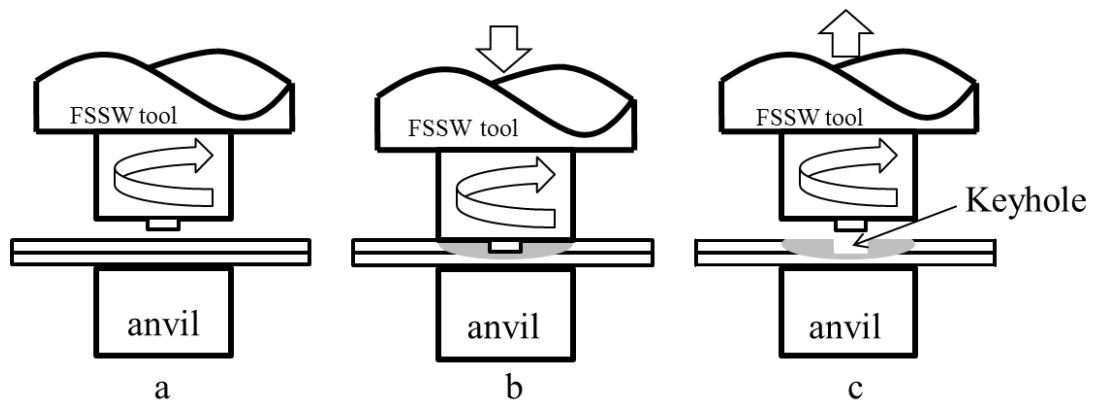


Figure 1: The friction stir spot welding process.

FSSW, as stated in the introduction, is a solid-state joining process, meaning the base metal is not melted during welding. Like in FSW, the process begins by plunging a rotating tool into the workpiece. During the plunge, the tool begins to heat the workpiece via frictional contact. As the temperature of the workpiece increases, the material in the immediate vicinity of the FSSW tool begins to soften, allowing for plastic flow of the weldment material. Once the tool reaches the desired level of penetration into the workpiece the plunge motion of the tool is halted and the tool continues to rotate for a specified length of time. During this “dwell period”, the material continues to experience plastic deformation. The shoulder of the FSSW tool provides a forging force and retains the plastically deformed material from being expelled from the weld zone. The forging

force places a large axial load (perpendicular to the workpiece) on the welding frame and it is supported by the use of a rigid backing anvil. After the dwell period is complete, the rotating tool is retracted from the workpiece. The weld is formed, almost immediately, when the tool disengages from the workpiece (Figure 1).

### Advantages of FSSW

The advantages of FSSW when compared to other welding technologies are the same as those identified by Mishra et al. for FSW and can be seen in Figure 2. Because of the advantages FSW/FSSW provides manufacturers, the process is beginning to see more applications ranging from the 2013 Honda Accord [Honda] to the newest Apple iMac desktop computers [Dillet]. Despite these advantages, FSSW is still a long ways from being used by the mechanic in your local auto-garage due to the large process forces during welding. These large forces incurred during the process necessitate the use of large rigid robots to perform the welds [Cook].

Metallurgical benefits	Environmental benefits	Energy benefits
<ul style="list-style-type: none"> <li>• Solid-phase process</li> <li>• Low distortion</li> <li>• Good dimensional stability and repeatability</li> <li>• No loss of alloying elements</li> <li>• Excellent mechanical properties in the joint area</li> <li>• Fine recrystallized microstructure</li> <li>• Absence of solidification cracking</li> <li>• Replace multiple parts joined by fasteners</li> <li>• Weld all aluminum alloys</li> <li>• Post-FSW formability</li> </ul>	<ul style="list-style-type: none"> <li>• No shielding gas required</li> <li>• Minimal surface cleaning required</li> <li>• Eliminate grinding wastes</li> <li>• Eliminate solvents required for degreasing</li> <li>• Consumable materials saving, such as rags, wire, or any other gases</li> <li>• No harmful emissions</li> </ul>	<ul style="list-style-type: none"> <li>• Improved materials use (e.g., joining different thickness) allows reduction in weight</li> <li>• Only 2.5% of the energy needed for a laser weld</li> <li>• Decreased fuel consumption in lightweight aircraft, automotive, and ship applications</li> </ul>

Figure 2: Advantages of FSW/FSSW [Mishra]

## Friction Stir Spot Welding Terminology

### *Process Terminology*

It is important to establish a common language when discussing FSSW and as such, key terms will be defined in this section. When appropriate the terminology outlined by Threadgill et al. will be used to discuss FSSW [Threadgill].

The FSSW tool is considered to be the “whole of the rotating device between the machine spindle and the workpiece.” The shoulder of the tool can be defined as the component of the tool that rests on top of, or slightly beneath, the workpiece and is designed to generate heat via frictional contact. The pin or “probe” of the tool can be defined as being invariably smaller in diameter than the shoulder and completely plunged into the workpiece during welding (Figure 2).

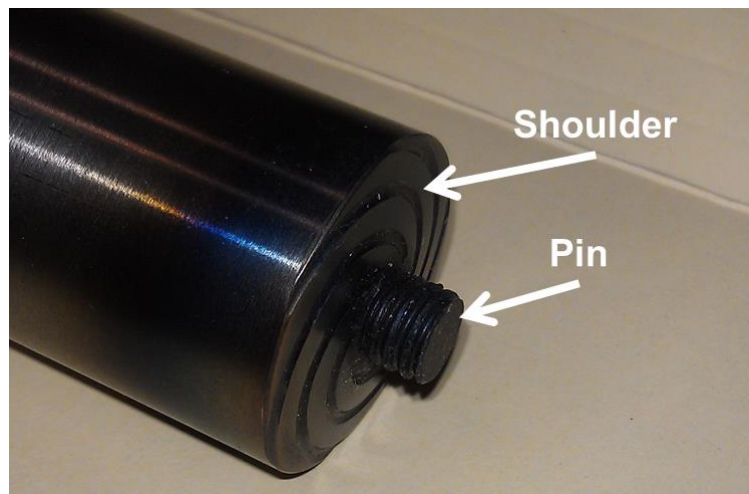


Figure 3: An FSSW tool with the shoulder and pin identified



The term “tool rotation speed” is the preferred term to describe tool rotation. The direction of rotation is defined from a top-down view; the use of the terms clockwise or counter-clockwise is appropriate.

The distance the tool’s shoulder penetrates into the workpiece during welding is defined as the “heel plunge depth” or “plunge depth”. This term is sometimes incorrectly used by members of the FSSW welding community to describe the amount the pin penetrates into the workpiece or, even worse, used to describe the length of the pin. Any alternate uses of this term should be avoided as it is misleading for the reader.

The time the tool remains plunged into the material is defined as the “dwell time”. The velocity at which the tool plunges into the material is defined as the “plunge rate” and the velocity at which the tool is withdrawn from the weld be defined as the “extraction rate”.

The process forces of concern during FSSW are the axial force, defined as the force experienced by the tool during welding perpendicular to the workpiece, and the spindle torque, defined as the torque acting about the tool’s vertical axis (of rotation) during welding.

The keyhole is a result of the FSSW process and occurs when the tool is retracted from the weld. The shape and size of the keyhole are dependent upon the geometry (dynamic or swept volume) of the tool used to make the spot weld and the plunge depth selected.

## *Weld Zone Terminology*

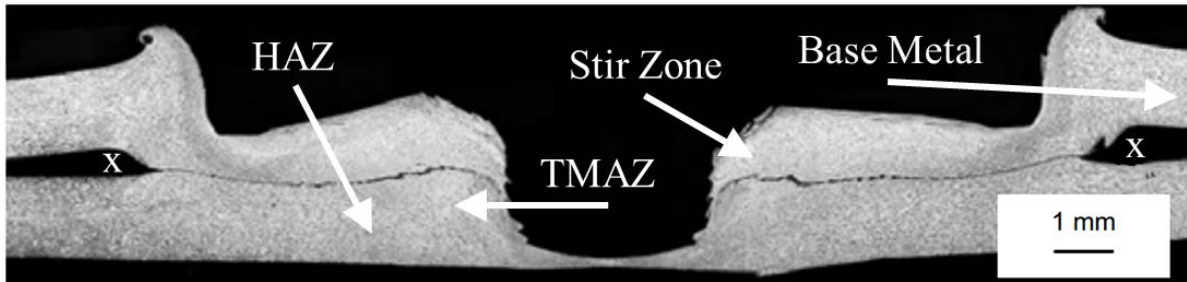


Figure 4: Cross-section view of an FSSW spot weld [Arul]

The cross section view of a spot weld made using FSSW (Figure 3) has a significantly different appearance than that of a conventional FSW weld, the most notable being the presence of the keyhole. The area around the pin and shoulder represent the stir zone while the slightly darker area represents the thermomechanically affected zone (TMAZ). The stir zone is defined as being the material in immediate contact with the tool during welding. The TMAZ is defined as being affected by both heat and deformation. Two unwelded regions of the interface, labeled with x's in Figure 3, can be seen at the edge of the weld zone. The heat affected zone (HAZ) is defined as being affected only by heat [Threadgill]

## *Joint Configurations*

FSSW is typically restricted to primarily one or two joint configurations. The most common being the lap joint. In the lap joint configuration, one sheet or plate is placed directly on top of another sheet. The weld is then made by plunging the tool into

the workpiece such that the shoulder rests on the top sheet while the pin penetrates into the bottom sheet. This joint type is illustrated in Figure 4.

The other less common joint type for FSSW is the butt joint (Figure 4.b). In the butt joint configuration two sheets of identical thickness are abutted against each other. For this case, the spot welding tool is plunged into the seam between the two plates.

For either case the joint-line is semi-infinite. Simply put, it is an unavoidable consequence that there will be a “crack” that will terminate somewhere along the interface between the base material and weld zone. This “crack” will occur whenever the joint line is not completely eliminated during the welding process and is not limited to FSSW e.g. the use of FSW for a lap joint configuration would also encounter this issue.

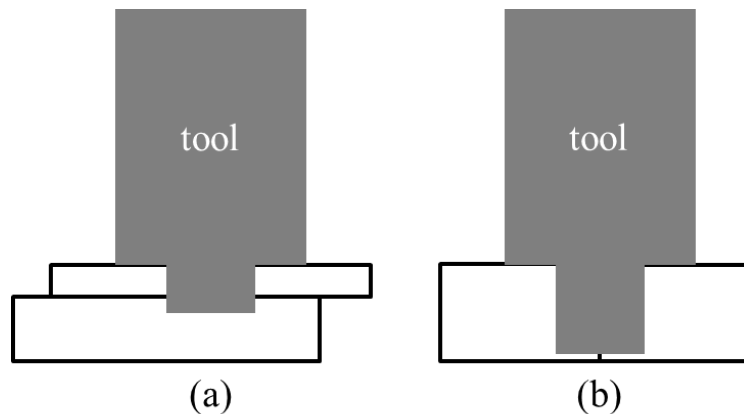


Figure 5: Joint configurations for FSSW

## Process Parameters

As stated in the previous sections, the FSSW process is dependent on a handful of process parameters that include tool rotation speed, plunge rate, dwell time, and plunge depth. Other parameters may be of interest, especially for some of the variants of FSSW that will be discussed in later sections, and should be noted when relevant. In this section the process parameters investigated in the literature will be discussed.

The tool rotation rate is a dominant process parameter in FSSW as it is responsible for the heat input into the weld. A wide range of rotation rates can be used for FSSW depending on the application and is more often restricted by the capabilities of the spot welding machine being used. A study by Karthikeyan et. al. [Karthikeyan] evaluated tool rotation rates between 600 and 1800 rpm while Arul et. al.[Arul] evaluated rotation rates between 1500 and 3000 rpm. These two studies effectively capture the majority of the tool rotation rates presented in the literature concerning the joining of aluminum alloys. The tool rotation rate is proportional to the heat input into the weld. The optimal condition for tool rotation rate will depend on the selection of the other process parameters, tool geometry, and the material(s) being welded.

The plunge rate largely goes unreported in the FSSW literature despite being identified by Karthikeyan et al. as being the parameter with the greatest influence on the tensile shear fracture load [Karthikeyan] of the resultant spot weld. The time to complete the plunge will depend on the geometry of the FSSW tool, primarily the pin length, the plunge depth, and plunge rate. Higher plunge rates will place higher axial loads on the welding machine. Plunge rates reported in the literature range from 0.4 [Tozaki 2007] – 6.0 [Bakavos] inches per minute. Depending on the combination of FSSW tool and

plunge rate the plunge stage process can require anywhere from less than a second to more than a minute.

The dwell time of the process is the window during which the weld is created by maintaining the tool at the desired weld height and may or may not be longer than the plunge and extraction times. The depiction of the process in Figure 6 shows the dwell time as being longer than the plunge and extraction times. As previously stated, during this part of the process, the material beneath the FSSW tool is experiencing severe plastic deformation which will lead to the formation of the weld. The short dwell times associated with FSSW, 0 – 10 seconds, result in a transient, or dynamic, process, much different than that of the relatively steady-state FSW process. This short timespan may increase the difficulty of implementing a closed-loop feedback control like those used for FSW.

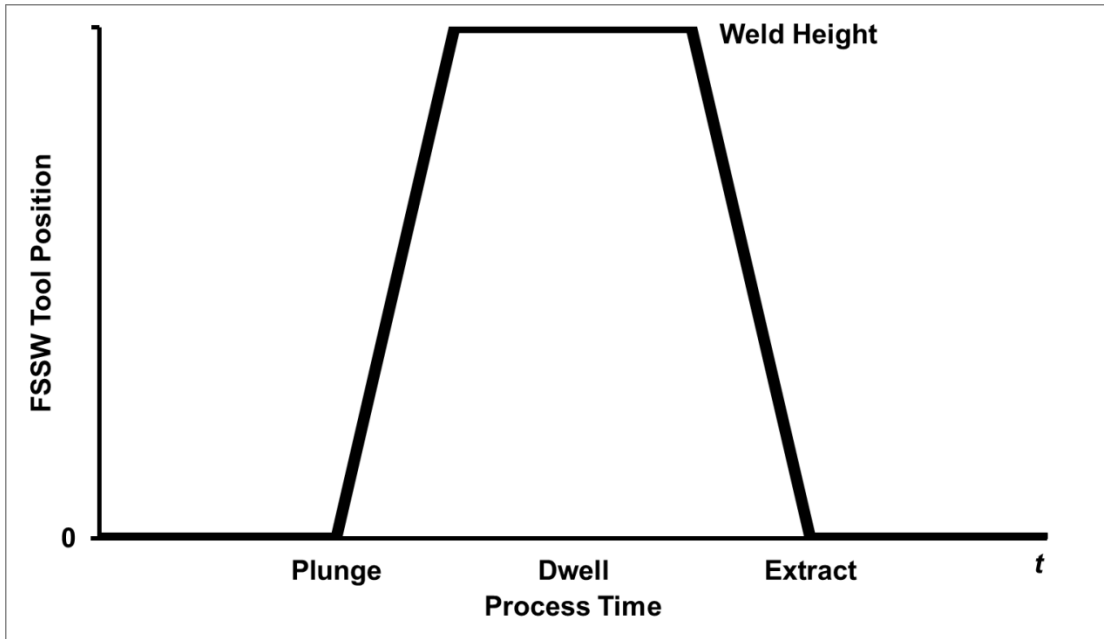


Figure 6: The FSSW cycle

The plunge depth can be thought of as the contact condition or rather the amount of contact that exists between the FSSW tool's shoulder and weldment during welding. If the plunge depth is too large, more material will be displaced than the shoulder is designed to contain and excess weld flash will form. If the plunge depth is too shallow there will not be a sufficient forging force and the weld may not be properly formed. For a traditional flat-shouldered tool this acceptable window of plunge depths ranges has been experimentally observed to be only  $\pm 0.003$  of an inch. A poor selection of plunge depth is tied to the observation of several different types of flaws and defects and will be discussed in a later section. In FSW, the plunge depth (contact condition) is often time maintained via force control, which as previously mentioned, may not be a viable option for FSSW. This issue may be addressed by creating more robust FSSW tool designs.

## Tool Design

The design of the FSSW tool is paramount for weld quality and as such, is a popular topic for researchers working with FSSW. In addition to weld quality, the selection of the tool design has a profound effect on tool performance, load bearing ability, tool lifetime, and process economics. The focus of this work will be in joining materials with relatively low melting points, such as aluminum, which are commonly welded using steel tools [Rai]. The observed wear experienced by tools made from steel during the FSSW of traditional aluminum alloys is negligible and will not be discussed at length in this work.

The geometry of the tool affects the heat generated during welding, plunge force, spindle torque, and the material flow during welding. Dimensions of the shoulder and probe, the inclusion of features on the probe and/or shoulder, and the shape of the shoulder and probe for FSSW will be discussed in this section.

### *Probe Geometry*

A wide variety of probe shapes have been investigated for FSSW. Bilici et al. reviewed six different probe shapes to identify the optimal geometry for joining polyethylene sheets using FSSW (Figure 7). The geometry of the probe was found to significantly affect the thickness of the weld nugget and tensile strength. Of those, the tapered cylinder (TC) was found to create the strongest welds at similar plunge depths [Bilici].

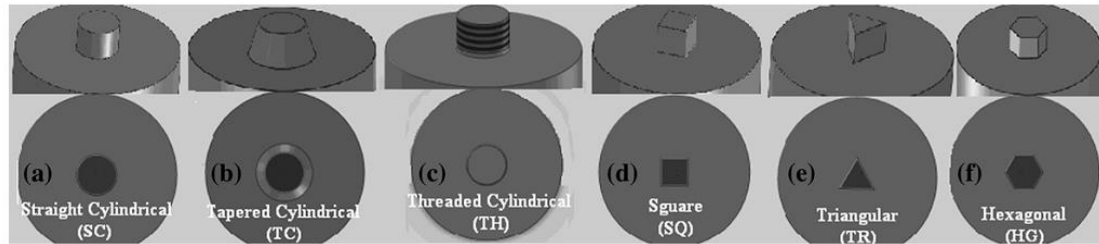


Figure 7: FSSW tool profile and pin size (d): (a) straight cylindrical, (b) tapered cylindrical, (c) threaded cylindrical, (d) square, (e) triangular and (f) hexagonal. [Bilici]

A modified triangular probe design was introduced by Badarinarayan et al. and was compared to a more traditional threaded probe tool for joining Al 5083 (Figure 8). The tool geometry was found to affect the formation of a “hook” at the joint interface, a common defect found to occur when welding in the lap-joint configuration. The severity and shape of the hook was reduced when using the triangular shaped pin and resulted in welds that were twice as strong as those created with the threaded cylindrical probe. Successive rotation of the asymmetric geometry of the triangular probe was found to improve material flow around the probe in the radial direction while the threads were found to improve material flow in the vertical direction [Badarinarayan 142-48]. A more detailed look at material flow during FSSW will be presented in the following sections.



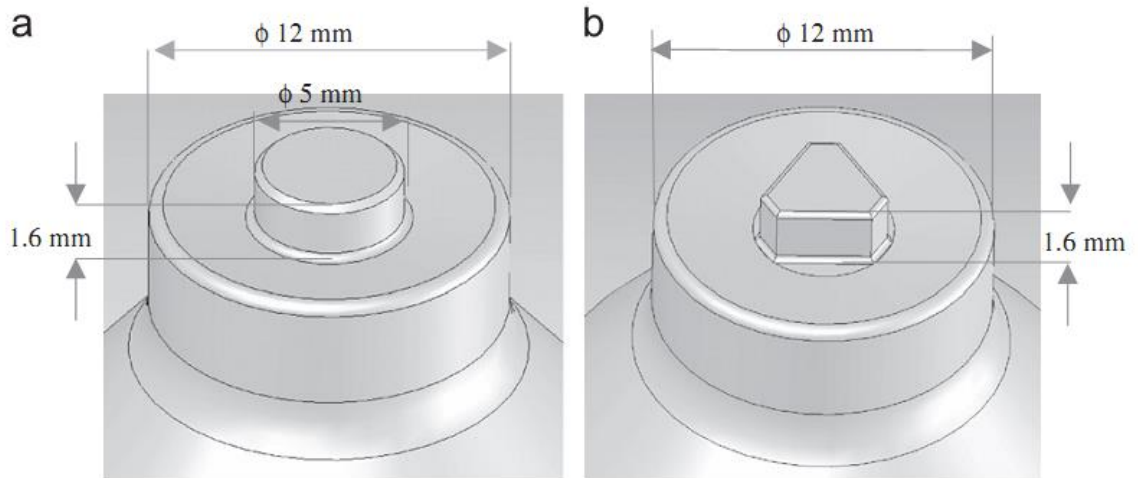


Figure 8: Schematic illustration of FSSW tool geometries (a) cylindrical pin shape (threads not shown in illustration) and (b) triangular pin shape [Badarinarayan 142-48].

The tool probe designs presented thus far are fairly standard and their forms can be found in-use for FSW as well. Yuan et al. presented two unique tool probe designs for spot welding Al 6016-T4 using FSSW; the first being a long step spiral pin (CP) and the second being an off-center feature tool with three hemispherical pin features (OC) (Figure 9) [Yuan].

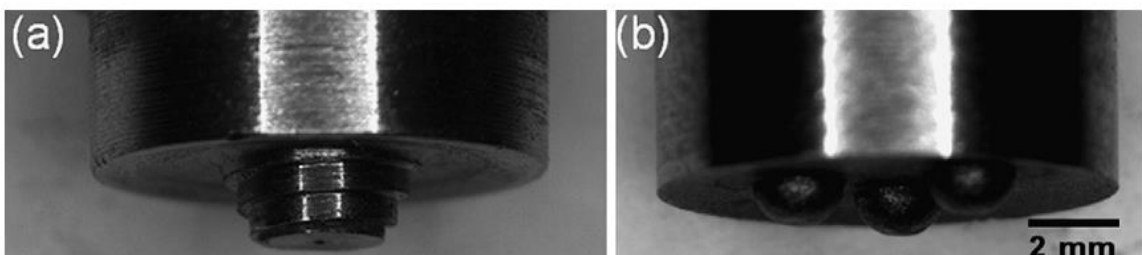


Figure 9: Macro images of a) long step spiral pin (CP) and b) off-center hemisphere pin (OC) [Yuan]

Their results indicated that both tool pin designs resulted in spot welds of about the same maximum mechanical strength,  $\approx 3.3$  kN, at the same process parameters (Figure 10).

This work by Yuan et al. is one of only a few that compares a traditional pin tool to one without a pin (sudeo-pinless in this instance). More discussion will follow on the differences between a pin and pinless tool design.

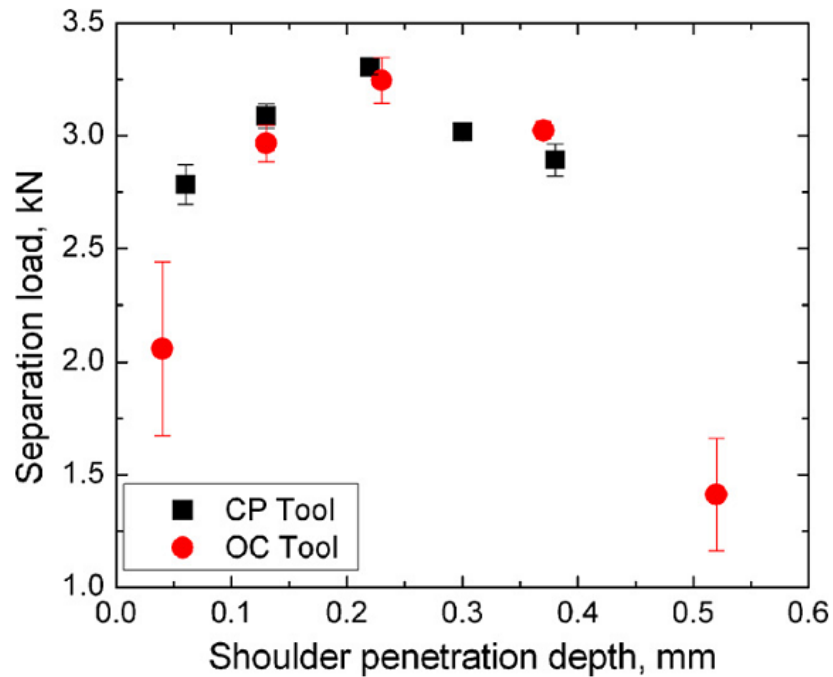


Figure 10: Lap-shear separation load as a function of shoulder penetration depth [Yuan]

### *Probe Length*

The length of the FSSW probe, or pin, is typically selected on the basis of workpiece thickness, i.e. thicker workpiece requires a longer probe. Tozaki et al. found that the tensile shear strength of the weld increased with increasing probe length (above 25% bottom sheet penetration) regardless of tool rotational speed or dwell time. The

increase in shear strength associated with the longer probe lengths was attributed to an increase in the size of the weld nugget [Tozaki 2007]. Bakavos et al. found that the probe lengths that penetrated the bottom sheet by more than 20% negatively affected the tensile shear strength of the weld. In the same study, a pinless tool was found to create welds of comparable strength to those created with a traditional tool with a probe (Figure 11).

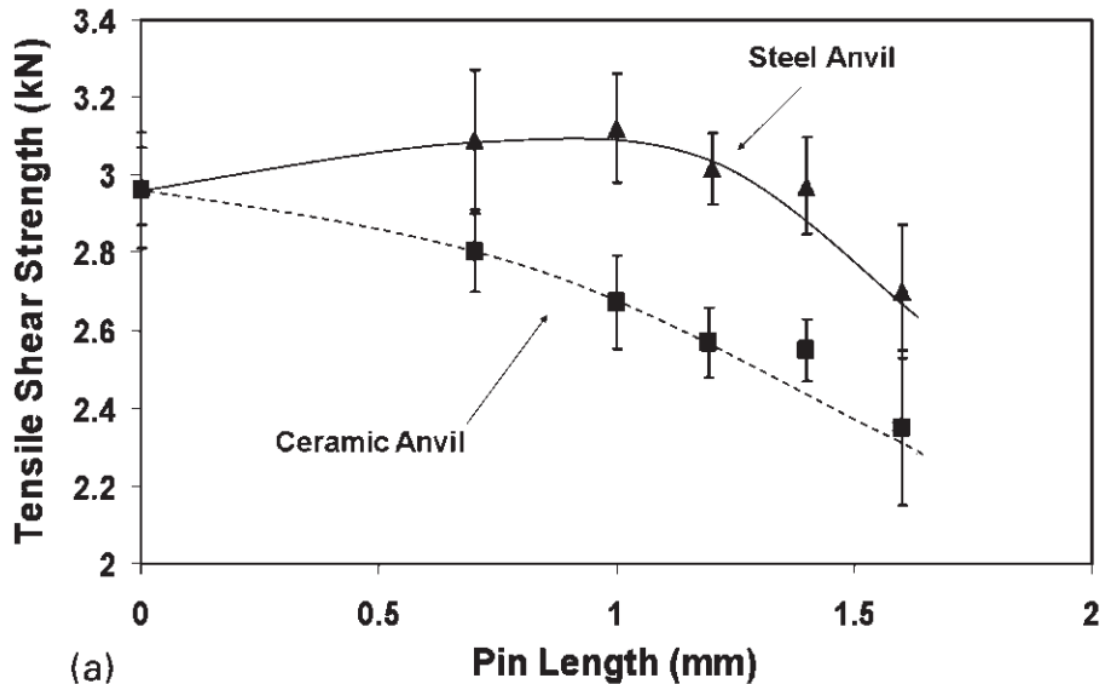


Figure 11: Effect of FSSW pin length (x-axis) and anvil insulation on 6111 aluminum alloy tensile shear strength (y-axis) [Bakavos 2009]

### *Shoulder Geometry*

The shoulder geometry of the FSSW tool largely contributes the heat generated during welding, provides the forging force needed to create the weld, and retains the plasticized material within the weld zone. By manipulating the shape and form of the shoulder researchers have been able to improve upon these important functions. The

inclusion of features on the shoulder has been shown to increase the shoulder's effect on the plasticized material's flow field. The diameter of the shoulder is proportional to heat generated during the weld, spindle torque, axial load, and the volume of the weld zone. The details of these relationships will be discussed in later sections.

The shape of the FSSW tool's shoulder is typically concave, flat, or convex (Figure 12). Badarinarayan et al. investigated the differences these different geometries may have on the mechanical properties of spot welds made at identical parameters. The authors claim a 15% improvement in mechanical strength using the concave shoulder when compared to the convex shoulder [Badarinarayan 814-23]. However, in the discussion of their experimental approach they are not clear as to why they chose the selected plunge depth. As previously stated, the selection of a plunge depth for an FSSW tool is very sensitive to position and as such, a large difference in mechanical properties would be expected if an arbitrary plunge depth was selected for three different shoulder geometries. For example, the optimal plunge depth for a concave shoulder may not be the same as that of a flat or convex shoulder.

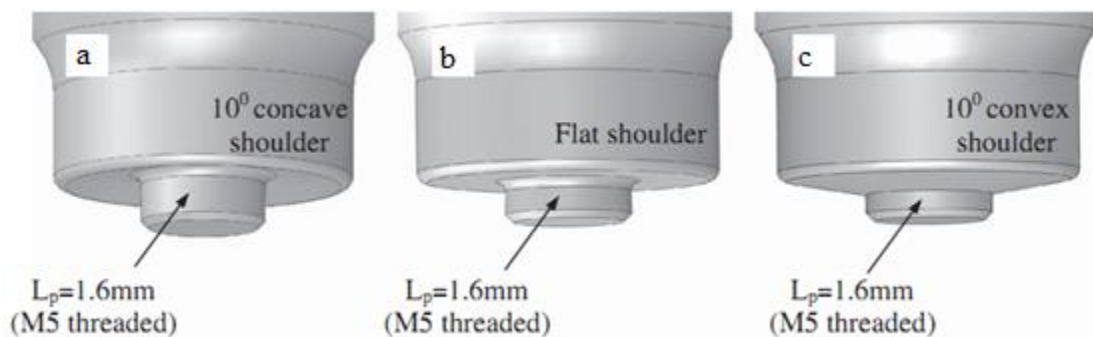


Figure 12: Schematic of FSSW tool shoulder geometries a) concave, (b) flat, (c) convex [Badarinarayan 814-23]

The shoulder of the FSSW tool may include features to better contain material and improve upon its contribution to stirring during welding. The inclusion of shoulder surface features has been confirmed to greatly affect surface roughness and metal deformation in the uppermost layers of the weld zone. Additionally, by incorporating these shoulder features in the design researchers have been able to improve the fatigue resistant properties of the weld zone [Burford].

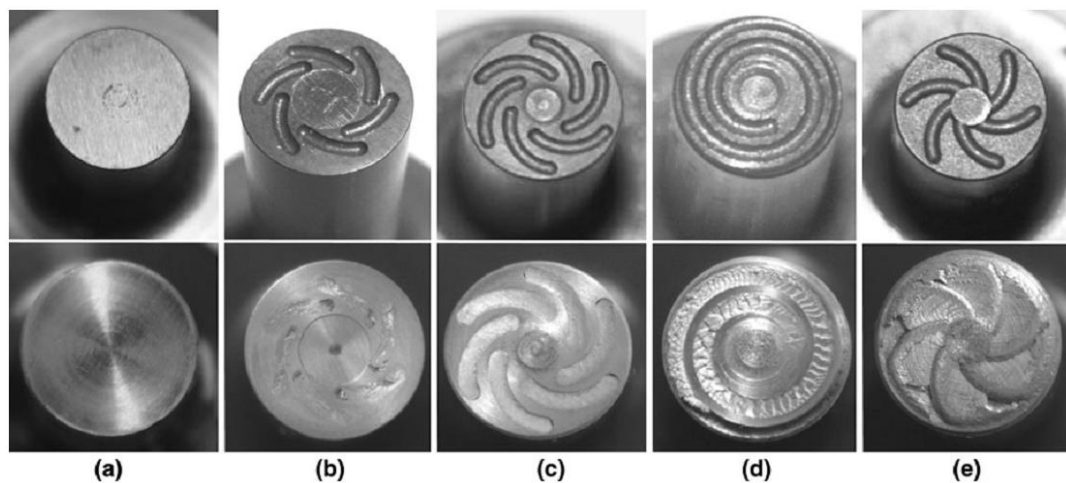


Figure 13: Different FSSW shoulder features shown before and after twenty welds: (a) featureless tool, (b) the short flute wiper tool (ii), (c) the long flute wiper tool (iii), (d) the fluted scroll tool (iv), and (e) the proud wiper tool (v) [Bakavos 2011].

Bakavos et al. studied different shoulder geometries for FSSW using a pinless tool design (Figure 13). The features investigated were variations of a “wiper” and “scroll” design. The variations of the wiper tools had six symmetrically arranged machined flutes cut into the surface of the shoulder that ended before the outer diameter. The scroll tool design consisted of a machined fluted scroll that started at the center of the shoulder and ended at the outer diameter. As previously mentioned, a pinless FSSW tool design is an attractive alternative to the traditional probe tool design because of the

elimination of the key-hole. When using shoulder features on a pinless tool, it was found that a balance must be kept between the tool coupling with top sheet before the temperature of the material becomes high enough to achieve bonding in the radial and vertical directions [Bakavos 2011]. If the tool couples too strongly with the top plate it may be difficult to create a quality weld due to cracking in the parent material. The use of the scroll and wiper features on a pinless shoulder design was found to strongly influence the flow of material during welding.

### Material Flow

The flow of plasticized metal during spot welding with a pinless tool is dependent upon the selection of process parameters and the design of the FSSW tool's shoulder which has been discussed at length. During welding, the material from the top sheet is pushed down into the bottom sheet where material is displaced outward in the radial direction and, given enough process time, back up into the top sheet where it will be re-incorporated into the stir zone (Figure 14). The displacement of the material from the bottom sheet into the top sheet may result in a hooking defect which will become more pronounced with longer dwell periods.

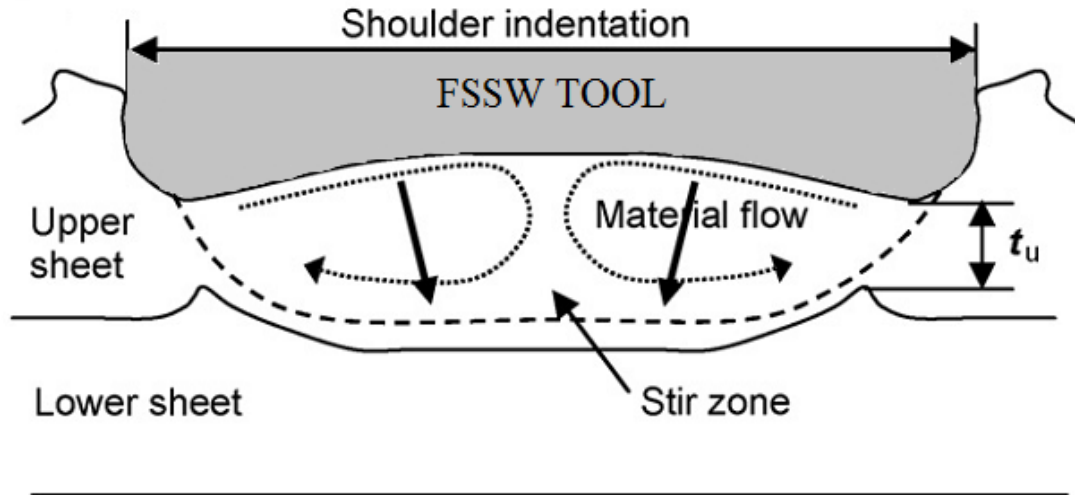


Figure 14: Schematic illustration of material flow with a pinless tool [Tozaki 2010]

Using aluminum alloys with different copper content and metallographic techniques, Bakavos et al. [Bakavos 2011] were able to experimentally visualize the material flow of a spot weld made using a pinless tool with features (Figure 15). The weld samples were prepared by using a three-plate approach in which the bottom sheet was split along the weld center. The result nicely captures the evolution of the material flow from the top sheet into the bottom sheet. For a dwell time of just 0 seconds, it can be seen that stir zone is limited to the top sheet however the joint line in the bottom plate has experienced slight displacement. After 2.5 seconds the stir zone can be observed to completely penetrate into the bottom plate and the joint line in the bottom plate is completely incorporated into the weld zone. The development of the hooking defect during welding is also shown (highlighted by the dashed line).

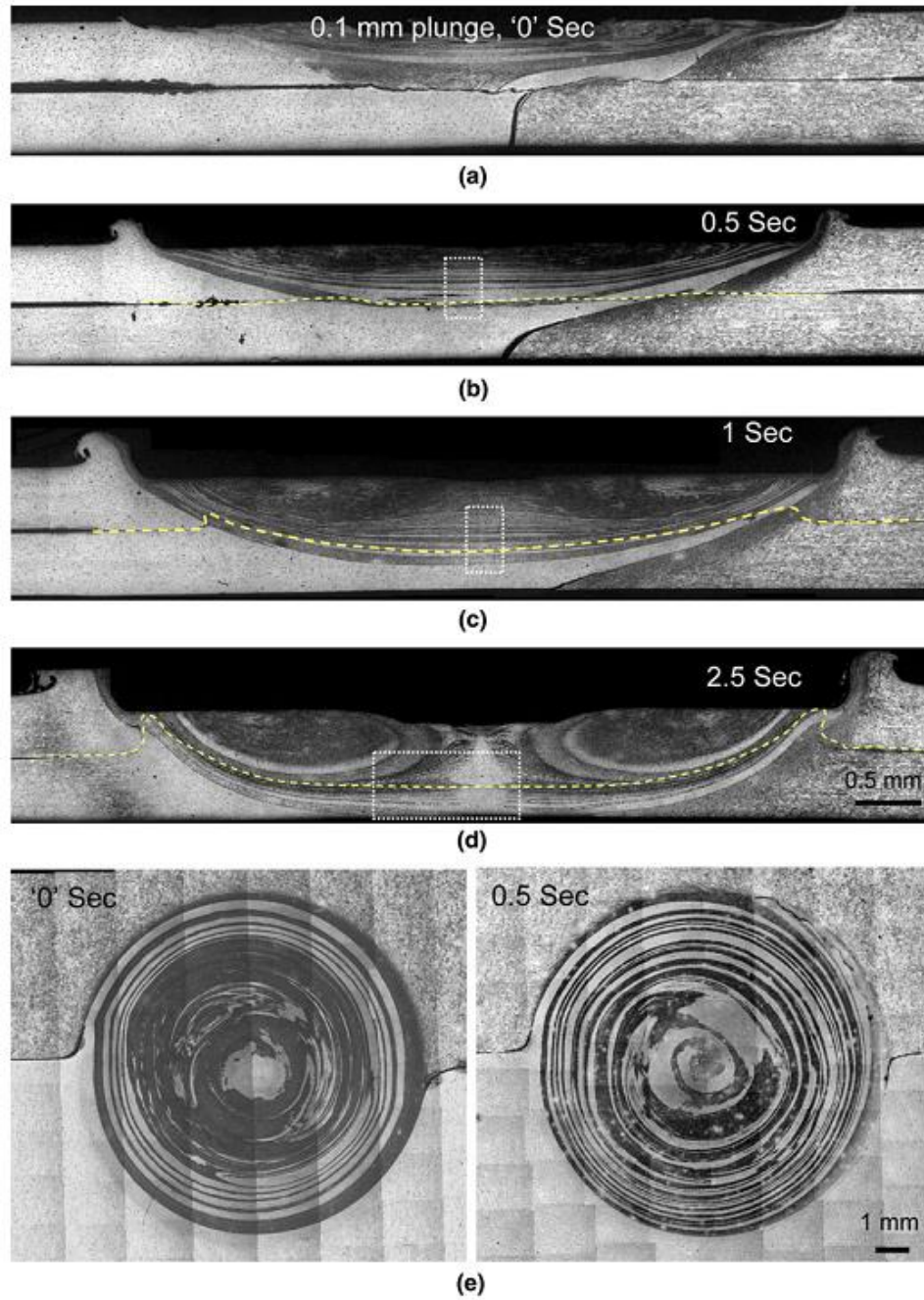


Figure 15: Material flow observed during FSSW. (a-d) cross section views of the weld formation sequence, (e) plan view below top surface of weld for 0 and 0.5 seconds of dwell time [Bakavos 2011].



## Defects and Failure Modes

Spot welds made using FSSW are not immune to defects. In common with other friction welding processes, the FSSW metallurgical bond is created through the application of high pressure, heat, and a means for deformation. However, due to a lack of tool translation and a probe, it is sometimes difficult to create a strong bond due to a lack of material flow when using a pinless FSSW tool design. The most common defects encountered with FSW are voids, joint line remnants, hooking defects, top-sheet thinning, and root flaws. Voids, or volumetric defects, are not typically observed in FSSW due to the symmetric nature of the process. A root flaw, or incomplete root penetration, is a defect associated with the butt-joint and is not an issue for FSSW of lap-joints.

The most detrimental weld defect, a defect unique to FSSW with a pinless tool, is a total lack of weld consolidation stemming from a combination of insufficient forging force, rotation rate, and/or dwell time. Insufficient forging force can be caused by a poor selection of the plunge depth parameter, run-to-run variations in workpiece dimensions, or robotic linkage deflection. Other contributing factors could be tool geometry, excessive weld surface contamination, or material thickness (material selection is too thick i.e. beyond the capability of the process). In the case of this defect, the stir zone never fully propagates into the bottom sheet and the joint is never formed.

The hooking defect, named for its distinct shape, is a characteristic flaw found in both FSW and FSSW of lap-joints. A partial metallurgical bond, the hook is formed in the weld zone at the interface of the workpieces. The severity of the “hook” depends largely upon the geometry of the tool and the process parameters selected. The hook forms when the weld zone penetrates into the bottom sheet which in turn creates an

upward bending of the joint interface. The oxides that are present on the surface of the workpiece may or may not be completely incorporated into the weld zone which results in the variation of the bonding condition. The presence of the hook may diminish the mechanical properties of the spot weld since failure can occur along the hook when placed under a load [Badarinarayan 142-48]. In Figure 16 the distinction between an unbonded, partially bonded, and completely bonded region can be seen.

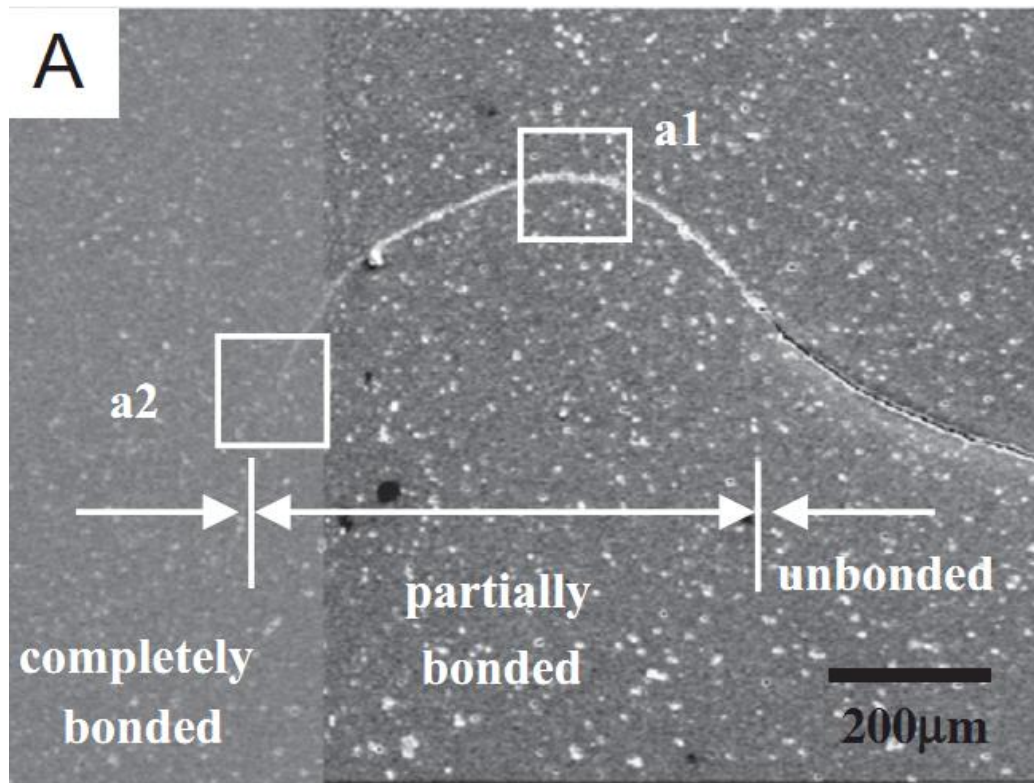


Figure 16: The hooking defect observed in a FSSW spot weld [Badarinarayan 142-148]

The thin oxide layer that exists along the joint interface before welding may also remain within the weld zone after the joint has been formed. Though it is referred to as a defect or imperfection, this is not an accurate classification as it is virtually unavoidable. The oxide particles are observed to form a wavy path that delineates from the original

joint line. The joint line remnant does not typically negatively affect the mechanical properties of the spot weld [Threadgill].

Top-sheet thinning, or effective thickness, is a term used to describe the minimum thickness of the spot weld measured beneath the shoulder (not within the key-hole) and is a result of the selected plunge depth. This effect is caused by the shoulder mechanically displacing material during the plunge and dwell phases of the process. While more stirring can be achieved by increasing the plunge depth the load-bearing capability may begin to suffer as the cross-section of the weld decreases.

During the spot welding process excess material displaced by the FSSW tool is expelled from under the shoulder and out of the weld zone (Figure 4). This can result in thin flakes of material that can easily be brushed off of the weld surface to a thick ring of material that surrounds the spot weld. In addition to being a cosmetic nuisance, the formation of weld flash removes material that would otherwise be in the weld zone and can lead to a weaker weld joint. Weld flash can be reduced or eliminated by proper tool geometry and parameter selection.

When a FSSW spot weld is subjected to excessive loading three distinct failure modes are typically observed, the first being the “shear mode”. This mode is characterized by a complete separation of the top and bottom plate with the weld nugget remaining in the top sheet. The fracture occurs along the original joint line interface between the top and bottom plates. The “nugget pullout” failure mode is again characterized by a complete separation of the top and bottom plate. However for this mode the nugget remains attached to the bottom sheet. For this mode the fracture occurs along the perimeter of the weld zone in the top plate. The “mixed” mode is a combination

of the other two modes but without plate separation. In this mode the nugget is partially separated from both the top and bottom plates, though the nugget may “peel” away from the bottom plate. The fracture occurs along the perimeter of the weld zone in both the top and bottom plate.

### Notable FSSW Variations

There are two notable variations of the FSSW process; refill FSSW and swing FSSW. The refill FSSW process was developed by GKSS in 2003. In refill FSSW, a purpose-built machine is used to create a spot weld without a keyhole that is nominally flush with the original workpiece surface. This is accomplished by actuating the three components of the system, a clamp ring, shoulder, and pin, independently during welding. The process begins with the clamp firmly holding the weldment in place. The rotating shoulder then makes contact (the probe at this point is completely retracted) and begins to heat the workpiece. Once the temperature of the workpiece is sufficient, the probe is extended into the workpiece. As the probe penetrates the workpiece, the shoulder retracts enough to create a reservoir that will allow for the material displaced by the probe to be contained. When the probe retracts the shoulder is lowered back toward the workpiece, pushing the expelled material back into the weld zone, filling the keyhole. The weld is completed when the pin is completely retracted back into the shoulder.

In swing FSSW the tool is traversed a short distance during the dwell phase of the process. This short tool translation results in a larger contact area that may result in higher joint strength. A keyhole would be present in the resultant spot weld unless a pinless tool was used.

While both of these alternative FSSW processes result in quality spot welds with the possibility of higher joint strengths only one of them eliminates the undesirable keyhole. The downside of these alternatives is that they require expensive, highly specialized equipment to make the spot welds.

## CHAPTER III

### FSSW MODELING AND SIMULATION

#### Introduction

Gathering information experimentally about a process can be time consuming and cost-prohibitive. While experimentally varying a parameter or set of parameters and noting a change in the response may eventually lead to new understandings, the ability to model the process is an invaluable tool for a researcher. The primary goal of any model is the ability to predict how a system will respond given a change of an input. Whether it is through an analytic or numeric approach, the use of modeling is not unique to FSSW and is par for the course for more mature manufacturing processes.

In this chapter several different modeling techniques will be presented as they apply to FSSW, though the steps needed to obtain a numerical simulation will be the main focus. Analytic models are ideal as they are closed-form and have definite solutions. These analytic models are based on a sound physical understanding of the process and can be used to make reliable predictions about the system. Another approach would be to generate an empirical based model, that is, a model based on experimental observation. This type of model is susceptible to experimental error and can be misleading if the fundamental understanding of the process is lacking. Great care should be taken when creating an empirical model. Empirical models are however very useful in characterizing a system, capturing the relationship between parameters, and optimizing a process. For more complex systems a numerical model may be useful to the researcher.

Numerical models require inputs based on the process in order to accurately establish initial conditions, boundary conditions, and material properties. Input data is commonly taken from a combination of analytic models and experimental observation. This approach is preferable because it provides the researcher more intuitively useful results [Lammlein].

### Analytic (Process) Models

#### *Heat Generation*

The heat generated during FSSW is a result of the intimate (rotating) contact that exists between the FSSW tool and workpiece during welding. The relationship between the heat generated and the process is complex and depends on the welding tool geometry, process parameters, the workpiece and tool materials, workpiece deformation, the contact condition between the workpiece and welding tool, etc. (Figure 17). Understanding the heat generation in FSSW may help in the selection of ideal welding parameters (rotation rate, dwell time, plunge depth, etc.) for the process.

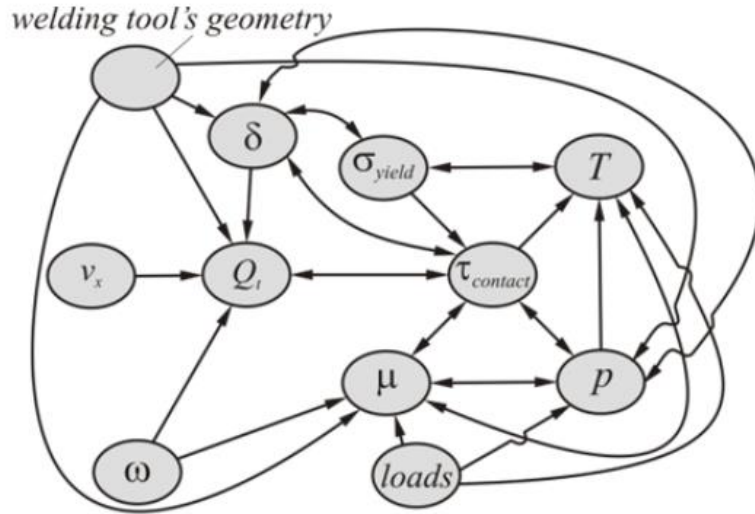


Figure 17: Relationship between generated heat and process parameters during FSSW [Mijajlovic]

The heat generated during the FSSW process is equivalent to the power input into the weld by the tool [Lammlein, Hamilton]. The power input into the weld can be determined using the rotational speed of the tool and the weld torque (eqn. 3.1):

$$P = M * \omega \quad (3.1)$$

where P is the weld power (watts), M is the weld torque (N·m), and  $\omega$  is the tool's angular velocity (rad/s) [Pew, Khandkar]. While a majority of this heat is transferred into the workpiece, some of this heat is lost to the welding environment. If  $\eta P$  represents a heat transformation, the total amount of heat generated during FSSW,  $Q_{total}$ , is a function of the mechanical power delivered by the welding tool [Mijajlovic].

$$Q_{total} = \eta P \quad , \quad 0 < \eta < 1 \quad (3.2)$$



Where  $Q_{total}$  is the heat transferred into the workpiece. Values of  $\eta$  can be estimated using inverse modeling [Ferro]. The amount of heat generated by the tool depends on the surface contact area between the welding tool and workpiece:

$$dQ_{total} = \omega dM = \omega r dF = \omega r \tau_{contact} dA \quad (3.3)$$

where  $dF$ ,  $r$ , and  $dA$  are an infinitesimal force, segment, and area respectively, and  $\tau_{contact}$  is the contact shear stress within the weldment. Heat is generated by each surface of the tool during welding e.g. the shoulder, pin sides, and pin bottom. Integrating equation 3.3 for a simple flat shoulder (featureless), pinless FSSW tool yields:

$$Q_{total} = \frac{2}{3} \pi \omega \tau_{contact} R^3 \quad (3.4)$$

where  $R$  is the radius (m) of the shoulder. The heat generated during welding is attributed to both friction and deformation heating [Mijajlovic, Schmidt]. In some instances FSW/FSSW models are presented in the literature with the assumption that the heating is entirely due to friction [Aljoaba, Heurtier]. Both friction and deformation heat generation occur simultaneously and mutually affect one another. The total amount of heat generated during welding is expressed as:

$$Q_{total} = (1 - \delta) Q_{Friction} + \delta Q_{Deformation} \quad (3.5)$$

where  $\delta$  represents the dimensionless contact state variable (slip) at the shoulder surface [Atharifar, Mijajlovic, Schmidt]. The amount of heat generated by friction and deformation with respect to the contact shear stress is:

$$\tau_{contact} = \begin{cases} \mu_f P, & \text{friction heating} \\ \tau_{yield}, & \text{deformation heating} \end{cases} \quad (3.6)$$

where  $\mu_f$  is the coefficient of friction,  $P$  is the contact pressure ( $\text{N/m}^2$ ), and  $\tau_{yield}$  is the shear yield strength of the material. The shear yield strength of a material can be obtained from the yield strength by applying the von Mises yield criterion in uniaxial tension and pure shear [Schmidt, Lammlein], expressed as:

$$\tau_{yield} = \frac{\sigma_{yield}}{\sqrt{3}} \quad (3.7)$$

While values of weld torque, axial force (N) (used to calculate the contact pressure), and temperature ( $^{\circ}\text{C}$ ) can be experimentally measured, values of the friction coefficient and slip cannot and therefore must be estimated. The coefficient of friction is often estimated to have a value of somewhere between 0.3-0.4 [Nandan 2006, Schmidt]. Nandan et al. state that “a problem with the calculations of heat generation is that the friction coefficient cannot be determined from fundamental principles or it seems, by straightforward representative experiments of relevance to the conditions of FSW” [Nandan 2008].

Alternatively, Kumar et al. have proposed a model of the friction coefficient that is based on an experimental estimation of the momentum of friction and axial force for

the plunge and dwell stage of traditional FSW. The momentum of friction is calculated using a measurement of the resultant lateral force acting on the tool and an experimental “pole” attached to the welding anvil which can be seen in Figure 18(11).

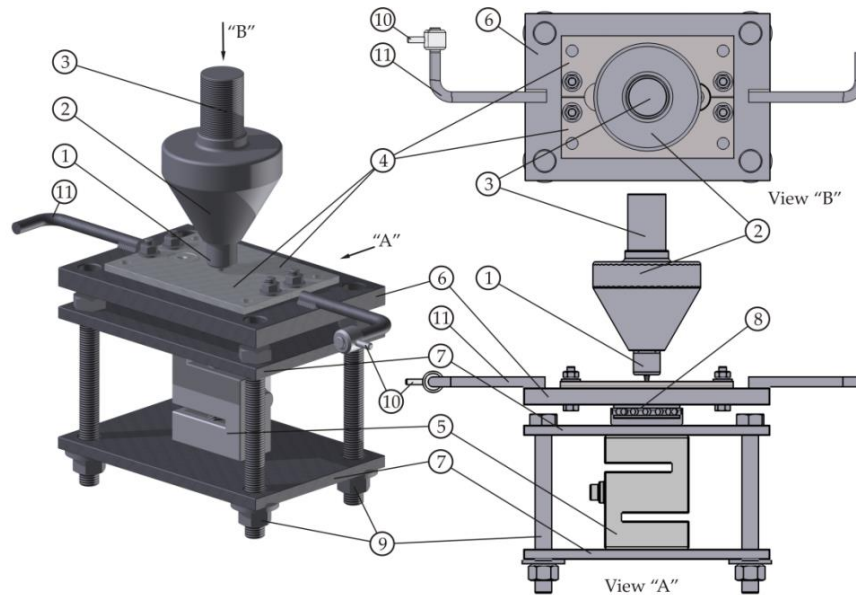


Figure 18: Experimental apparatus for measuring momentum of friction and axial force [Mijajlovic].

The coefficient of friction is expressed by Kumar et al. as:

$$\mu_f = \frac{3F_t(t)L_t}{F_z(t)d(t)} \quad (3.8)$$

where  $F_t(t)$  is the measured lateral force,  $L_t$  is the length of the “pole (Figure 18)”,  $F_z(t)$  is the measured axial force, and  $d(t)$  the diameter of the welding tool in contact with the workpiece. This model is only applicable to the early stages of FSW (plunge and initial

dwell) due to fixture instability during the traverse stage. Because the tool does not move in the lateral/traverse direction during the traditional FSSW process, this proposed method may be suited for making measurements of the friction coefficient [Kumar].

The contact condition slip ( $\delta$ ) relates friction and deformation heating during FSSW. This contact condition is the most critical part of the numerical model according to Reynolds et al. [Reynolds]. A maximum  $\delta$  value of 1 indicates that all of the heat is due to plastic deformation, while a minimum value of 0 suggests pure friction heating (eqn. 3.5) [Schmidt]. The value of slip is often set so that the results of the numerical simulation are in good agreement with experimental observations. It should be noted that Nandan et al. utilize an opposite relation in which a maximum  $\delta$  value of 1 indicates that all of the heat generation is due to friction while a minimum value attributes all of the heating to deformation. The resultant prediction of heat generation produced by both author's models are identical. When addressing discussions of slip in the literature it will be noted as to which author's model is being used. The true value of slip during welding is thought to be somewhere slightly less than 1. The extent of slip can be estimated by curve fitting the measured values at various relative velocities [Nandan 2008].

$$\delta = 1 - \exp\left(-\frac{1}{\delta_o} \frac{\omega r}{\omega_o R}\right) \quad (3.9)$$

where  $\delta_o$  is an adjustable parameter, and  $\omega_o$  is the normalizing rotational velocity. This model suggests that slip is spatially dependent (on  $r$ ). Figure 19.a shows the variation of slip for multiple locations along the radius of the tool. A range of values, 0.3-0.5 was

used for  $\delta_o$ . Based on experiments in the friction welding of steel bars, the coefficient of friction during FSSW can be calculated using the relative velocity between the tool and workpiece and has the form [Nandan]:

$$\mu_f = \mu_o * \exp(-\lambda\delta\omega r) \quad (3.10)$$

where  $\mu_o$  is a constant and  $\lambda$  was 1 s/m. Calculated values of the coefficient of friction are shown in Figure 19.b.

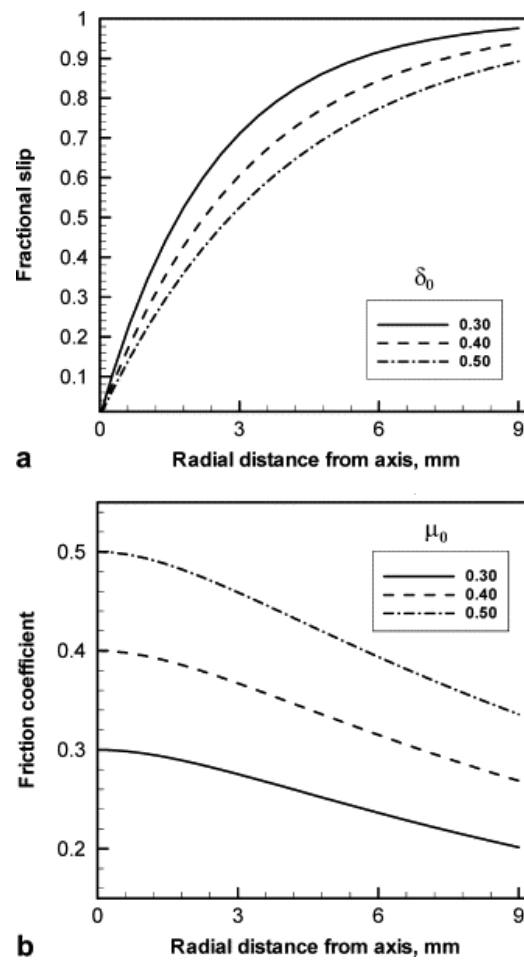


Figure 19: Variations of (a) fractional slip and (b) the friction coefficient [Nandan 2006]

Hamilton et al. found the slip (Nandan Model) rate to be primarily influenced by the welding energy (energy per unit length) and the proximity of welding temperature to the solidus temperature of the workpiece for FSW [Hamilton]. This led to an alternative expression of slip:

$$\delta_E = \exp\left(-\frac{(E_l)_{eff}}{(E_l)_{max}}\right) \quad (3.11)$$

where  $(E_l)_{max}$  (J/mm) is defined as the energy level for which the welding temperature is equal to the solidus temperature of the alloy.  $\delta_E$  represents the efficiency of heat rather than the relation of heating due to friction and deformation [Hamilton]. As the ratio of  $(E_l)_{eff}/(E_l)_{max}$  approaches 1, “sticky friction” heating becomes dominant. Equation 3.10 places a limit on the maximum value of  $\delta_E$  to be 0.37. This observation by Hamilton et al. suggests that welding at a lower weld temperature results in more plastic deformation.

Equation 3.6 uses the Coulomb law of Friction to describe the shear forces during welding. This law predicts the interaction caused by the relative motion between the rotating tool and workpiece as being either slip or stick. The standard interpretation of this law is not sufficient for FSSW and an alternative FSW/FSSW specific interpretation is described (Figure 20) [Schmidt]. In the sticking condition ( $\delta = 1$ ) the workpiece will stick to the moving surface of the tool if the friction shear stress exceeds the yield shear stress of the workpiece. If the contact shear stress is smaller than the yield shear stress of the workpiece then a sliding condition is observed ( $\delta = 0$ ). The final condition exists when the contact shear stress equals the yield shear stress of the workpiece due to a

quasi-stationary plastic deformation rate [Schmidt]. This condition is referred to as partial sliding/sticking (slip/stick). Schmidt et al. define  $\delta$  as:

$$\delta = \frac{v_{workpiece}}{v_{tool}} = 1 - \frac{\dot{\gamma}}{v_{tool}} \quad (3.12)$$

where  $\dot{\gamma}$  is the slip rate  $v_{tool}$  is the position dependent velocity on the tool surface [Schmidt].

Condition	Matrix velocity	Tool velocity	Shear stress	State variable
Sticking	$v_{matrix} = v_{tool}$	$v_{tool} = \omega r$	$\tau_{friction} > \tau_{yield}$	$\delta = 1$
Sticking/sliding	$v_{matrix} < v_{tool}$	$v_{tool} = \omega r$	$\tau_{friction} \geq \tau_{yield}$	$0 < \delta < 1$
Sliding	$v_{matrix} = 0$	$v_{tool} = \omega r$	$\tau_{friction} < \tau_{yield}$	$\delta = 0$

Figure 20: Definition of contact condition, velocity/shear relationship, and contact state variable [Schmidt]

In general, one wishes to avoid tool slippage ( $\mu P \leq \tau_{shear}$ ) at the welding interface because the welding mechanism (stirring) depends upon flow within the workpiece to bring fresh metal surfaces into contact. High welding forces (axial), the inclusion of features on the tool, and high local temperatures (in the weld zone) promote sticking [Nunes 2011].

As expressed in Equation 3.4 the heat generated during FSSW along the shoulder is dependent on the geometry of the tool as well as the selected welding parameters. Tools with a larger shoulder (and pin) radius will generate more heat. Approximately 90% of the total heat generated is attributed to the tool shoulder [Schmidt]. Likewise,

increasing the rotation rate of the tool will result in more heat generation. The relative velocity increases along the tool/workpiece interface at distances further from the axis of rotation. As a result, more heat is generated at the edge of the tool's shoulder. Figure 21 shows the spatial variation of heat generation at the welding interface of a standard FSW tool with a pin [Nandan 2007].

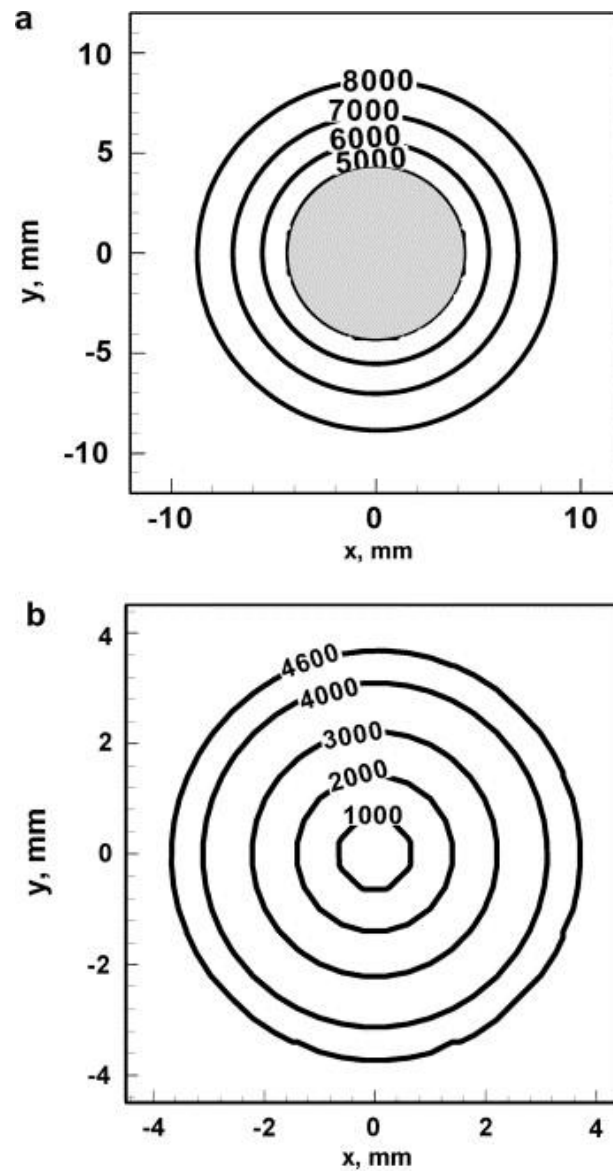


Figure 21: Spatial variation of heat generation (watts) along the tool/workpiece interface for a) the shoulder b) the pin bottom [Nandan 2007]



### *Weld Torque*

The torque acting on the tool during welding can be experimentally measured [Gibson, Longhurst] and analytically calculated. More accurately, the torque can be estimated quantitatively due to the unknown material properties at the temperatures and deformation rates experienced during FSW/FSSW. Nevertheless, simple models can be constructed to provide limited understanding of tool forces [Nunes 2000]. By approximating the geometry of the metal rotating with the tool during welding (Figure 22), the weld torque,  $M$  (Nm), is the sum of the torques acting along the shearing surface as well as any part of the tool the slips against the workpiece. If tool slip (Nandan Model) is assumed to be zero (all deformation heating) for simplicity the weld torque can be expressed as:

$$M \approx \int 2\pi r^2 \tau \sqrt{dr^2 + dz^2} \quad (3.13)$$

where  $\tau$  is the flow stress at the boundary of the flow. If the rotating material geometry is taken to be the same as the contact interface between the tool and workpiece the torque is:

$$M = \int_0^r 2\pi r^2 \tau dr + 2\pi r^2 t \tau + \int_r^R 2\pi r^2 \tau dr \quad (3.14)$$

where  $r$  is the radius of the pin (m),  $R$  is the radius of the shoulder (m), and  $t$  is the length of the tool pin (m). Larger tool dimensions (shoulder and pin radius, pin height) will result in more torque acting on the tool and more heat generation.

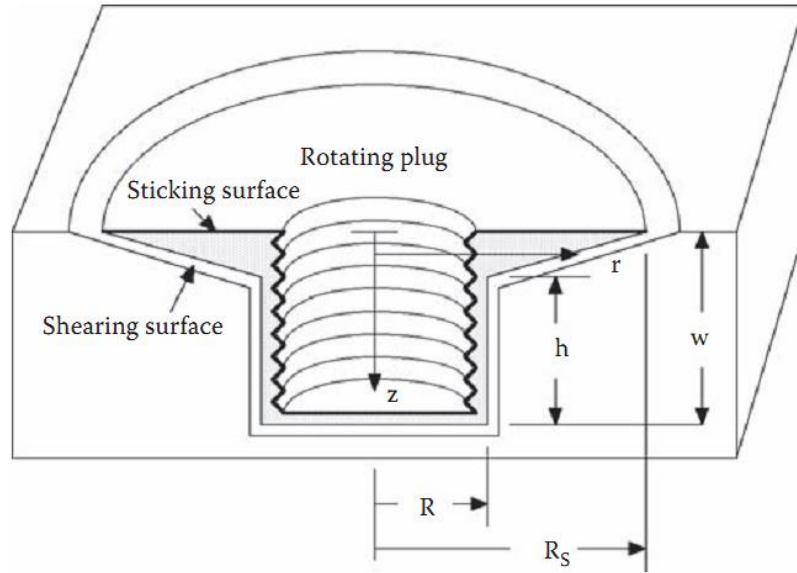


Figure 22: Simplified geometry of the Nunes Rotating Plug model during FSW [Nunes 2011]

Solving Equation 3.14 for a pinless FSSW tool yields:

$$M = \frac{2}{3}\pi R^3 \tau_{yield} \quad (3.15)$$

This expression is identical to the combination of Equations 3.1, 3.4, and 3.6. This comes as no surprise since the weld power is defined as the product of the weld torque and rotation rate. If the tool slip (Nandan Model) is assumed to be 1 (all friction heating) then the weld torque for a pinless FSSW tool can be expressed as:

$$M = \frac{2}{3}\pi R^3 \mu_f P \quad (3.16)$$

Rewriting Equation 3.16 in terms of axial load ( $F_z$ ) yields:

$$M = \frac{2}{3}R\mu_f F_z \quad (3.17)$$

Hamilton et al. use an expression similar to Equation 3.17 to define total weld torque and equate it with Equation 3.16. By equating the two expressions it suggests the contribution to torque (heating) of friction and deformation is equal. This approach is incorrect due to the assumptions made about the value of the contact state variable at which each expression (3.15 and 3.17) is obtained. The total weld torque is:

$$M_{Total} = (\delta)M_{friction} + (1 - \delta)M_{deformation} \quad (3.18)$$

For a pinless FSSW tool (based on the Nandan Model of slip) the total torque can be written as:

$$M_{Total} = (\delta)\frac{2}{3}R\mu_f F_z + (1 - \delta)\frac{2}{3}\pi R^3 \tau_{yield} \quad (3.19)$$

The estimates made using Equation 3.18 are in good agreement with measured experimental values. Nandan et al. reported a predicted torque value of 56.7 N·m for welding AISI 1018 Steel and an observed value of 55 N·m at steady state [Nandan 2007]. Arora et al. demonstrated the ability to accurately predict weld torque for a range of rotation rates (using Equation 3.18) for joining AA2524 and Ti-6Al-4V (Figure 23),

where slip and the coefficient of friction were calculated using Equations 3.9 and 3.10 respectively [Arora].

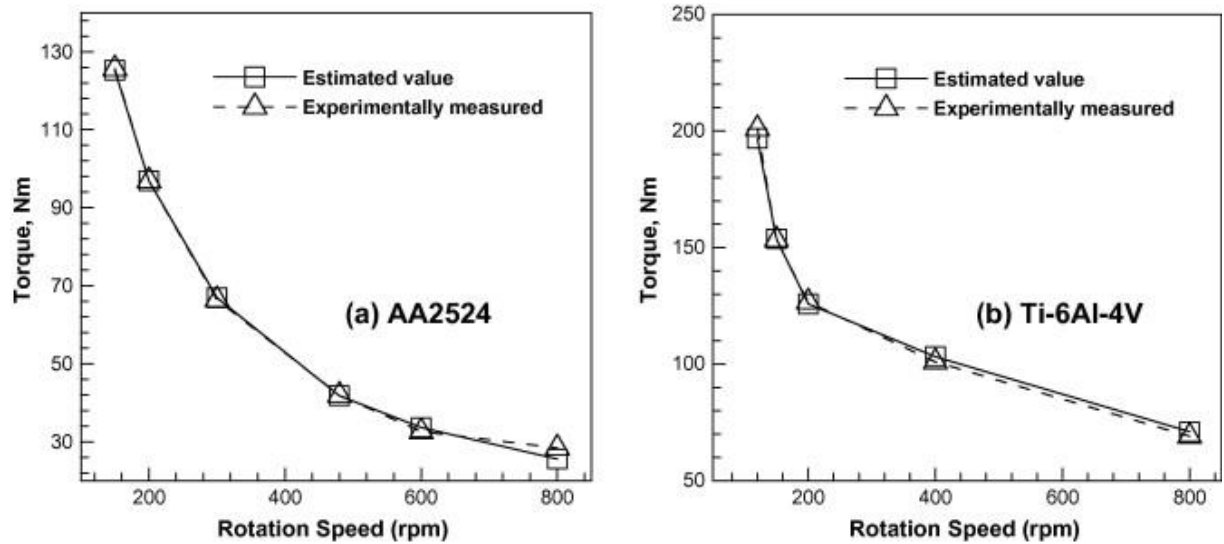


Figure 23: Estimated and experimental torque values for FSW of a) AA2524 and b) Ti-6Al-4V [Arora]

The surface contact area between the tool and workpiece is proportional to the torque acting on the tool during welding (Equation 3.18). Understanding this relationship may allow engineers to select appropriate welding parameters and tool designs for their specific welding system, e.g. knowing the maximum amount of torque the spindle motor can output places limits (max/min) on the size of the welding tool and the selection of rotation rate.

### *Axial Force*

Despite being an important process parameter for ensuring weld quality there are very few analytic expressions for accurately predicting the axial forces acting on the FSW/FSSW tool during welding. Numerical work by Crawford investigated the effect tool geometry and process parameters (traverse and rotation rate) have on the axial load experienced by the tool [Crawford]. Nunes et al. state that the stress required to indent the surface of a material is on the order of the 6 times the shear flow stress and that the plunge force should be about  $6\tau$  times the area of the FSSW tool's shoulder [Nunes 2000]:

$$F_z = 6\pi R^2 \tau \quad (3.20)$$

Because the shear flow stress decreases with temperature, the calculated axial force decreases with an increase in rotation rate (Figure 24). This calculated trend is in good agreement with both the numerical and experimental data presented in the literature [Crawford].

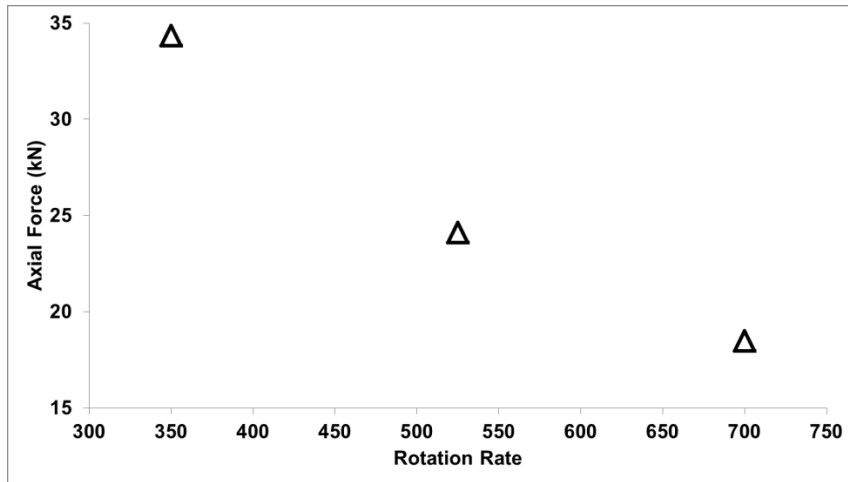


Figure 24: Computed axial force using Equation 3.20 (Data from Nunes RP et al.)

In a separate work, Nunes et al. consider the plunge force (axial force) to be the force needed to squeeze the material from beneath the tool and out to the sides (Figure 25).

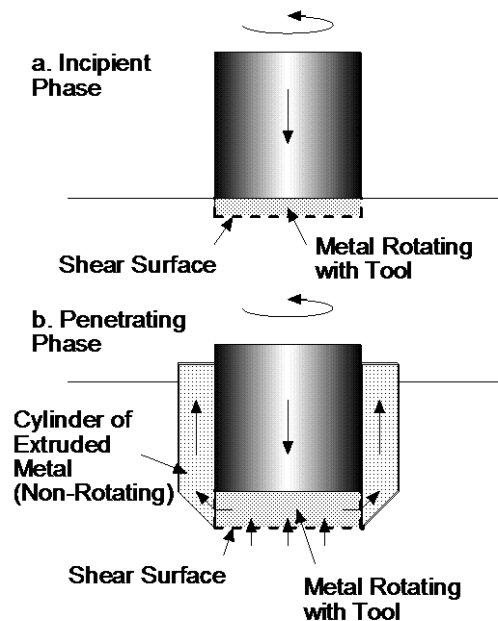


Figure 25: Idealization of weld metal flow around a FSW tool during the plunge stage [Nunes 2012]

Consider the free body diagram shown in Figure 26. In this diagram the stresses acting on the extruded cylinder allowing for the calculation of the plunge force ( $F_z$ ). A vertical equilibrium on the extruded cylinder (rotating disk) requires:

$$\pi[(R + h)^2 - R^2]P_1 = 2\pi(R + h)\alpha\tau \quad (3.21)$$

where  $R$  is the radius of the tool,  $h$  is the thickness of the rotating disk, and  $\alpha$  is the plunge distance. Equilibrium of the corner element requires:

$$P_2 \left( \frac{1}{\sqrt{2}} \right) = P_1 \left( \frac{1}{\sqrt{2}} \right) + \sqrt{2}\tau \quad (3.22)$$

The total pressure ( $P$ ) is:

$$P = P_2 + 2\tau \ln \frac{R}{r} + 2\tau \left( 1 - \frac{r}{R} \right) \quad (3.23)$$

Integrating this pressure over the area of the rotating disk yields the axial force ( $F_z$ ):

$$F_z = 2\pi R^2 \tau \left[ \frac{11}{6} + \left( \frac{1 + \frac{R}{h}}{1 + 2\frac{R}{h}} \right) \frac{\alpha}{h} \right] \quad (3.24)$$

If a value for the shear flow stress calculated from Equation 3.13 (torque) is inserted into Equation 3.24 a value of the plunge force in good agreement with experimental results is obtained [Nunes 2012].

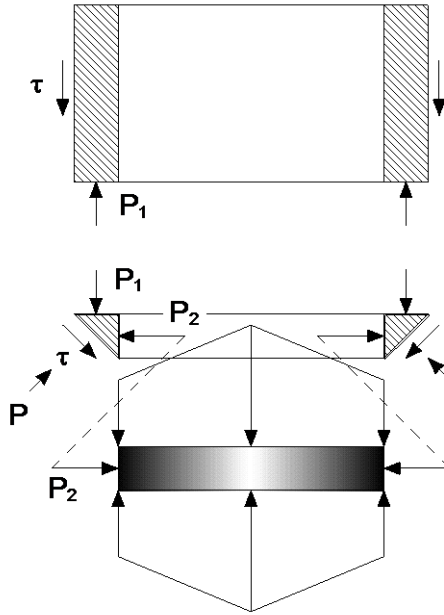


Figure 26: Free body diagram for flow elements around the FSW tool [Nunes 2012]

### *Thermal Boundary Conditions*

$$\rho c_p \frac{\partial T}{\partial t} + q = \nabla \cdot k \nabla T \quad (3.25)$$

Equation 3.25 [Awang, Ferro] governs the heat transfer in FSSW.  $q$  is the heat generated during welding from friction and deformation,  $\rho$  is the density ( $\text{kg/m}^3$ ) of the workpiece,  $c_p$  is the specific heat capacity ( $\text{J/g}^\circ\text{K}$ ) of the workpiece,  $k$  is the thermal conductivity ( $\text{W/m-K}$ ) of the workpiece,  $T$  is the temperature ( $^\circ\text{C}$ ), and  $t$  is the time.

In order to compute the temperatures present in the FSSW process thermal boundary conditions must be defined throughout the model (Figure 27). Heat losses in the model are attributed to conduction losses to the workpiece, anvil, and spindle, in addition to the convective heat loss to the workpiece [Querin].



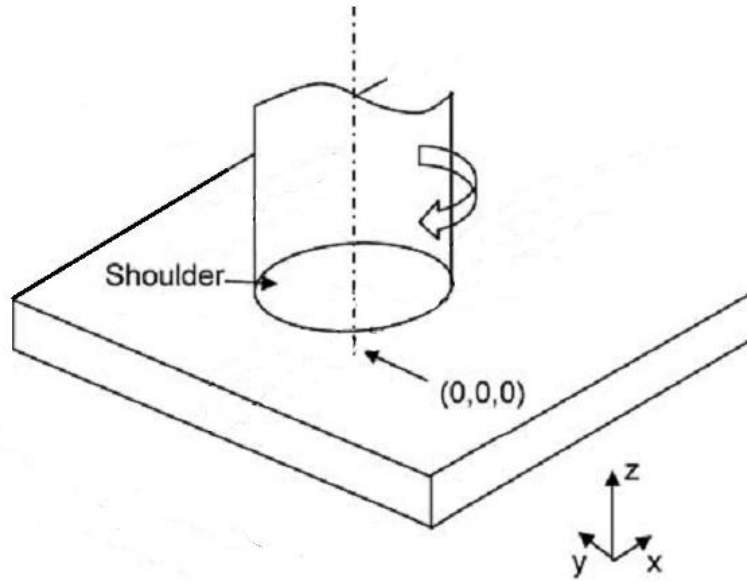


Figure 27: Schematic diagram of the pinless FSSW system considered in the model for thermal boundary conditions [Nandan 2006]

Some of the heat generated at the tool/workpiece interface is transported into the tool while the rest enters the workpiece. The total heat generated can be divided ( $f$ ) between heat that enters the workpiece and heat that is lost to the FSSW tool based on their thermal properties:

$$f = \frac{J_W}{J_T} = \frac{\sqrt{k\rho c_{pW}}}{\sqrt{k\rho c_{pT}}} \quad (3.26)$$

where the subscript W and T represent the workpiece and tool respectively. The heat flux is estimated to be 90% of the total heat generated and is in good agreement with experimental observation [Nandan 2006, Awang]. The heat flux is defined at the tool/workpiece interface as:

$$k \frac{\partial T}{\partial z} \Big|_{top} = \frac{J_W}{J_W + J_T} q, \quad 0 < r < R \quad (3.27)$$

where  $R$  is the radius of the shoulder and  $q$  represents the total rate of heat generation at the tool/workpiece interface ( $Q_{total}$  Equation 3.2) [Perivilli, Nandan 2006]. The top surface of the workpiece not in contact with the welding tool is modeled as a convective boundary:

$$k \frac{\partial T}{\partial z} \Big|_{top} = h_{top}(T - T_0) \quad (3.28)$$

where  $h_{top}$  is the convection coefficient for the top of the workpiece,  $T_0$  is the initial temperature of the workpiece. The interface between the workpiece and the supporting anvil (Figure 1) is modeled as a convective boundary condition (though it is not the same as free convection) [Perivilli]. The heat transfer coefficient along this boundary is determined by optimization [Nandan].

$$k \frac{\partial T}{\partial z} \Big|_{bottom} = h_{bottom}(T - T_0) \quad (3.29)$$

The initial condition for temperature throughout the workpiece is defined as:

$$T(x, y, z, 0) = T_0 \quad (3.30)$$

Equation 3.25 and the stated boundary conditions will be used to simulate the thermal environment of FSSW. The edges of the workpiece are not typically modeled as a convective boundary but are instead set to a constant temperature  $T_0$ .

### *Material Flow*

As discussed previously, material flow during welding is dictated by the process parameters (rotation rate, plunge depth) and the geometry of the welding tool. Schneider and Nunes breakdown the flow about the tool during welding into three component incompressible flow fields (Figure 28). The flow associated with uniform translation (b) is not present in traditional FSSW. The rigid body rotation (a) (the “rotating plug”) is assumed to stick to the FSSW tool (no slip). The rotational speed is assumed to be the same as that of the tool. This flow will stick to the shoulder along the radius towards the edge of the tool until the shear stress gives way to frictional slip. The nature of the ring vortex flow (c) is in good agreement with experimental observations made during FSSW. The ring vortex flow brings metal up on the outside, in towards the center near the shoulder, back down on the inside (center of the tool), and back out toward the bottom of the weld zone. This explanation of the material flow is in agreement with experimental observations made during Colligan’s shot tracer experiments and Schneider’s lead wire experiments (both experiments were designed to help visualize the flow field experimentally)[Colligan, Schneider].

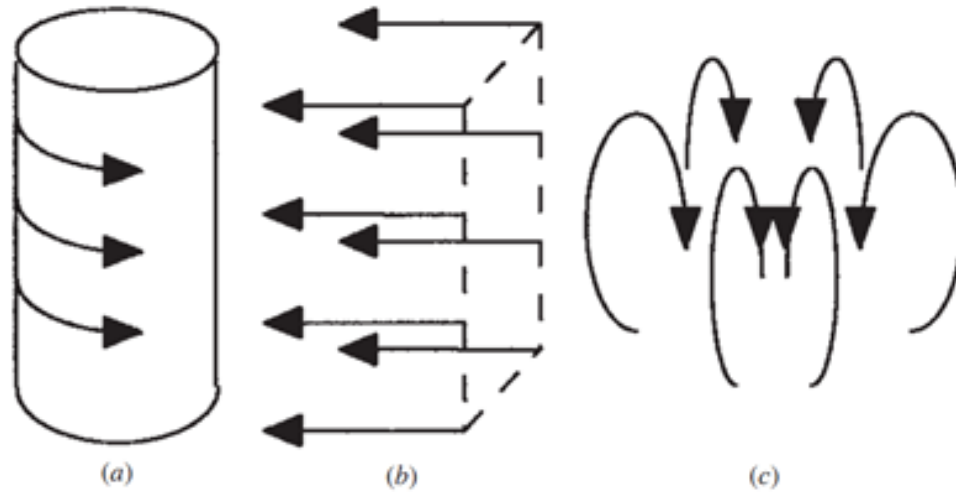


Figure 28: Three incompressible flow fields of FSW. a) rigid body rotation b) uniform translation c) ring vortex [Schneider]

Arora et al. developed an analytic model for the 3-D velocity field during FSW. For this model a simple tool geometry is used, the flow is assumed to primarily result from the shoulder, and a known geometry of the flow field based on experimental observation is used (Figure 29.a). The material flow is estimated by modifying an analytic solution for the steady state flow of an incompressible fluid between two solid discs, one rotating and the other stationary [Arora]. The components of velocity  $u$ ,  $v$ ,  $w$  in  $r$ ,  $\theta$ , and  $z$  directions, respectively, are given by:

$$u = r\omega F, v = r\omega G, w = d\omega H \quad (3.31)$$

where  $r$  is the radial distance,  $\omega$  is the rotational velocity, and  $d$  is the distance between the two discs.  $F$ ,  $G$ , and  $H$  are functions of  $z/d$  where  $z$  is the distance beneath the rotating disk. The entire 3-D velocity field (Figure 29.c) can be calculated using Equation 3.31.

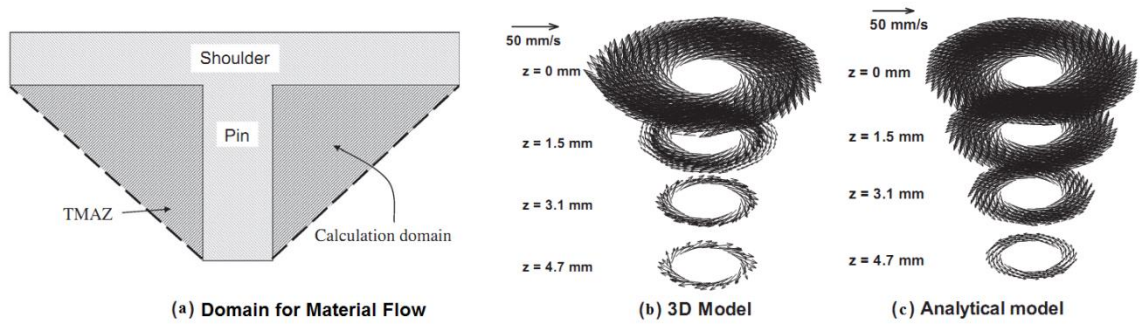


Figure 29: a) schematic of the velocity field domain. b) flow field from well-tested visco-plastic flow code c) flow field from analytic expression [Arora]

The results of the predicted flow field are in good agreement with the results from a 3-D visco-plastic model (Figure 29.b). Discrepancies between the two models are attributed (by the authors) to the assumption of the flow field shape, the presence of the pin (in the 3-D visco-plastic model), and the welding (traverse) velocity which were not considered directly in the analytic model.

Nunes considered how close the bottom of the tool pin needs to be to the supporting anvil to avoid lack of penetration (Figure 5.b). Simply put, how much material is “stirred” beneath the pin? Suppose that the bottom of a cylindrical tool pin of radius  $R$  is some distance  $\phi$  (penetration ligament) above the anvil during welding. It has been shown previously that the torque contributed by the shear surface enclosing the pin bottom is given by Equation 3.15. If the shear surface drops from the bottom of the pin to the anvil the change in torque can be expressed as:

$$2 \frac{2\pi R^3}{3} (\tau_A - \tau) + 2\pi R^2 \phi \tau \quad (3.32)$$

where  $\tau_A$  is the frictional shear stress located at the interface between the workpiece and anvil. Once this torque configuration occurs (Equation 3.31) the torque will not rise enough for a higher torque deformation mode to occur and therefore a lack of penetration should not occur when shear surface drops to the anvil [Nunes 2011].

$$\varphi = \frac{R}{3} \left(1 - \frac{\tau_A}{\tau}\right) \quad (3.33)$$

Equation 3.33 provides an estimate of the distance permissible between the bottom of the tool and the support anvil during welding. Assuming that  $\tau_A$  is significantly less than the metal shear stress the maximum distance (penetration ligament) is:

$$\varphi \sim \frac{R}{3} \quad (3.34)$$

Equation 3.33 may also be applicable for a pinless FSSW tool and in that case, may help in predicting the maximum thickness a specific FSSW tool may be able to join. For example, a pinless FSSW tool with a diameter of 0.4 inches may be able to join (in a lap joint configuration) workpieces up to 0.067 inches thick.

Simulating the material flow in a numerical environment such as COMSOL or FLUENT (commercially available CFD packages that are used in this work) requires that we define the continuity equation (like for Heat Transfer in Equation 3.25) (in index notation) for incompressible single-phase flow.

$$\rho \frac{\partial u_i u_j}{\partial x_i} = -\frac{\partial P}{\partial x_i} + \frac{\partial}{\partial x_i} \left( \mu \frac{\partial u_j}{\partial x_i} + \mu \frac{\partial u_i}{\partial x_j} \right) - \rho V \frac{\partial u_j}{\partial x_j} \quad (3.35)$$

where  $\rho$  is the density,  $\mu$  is the non-Newtonian viscosity,  $V$  is the welding speed, and  $P$  is the pressure [Nandan, Atharifar]. The non-Newtonian viscosity is defined in several different ways by different researchers for the purpose of numerical simulation. For this work two different methods are used to define the viscosity of the plastically deformed Al alloy during welding. The viscosity can be based on flow stress following a formulation by Sheppard and Wright:

$$\sigma_e = \frac{1}{\alpha} \sinh^{-1} \left[ \left( \frac{Z}{A} \right)^{1/n} \right] \quad (3.36)$$

where  $A$ ,  $\alpha$  (Figure 30,  $\alpha = 1/\sigma_R$ ), and  $n$  are material constants and  $Z$  is the Zener-Holloman parameter which represents the temperature-compensated effective strain rate and is given by [Nandan, Aljoaba, Ulysse, Lammlein]:

$$Z = \dot{\epsilon} \exp \left( \frac{Q}{RT} \right) \quad (3.37)$$

where  $Q$  is the temperature-independent activation energy,  $R$  is the universal gas constant, and  $\dot{\epsilon}$  is the strain rate. The viscosity of the material is defined as a function of the flow stress and effective strain rate:

$$\mu = \frac{\sigma_e}{\dot{\epsilon}} \quad (3.38)$$

The viscosity defined by Equation 3.38 decreases significantly with temperature and strain rate though strain rate is the more dominant factor (Figure 31) [Nandan 2007, Colegrove]. A criticism of this expression of flow stress (Equation 3.36) is that it does not account for structural events occurring during deformation [Sheppard]. This method is implemented in the CFD package via a user-defined function which can be computationally expensive. This use of this expression to define the material's viscosity is the prevailing method used by researchers when modeling FSW/FSSW using CFD.

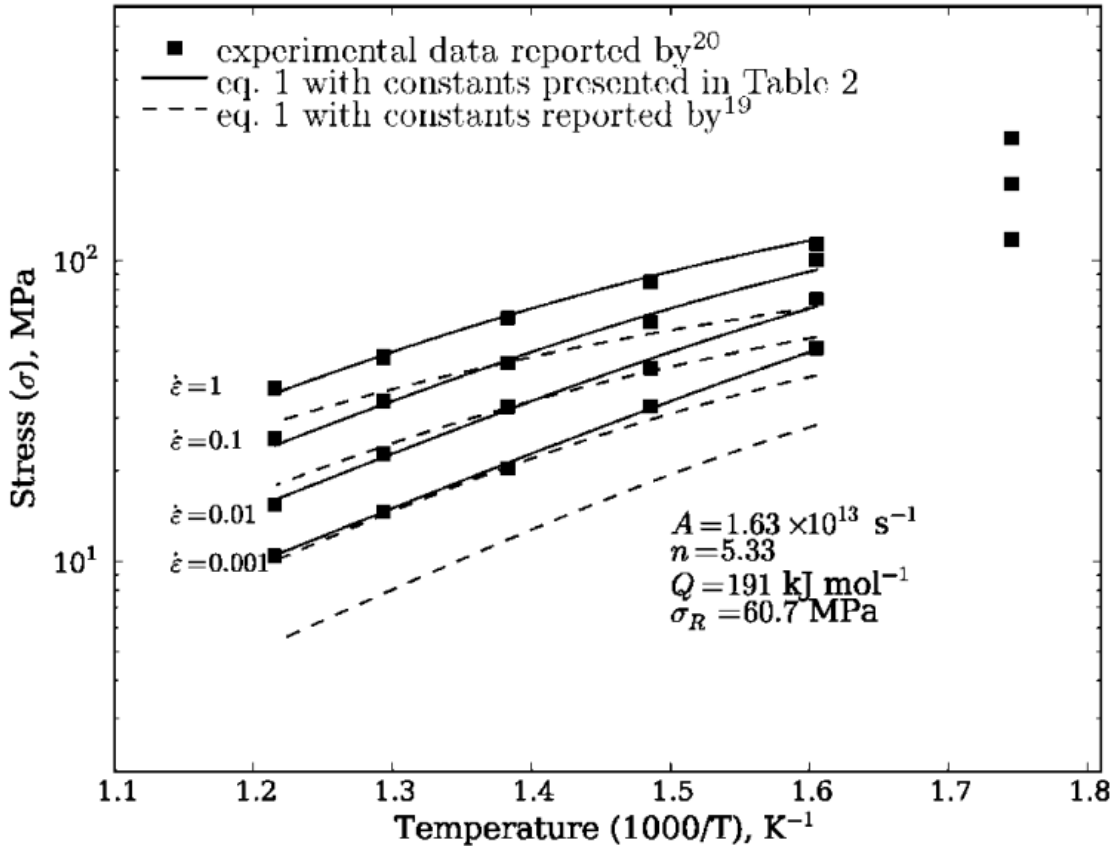


Figure 30: Flow stress data for Al 6061 and curve fitting values:  $R^2 = 0.996$  [Tello]



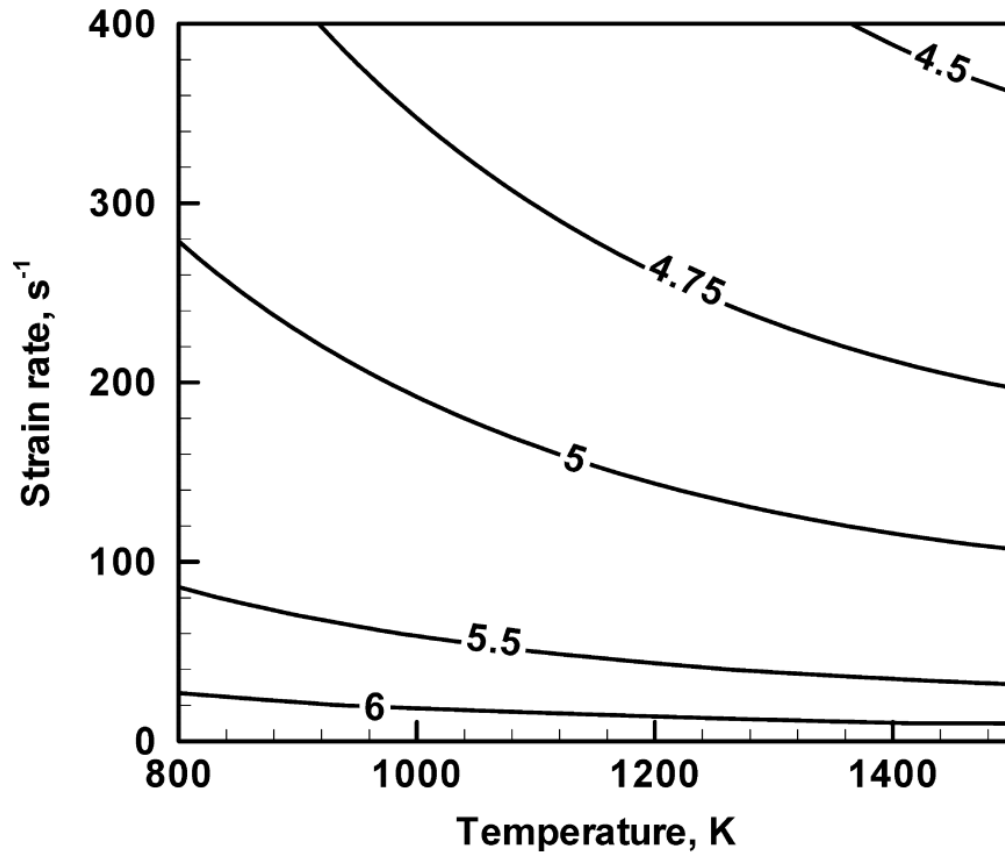


Figure 31: Computed contours of viscosity. The contour labels represent logarithm to the base 10 of viscosity in Pa·s [Nandan 2007]

Alternatively, the viscosity can be modeled using the Carreau viscosity model [Lammlein, Atharifar, Sinclair]. The temperature dependent Carreau viscosity model (Equation 3.39) can be applied to both the Newtonian and Non-Newtonian fluid domains of the model and fits very well to the results of Equation 3.38 [Fluent].

$$\mu = \mu_{\infty} + (\mu_0 - \mu_{\infty}) \left[ 1 + \left( \dot{\gamma} \lambda \exp\left(\frac{T_0}{T}\right) \right)^2 \right]^{\frac{m-1}{2}} \quad (3.39)$$

where  $\lambda$  is the time constant,  $m$  is the power law index for the Non-Newtonian fluid,  $\dot{\gamma}$  is the shear strain-rate,  $T_0$  is the reference temperature, and  $\mu_0$  and  $\mu_\infty$  are the zero and infinite shear viscosities. At low and high shear rates the viscosity is limited by  $\mu_0$  and  $\mu_\infty$  respectively (Figure 32).

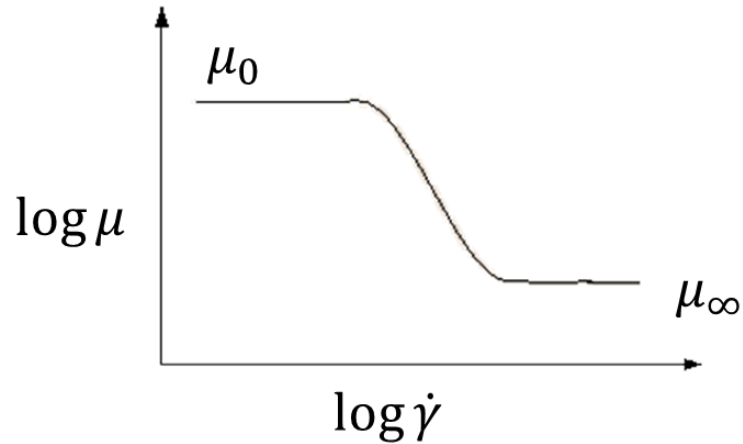


Figure 32: Variation of viscosity with shear rate according to the Carreau model [Fluent]

Atharifar et al. estimate the parameters of Equation 3.38 for Al 6061 as  $\lambda = 10$ ,  $m = 0.2$ ,  $T_0 = 300$  K,  $\mu_0 = 1E8$  m<sup>2</sup>/s and  $\mu_\infty = 0$  m<sup>2</sup>/s. The results of using the Carreau model of viscosity in a numerical simulation of FSW can be seen in Figure 33. In addition to producing results that are in good agreement with experimentally observed material flow, the Carreau model is a built-in function for both COMSOL and FLUENT which can reduce the computation time.

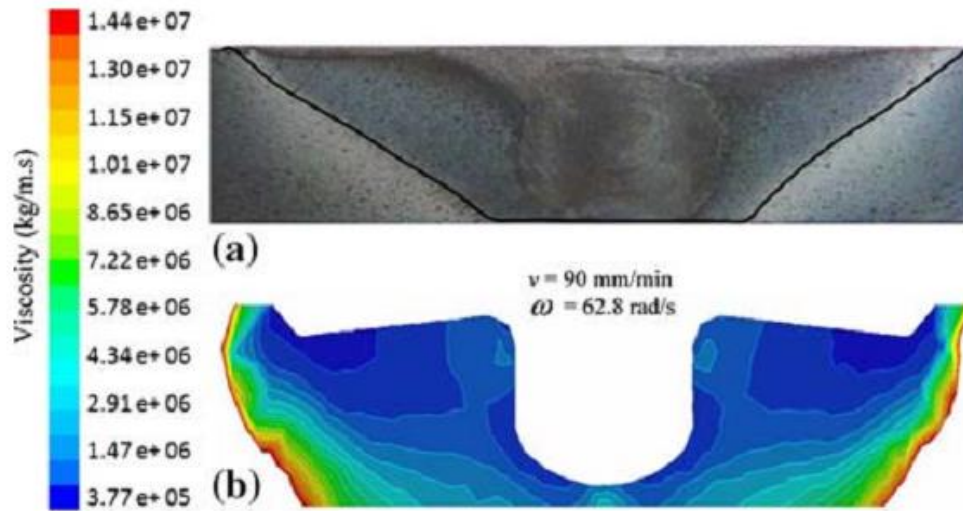


Figure 33: Comparison between experimental and numerical results a) weld cross section b) contour graph of dynamic viscosity [Atharifar]

### Computational Modeling Studies

Awang et al. simulated the temperature distribution and workpiece deformation during the FSSW process using an explicit finite element model (ABAQUS). Due to the complexity of modeling the process several assumptions were made to reduce the runtime of the model, including:

1. Only the workpieces may experience deformation (tool and workpiece are rigid)
2. Frictional contact is governed by Coulomb's Law (Equation 3.6) and is temperature dependent.
3. The frictional coefficient is zero at  $T_{\text{melting}}$ .
4. 100% of the dissipated energy was converted to heat.

The workpieces are oriented in a lap-joint configuration for spot welding. In order to have a refined mesh for better analysis near the tool, the workpieces were modeled in a circular geometry (Figure 34.a). The boundary conditions used in the FE model can be seen in Figure 34.b.

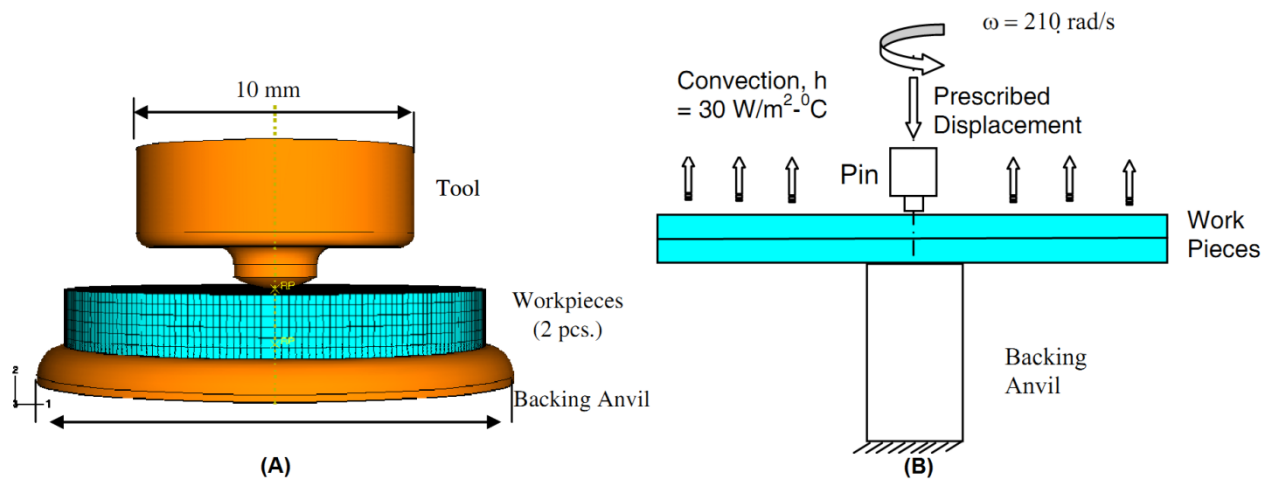


Figure 34: Mesh representation for FSSW tool, workpiece, and anvil. b) Boundary Conditions [Awang]

The prediction of the workpiece deformation (Figure 35) shows that the edges of the two workpieces separate during welding. This predicted deformation resembles the experimentally observed plate separation. The shape of the deformed joint line also resembles experimental observation (Figure 4). The explicit FEM modeling approach used in this study was capable of handling the large amount of deformation occurring in the FSSW process. The maximum temperature was found to be  $948 \text{ }^\circ\text{C}$  which is significantly higher than the temperature expected ( $\approx 400 \text{ }^\circ\text{C}$ ) at the tool/workpiece interface (Figure 36). This over estimation was attributed to the assumption that all of the heat is transferred into the workpiece and the selected values for the friction coefficient.

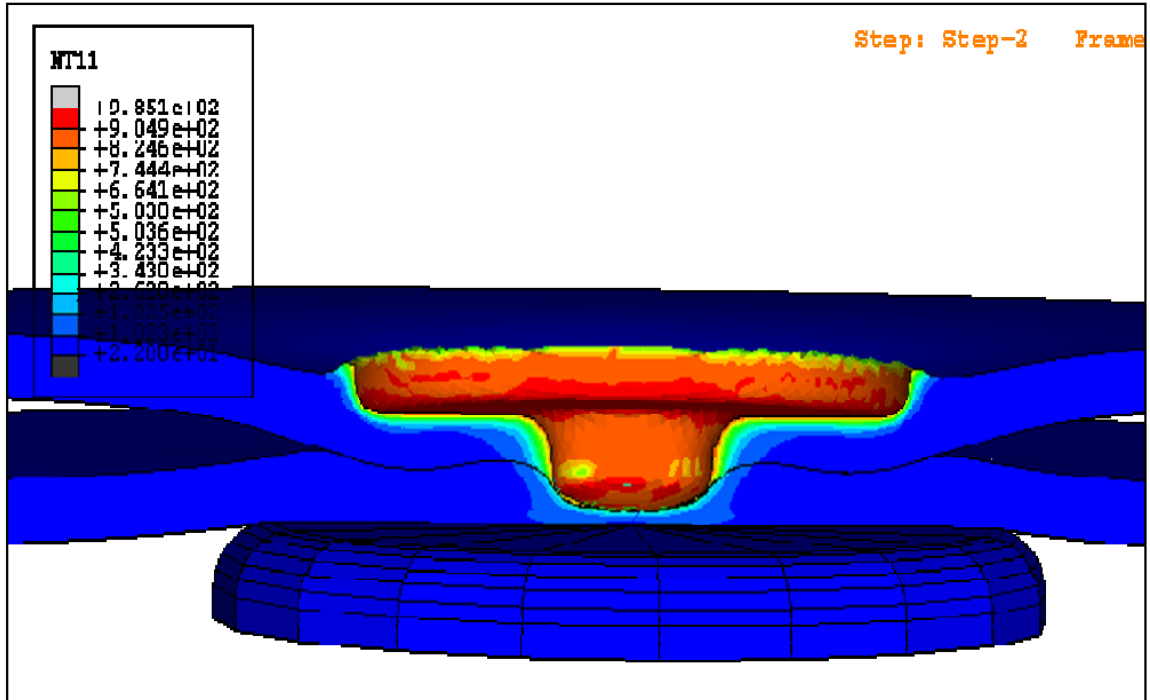


Figure 35: Deformation and temperature distribution [Awang]

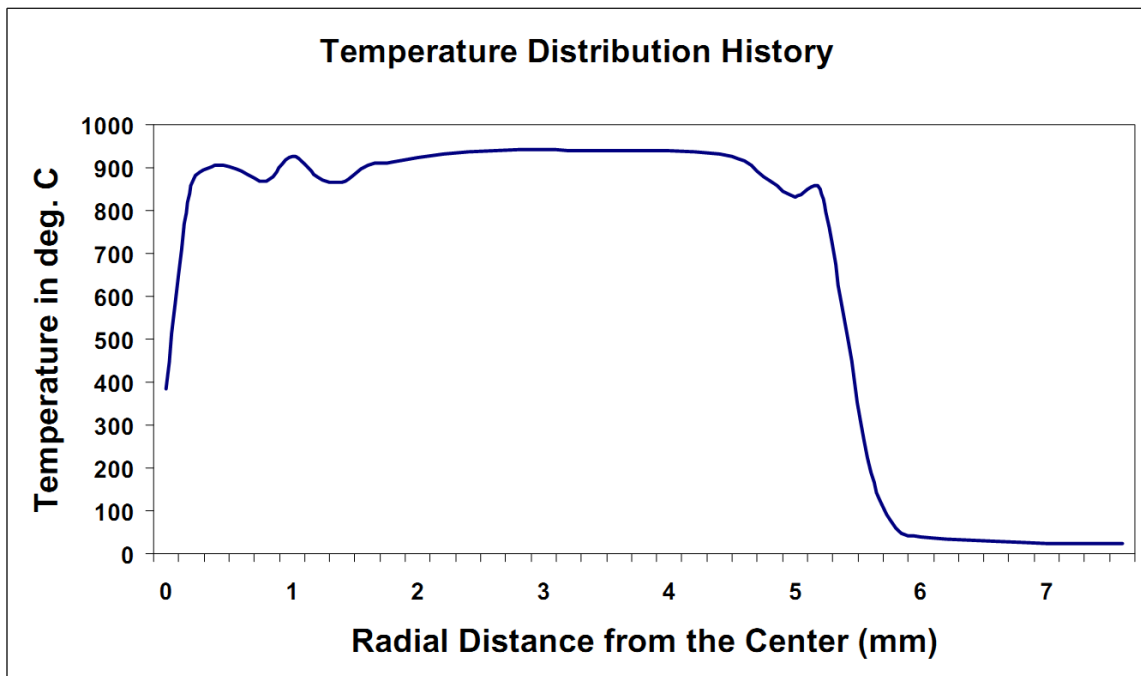


Figure 36: Temperature vs. radial distance from the center of the tool [Awang]

A 3-D transient heat transfer model of the FSW process was created by Song et al. Using an explicit central difference scheme (Equation 3.39, a finite difference method), the authors solved the heat transfer equation (Equation 3.24) for the plunge, traversing, and extraction phases of FSW. The model was implemented using FORTRAN code. The heat input by the shoulder was modeled as friction heat and the heat input by the tool pin was modeled as a uniform volumetric heat generated by plastic deformation. The thermal boundary conditions used by the authors followed Equations 3.25 – 3.29. The results of the thermal model were validated by comparing the results with experimental thermocouple data (Figure 37). The location of the measuring points 1, 2, 3, and 4 are 2.0 mm (0.079 in) beneath the upper surface and 8, 12, 16, and 25 mm (0.31, 0.47, 0.63, and 0.98 in) from the joint line respectively.

$$T_{i,j,k}^{(n+1)} = T_{i,j,k}^{(n)} + \frac{1}{\rho c} \times \left[ \begin{array}{l} k_x \frac{T_{i+1,j,k}^{(n)} - 2T_{i,j,k}^{(n)} + T_{i-1,j,k}^{(n)}}{\Delta x^2} + \dots \\ \dots k_y \frac{T_{i,j+1,k}^{(n)} - 2T_{i,j,k}^{(n)} + T_{i,j-1,k}^{(n)}}{\Delta y^2} + \dots \\ \dots k_z \frac{T_{i,j,k+1}^{(n)} - 2T_{i,j,k}^{(n)} + T_{i,j,k-1}^{(n)}}{\Delta z^2} + S \end{array} \right] \Delta t \quad (3.39)$$

Where i, j, and k are spatial indexes (x, y, and z respectively), n is the time index, S represents the heat generation source term, and  $\Delta t$  is the time step (0.02 sec). Song et al. found that a significant increase in rotation rate did not cause a significant increase in the peak temperature measurement experimentally. During FSW/FSSW the material flow stress drops rapidly near the materials melting point, thus causing the heat generation rate in the workpiece to go to near zero, even though the tool rotation rate has increased. This has a self-regulating effect that helps keep the FSW/FSSW weld in the solid-state [Song].

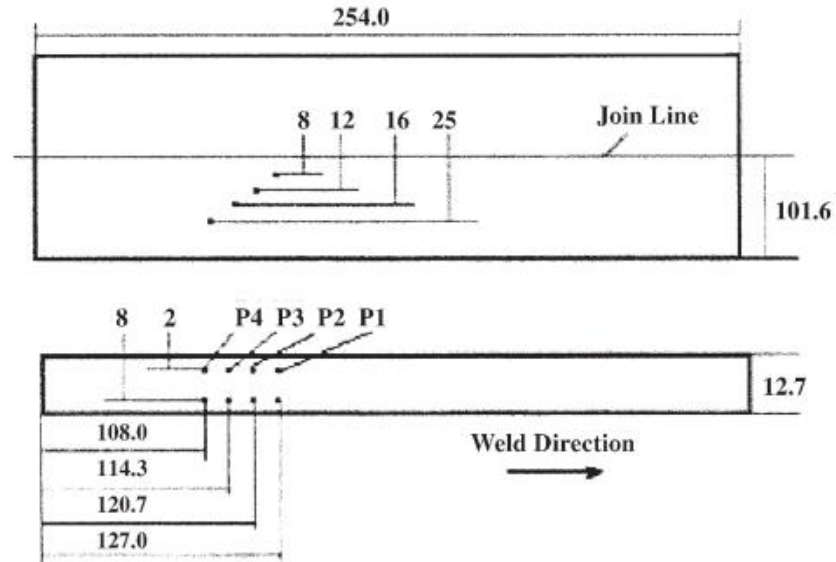


Figure 37: Location of thermocouples imbedded in the workpiece (butt joint) [Song]

A plunge rate of 5 mm/s (11.81 in/min) was used for this study, resulting in 2.54 sec of plunge time. Figure 38.a shows the calculated temperature contours during the plunge stage. It can be seen that the temperatures near the pin increase rapidly as the pin plunges deeper into the workpiece and the volumetric heat source moves at the plunge speed. During the extraction stage (Figure 38.b) the heat flux generated by the tool was removed and the tool pin was withdrawn from the sample. At the instant the tool is removed, the temperature of the workpiece is still high and then gradually drops down. Modelling the heat generated by plastic deformation as a uniform volumetric heat source was found to be acceptable.

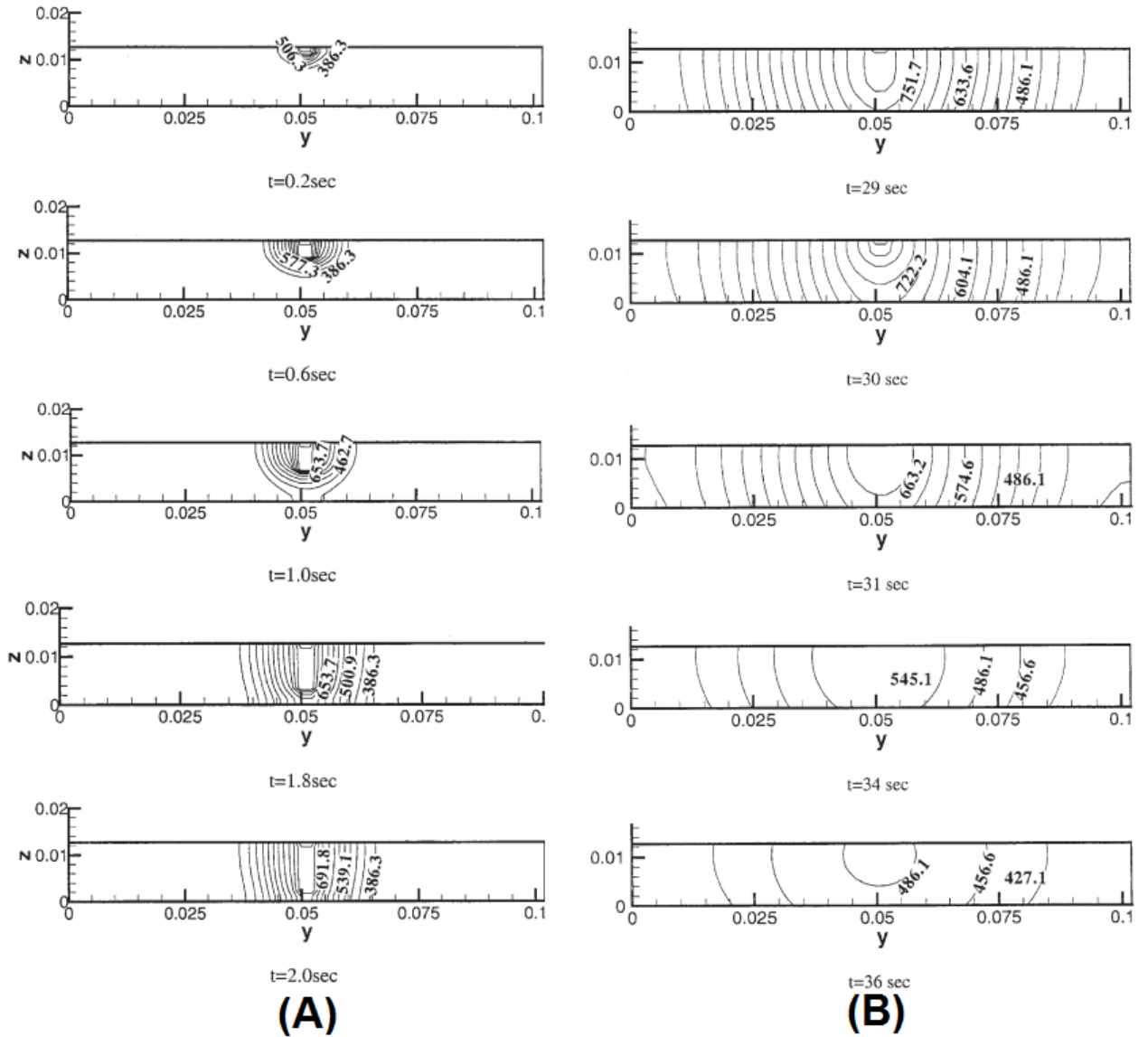


Figure 38: Temperature contours during the a) plunge stage, and b) the extraction stage of FSW [Song]

Kim et al. modeled the effect that two different pin geometries (cylindrical and triangular) have on the temperature distribution and material flow during FSSW [Kim]. Their thermo-mechanical simulation of the FSSW process was performed using the CFD code STAR-CD. In this model the plunge and extraction portion of the process were



ignored for simplicity; only a 2 second dwell stage is modeled. For both tool geometries, a convex shoulder was modeled. The mesh was most refined (Figure 39.b) near the tool pin and more coarse toward the edges of the workpieces. Like in the model developed by Awang et al., a circular geometry was used to model the workpieces. The area labeled as “Fluid” in Figure 39.c is the area where plastic deformation is permitted to occur while the rest of the workpiece, labeled as “Solid”, was assumed to be a rigid body in order to reduce computational time.

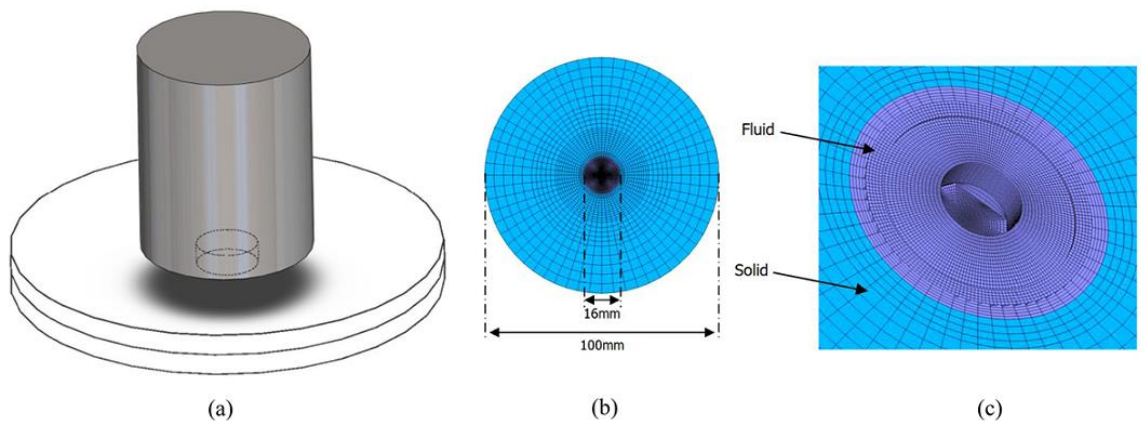


Figure 39: a) FSSW geometry used for CFD Simulation b) mesh scheme for cylindrical pin c) close up view of mesh scheme [Kim]

The resultant temperature distributions can be seen in Figure 40 for both the cylindrical pin (left) and triangular pin (right). The temperature of the workpiece (Al 5083-H18) beneath the outermost edge of the shoulder quickly reached a temperature (574 °C) very near the melting point in 0.3 seconds, after which the heat propagated throughout the workpiece. The peak predicted temperature for both pin geometries was similar due to the shoulder’s dominant contribution to heat generation. The material flow predicted by both the cylindrical and triangular pin can be seen in Figure 41. The triangular pin was found

to have a greater effect on the material flow due to the dynamic volume created when the pin is rotated. This increase in stirring resulted in joint strengths that were up to twice as strong as those created with a cylindrical pin [Kim]. The predicted material flow patterns were identified as being a useful tool in understanding the occurrence and location of defects within the weld zone.

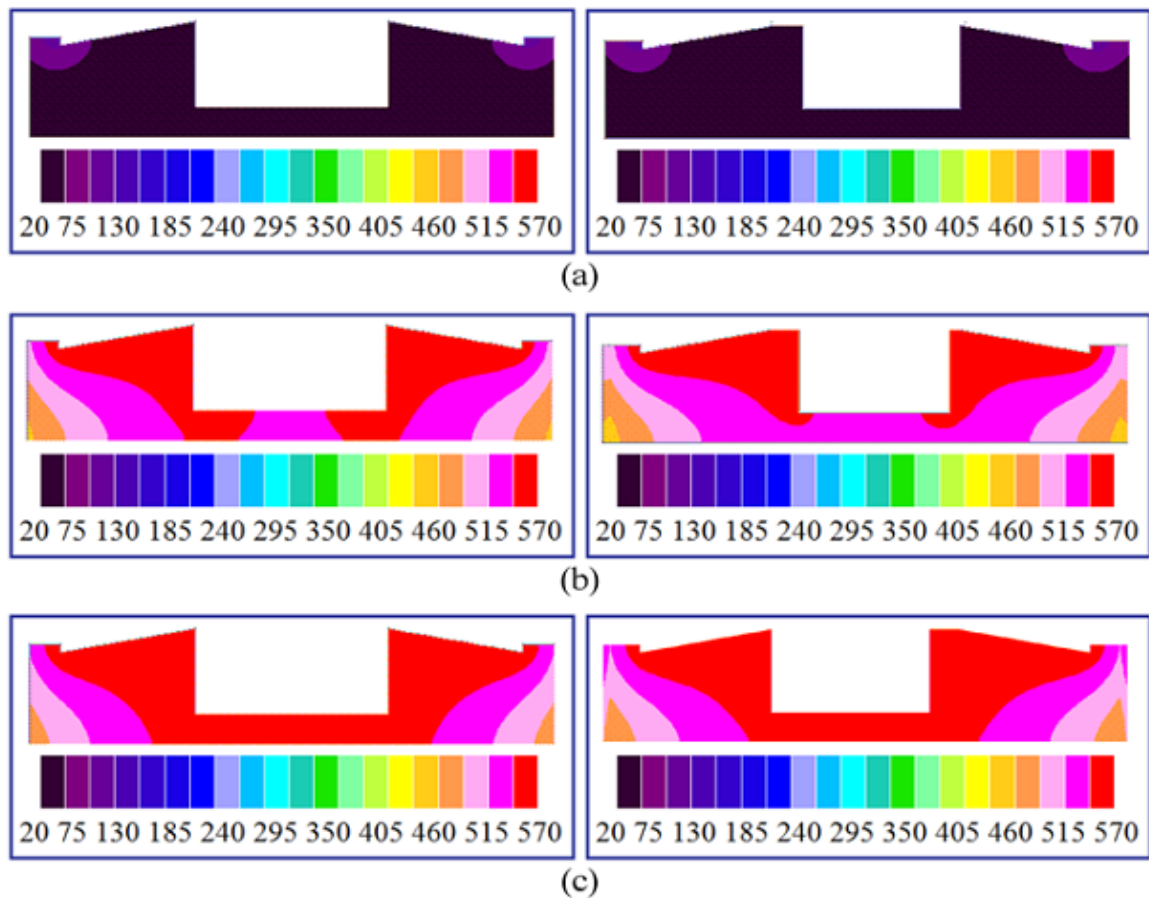


Figure 40: Temperature distribution during FSSW for a cylindrical pin (left) and triangular pin (right) at t = a) 0.01 sec b) 1.0 sec c) 2.0 sec [Kim]

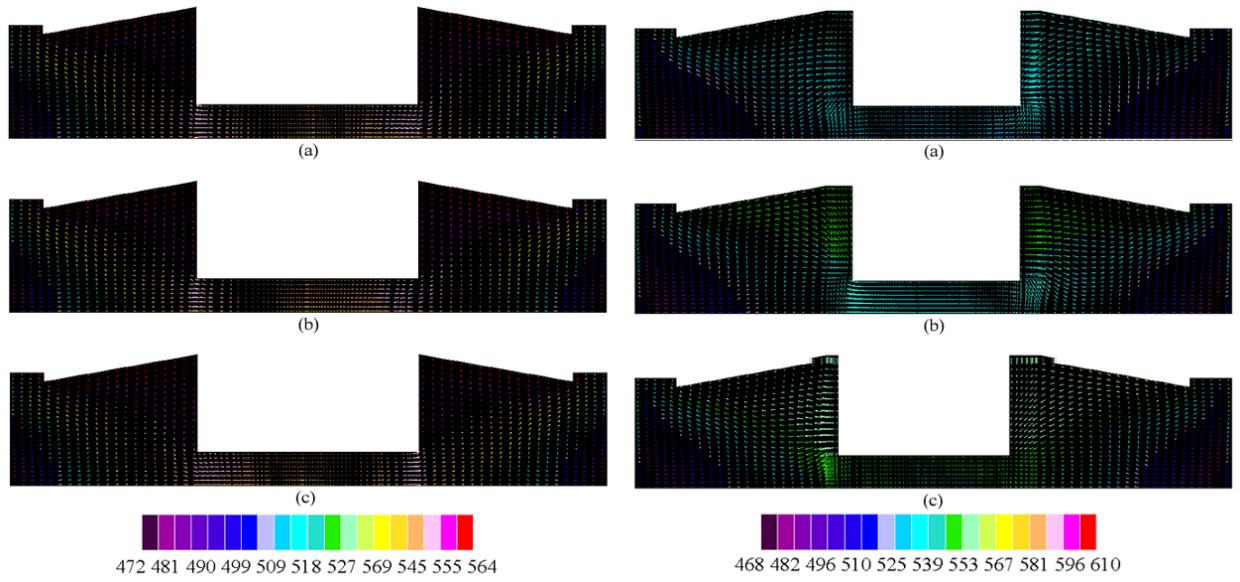


Figure 41: Material flow during FSSW for a cylindrical pin (left) and triangular pin (right) at t = a) 1.94 sec b) 1.95 sec c) 1.96 sec

## CHAPTER IV

### EFFECT OF PIN LENGTH AND ROTATION RATE ON THE TENSILE STRENGTH OF A FRICTION STIR SPOT-WELDED AL ALLOY: A CONTRIBUTION TO AUTOMATED PRODUCTION

*C.D. Cox, B.T. Gibson, A.M. Strauss, G.E. Cook. "Effect of Pin Length and Rotation Rate on the Tensile Strength of a Friction Stir Spot-Welded Alloy: A Contribution to Automated Production." Materials and Manufacturing Processes, 27:4, 2012; 472-478.*

#### Abstract

Friction stir spot welding is performed on thin plates of an aluminum alloy in a lap joint configuration with tools of different pin lengths and various rotation rates. The effects these process parameters have on the joint properties of the welds are investigated. The tensile strength of the welds decreased when the rotation rate was increased. The tensile strength of welds made with a pin-less tool is on average 90% the strength of the full penetration spot welds. Intermediate pin lengths were tested between these two extremes. It was found that the tensile strength decreases as the pin length increases from pinless to 10% bottom plate penetration. Three distinct failure modes were identified when the welds were placed under tensile loading: shear mode, mixed mode, and nugget-pullout mode. The dependence of static joint strength on these process parameters is discussed.

## Introduction

Reducing the weight of vehicles is a challenging problem facing automotive manufacturers that seek to improve overall performance and fuel economy. One means of accomplishing these goals is to use lightweight metals such as aluminum for structural and cosmetic components of the vehicle in lieu of heavier steel alloys. However current welding processes such as resistive spot welding are difficult to implement on these light weight metals due to their high thermal conductivity. While these metals can be joined with alternative methods such as self-piercing rivets, the use of such fasteners are accompanied by an increase in manufacturing costs and complexity [Mishra 2007].

Friction stir spot welding (FSSW) is a solid state joining technique derived from friction stir welding (FSW). In FSSW, the spot weld is created by plunging a rotating tool into the weldment, dwelling for a short period of time, and then retracting the tool. A typical FSSW tool consists of a cylindrical shoulder and pin similar to tools used in FSW. The spot weld is formed by plastically deforming the metal in the immediate vicinity of the tool. The heat and shear stress are generated by the friction caused by the rotation of the shoulder and to a lesser extent the pin when in contact with the work-piece. The amount of heat generated in the weld zone depends on rotation rate, tool penetration depth, and dwell time [Lathabai]. The use of FSSW presents several advantages over conventional spot welding processes in joining these light-weight aluminum alloys: higher joint strengths, grain refinement within the weld zone and reduced production costs. [Badarinarayan 142-48]

One of the issues associated with using FSW for spot welding applications is the keyhole defect. The keyhole is a consequence of both the solid state process and the

geometry of the tool used to make the weld. This defect can be seen in Figure 42. When the tool retracts from the weld, a shadow of its dynamic volume remains in the weld zone. In traditional FSW this defect is removed via post processing or eliminated using a specialized tool design. Previous research has demonstrated that it is possible to eliminate this defect for FSSW by using a pinless tool [Bakavos 2010, Tozaki 2010].

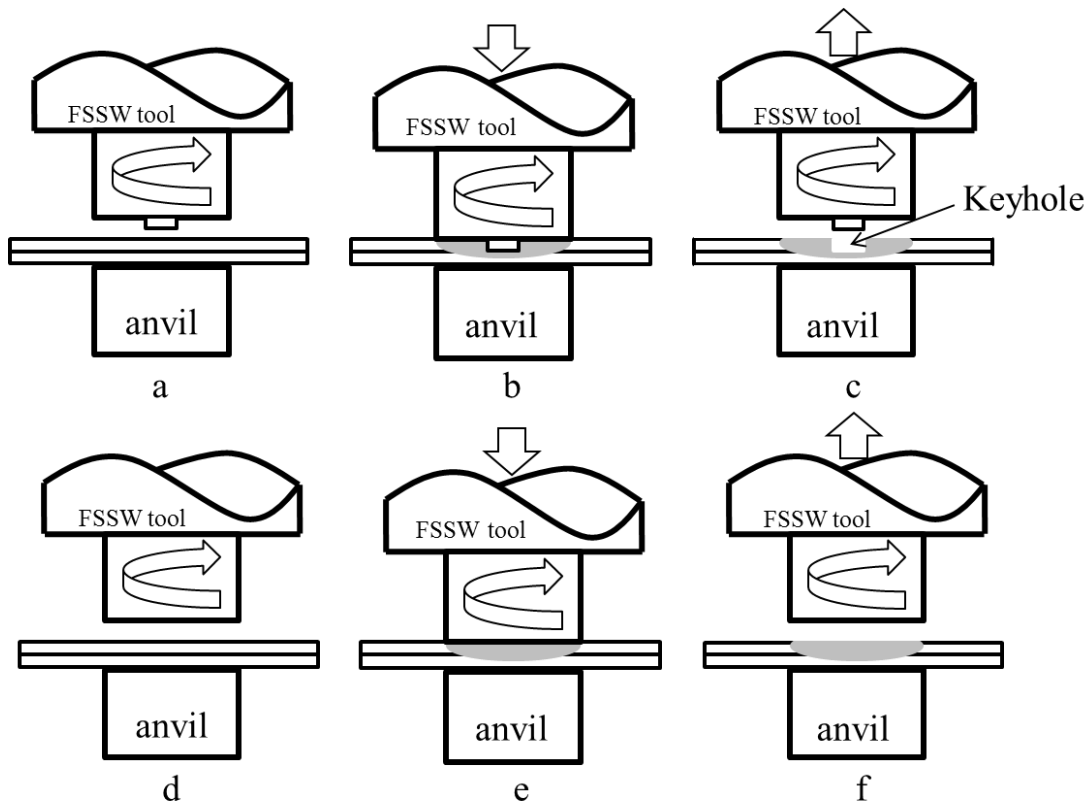


Figure 42 The Friction Stir Spot Welding Process. A-C: represents the traditional FSSW process using a tool with a pin. The resulting keyhole defect is illustrated. D-F: represents the FSSW process using a pinless tool. The lack of the keyhole defect is illustrated.

The rotation rate has been reported in the literature to be directly proportional to tensile strength [Arul, Yuan, Tozaki 2007 *Fract.*]. A study by Bakavos et al. investigated the effect of pin length on weld strength. The results of this work indicated that the maximum

joint strength occurred when the pin length fully penetrated the bottom plate by 32%. The joint strength of the pinless tool was 93% that of the full penetration tool [Bakavos 2009].

In this study, pin lengths are tested that address the effects of penetration depths that do not penetrate the bottom plate. Spot welds will also be performed at two “shallower” lower plate penetration depths, than those performed by Bakavos et al. including 5%, and 10% bottom plate penetration. Additionally, four different rotation rates will be evaluated in combination with each of the pin lengths for their effect on the mechanical properties of the weld. The resulting welds are presented and examined by tensile strength evaluations and optical macro-sections.

### Experimental

Spot welds were created on 0.040” thick plates of Al 6061 T6. The dimensions of the plate were 2” x 9” x 0.040” with a 1.25” overlap. The dimensions for each of the tools used can be seen in Table 1. Each of the tools used was made of O-1 Steel.

Table 1: FSSW tool dimensions and material

<i>Tool ID</i>	<i>Pin Length</i>	<i>Penetration Depth</i>	<i>Shoulder Diameter</i>	<i>Pin Diameter</i>	<i>Tool Material</i>
<i>Probe 1</i>	<i>0.000”</i>	<i>0.006”</i>	<i>0.50”</i>	<i>0.02”</i>	<i>O-1 Steel</i>
<i>Probe 2</i>	<i>0.010”</i>	<i>0.016”</i>	<i>0.50”</i>	<i>0.02”</i>	<i>O-1 Steel</i>
<i>Probe 3</i>	<i>0.032”</i>	<i>0.038”</i>	<i>0.50”</i>	<i>0.02”</i>	<i>O-1 Steel</i>
<i>Probe 4</i>	<i>0.036”</i>	<i>0.042”</i>	<i>0.50”</i>	<i>0.02”</i>	<i>O-1 Steel</i>
<i>Probe 5</i>	<i>0.038”</i>	<i>0.044”</i>	<i>0.50”</i>	<i>0.02”</i>	<i>O-1 Steel</i>

Each spot weld was created using a modified Kearney and Trecker 3-axis vertical mill. For all of the spot welds a fixed plunge depth of 0.006” was used. This value was determined experimentally to produce the best spot welds. The total tool penetration depth is calculated by adding the plunge depth to the pin length. A constant dwell time of

5 sec and plunge rate of 0.1 in/min were used for each of the spot welds. For each spot weld a clamp was placed on the weldment to prevent the top plate from pulling up due to the pressure created during the spot welding process (see Figure 43). The top clamp was made with holes to allow a series of 8 spot welds to be placed on each weld sample. The holes on the top clamp plate were made to allow for 0.20" of clearance around the pin.

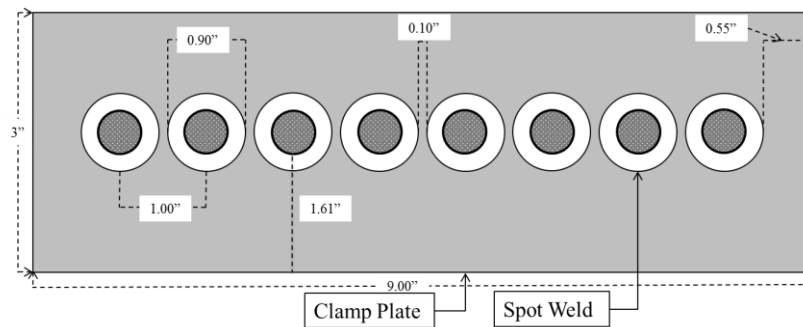


Figure 43: Clamp orientation relative to the spot welds for each sample. This clamp prevented the top plate from pulling away from the bottom plate during the spot welding process. The holes in the top plate were created off center for alignment purposes with the FSW machine.

Each of the spot welds was created using position control (open-loop). An automated welding routine was created to place spot welds at some interval, 1 inch, for this experiment, along the centerline of the overlapped material. This program also varied the rotation rate from weld to weld. Rotation rates of 750, 1250, 1500, and 2000 rpm were used. The range of rotation rates were selected based on the operational limits of the FSW machine.



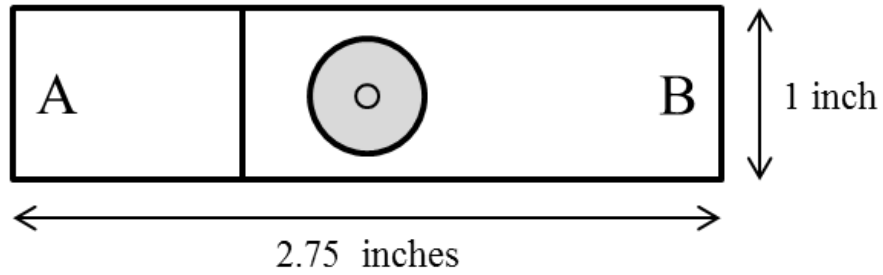


Figure 44: Lap tensile specimen.

To measure the effect that pin length and rotation rate have on the strength of the spot weld, tensile specimens were taken from each weld sample and were evaluated based on yield strength. The dimensions of the tensile specimens appear in Figure 44. In order to gain a better understanding of the relationship between these parameters, macro-section analysis was performed to image the weld zone structure.

## Results

### *Effect of Pin Length and Rotation Rate on Static Weld Strength*

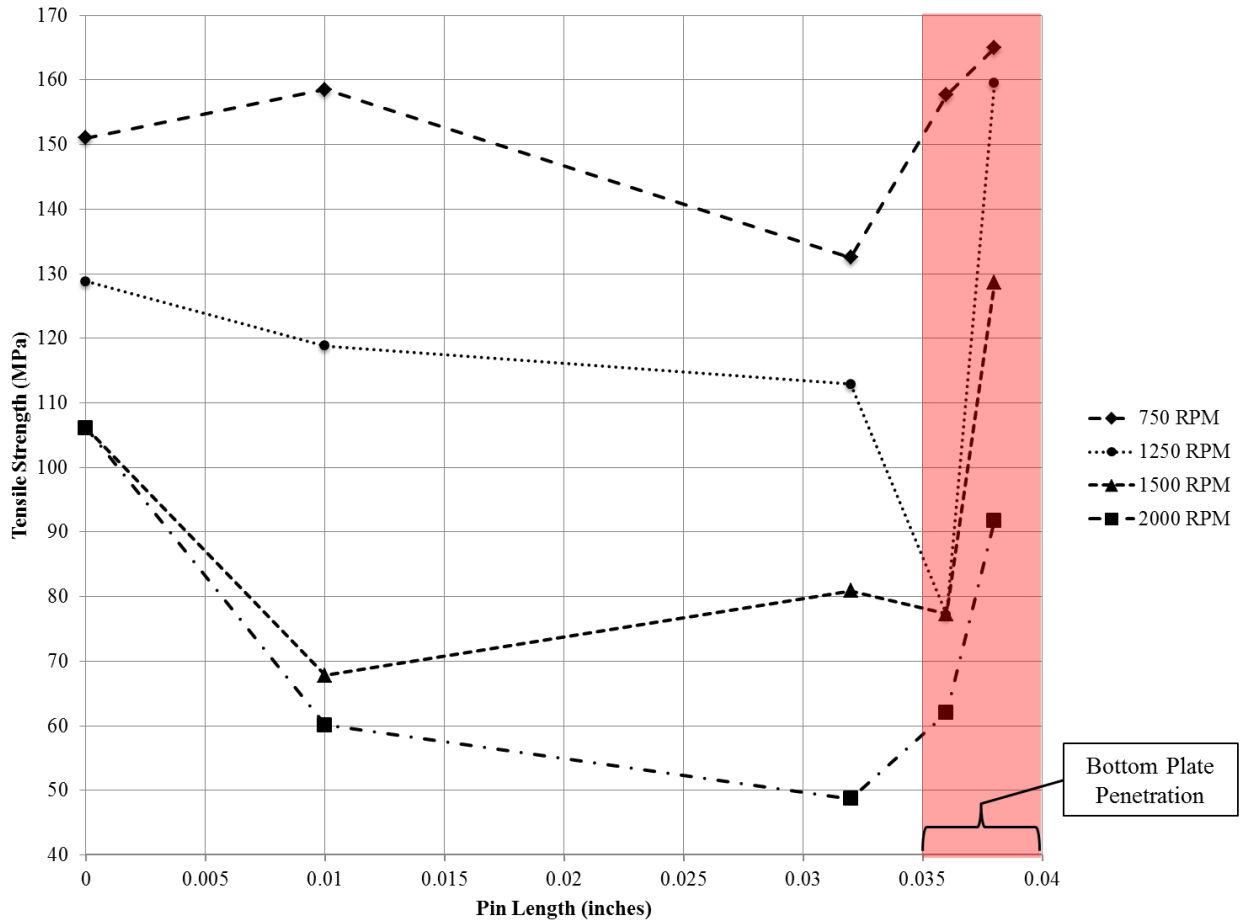


Figure 45: Effect of pin length and rotation rate on static joint strength of spot welds

The relationship between pin length, rotation rate and tensile strength can be seen in Figure 45. It is evident that the tensile strength decreases with an increase in rotation rate. The relationship between pin length and tensile strength is nonlinear. As the pin length increases from the no-pin FSSW tool to 0.010 inch pin length, the tensile strength decreases. As the pin length increases to 0.032 and 0.036 the tensile strength continues to decrease. When the pin length is long enough to penetrate the bottom plate the tensile

strength increases, recovering (and surpassing in all but one instance) the tensile strength of the no-pin FSSW tool.

*Failure Analysis*


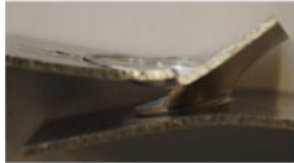

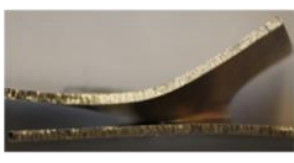

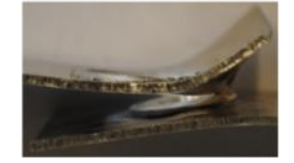

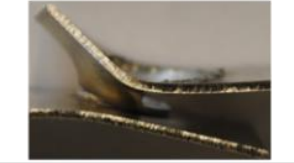


Pin Length	Top	Bottom	T.S. MPA
No pin			151
0.010			158.5
0.032			132.5
0.036			157.7
0.038			165

Figure 46: FSSW Failure Modes for 750 RPM


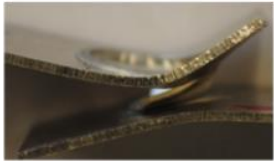



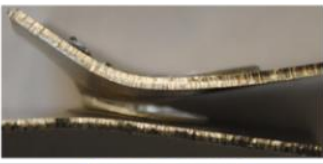




Pin Length	Top	Bottom	T.S. MPA
No pin			128.8
0.010			118.8
0.032			112.9
0.036			77.2
0.038			159.6

Figure 47: FSSW Failure Modes for 1250 RPM







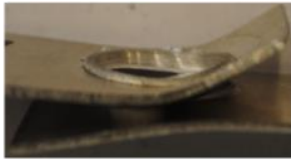



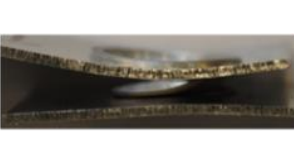
Pin Length	Top	Top (bottom)	Bottom	T.S. MPA
No pin				106.1
0.010				67.8
0.032				80.9
0.036				77.3
0.038				128.6

Figure 48: FSSW Failure Modes for 1500 RPM












Pin Length	Top	Top (bottom)	Bottom	T.S. MPA
No pin				106.1
0.010				60.1
0.032				48.7
0.036				62
0.038				91.8

Figure 49: FSSW Failure Modes for 2000 RPM

During the evaluation of the tensile strength of the spot welds, three distinct failure modes occurred. The aluminum plate experienced out of plane bending during the tensile tests causing the weld to experience a “peel” force in addition to pure shear [Bakavos 2010]. The peel force is a result of the geometry of the weld joint being evaluated and the thickness of the plate. The observed failure modes were:

- i. *Shear Mode*: This mode is characterized by a complete separation of the top and bottom plate with the weld nugget remaining in the top plate. The fracture occurs along the original boundary between the top and bottom plates.

- ii. *Mixed Mode*: This mode represents a combination of the shear and nugget pullout modes. The failure in this mode occurs in the top plate partially along the perimeter of the weld zone. Unlike the nugget pullout mode, the top plate does not completely separate from the weld zone. The weld nugget remains attached to the bottom plate but is partially “peeled” away revealing the interface between the two.
- iii. *Nugget Pullout Mode*: This mode is characterized by a complete separation of the top and bottom plate. In this mode however, the interface fails in the top plate along the perimeter of the weld zone. The weld nugget is left attached to the bottom plate.

Images of the failure modes observed during testing for each of the pin length and rotation rate combinations can be seen in Figures 46 through 49. The welds that experienced the shear mode were imaged from above (looking down at the keyhole), from the underside of the top plate, and from above the bottom plate. For the mixed mode, each weld is imaged from above and from the side to illustrate the “nugget-peel.” The nugget pullout mode was imaged from above for the top and bottom plates. The crack in the top plate originated on the lapped side (“A” side in Figure 44) for modes ii and iii while the nugget-peel failure mode originated on the under-lapped side (“B” side in Figure 44) for mode ii.



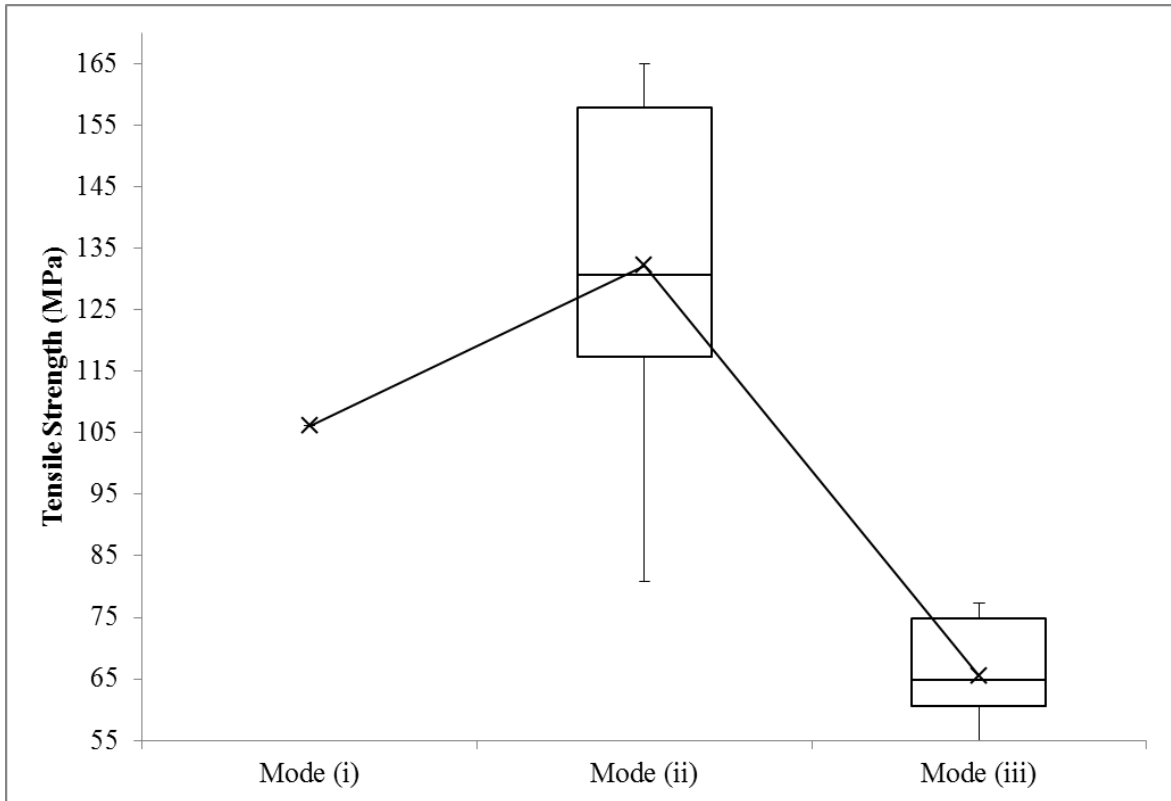


Figure 50: Comparison of failure mode to weld strength. Only 2 welds in the experiment were classified as a mode (i) failure while 12 (60%) of the welds were classified as a mode (ii). The mode (ii) type failures exhibited the highest joint strength when compared to the other failure modes. The remaining welds were classified as mode (iii) failures.

In Figure 50 it can be seen that failure mode (ii) corresponds to the strongest welds in the study. The average strength of the welds classified as a mode (ii) failure was 22.5% stronger than that of the other modes. Failure mode (ii), or the “Mixed Mode”, most commonly occurred at the lower rotation rates of 750 and 1250 rpms. Failure mode (iii), or the nugget pullout mode, occurred in the weakest welds of the experiment. This failure mode more frequently occurred at the higher rotation rates of 1500 and 2000 rpms and for the mid-range pin lengths of 0.010, 0.032 and 0.036 inches. Failure mode (i), or the shear mode, was solely associated for the no-pin FSSW tool at the higher rotation rates.

As the rotation rate increased, the failure mode for each of the pin lengths shifted from mode (ii) to mode (iii) for the mid-range pins, and from mode (ii) to mode (i) for the pinless FSSW tool.

### *Weld Zone Imaging*

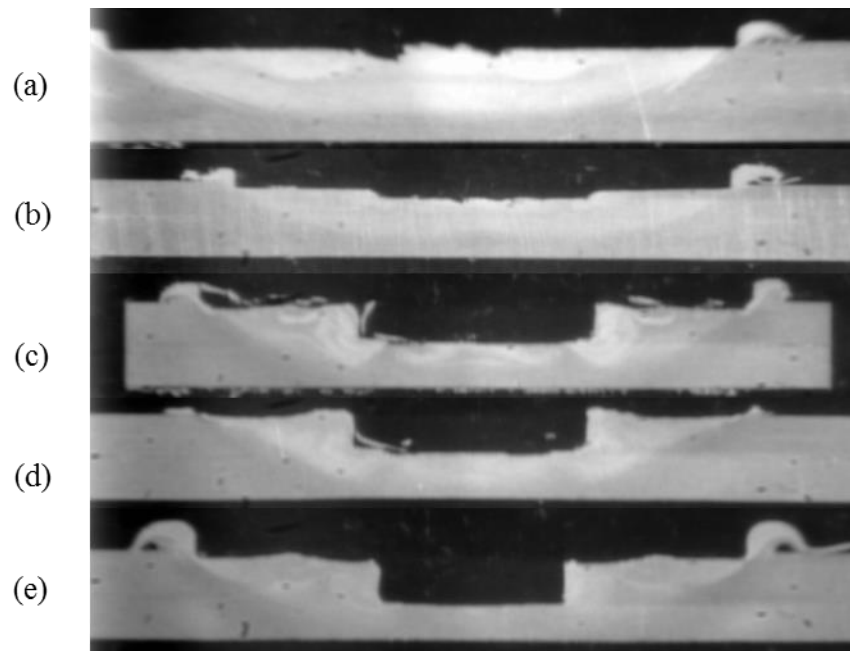


Figure 51: Macrosection images of cross-sections of welds. (a) 750 rpm/pinless, (b) 750 rpm/0.010'' pin, (c) 750 rpm/0.032'' pin, (d) 750 rpm/0.036'' pin, (e) 750 rpm 0.038'' pin

Macrosection images of the 750 rpm weld cross sections can be seen in Figure 51. As the pin plunges into the surface the material from the top and bottom sheet are stirred. When the shoulder of the tool makes contact with the surface of the top sheet the stirred material is forced down. When this happens some of the stirred material is forced out of the weld zone and forms a ring of weld flash around the shoulder of the tool. The amount of weld flash is related to the selected plunge depth and the  $0^\circ$  tilt angle used. Keller's reagent was used to etch each cross section in order to enhance the visibility of the

thermo-mechanically affected zone (TMAZ). For every pin length, the TMAZ extends from the edges of the tool shoulder into the bottom sheet; the size and shape of the TMAZ is similar across all welds. For each of the shorter pin lengths (no pin, 0.010, 0.032, 0.036 inch) the TMAZ had no distinguishable difference in bottom sheet penetration. The TMAZ created by the longer pin lengths extended completely through the bottom sheet.

At the interface between the top and bottom sheet several bond conditions were observed: a partial metallurgical bond, a complete metallurgical bond and a kissing bond. The partial metallurgical bond (bond (i)) contains irregularly spaced joint line oxides and voids along the joint line. A complete metallurgical bond (bond (ii)) exists when no voids or oxides are present at the interface. For the kissing bond (bond (iii)) a faint oxide layer is observed with an irregular formation at the interface.

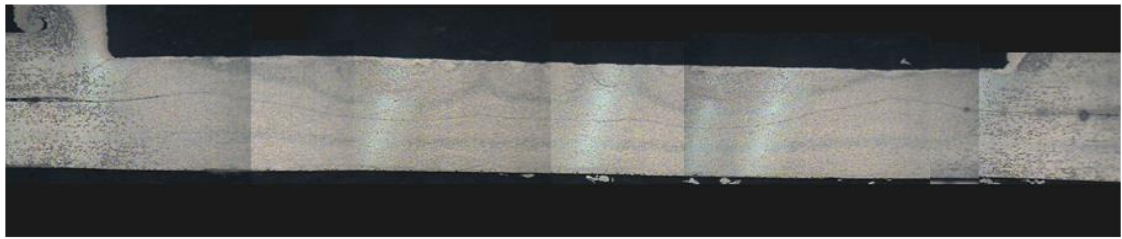
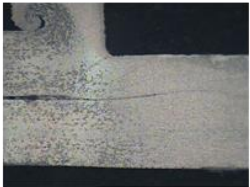

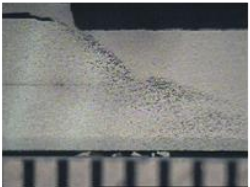
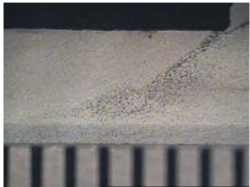
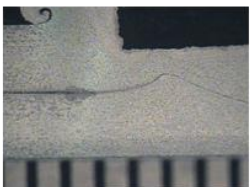
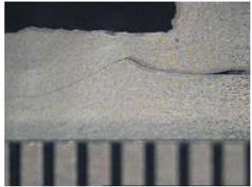

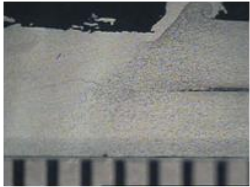




				No Pin
(a) compiled      bond(i & iii)				
				No Pin
(a) left      bond(i)	(a) right      bond(i)	(b) left      bond(ii)	(b) right      bond(ii)	
				0.032"
(c) left      bond(i)	(c) right      bond(i)	(d) left      bond(ii)	(d) right      bond(iii)	
				0.038"
(e) left      bond(i)	(e) right      bond(i)	(f) left      bond(ii)	(f) right      bond(ii)	
2000 rpm		750 rpm		

Figure 52: Images of bond interface modes and notable failures. (a) A compiled image for the cross section of the pinless tool at 2000 rpm. Bond (i and iii) account for 100% of the interface for this weld. (b) The combination of 750 rpm and a pinless tool resulted in a well formed stir zone with good metallurgical bonding. (c) The 0.032" pin length at 2000 rpm resulted in a weld exhibiting bond (i). (d) The 0.032" pin length at 750 rpm resulted in a good metallurgical bond. A small amount of bond (iii) was observed at the right edge of the interface between the plates. (e) The 0.038" pin length at 2000 rpm resulted in a weld exhibiting bond (i). (f) The 0.038" pin length at 750 rpm resulted in a good metallurgical bond.

The welds created at the lowest rotation rate were characterized by very good metallurgical bonding. The welds created at the highest rotation rate exhibited all three of the observed bond types. In the case of the pinless tool at 2000 rpm (Figure 52 (a)) it can be seen that a combination of bonds (i) and (iii) traversed the entire cross section of the weld. For the 0.032” length pin (Figure 52 (c)) a hooking defect was observed on both sides of the weld. For this parameter set the hooking defect extends from the original joint line into the top plate where it sharply turns downward back into the bottom plate. The 0.038” length pin (Figure 52 (e)) was observed to have a similar but less severe defect.

### Discussion

A strong correlation was found to exist between rotation rate and joint strength. The highest joint strength corresponds to the lowest rotation rate of 750 rpm; the highest rotation rate (2000 rpm) resulted in an approximately 50% reduction in joint strength. Figure 52 shows the differences observed in the bond types created at 750 and 2000 rpm. The bond types created at higher rotation rates were found to result in failure modes (i) & (iii), which were also associated with a reduction in joint strength (Figure 50). Hooking defects which have been shown to be detrimental to the strength of the weld were observed at 2000 rpm. The hooking defect is an unbounded region that is located in the TMAZ and may extend into the stir zone (SZ). This crack like feature acts as a stress concentration at the interface between the SZ and the TMAZ, reducing the “effective sheet thickness” (EST) of the material. The EST is defined as the minimum distance between an unbounded surface at the interface and the top surface of the upper sheet.

Higher ESTs have been shown to carry larger tensile loads in aluminum alloys [Cederqvist]. In Figure 52 it can be seen that for the 750 rpm welds the EST was approximately equal to the original sheet thickness; for the 2000 rpm welds, the EST reduced by as much as 45%.

The heat generated during FSSW is dictated by the shoulder diameter, rotation rate and dwell time. For this experiment the shoulder diameter and dwell time were held constant. Using the expression introduced by Roy et al. it is possible to calculate the non-dimensional heat input  $Q'$  by the tool [Roy].

$$Q' = \frac{\sigma_g A \omega C_p \phi}{k U^2} \quad (4.1)$$

Where  $\sigma_g$  is the yield stress of the material at a temperature of 80% of the solidus temperature,  $C_p$  is the specific heat capacity of the workpiece,  $\phi$  is the ratio in which heat generated at the shoulder/material interface is transported into the workpiece,  $k$  is the thermal conductivity of the workpiece and  $U$  is the traverse velocity. Since each of these parameters represents a constant, their specific values are not needed: these constant will combined into a single scaling parameter. A value of 1 was used for each of the calculations. The parameters  $A$  and  $\omega$  represent the cross sectional area of the shoulder and the rotation rate of the tool, respectively. The cross sectional area of the shoulder is larger for the pinless tool than that for the tools with pins. Equation 4.1 assumes that the majority of the heat is generated by the shoulder. The calculated non-dimensional heat input for the combinations of pin length and rotation rate can be seen in Figure 53. The results of the calculation show that for the 2000 rpm welds there is as much as a 60%

increase in the heat generated at the shoulder/workpiece interface when compared to the 750 rpm welds. The higher temperatures associated with the heat generation may be a cause of the partial metallurgical interfaces and joint defects associated with reduced joint strengths. These defects may be reduced by using shorter dwell times for higher rotation rates.

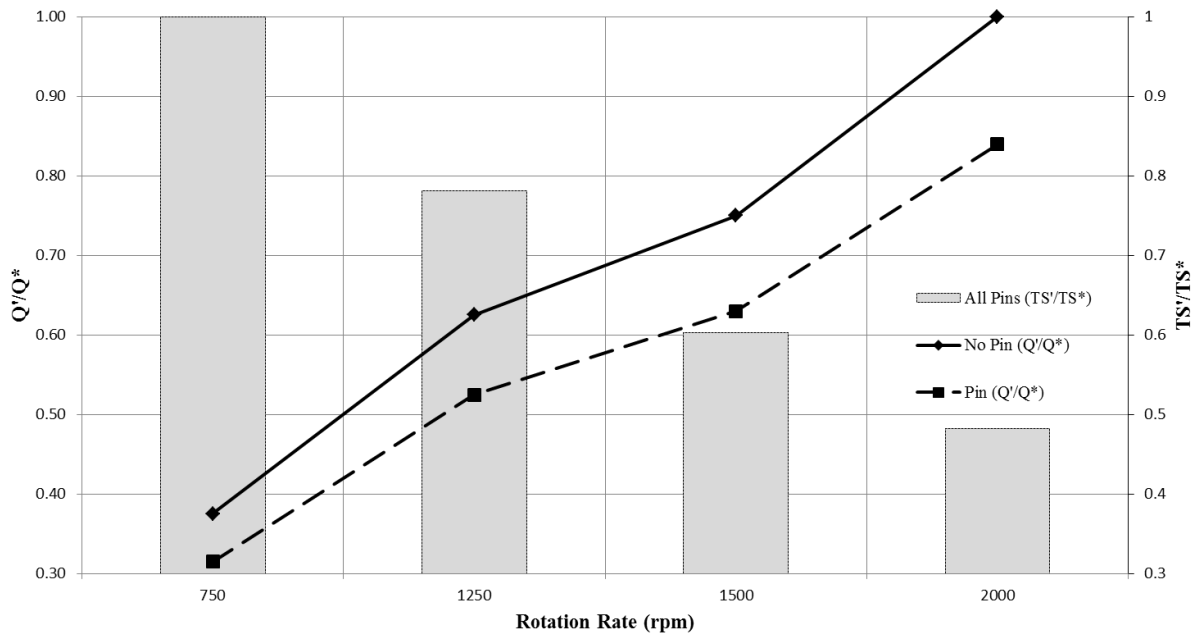


Figure 53: Comparison of theoretical heat generated by the FSSW tools used at the various rotation rates and their resulting average tensile strength.  $Q'/Q^*$  represents the normalized theoretical heat input calculated for each rotation rate used.  $Q'$  is the individual calculated value for each tool and rotation rate combination and  $Q^*$  is the maximum calculated value. The average tensile values represented as  $TS'/TS^*$  were calculated by averaging each of the measured tensile strengths for a given rotation rate for all pin lengths used.  $TS'$  and  $TS^*$  represent the individual average tensile strength for a given rotation rate and the maximum average tensile strength respectively.

It was found that pin length has two distinct effects on the tensile strength of the spot weld (see Figure 45). Pin lengths that do not penetrate the bottom sheet reduce the spot weld tensile strength. At this time there is very little published data available for pin

lengths that do not penetrate the bottom sheet. Pin lengths that penetrate the bottom sheet produced an increase in joint strength, a result that is in good agreement with data available in the literature [Bakavos 2009]. It is thought that there are three main causes that lead to this observation.

1. In FSW the heat generated during welding is generated largely by the surface of the shoulder in contact with the workpiece. As a result, Arora et al. conclude that this contact condition and the rotation of the shoulder are primarily responsible for the material flow during welding [Arora]. Unless the geometry of the pin is such that it can significantly contribute to the heat generation and material flow, its effect will be detrimental to the strength of the spot weld.
2. As previously stated, pin lengths that do not penetrate the bottom sheet can reduce the EST of the top sheet, an effect which in turn reduces the tensile load that the spot weld can withstand.
3. The keyhole left by a non-zero pin length reduces the cross section of the tensile coupons being evaluated. Longer pin lengths that do not penetrate the bottom sheet were found to amplify this effect. See Figure 51 for images of the keyholes for each pin length.

An analytical solution for the 3-D velocity field was presented by Arora et al. [Arora]. Their model made the following assumptions: the tool is a smooth cylinder, the flow results from the rotation of the shoulder, and that the geometry of the material flow can be empirically determined. The estimate of the material flow field was created by modifying an analytic solution for the flow of an incompressible fluid between two discs,



one rotating (the shoulder) and the other stationary. The three components of velocity in cylindrical coordinates are given by Equation 4.2:

$$u = r\omega F\hat{r}, v = r\omega G\hat{\theta}, w = d\omega H\hat{z} \quad (4.2)$$

$r\omega$  is the tangential velocity directly beneath the shoulder,  $d$  is the distance between the two discs, and  $F$ ,  $G$  and  $H$  are functions of  $z/d$  [Arora]. The assumed geometry of the material flow zone has the shape of an inverted cone; the shoulder of the tool forms the cone base. The contact condition of the plasticized metal beneath the shoulder is modeled as partial-slip. Using the tangential velocity of the tool the respective velocity of the material in contact with the shoulder can be evaluated as  $(1 - \sigma)r\omega$ , where  $\sigma$  is the fraction of slip at the interface. Using equation (4.2) the velocity profile was calculated at various depths for the FSSW tool's shoulder and pin (see Figure 54).

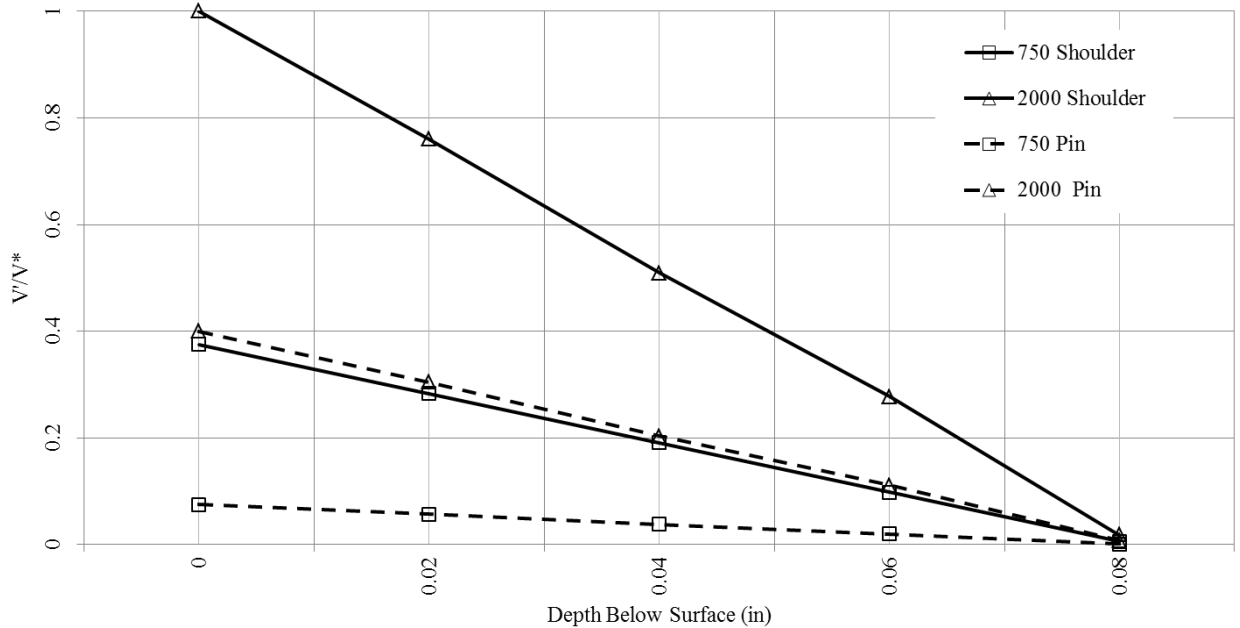


Figure 54: Comparison of velocity field at various depths (0.02, 0.04, 0.06 and 0.08) created beneath the shoulder during FSSW. Two rotation rates were considered; 750 and 2000 rpm. A pinless and non-zero pin design were considered.  $V'$  represents the magnitude of the 3 dimensional velocity field for a given parameter set ( $u, v, w, r, z$ ). The velocity is calculated such that  $r$  = radius of shoulder or pin.  $V^*$  represents the maximum calculated value.

It can be seen in Figure 54 that the shoulder's contribution to the velocity field is greater than that of the pin. The resulting velocity fields are presented at some linear distance beneath the surface being considered (either the shoulder or pin bottom.) For the 2000 rpm case directly beneath the tool pin the calculated velocity field of the material is approximately 50% that of the velocity field directly beneath the shoulder. However the pin bottom is located at some distance beneath the shoulder which results in its contribution increasing significantly. If the pin bottom is offset by a distance of 0.04 inches (or a pin length of 0.04 inches) beneath the shoulder it can be seen that its contribution to the velocity field would be significantly higher ( $\approx 80\%$ ) and would surpass

the shoulder's contribution at greater depths beneath the pin. As the length of the pin increases, its relative contribution to the total velocity field increases. At a sufficient length, the pin will positively affect the size of the weld zone, which may improve the strength of the weld joint (see Figure 55).

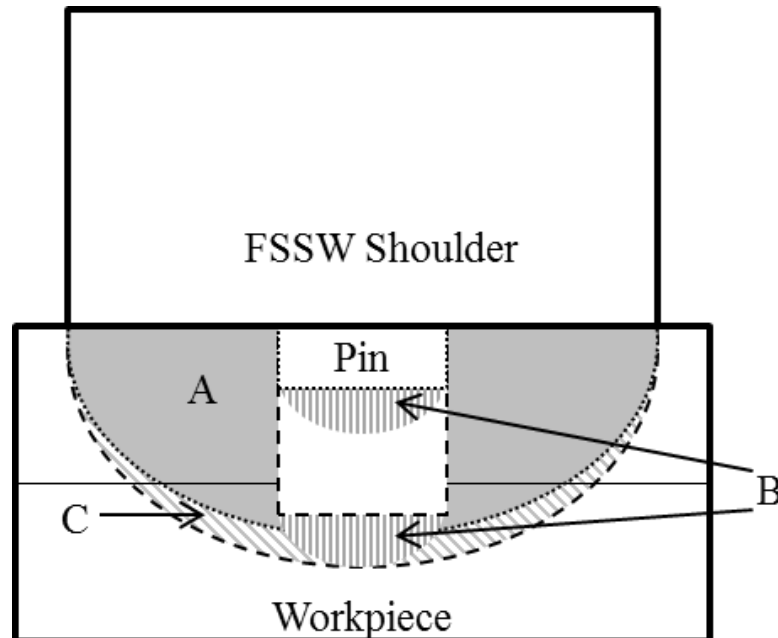


Figure 55: Graphical representation of the observed pin length effect on joint strength. Region "A" represents the velocity field created by the shoulder. Region "B" represents the velocity field created by two different pin lengths. It can be seen that in the case of the longer pin length, the total velocity field is increased by the pin bottom's contribution. Region "C" represents the resultant velocity field.

However, if a pin length is used that extends beyond the zone of material flow created by the shoulder, the quality of the weld may be reduced. Evidence of this can be found in the literature [Bakavos 2009]. When choosing a pin length for FSSW consideration should be given to the fact that a limited window of optimal length exists. This length depends on the diameter of the shoulder to be used as well as features to be included on the pin.

For FSSW, the cross section of the weld zone includes the void created by the keyhole defect. This property reduces the overall area of the weld which undergoes tensile loading. Longer pin lengths that do not penetrate the bottom plate greatly reduce the overall joint strength of the spot welds. The keyhole can be eliminated by using a pinless FSSW tool [Bakavos 2010, Tozaki 2010, Bakavos 2009]. The tensile strength of the pinless tool was, on average, 90% as strong as the strongest full penetration spot welds.

### Conclusions

The effect that pin length and rotation rate have on the tensile strength of FSSW welds created in 0.04” thick Al 6061 T6 plate in a lap joint configuration has been investigated. For the welding parameters studied, it was found that lower rotation rates resulted in the welds with the highest tensile strengths. The use of higher rotation rates produced partial metallurgical bonds and defects along the joint line. Non-zero pin lengths that did not penetrate the bottom plate were found to be detrimental to the quality of the welds. When compared to the full penetration spot welds, the pinless tool performed very well. The strength of the spot welds was on average 90% as strong as those created by more conventional full penetration tools. At the highest rotation rate, the pinless tool produced the strongest spot welds.

Heat generated during the spot welds was found to strongly correlate with joint strength of the spot welds. By using shorter dwell times for higher rotation rates it may be possible to reduce the observed defects and improve weld strength. Of the three failure modes, the mixed-mode is preferable because it generally failed at under higher tensile loading. This mode occurred most frequently for lower rotation rates in both pinless and full length penetration tools.

The pinless tool offers several advantages over conventional FSSW tools: a simplified geometry that is easier to model and manufacture and creating a spot weld that is more aesthetically appealing due to the lack of a keyhole defect.

## CHAPTER V

### THE APPLICATION OF A PINLESS TOOL IN FRICTION STIR SPOT WELDING: AN EXPERIMENTAL AND NUMERICAL STUDY

Chase D. Cox, Jason R. Aguilar, Marjorie C. Ballun, Alvin M. Strauss, George E. Cook.  
“The Application of a Pinless Tool in Friction Stir Spot Welding: An Experimental and  
Numerical Study.” Proceedings of the Institution of Mechanical Engineers, Part D:  
Journal of Automobile Engineering, Accepted: 2013.

#### Abstract

A pinless friction stir spot welding tool with a scrolled convex shoulder is used to create spot welds on aluminum alloy plates. The effect that rotation rate, dwell time, plunge depth and plunge rate have on the spot welding process is investigated. A strong correlation was found to exist between joint strength versus the tool rotation rate and dwell time. Low rotation rates and short dwell times resulted in significantly stronger welds and conversely, higher rotation rates and longer dwell times resulted in spot welds with hooking defects and lower joint strengths. Using shear tests and macrosection analysis on the spot welds, the dependence of joint strength, spindle torque, temperature and axial force on the identified process parameters will be discussed. A computational fluid dynamic model is created to simulate the effect the tool rotation rate has on the heat generated and material flow during spot welding.

## Introduction

Friction stir spot welding (FSSW) is a solid state joining process that is currently being used by automotive and aerospace manufacturers as an alternative to rivets and resistance spot welding. To reduce the operating costs of their finished products, manufacturers can use FSSW to create high strength welds in light-weight alloys such as aluminum. Furthermore, as the cost of the fuel required for operating vehicles continues to increase, or alternatively as the demand for “green” vehicles increases, the demand for lighter vehicles will also increase. By using FSSW, it has been reported that it is possible to reduce the energy use by 99% and the cost of installation by 40% when compared to resistive spot welding [Feldman]. Presently there are over 200 FSSW robots being used in industrial applications and there are approximately 30,000 cars per month created that contain friction stir spot welds [Fujimoto].

In FSSW, the spot weld is created by plunging a rotating tool into the weldment, dwelling for a short period of time and then retracting the tool. A typical FSSW tool consists of a cylindrical shoulder and pin similar to tools used in linear Friction Stir Welding. The spot weld is formed by plastically deforming the metal in the immediate vicinity of the tool. A drawback associated with using FSW for spot welding applications is the keyhole (see Figure 1). When the tool retracts from the weld, only a shadow of its dynamic volume remains in the weld zone, meaning the keyhole is a consequence of both the solid state process and the geometry of the tool that was used to make the weld (Figure 56). In traditional FSW, the keyhole is removed via post processing or eliminated using a costly and highly specialized tool design. Alternatively, it is possible to eliminate the keyhole for FSSW by using a simple and low cost pinless tool.

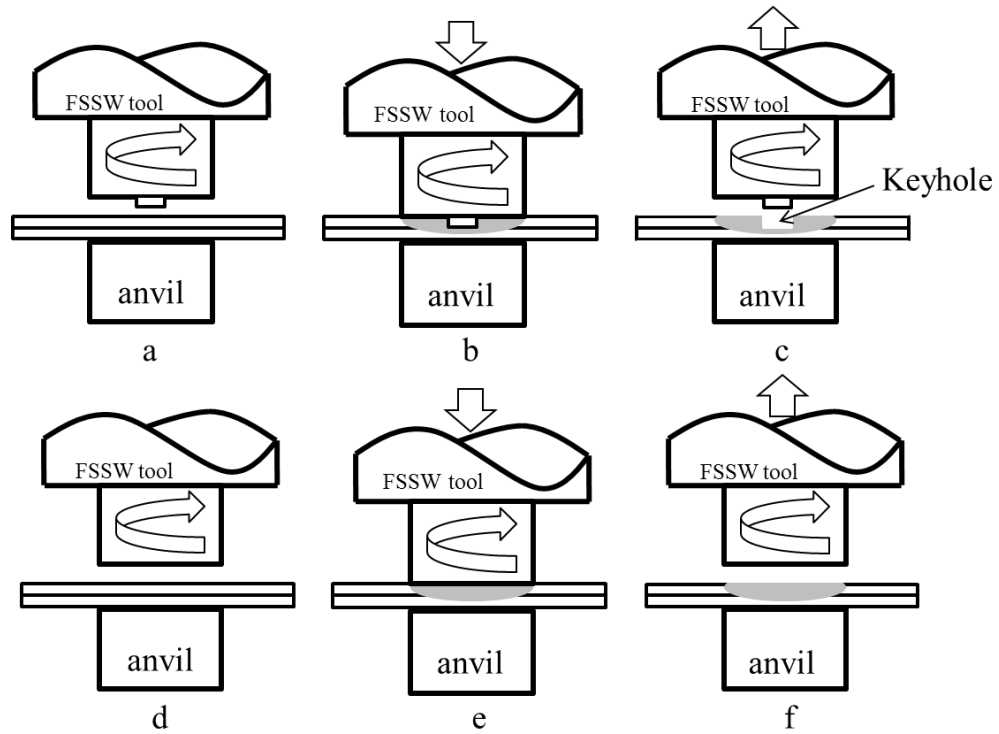


Figure 56: The Friction Stir Spot Welding Process. A-C: represents the traditional FSSW process using a tool with a pin. The resulting keyhole defect is illustrated. D-F: represents the FSSW process using a pinless tool. The lack of the keyhole defect is illustrated.

Since the majority of the literature recommends that the tool pin penetrate into the bottom sheet by at least 25%, it may seem somewhat counterintuitive that a pinless tool can be used to create quality spot welds. The existing literature concerning the use of a pinless tool for FSSW has demonstrated the ability to create quality joints in thin aluminum plates. In previous research it was found that a pinless tool without any features on the shoulder can be used to create joint strengths that are  $\approx 90\%$  of those created with a pinned tool [Cox]. It has been found by Tozaki et al. that the use of a spiral type feature on the surface of the shoulder can be used to dramatically improve the mechanical properties of the resulting spot welds and in some cases, even surpass those created with a traditional pinned tool. These higher joint strengths were attributed to an



increase in stirring caused by the features on the shoulder. By investigating the effects shoulder geometries may have on joint strengths, Bakavos et al. found that while using shorter dwell times, a “long flute wiper tool” created the best welds.

Investigations into the roll process parameters have been performed for FSSW as well. Karthikeyan performed an extensive study on the roll the process parameters involved in joining AA 2024-T3 using FSSW with a threaded pinned tool. However, limited information exists for the use of a pinless tool to join aluminum alloys. Tozaki investigated the effect rotation rate and plunge depth when using a pinless tool had on joint strength, but limited the scope to only two rotation rates and relatively large plunge depths (25% - 45% of the top sheet thickness). The goal of this investigation to gain a greater understanding of the effect that process parameters have on spot weld quality and to identify the conditions needed to obtain maximum tensile shear strength when using a pinless tool.

### Experimental

In this study, 0.040 inch thick sheets of Al 6061-T6 were used to create the joints. The samples were prepared to the dimensions seen in Figure 57. The chemical composition and mechanical properties of the parent material can be seen in Tables 2 and 3.

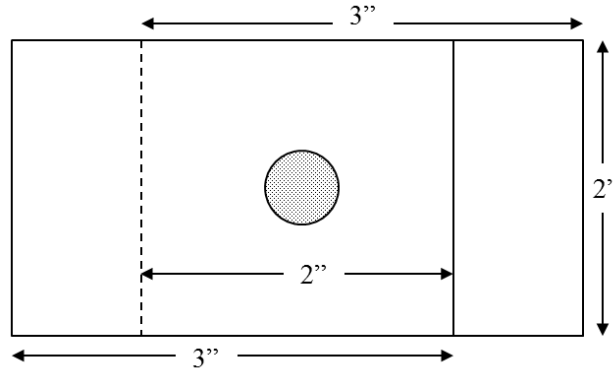


Figure 57: Spot weld sample geometry

Table 2: Chemical composition (% weight) of Al 6061-T6

Si	Fe	Cu	Mn	Mg	Cr	Zn	Ti	Other	Al
0.4-0.8	Max 0.7	0.15-0.4	Max 0.15	0.8-1.2	0.04- .035	Max 0.25	Max 0.15	Max 0.15	95.8- 98.6

Table 3: Mechanical properties of Al 6061-T6

Ultimate Tensile Strength (MPa)	Tensile Yield Strength (MPa)	Shear Strength (MPa)	Hardness (HB)
310	276	207	95

A lap joint configuration was used such that the rolled direction would be parallel to the loading direction during testing. Rigid fixturing was used to ensure that the samples did not shift during the spot weld process. In order to monitor the temperatures along the bottom side of the spot weld, a steel anvil (7 in x 3 in x 0.75 in) was instrumented with two thermocouples. The thermocouples were centered about the axis of the tool's rotation, imbedded 0.0625 in beneath the top surface of the anvil and spaced 0.5 in apart from one another (Figure 58).

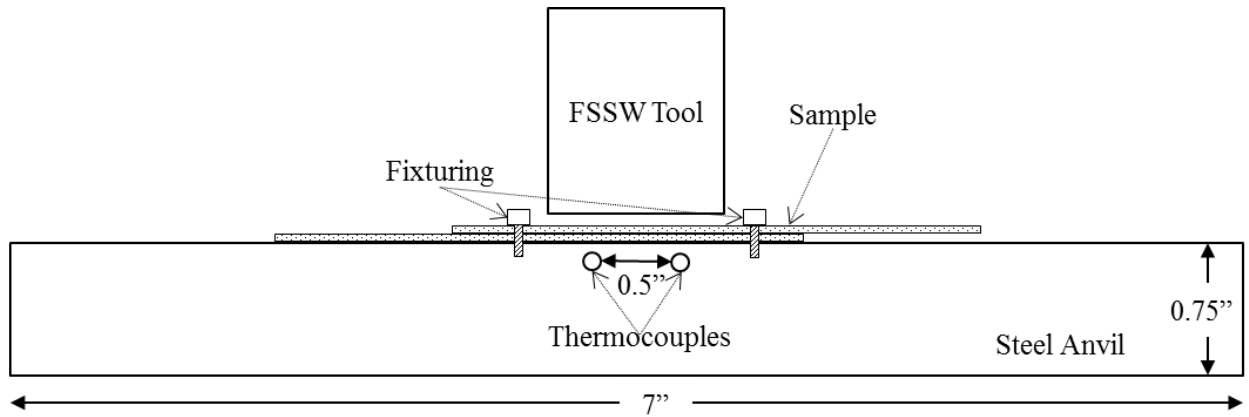


Figure 58: Instrumented Anvil. Thermocouples are located  $1/16^{\text{th}}$  of an inch beneath the surface of the anvil beneath the weld zone.

A custom wireless force transducer was used to measure the torque and axial load experienced by the FSSW tool during welding [Gibson 2011]. The pinless FSSW tool designed for this study was made of O1 tool steel, and consisted of a scrolled, spherically tapered (convex) shoulder (3 inch radius) with a 0.4 inch flat (Figure 4) and had a maximum overall tool diameter of 1 inch (Figure 59) (Appendix A). The spot welds were created by specifying a desired plunge depth and then lowering the tool into the workpiece until this position was obtained.



Figure 59: FSSW tool with scrolling

The important process parameters for FSSW using a conventional tool can be found in the literature, and they are reported as being the tool's rotation speed (rpm), plunge speed (ipm), plunge depth (in) and dwell time (s). The plunge depth is defined as the depth at which the FSSW tool penetrates into the top sheet and the dwell time is defined as the time the tool remains at the desired plunge depth. The experimental limits of these values were selected based upon the operational limitations of the FSSW machine and the capability to produce spot welds. The selected spot welding parameters for this investigation can be seen in Table 3.

Table 4: Experimental factors and levels

Factor	Units	Levels				
		-2	-1	0	1	2
Rotation Speed	rpm	750	1000	1250	1500	1750
Plunge Speed	ipm	0.3	0.4	0.5	0.6	0.7
Plunge Depth	in	0.006	0.007	0.008	0.009	0.010
Dwell Time	sec	2	3	4	5	6

Given the range of parameters and the large number of possible combinations, a central composite design was selected. Using the statistical software package Minitab 15, the experimental design was analyzed and it can be seen in Table 4. The experimental design was comprised of 29 data points (4 factors with 5 levels; 16 points, 8 star points, and 5 center points). The coded values can be calculated using Equation 5.1.

$$X_D = \frac{x - \bar{x}}{(X_{HI} - X_{LO})/2} \quad (5.1)$$

X is the value of the level,  $X_{HI}$  is the high level,  $X_{LO}$  is the low level,  $\bar{x}$  is the average of  $X_{HI}$  and  $X_{LO}$  and  $X_D$  is the design unit level. According to the specifications of the experimental design, each spot weld was made in a random order. After all of the welding was completed, samples were prepared for shear and macrosection analysis.

## Results

The shear strength of each spot weld is reported as the peak (failure) load (kgf) experienced during the shear test. Additionally, the averaged peak temperature (°C),

steady state axial load (N) and spindle torque (Nm) can be seen in Table 4. The statistical software package Minitab 15 was used to analyze the experimental design.

Table 5: Experimental design for FSSW using a pinless tool

ID	Coded Value				Variable				Response			
	T	D	P	R	$\omega$ (rpm)	Dwell Time (sec)	Plunge Depth (in)	Plunge Rate (ipm)	Failure Load (kgf)	Temp (°C)	Axial Load (N)	Spindle Torque (Nm)
1	-1	-1	-1	-1	1000	3	0.007	0.4	332.1975	267.82	9277.67	27.802
a	1	-1	-1	-1	1500	3	0.007	0.4	252.141	274.35	8491.17	16.025
b	-1	1	-1	-1	1000	5	0.007	0.4	320.6255	305.685	8726.67	24.802
ab	1	1	-1	-1	1500	5	0.007	0.4	247.4025	309.965	8797.67	18.074
c	-1	-1	1	-1	1000	3	0.009	0.4	286.319	290.81	9179.67	33.31
ac	1	-1	1	-1	1500	3	0.009	0.4	269.446	299.285	9831.67	17.353
bc	-1	1	1	-1	1000	5	0.009	0.4	279.354	323.005	9837.67	29.013
abc	1	1	1	-1	1500	5	0.009	0.4	262.0395	295.915	8268.99	17.902
d	-1	-1	-1	1	1000	3	0.007	0.6	342.722	271.57	9209.67	29.619
ad	1	-1	-1	1	1500	3	0.007	0.6	266.424	280.56	8996.67	16.194
bd	-1	1	-1	1	1000	5	0.007	0.6	288.4555	305.415	8841.67	26.595
abd	1	1	-1	1	1500	5	0.007	0.6	260.7755	309.93	8660.67	16.252
cd	-1	-1	1	1	1000	3	0.009	0.6	307.312	279.45	9198.67	27.171
acd	1	-1	1	1	1500	3	0.009	0.6	279.633	290.9	9667.67	17.116
bcd	-1	1	1	1	1000	5	0.009	0.6	326.5245	318.38	9577.67	24.605
abcd	1	1	1	1	1500	5	0.009	0.6	211.6425	329.05	9328.67	20.424
$\alpha\alpha$ -	-2	0	0	0	750	4	0.008	0.5	400.208	296.895	9392.67	46.581
$\alpha\alpha$ +	2	0	0	0	1750	4	0.008	0.5	231.429	305.85	8146.97	14.447
$\alpha\beta$ -	0	-2	0	0	1250	2	0.008	0.5	267.765	254.095	9230.67	21.36
$\alpha\beta$ +	0	2	0	0	1250	6	0.008	0.5	254.6125	332.145	9669.67	17.894
$\alpha\gamma$ -	0	0	-2	0	1250	4	0.006	0.5	291.7945	285.87	8422.97	20.893
$\alpha\gamma$ +	0	0	2	0	1250	4	0.01	0.5	263.8235	313.155	9774.67	22.06
$\alpha\delta$ -	0	0	0	-2	1250	4	0.008	0.3	232.1675	305.605	9260.67	22.689
$\alpha\delta$ +	0	0	0	2	1250	4	0.008	0.7	243.9135	293.225	9102.67	17.137
zero	0	0	0	0	1250	4	0.008	0.5	237.413	305.195	9580.67	23.622
zero	0	0	0	0	1250	4	0.008	0.5	243.0715	299.42	9321.67	22.599
zero	0	0	0	0	1250	4	0.008	0.5	248.0275	299.25	9045.67	21.97
zero	0	0	0	0	1250	4	0.008	0.5	253.0015	300.03	9325.67	21.885
zero	0	0	0	0	1250	4	0.008	0.5	256.2705	293.32	9109.67	21.24

### Joint Strength

Contour plots of shear load vs. the selected parameters for all of the spot welds can be seen in Figure 60. In general, the weld strengths created at lower rotation rates and shorter dwell times resulted in stronger welds. The maximum joint strength observed was achieved with the lowest rotation rate of 750 rpm, a dwell time of 4 sec, a plunge depth of 0.008 in and a plunge rate of 0.5 ipm (weld ID  $\alpha\alpha$ -). It should be noted however, that this

was the only data point in the study that used this rotation rate. It was observed that an increase in the rotation rate and dwell time was detrimental to the strength of the spot welds. The lowest recorded joint strength occurred at a rotation rate of 1500 rpm, a dwell time of 5 sec, a plunge depth of 0.009” and a plunge rate of 0.6 ipm (weld ID abcd). The joint strength measured at the highest rotation rate (weld ID aa+) was  $\approx$  230 kgf (2.3 kN) and this is concurrent with the reported joint strengths seen by Tozaki when using similar welding parameters. The data gathered in this experiment suggests that the plunge rate does not have a significant effect on the shear strength of the spot welds. The high joint strengths associated with lower dwell times is particularly beneficial for manufacturers, as it allows for a low process cycle time.

### Contour Plots of Shear Load (kgf)

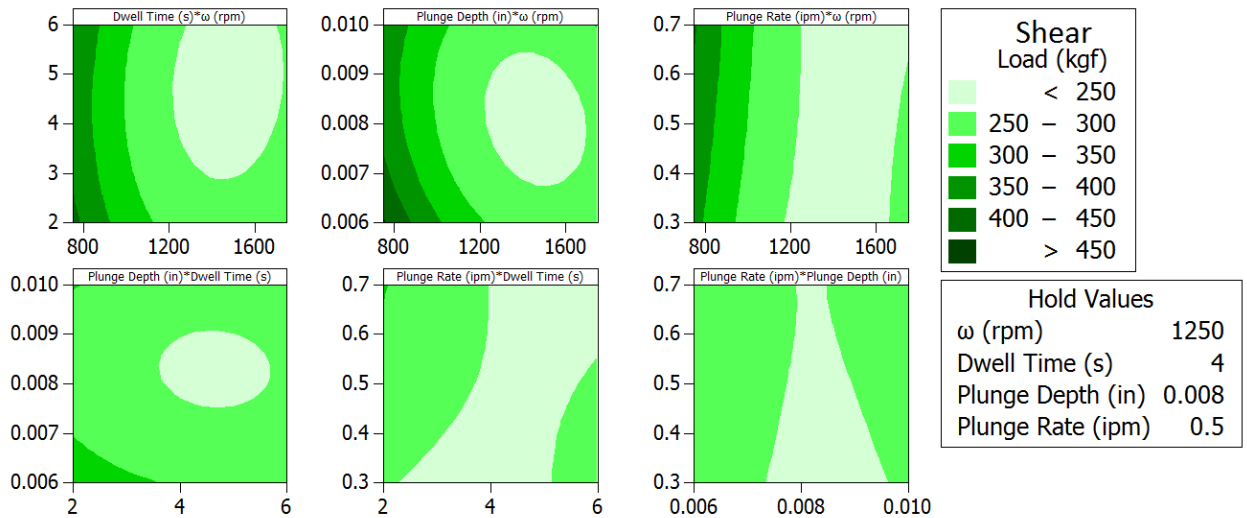


Figure 60: Contour plots of shear load of spot welds vs. all parameters. The label of each access can be seen in the title of each subplot (y-label \* x-label)

Using the response surface method within the Minitab software package, an empirical relationship relating the selected parameters and the measured shear loads was created. The analysis considered both a linear and squared relationship for the chosen parameters as well as all interactions between the parameters (14 degrees of freedom). Significant values were selected as those having p values less than 0.05 (Table 5). The resulting empirical relationship can be expressed as:

$$\textit{Shear Load} = [247.557 - 64.297T + 74.994T^2 + 36.985P^2]kgf \quad (5.2)$$

where “T” and “P” are the coded values for rotation rate and plunge depth. The fit of the model can be checked by looking at the R-Sq value. Which indicates how much of the variation can be explained using the model, e.g. an R-Sq value of 1.0 would account for 100% of the variation. For this model an R-Sq value of 0.8632 was calculated.



Table 6: Regression coefficients for shear load, spindle torque and temperature

Estimated Regression Coefficients for Shear Load (kgf)				
Term	Coef	SE Coef	T	P
Constant	247.557	9.376	26.403	0.000
$\omega$ (rpm)	-64.297	8.559	-7.512	0.000
Dwell Time (s)	-13.807	8.559	-1.613	0.129
Plunge Depth (in)	-12.035	8.559	-1.406	0.182
Plunge Rate (ipm)	4.788	8.559	0.559	0.585
$\omega$ (rpm)* $\omega$ (rpm)	74.994	16.464	4.555	0.000
Dwell Time (s)*Dwell Time (s)	20.365	16.464	1.237	0.236
Plunge Depth (in)*Plunge Depth (in)	36.985	16.464	2.246	0.041
Plunge Rate (ipm)*Plunge Rate (ipm)	-2.784	16.464	-0.169	0.868
$\omega$ (rpm)*Dwell Time (s)	-8.048	20.966	-0.384	0.707
$\omega$ (rpm)*Plunge Depth (in)	20.127	20.966	0.960	0.353
$\omega$ (rpm)*Plunge Rate (ipm)	-14.768	20.966	-0.704	0.493
Dwell Time (s)*Plunge Depth (in)	3.269	20.966	0.156	0.878
Dwell Time (s)*Plunge Rate (ipm)	-19.503	20.966	-0.930	0.368
Plunge Depth (in)*Plunge Rate (ipm)	5.486	20.966	0.262	0.797
S = 20.9656    PRESS = 34485.3				
R-Sq = 86.32%    R-Sq(pred) = 23.36%    R-Sq(adj) = 72.65%				
Estimated Regression Coefficients for Spindle Torque (Nm)				
Term	Coef	SE Coef	T	P
Constant	22.2632	1.0492	21.220	0.000
$\omega$ (rpm)	-12.3204	0.9578	-12.864	0.000
Dwell Time (s)	-1.1546	0.9578	-1.205	0.248
Plunge Depth (in)	1.1554	0.9578	1.206	0.248
Plunge Rate (ipm)	-1.4508	0.9578	-1.515	0.152
$\omega$ (rpm)* $\omega$ (rpm)	8.0898	1.8423	4.391	0.001
Dwell Time (s)*Dwell Time (s)	-2.7972	1.8423	-1.518	0.151
Plunge Depth (in)*Plunge Depth (in)	-0.9477	1.8423	-0.514	0.615
Plunge Rate (ipm)*Plunge Rate (ipm)	-2.5112	1.8423	-1.363	0.194
$\omega$ (rpm)*Dwell Time (s)	4.7128	2.3460	2.009	0.064
$\omega$ (rpm)*Plunge Depth (in)	0.2422	2.3460	0.103	0.919
$\omega$ (rpm)*Plunge Rate (ipm)	1.8923	2.3460	0.807	0.433
Dwell Time (s)*Plunge Depth (in)	0.2278	2.3460	0.097	0.924
Dwell Time (s)*Plunge Rate (ipm)	0.6187	2.3460	0.264	0.796
Plunge Depth (in)*Plunge Rate (ipm)	-2.5548	2.3460	-1.089	0.295
S = 2.34604    PRESS = 430.254				
R-Sq = 93.63%    R-Sq(pred) = 64.42%    R-Sq(adj) = 87.26%				
Estimated Regression Coefficients for Temperature (°C)				
Term	Coef	SE Coef	T	P
Constant	299.443	3.363	89.052	0.000
$\omega$ (rpm)	3.811	3.070	1.241	0.235
Dwell Time (s)	33.225	3.070	10.824	0.000
Plunge Depth (in)	13.006	3.070	4.237	0.001
Plunge Rate (ipm)	-0.528	3.070	-0.172	0.866
$\omega$ (rpm)* $\omega$ (rpm)	1.030	5.904	0.174	0.864
Dwell Time (s)*Dwell Time (s)	-7.223	5.904	-1.223	0.241
Plunge Depth (in)*Plunge Depth (in)	-0.830	5.904	-0.141	0.890
Plunge Rate (ipm)*Plunge Rate (ipm)	-0.928	5.904	-0.157	0.877
$\omega$ (rpm)*Dwell Time (s)	-10.767	7.519	-1.432	0.174
$\omega$ (rpm)*Plunge Depth (in)	-5.203	7.519	-0.692	0.500
$\omega$ (rpm)*Plunge Rate (ipm)	10.857	7.519	1.444	0.171
Dwell Time (s)*Plunge Depth (in)	-7.697	7.519	-1.024	0.323
Dwell Time (s)*Plunge Rate (ipm)	9.497	7.519	1.263	0.227
Plunge Depth (in)*Plunge Rate (ipm)	-0.222	7.519	-0.030	0.977
S = 7.51894    PRESS = 4261.09				
R-Sq = 91.23%    R-Sq(pred) = 52.78%    R-Sq(adj) = 82.46%				

### *Spindle Torque*

Contour plots of spindle torque versus the selected parameters for all of the spot welds can be seen in Figure 61. The torque signal has been used successfully for control purposes and real-time quality monitoring in linear FSW [Gibson 2012, Longhurst, Prater]. It may also provide valuable insight into the FSSW process and has been investigated in this study. The highest measured torque, 46.6 Nm, occurred at the lowest rotation rate, 750rpm, and the lowest measured torque, 14.4 Nm, occurred at the highest rotation rate, 1750rpm. These two welds were ID  $\alpha\alpha^-$  and ID  $\alpha\alpha^+$  respectively. By monitoring the spindle torque and the rotation rate of the tool, it is possible to define the weld power (watts). The equation for weld power is expressed as:

$$P = (F_T \times V_T) + (M \times \omega) \quad (5.3)$$

where  $F_T$  is the traverse force,  $V_T$  is the traverse velocity,  $M$  is the motor torque and  $\omega$  is the rotation rate. Due to the nature of spot welding, there is no traverse motion and thusly, the first term of Equation 5.3 can be eliminated. The observed relationship between rotation rate and dwell time and the resultant spindle torque suggests that creating spot welds with higher power inputs will result in higher joint strengths.

## Contour Plots of Spindle Torque (Nm)

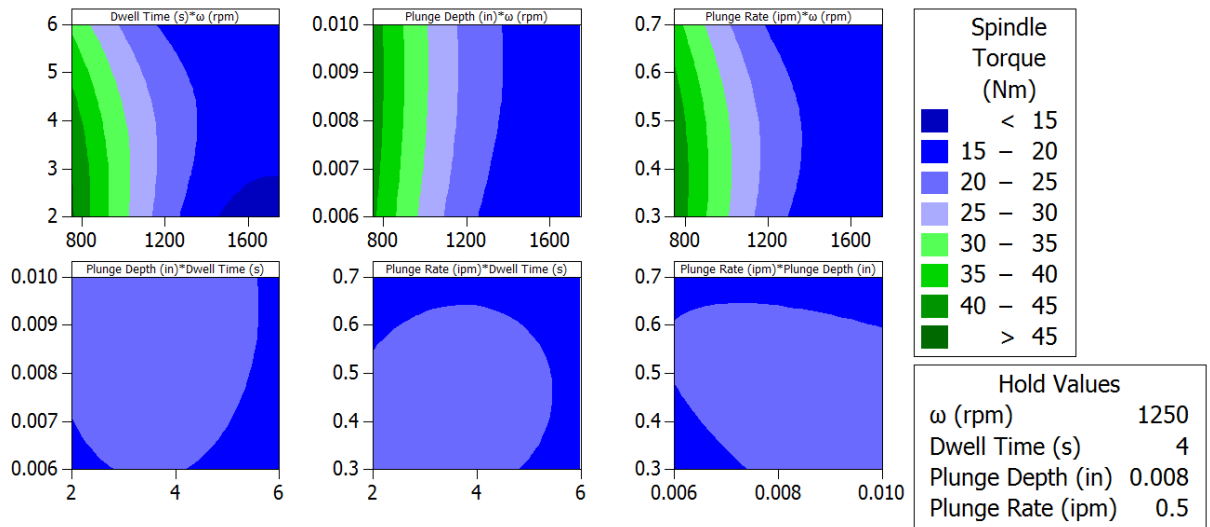


Figure 61: Contour plots of spindle torque. The label of each axis can be seen in the title of each subplot (y-label \* x-label)

Similar to the shear strength study in the previous section, a relationship relating the selected parameters and the measured spindle torque was created. Significant values were selected as those having p values less than 0.05 (Table 5). The resulting empirical relationship can be expressed as:

$$\text{Spindle Torque} = [22.2632 - 12.3204T + 8.0898T^2 + 4.7128TD]Nm \quad (5.4)$$

where “T” and “D” are the coded values for rotation rate and dwell time. For this model an R-Sq value of 0.9363 was calculated. This empirical formulation provides a reasonable estimate of the spindle torque for the rotation rates between the extremes of the experiment but provides an over-estimate the extremes. Alternatively the total torque acting on the tool can be calculated analytically using Equation 5.5 [Arora et al.]

$$M_{Total} = (\delta)^2 R \mu_f F_Z + (1 - \delta)^2 \pi R^3 \tau_{yield} \quad (5.5)$$

where  $\delta$  is the slip variable (Equation 5.6),  $R$  is the shoulder radius (m),  $\mu_f$  is the coefficient of friction (Equation 5.7),  $F_Z$  (N) is the axial force, and  $\tau_{yield}$  (MPa) is the temperature dependent shear strength of the material.

$$\delta = 0.2 + 0.8 * \left( 1 - \exp\left(-\delta_o \frac{\omega}{\omega_o}\right) \right) \quad (5.6)$$

$$\mu_f = \mu_o * \left( 1 - \exp\left(-\delta \frac{\omega}{\omega_o}\right) \right) \quad (5.7)$$

where  $\omega_o$  (130 rad/sec),  $\delta_o$  (0.1), and  $\mu_o$  (0.25) are constants. The computed values of torque using Equation 5.5 are compared to the predicted values from the empirical formulation (Equation 5.4) and the experimental values for different rotation rates in Figure 62. The torque required during welding is predicted to be inversely proportional to rotation rate. The analytic calculation of torque is in close agreement with the experimentally observed values.

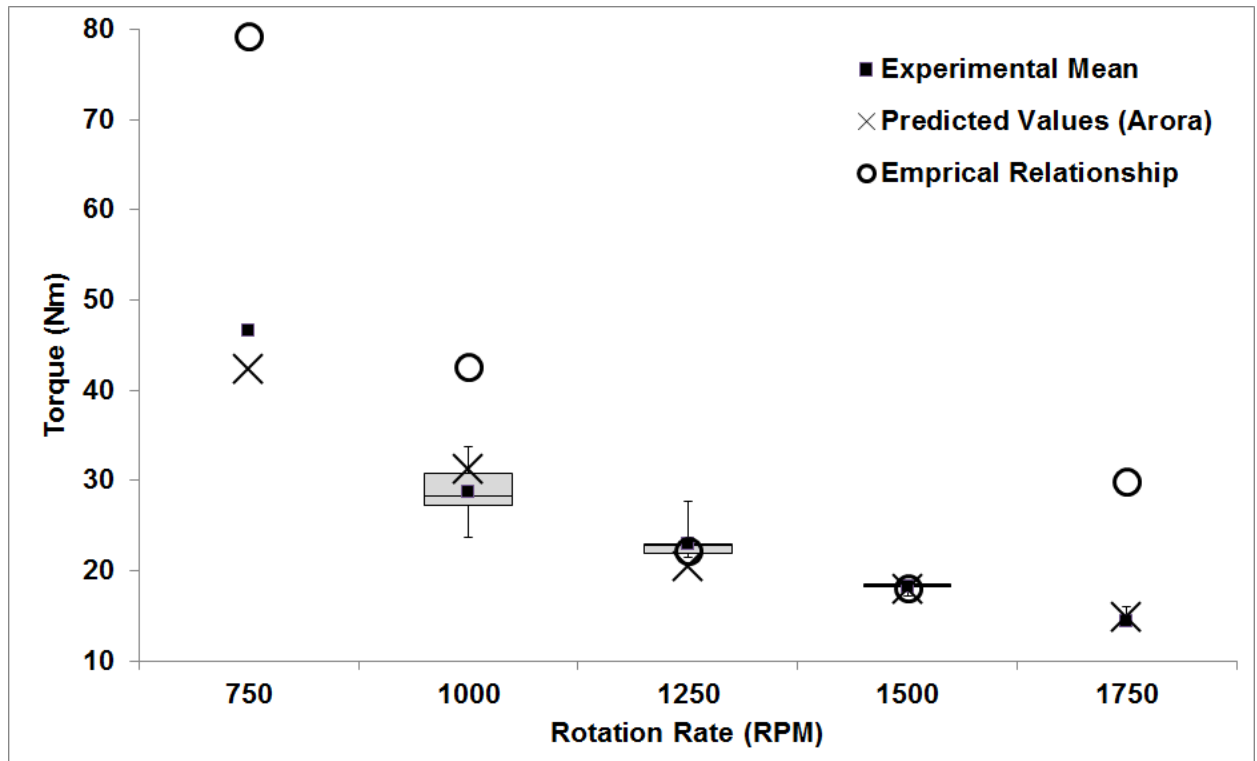


Figure 62: Comparison of experimental, empirical, and analytic torque values

### Temperature

Contour plots of temperature vs. the selected parameters for all of the spot welds can be seen in Figure 63. The range of recorded maximum temperatures for this study was between 254.1°C and 332.1°C, a difference of 78°C. This is not the maximum temperature within the weld zone, as the interface between the tool and workpiece is significantly hotter [Shibayanagi]. It was observed that the dwell time had the largest effect on the measured temperature. On average, the dwell time affected the temperature by a rate of 38.9°C/sec as opposed to only a 0.01 °C/rpm increase (Figures 64 and 65).

## Contour Plots of Temp (°C)

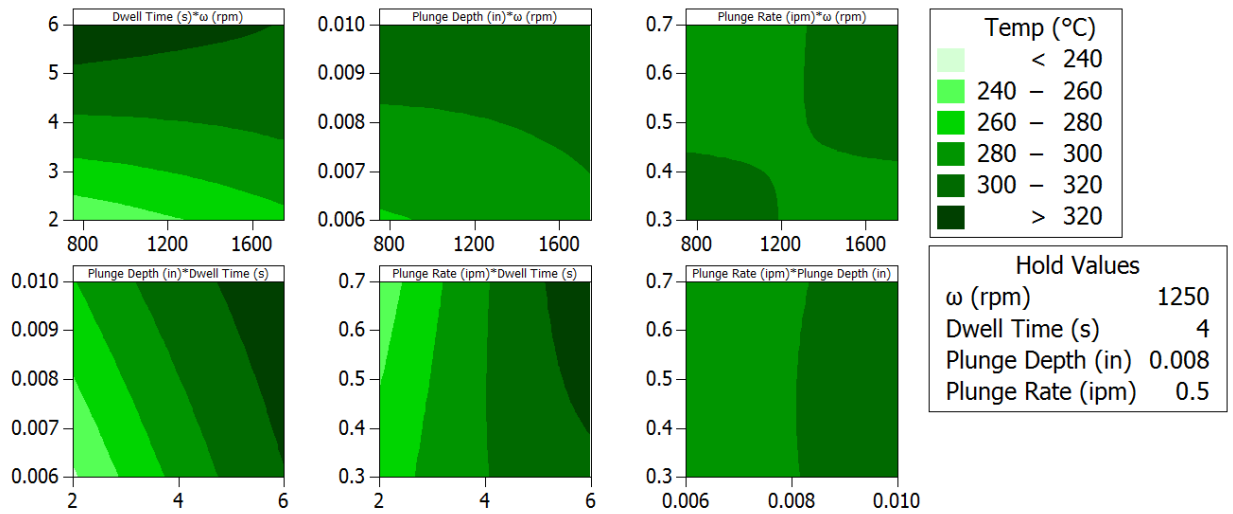


Figure 63: Contour plots of the peak temperature measured via the thermocouples. The label of each axis can be seen in the title of each subplot (y-label \* x-label)

As was done with the shear and torque studies, a relationship relating the selected parameters and the measured anvil temperature was created. Significant values were selected as those having p values less than 0.05 (Table 5). The resulting empirical relationship can be expressed as:

$$Temperature = [299.443 + 33.225D + 13.006P]^{\circ}C \quad (5.8)$$

where “D” and “P” are the coded values for dwell time and plunge depth respectively.

For this model an R-Sq value of 0.9123 was calculated.

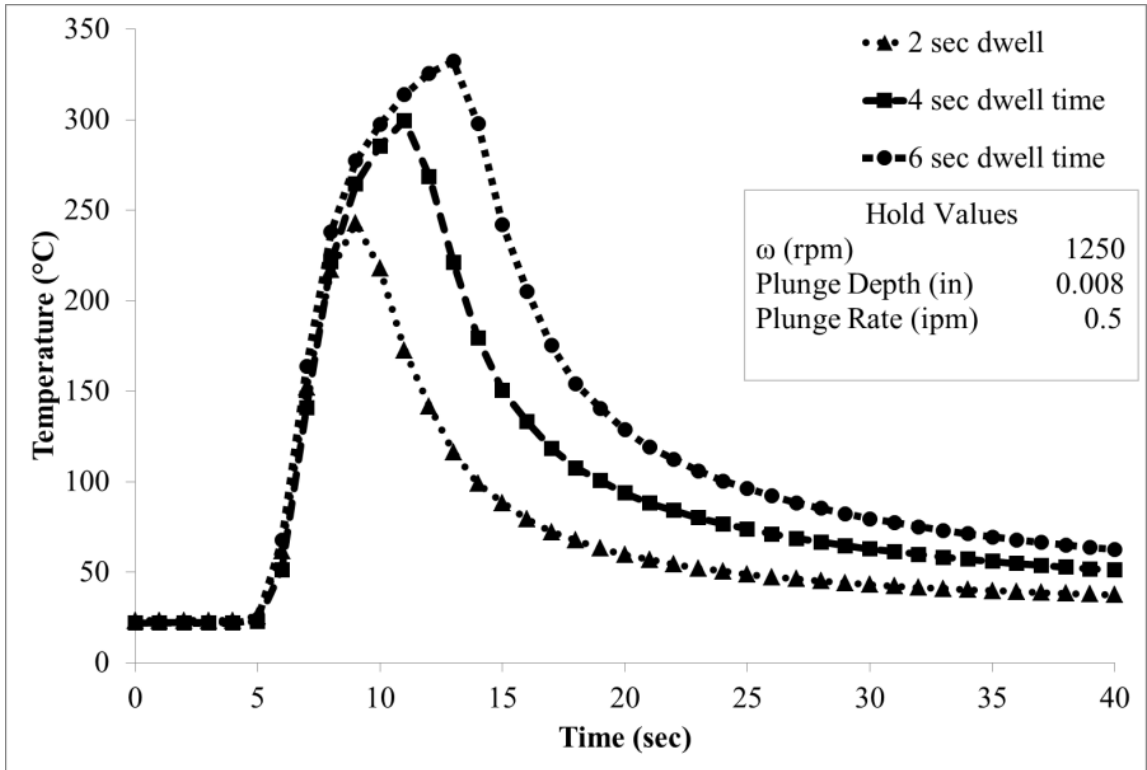


Figure 64: Temperature versus dwell time. The welding tool makes contact at 5 seconds.

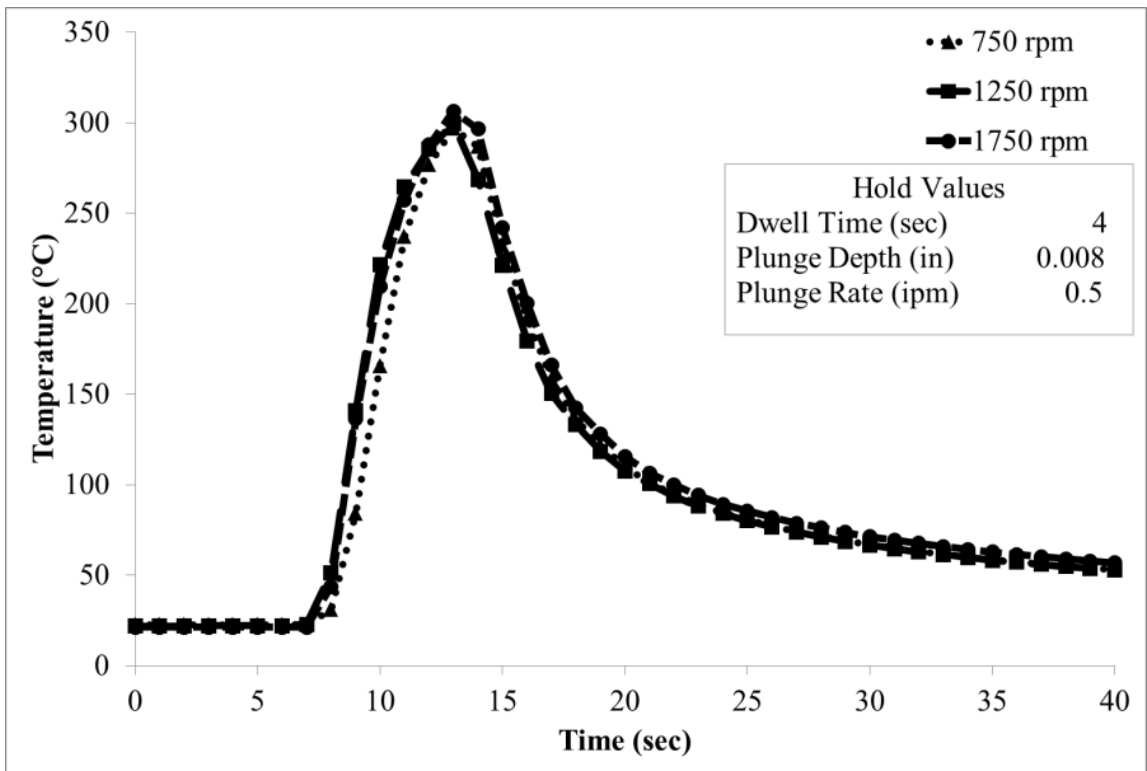


Figure 65: Temperature versus rotation rate. Tool contact at 7 seconds.

### *Failure Analysis*

During the shear strength tests, the weld pullout mode, characterized by a complete separation of the top and bottom plate, was the only observed failure. The failure occurs in the top plate along the perimeter of the weld zone (Figure 66.b), while the weld nugget remains in the bottom sheet (Figure 66.a). For traditional automotive spot welding (resistive spot welding) applications, this failure mode is preferred over the interfacial failure mode, which is characterized by a failure via crack propagation through the weld nugget. Interfacial failure, which is associated with lower load carrying capacity, is considered highly unsatisfactory and industry standards are often designed to avoid its occurrence [Chao].

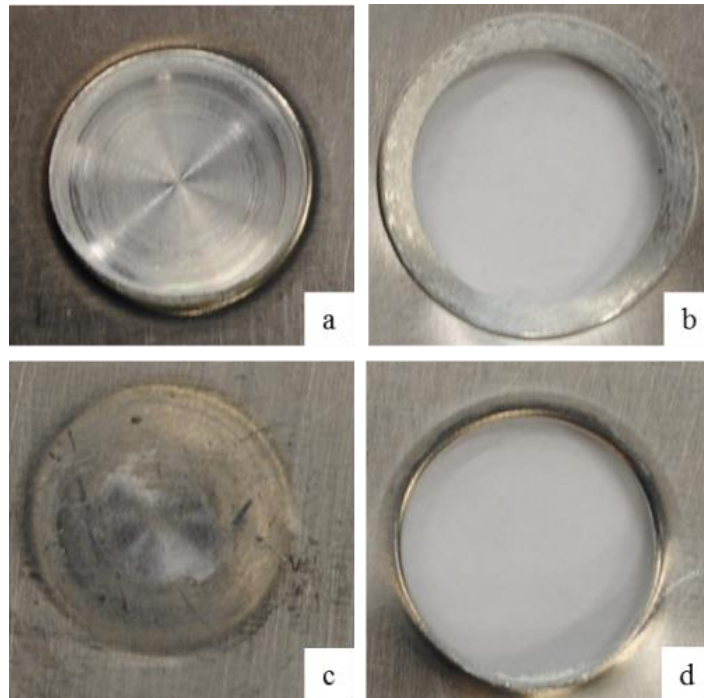


Figure 66: A shear specimen exhibiting the weld pullout mode. a) The top of the bottom plate. The weld nugget remains in the bottom plate. b) The top of the top plate. c) The bottom of the bottom plate. d) The bottom of the top plate.



The tested shear sample seen in Figure 66 had a nugget diameter of 0.6405 in and nugget thickness of 0.0375 in (Figure 66.a). The hole left in the top plate was ovoidal in shape due to the direction of the loading and the elongation that occurred during the shear test. The diameter measured along the major axis is 0.6580 in and a diameter of 0.6460 in along the minor axis. The area directly beneath the spot weld on the bottom of the bottom plate (Figure 66.c) is smooth.

### *Macrosection Analysis*



Figure 67: Macrosections of spot welds. Hold parameters: 2 sec dwell, 0.006 in plunge depth, 0.5 ipm plunge rate. a) 750 rpm b) 1000 rpm c) 1250 rpm d) 1500 rpm e) 1750 rpm

For macrosection analysis, five spot welds were created to visualize the effect rotation rate has on weld quality. The macrosections were prepared by taking a cross cut along the maximum diameter of each spot weld. The samples were then polished and etched using Keller's reagent (95 mL H<sub>2</sub>O, 2.5 mL HNO<sub>3</sub>, 1.5 mL HCl, and 1.0 mL HF). The plunge rate (0.5 ipm), plunge depth (0.006 in) and dwell time (2 sec) were held constant during these welds and rotation rates of 750, 1000, 1250, 1500 and 1750 rpm were used. Images of the macrosections of the five spot welds can be seen in Figure 67. Joint line remnants (JLR) can be seen in each of the spot welds and are formations of oxide bands. The presence of JLR does not affect the mechanical properties of the weld [Kumar]. As the rotation rate increases, it can be seen that the joint line moves upward into the top plate and additional bands can be seen. These bands also become more pronounced as the rotation rate increases. The stir zone was observed to have a unique "handle-bar mustache" shape as the material is observed to flow from the outer edge of the tool's shoulder toward the center of the tool. The material then moves downward and back toward the outer edge of the weld zone as fresh material is brought inward. This cyclical movement of material may be the cause for the formation of the observed bands. Directly beneath the center of the tool less material movement is observed (Figure 67.e) as a result of the lower local angular velocity and lower temperatures.

The appearance of expelled weld material, or flash, is less severe than for other tool geometries present in the literature. The extra surface area of the shoulder, the portion that is not plunged beneath the surface of the workpiece, is able to limit the formation of weld flash and at low rotation rates, completely eliminate it (Figure 67.a-b).

At high rotation rates, a hooking defect was observed along both sides of the macrosection. This defect is known to be detrimental to the strength of the weld.

### Numerical Simulation

A 2-dimensional axisymmetric transient numerical simulation of the pinless FSSW process was created using the COMSOL computational fluid dynamic (CFD) software package. COMSOL is used to create the workpiece geometry and mesh, and to perform the simulation. The workpiece is modeled as a solid disc measuring 0.080 inches thick by 1.4 inches in diameter. The FSSW tool contact with the workpiece is modeled as a heat flux boundary condition; it was not physically modeled to improve computation time. The effective diameter of the tool (length of the boundary is 0.2 inches) was 0.4 inches. The geometry of the model, the mesh, and the thermal boundary conditions can be seen in Figure 68. The heat flux across the tool/workpiece boundary was adjusted to be at its maximum value at the edge of the tool and a minimum value at the center of the tool. The mesh for the workpiece contained 6990 triangular elements, 851 quadrilateral elements, 368 edge elements, and 8 vertex elements. The simulation was performed in two parts: 1) a solution of the transient thermal model was obtained and 2) the resultant material flow field was computed.

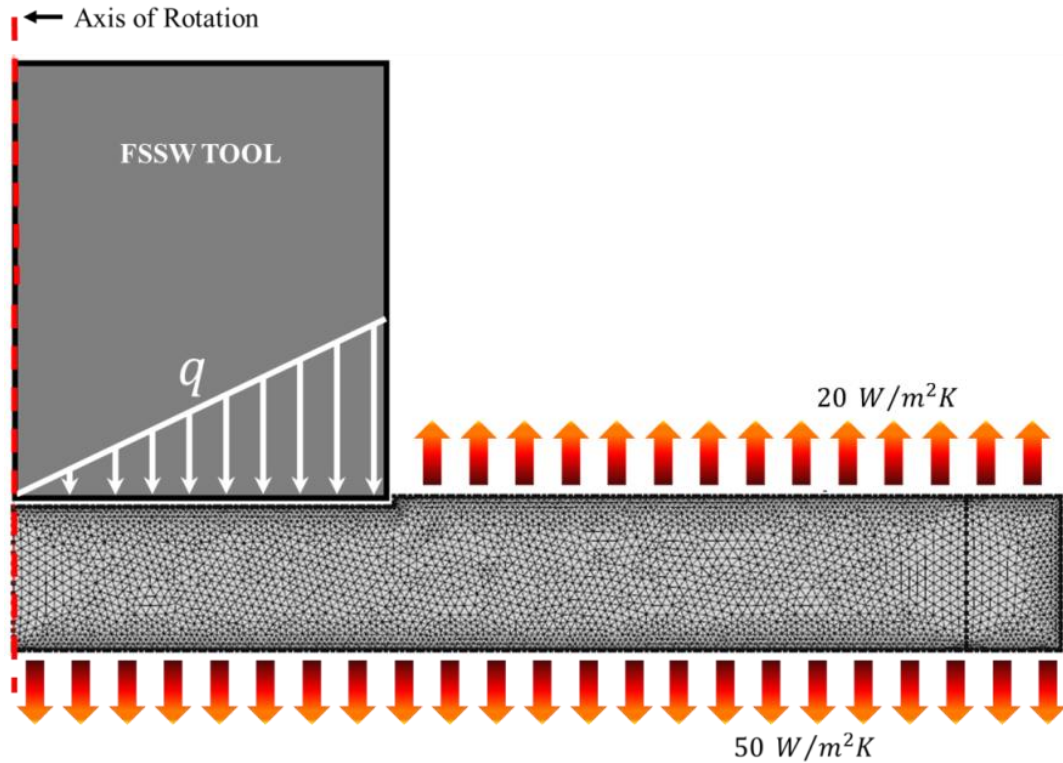


Figure 68: Geometry mesh for FSSW simulation

The heat generated ( $q$ ) during welding is estimated by the weld power method using the analytic expression of weld torque (Equations 5.3 and 5.5.) The heat input is set equal to zero if the temperature of the workpiece exceeds its melting temperature. To validate the thermal model the results are compared to experimental temperature measurements of a weld with a 6 second dwell period and are found to be in good agreement with each other. The temperature values presented in Figure 69 are taken at a point located at the bottom center ( $r = 0, Z = 0$ ) of the workpiece. The development of the temperature field within the workpiece is shown in Figure 70. This temperature data will be used for the material flow simulation.

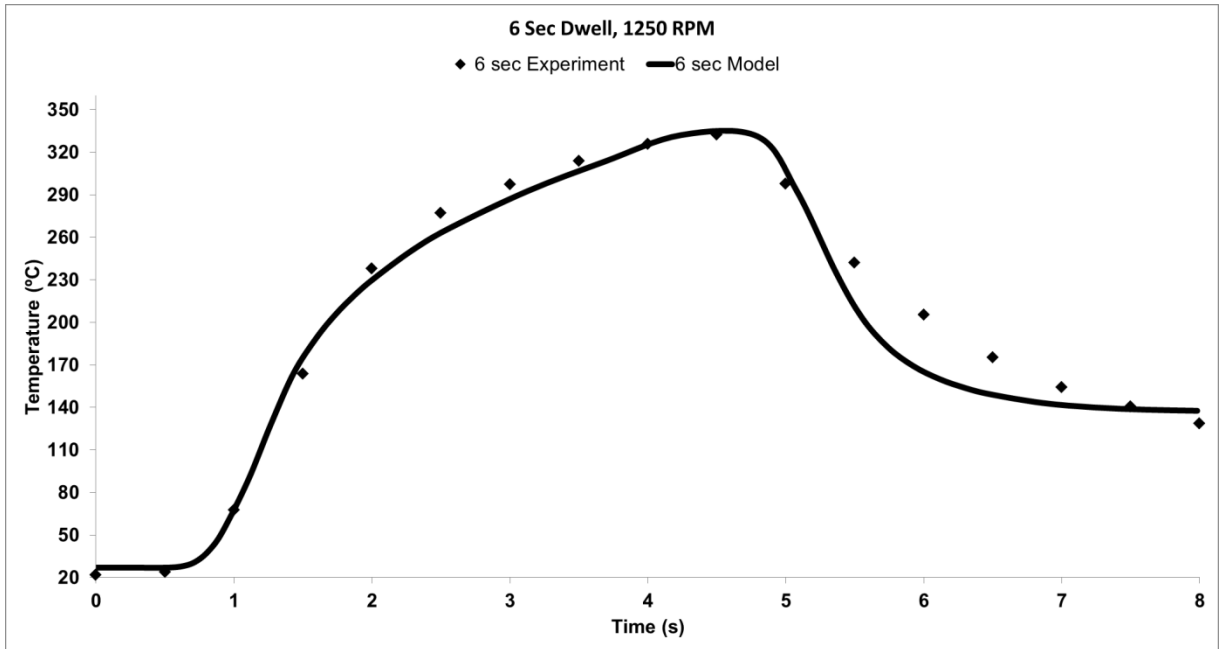


Figure 69: Maximum temperature value at a point located at the bottom-center of the workpiece during welding (1250 RPM, 6 Sec Dwell) for experimental measurement and the values predicted by simulation.

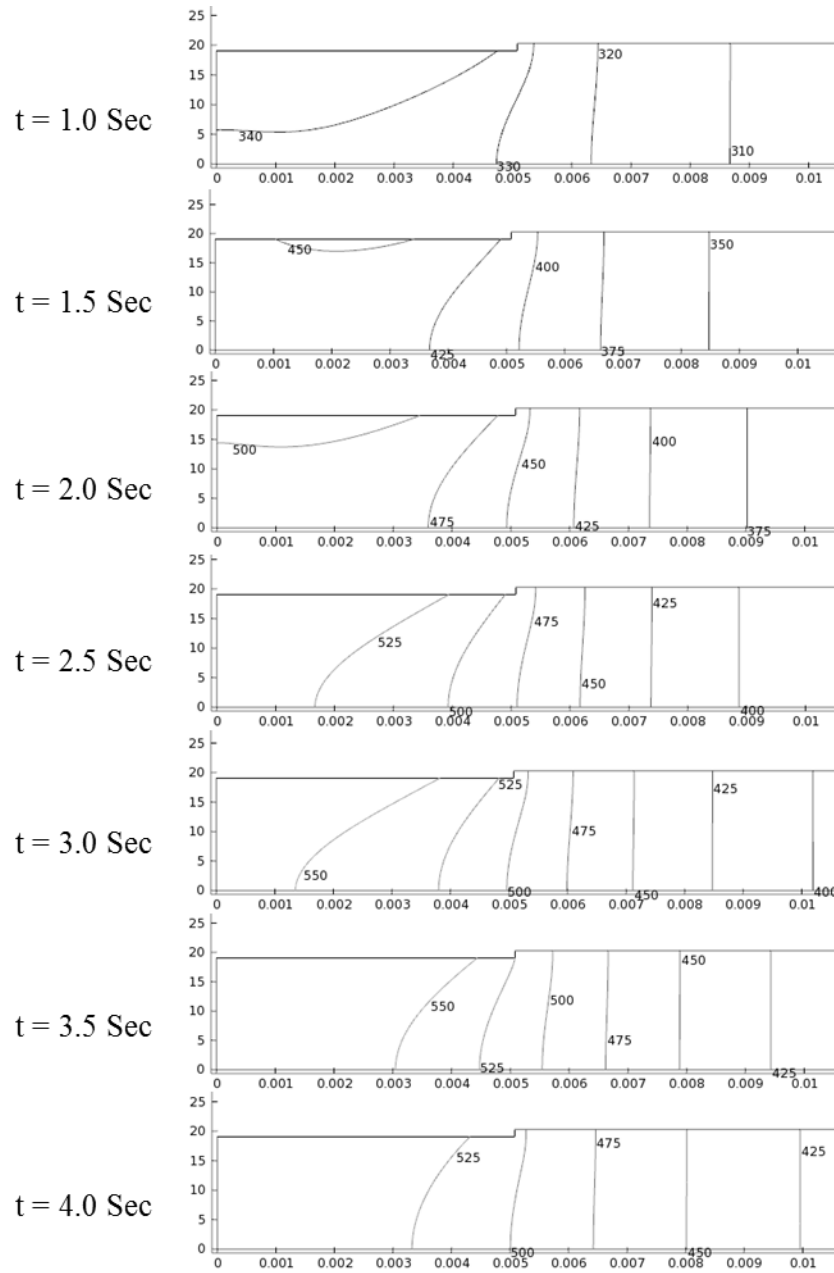


Figure 70: Development of temperature field within the workpiece during an FSSW spot weld. 1250 rpm, 4 sec dwell. Temperatures are reported in K. The y-axis has units of  $10^{-4}$  meters. The x-axis has units of meters.

When modeling the FSSW/FSW process using CFD it is a common practice to define a weld material viscosity. The weld material viscosity is defined using the Carreau Viscosity model (Equation 5.9).

$$\mu = \mu_{\infty} + (\mu_0 - \mu_{\infty}) \left[ 1 + \left( \dot{\gamma} \lambda \exp\left(\frac{T_0}{T}\right) \right)^2 \right]^{\frac{m-1}{2}} \quad (5.9)$$

where  $\lambda$  is the time constant,  $m$  is the power law index for the Non-Newtonian fluid,  $\dot{\gamma}$  is the shear strain-rate,  $T_0$  is the reference temperature, and  $\mu_0$  and  $\mu_{\infty}$  are the zero and infinite shear viscosities. Atharifar et al. estimate the parameters of Equation 5.9 for Al 6061 as  $\lambda = 10$ ,  $m = 0.2$ ,  $T_0 = 300$  K,  $\mu_0 = 1E8$  m<sup>2</sup>/s and  $\mu_{\infty} = 0$  m<sup>2</sup>/s. This viscosity model is defined throughout the workpiece in the simulation. Temperature dependent functions (interpolation) of density, thermal conductivity, and specific heat were used and implemented in COMSOL using the values in Table 6. The rotation rate of the spot welding tool was set by specifying a velocity profile along the interface between the tool and workpiece.

Table 7: Temperature dependent material properties

Material Properties (Al 6061)	Temperature	
	293 K	1073 K
Density (kg/m <sup>3</sup> )	2705	2372
Thermal Conductivity (W/mK)	195	92
Specific Heat (J/kgK)	870	1170

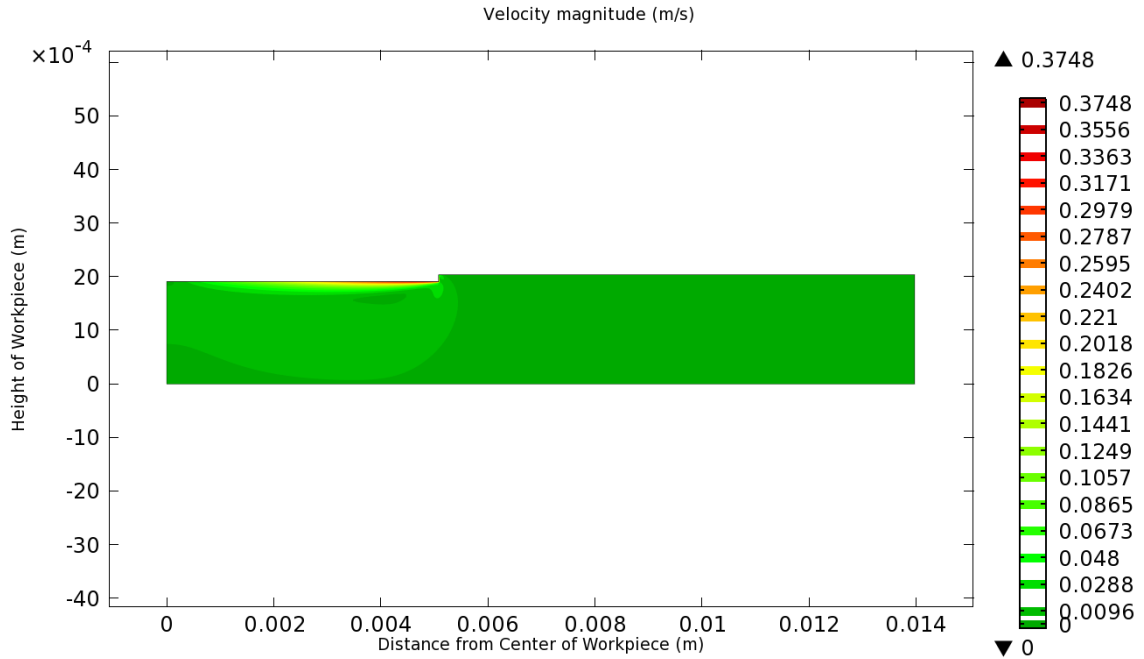


Figure 71: Cross section view of velocity magnitude contour from CFD model for a tool rotation speed of 750 RPM

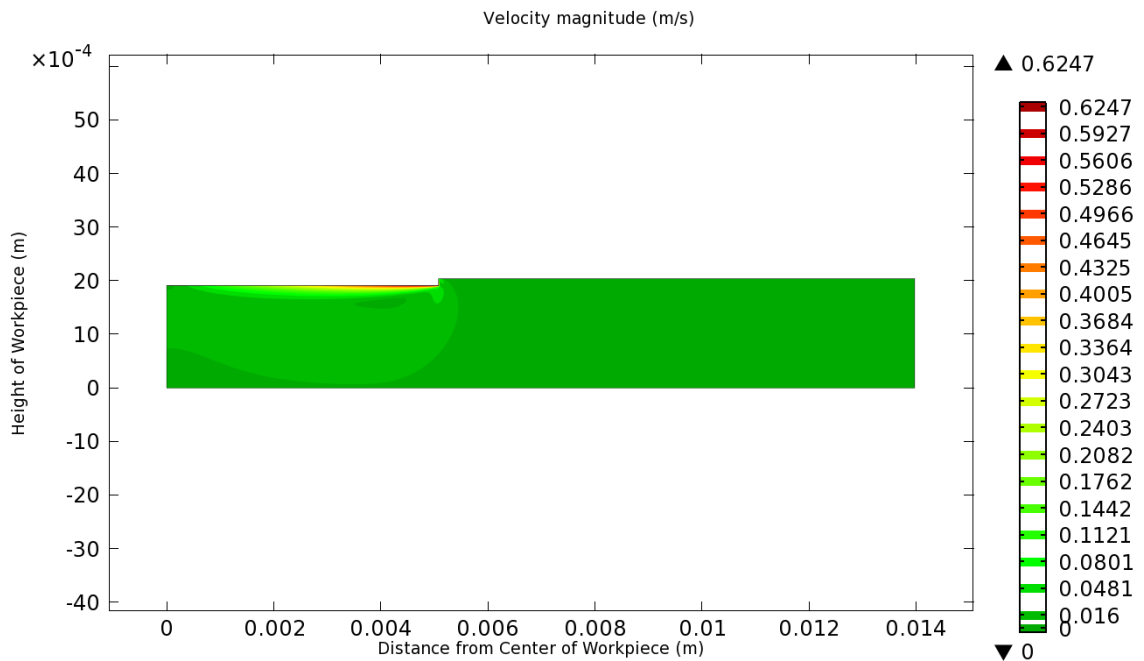


Figure 72: Cross section view of velocity magnitude contour from CFD model for a tool rotation speed of 1250 RPM



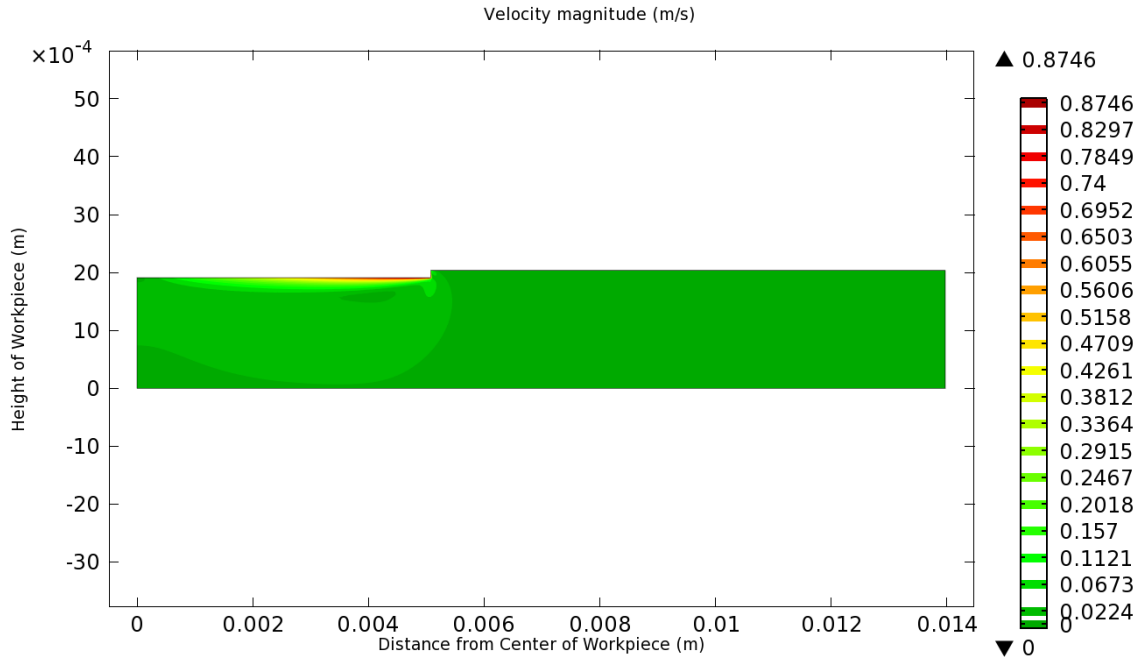


Figure 73: Cross section view of velocity magnitude contour from CFD model for a tool rotation speed of 1750 RPM

The resulting material velocity contours for 750, 1250, and 1500 RPM can be seen in Figures 71-73. The cross sections are taken at 3.5 seconds of a 4 second dwell phase. The majority of the weld zone can be seen to rotate at a significantly slower rate; approximately 2.4% that of the tool's rotation rate. The predicted size and shape of the weld zone is not observed to have a strong dependence on rotation rate. The velocity profile predicts that, for each rotation rate, the weld zone will fully penetrate into the bottom sheet.

## Discussion

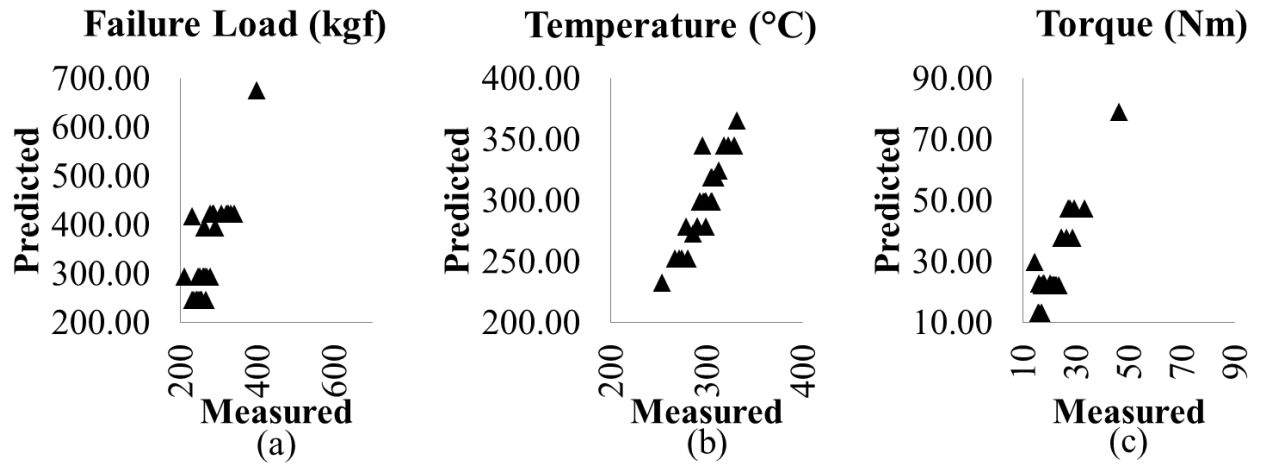


Figure 74: Regression graphs for a) Shear failure load b) Torque c) Temperature

The results of the empirical relationships for shear failure load, spindle torque and temperature were plotted against their respective experimentally measured values (Figure 74). When compared to the experimentally obtained values, the empirical relationships tended to overestimate, but they did capture the observed trends.

A maximum joint strength of 400.2 kgf was measured for weld ID  $\alpha\alpha$ - (750 rpm). The lowest joint strength of 211.6 kgf was measured for weld ID  $\alpha\alpha\alpha\alpha$  (1500 rpm). Weld ID  $\alpha\alpha+$  (1750 rpm) had a joint strength of 231.4 kgf, only slightly stronger than that of the weakest weld. Rotation rate and plunge depth had the largest effect on the strength of the spot weld. The plunge depth effectively controls how much of the tool area is in contact with the weldment during welding. Larger tool areas result in large weld zones which can support more loading.

The relationship between shear strength and rotation rate is dominant. However, for the discussion of FSSW it is more convenient to consider the number of tool rotations during welding instead of the conventional means of a rotation rate and dwell time e.g.

83.3 tool rotations = 1250 RPM with 4 seconds of dwell. In this study spot welds are made with as few as 42 and as many as 125 tool rotations. As previously stated, the results of the CFD model predict that the rotation rate of the weld zone to be 2.4% that of the tool's rotation rate. The rotation rate of the weld zone is predicted to range from 18 – 42 RPM depending on the selected tool rotation rate. The strength of the spot welds is plotted versus the number of rotations the weld zone makes during the weld in Figure 75.

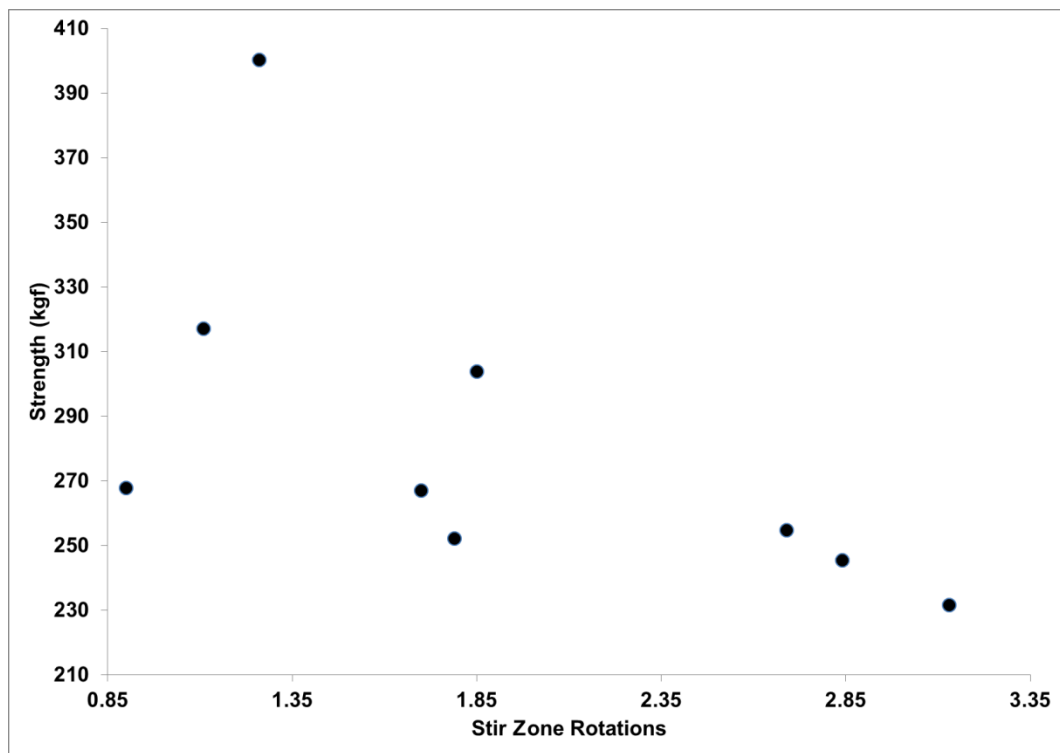


Figure 75: Strength of the spot welds vs. the number of rotations made by the weld zone during the weld.

The maximum joint strength occurred when the weld zone completed  $\approx 1.25$  rotations (750 RPM, 4 sec dwell). The spot welds that did not complete a single rotation were significantly weaker as were the welds that completed more than 1.5 rotations. Reducing the cycle time of the process may be achieved by increasing the rotation rate and

shortening the dwell time. This may have an additional benefit in that higher tool rotation rates required less power during welding.

For robotic applications of FSSW, it is beneficial to reduce the torque load on the spindle motor, as it will reduce the compliancy in the robotic links, as well as reduce the overall size and cost of the robotic manipulator. Rotation rate and dwell time had the largest effect on spindle torque. Using the empirical relationship obtained from the experiment, a parameter set was chosen (1750 rpm, 2 sec dwell) such that it would minimize the spindle torque. The predicted value for spindle torque is 11.1 Nm and the experimentally measured spindle torque was 6.8 Nm. As stated, the spindle torque is indicative of weld quality; higher values of spindle torque are generally associated with higher joint strength. However, by reducing the dwell time it may be possible to recover the loss in joint strength observed at the higher tool rotation rates.

Despite the large window of operating parameters a relatively narrow window of temperatures were measured during welding. Dwell time and plunge depth were found to have the largest effect on temperature. For spot welds made with a 2 second dwell time and 0.008 in plunge depth a temperature of 233°C was predicted compared to the experimentally measured value of 242.9°C.

The heat generated during FSSW is dictated by the contact area of the tool interface (plunge depth), rotation rate and dwell time. This relationship suggests that spot weld quality is strongly tied to the heat generated during the spot welding process. Welds created with high heat input, through combinations of high rotation rates, long dwell times and large plunge depths, are generally much weaker than those created at “cooler” parameters.

As in previous work, hooking defects were found in the spot welds created at 1250, 1500 and 1750 rpm (Figure 67.c-e). The hooking defect is an un-bonded region. It is detrimental to the quality of the weld due to the fact that it reduces the effective sheet thickness, which can reduce the spot weld's ability to bear a load. The hooking defect was not found to be present in the spot welds created at lower rotation rates. The occurrence of this defect may be related to the heat input generated at higher rotation rates. It may be possible to reduce the severity of this defect at higher rotation rates by welding at much shorter dwell times ( $< 1$  sec).

The plunge rate was not observed to have a significant effect on the spot welding process. This observation may appear to be in disagreement with the published understanding of the spot welding process for tools with pins. Karthikeyan reported that shear strength had a strong dependence on the plunge rate. However this observation does not contradict the results of this study. When compared to a pinless tool, more time is required to plunge a tool with a pin into the workpiece. The additional heating incurred by this step of the process could account for the reported dependence on plunge rate.

The axial force was monitored during each of the spot welds, but was not observed to have a significant relationship with any of the selected parameters. An average axial load of  $9.1 \pm 0.46$  kN was calculated for this study. Force control (axial) is a standard control method for FSW, but may not be as indicative of quality for spot welding as other response signals may be.

## Conclusions

The pinless spot welding tool was able to successfully create high strength joints in thin aluminum plate without leaving a keyhole. The effects that rotation rate, dwell time, plunge depth and plunge rate have on the FSSW process when using a pinless tool have been investigated. The tool plunge depth was identified as a significant parameter for optimizing joint strength. Although plunge depth was significant, the tool rotation rate and dwell time were found to have the largest impact on the welding process, largely dominating the resulting strengths of the welds and the spindle torque experienced during welding. Welds that were created using lower rotation rates and shorter dwell times resulted in welds that were significantly stronger than those created with higher rotation rates and/or longer dwell times. The hooking defect was observed only in the welds created at higher rotation rates. Heat generated during the spot weld process may play a vital role in joint quality, as welding at “cold” parameter combinations lead to defect free and mechanically stronger spot welds. The CFD model was able to successfully predict the temperature within the weld zone during welding. The model also suggests that the strength of the weld is highest when the weld zone completes 1.25 rotations. Excessive weld zone rotations were identified as a possible explanation for poor joint strengths at higher rotation rates.

## CHAPTER VI

### A METHOD FOR DOUBLE-SIDED FRICTION STIR SPOT WELDING

Chase D. Cox, Brian T. Gibson, Alvin M. Strauss, George E. Cook. "A Method for Double-Sided Friction Stir Spot Welding" *Journal of Manufacturing Processes*, Accepted, 2013.

#### Abstract

A rotating anvil similar to a pinless friction stir welding (FSW) tool can be applied to friction stir spot welding (FSSW) of thin metal plates. FSSW is a solid state joining process that is currently being used by automotive manufacturers as an alternative to rivets and traditional resistance spot welding. The principal detractor of this process is the keyhole left by pin extraction, which can be detrimental to the weld strength. A pinless tool can be used to eliminate the keyhole. However, this approach is limited to joining thin sheet ( $< 1$  mm). A rotating anvil with the pinless FSSW process permits the joining of thicker cross sections, decreases the cycle time and reduces the reaction forces and torques acting on the spot welding frame. The use of a rotating anvil for FSSW is currently not presented in the literature and it is the objective of this work to establish the ideal conditions for creating mechanically sound spot welds. Tensile shear tests, macrosection analysis and a numerical model of the process are used to evaluate the spot welds.

Macrosection and numerical analysis reveals that the material flow between the pinless tool and rotating anvil is complex and unique to this process. It has been found

that the use of a rotating anvil for FSSW is a viable means to repeatably create quality spot welds in thicker weldements.

### Introduction

Automotive manufacturers are facing challenging issues related to creating light weight automobiles in an effort to improve fuel economy (Figure 76). One approach to reducing the weight of their vehicles is to use lighter materials in the design of the structure e.g. aluminum in place of steel. However traditional joining processes such as resistive spot welding are difficult to implement on metals like aluminum due to their higher thermal conductivity. While these metals can be joined with alternative processes such as rivets the use of mechanical fasteners adds to the overall complexity, weight and cost of the manufactured product [Mishra].

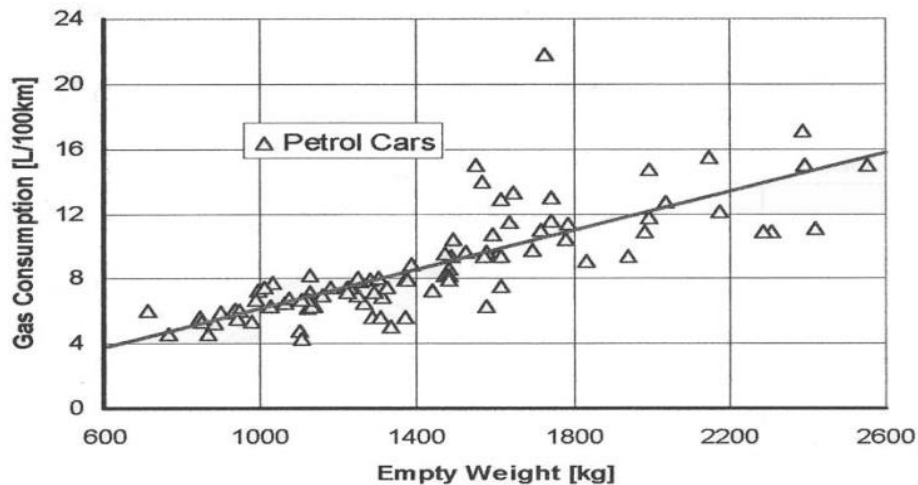


Figure 76: Dependence of gas consumption on the weight of an automobile [Prangnell]

FSSW is a solid state joining process derived from friction stir welding (FSW). In FSSW, the spot weld is created by plunging a rotating tool into the weldment, dwelling



for a period of time, and then retracting the tool. The spot weld is formed by severely plastically deforming the metal in the immediate vicinity of the tool. The amount of heat generated in the weld zone depends on rotation rate, tool penetration depth, and dwell time [Lathabai]. The use of FSSW presents several key advantages over conventional spot welding processes in joining these light-weight aluminum alloys: higher joint strengths, grain refinement within the weld zone and reduced production costs [Badarinarayan].

One identified drawback of this process is that the welding tool leaves a keyhole (the size of its dynamic volume) in the spot weld during retraction that requires removal via either post-processing or costly, highly specialized tool design (Figure 77). On such method is the refill FSSW process developed by GKSS in 2003. In refill FSSW, a purpose-built machine is used to create a spot weld without a keyhole that is nominally flush with the original workpiece surface. This is accomplished by actuating the three components of the system, a clamp ring, shoulder, and pin, independently during welding. The process begins with the clamp firmly holding the weldment in place. The rotating shoulder then makes contact (the probe at this point is completely retracted) and begins to heat the workpiece. Once the temperature of the workpiece is sufficient for welding, the probe is extended into the workpiece. As the probe penetrates the workpiece, the shoulder retracts enough to create a reservoir that will allow for the material displaced by the probe to be contained. When the probe retracts the shoulder is lowered back toward the workpiece, forcing the expelled material back into the weld zone, filling the keyhole. The weld is completed when the pin is completely retracted back into the shoulder. Alternatively, pinless tool designs have been identified in the literature as a

low-cost alternative in this situation [Tozaki, Bakavos]. However, the pinless tool design is limited by the thickness of the weldment in which it can create a spot weld of good quality ( $\leq 1$  mm).

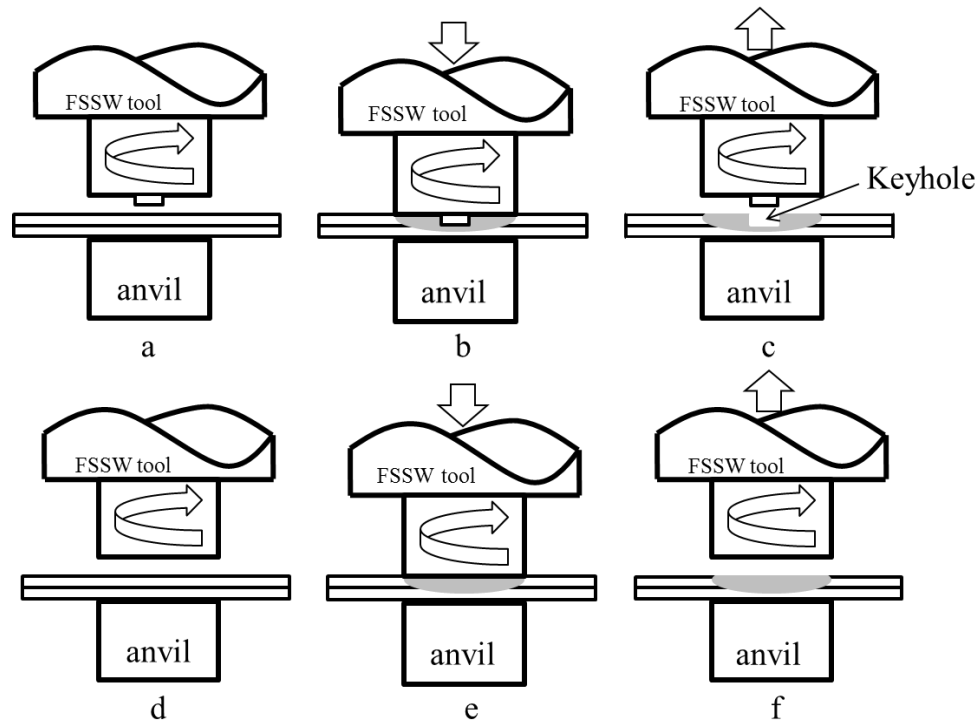


Figure 77: The Friction Stir Spot Welding Process. A-C: represents the traditional FSSW process using a tool with a pin. The resulting keyhole defect is illustrated. D-F: represents the FSSW process using a pinless tool. The lack of the keyhole defect is illustrated

It is commonplace in the FSW community to utilize a double-sided tool design for welding. The inclusion of a pin on these double-sided welding tools may have prevented this application from being implemented for spot welding. Using a pinless tool in a double-sided welding configuration may present a means to increase the thickness of the weldment used in FSSW. Traditionally in FSSW, the anvil (Figure 1) is used to support

the massive forging loads incurred during welding. For the proposed double-sided spot welding method (Rotating Anvil for Friction Stir Spot Welding) the anvil will be rotated during welding.

In this study a computational fluid dynamic (CFD) model is created to test the effects the use of a rotating anvil in FSSW may have on the process when joining thicker weldments. A rotating anvil is designed, implemented and evaluated on the FSSW machine located in the Vanderbilt University Welding Automation Laboratory (VUWAL). The results of the CFD model and experimental tests are presented.

## Numerical Model

### *Design*

A 2-dimensional axisymmetric computational fluid dynamic model was created to simulate the RAFSSW process using COMSOL. Two workpieces of different thicknesses are considered in two separate simulations; a 2 mm thick solid disc with a radius of 14 mm and a 4 mm thick solid disc with a radius of 28 mm. The workpieces in the simulations represent 1 mm and 2 mm thick plates in a lap joint configuration. In Figure 2 it can be seen that contact condition between the tool and rotation anvil are simulated to be plunged 0.13 mm beneath the top and bottom surfaces of the workpiece. The simulation is performed in two successive steps. A transient thermal model is created to simulate the temperatures within the workpiece during welding. The temperature dependent material flow field is then computed for a specified instance in time. For simplicity, material deformation associated with plunging the welding tool into the

workpiece is not considered. Additionally, the workpiece is restricted from any out-of-plane deformation and the model will not account the formation of weld flash, hooking defects or lack of bonding. The material simulation will be used in this application to better understand the flow characteristics within the stir zone during FSSW when using a pinless tool.

### *Thermal Model*

The FSSW tool and rotating anvil are modeled as a heat flux boundary condition for both thermal simulations; they are not physically modeled in order to improve computation time. The effective diameter of the tool (length of the boundary is 5 mm) is 10 mm. The heat flux across the tool/workpiece and rotating anvil/workpiece boundary was adjusted to be at its maximum value at the edge of the tool and a minimum value at the center of the tool. The power input into the weld can be determined using the rotational speed of the tool and the weld torque (Equation 6.1)

$$P = M * \omega \quad (6.1)$$

where P is the weld power (watts), M is the weld torque (Nm), and  $\omega$  is the welding tool's angular velocity (rad/s) [Khandkar, Pew]. A rotational rate of 1000 RPM was used for both the welding tool and rotating anvil. A previously obtained experimental torque (single-sided FSSW) value of 27.8 Nm (obtained using 1000 RPM, 3 sec dwell) is used, resulting in a calculated heat input of  $\approx 2900$  watts for both the welding tool and rotating anvil. The heat input was distributed across the weld interface between the welding tool

and workpiece as well as the boundary between the rotating anvil and workpiece by applying the heat locally in proportion to the local tangential velocity. The initial workpiece temperature before welding is set to be 293 °K. The heat input along the tool/workpiece and rotating anvil/workpiece boundaries is initially set to zero. During the first 0.5 seconds of the simulation the heat input is increased to the specified value. Some percentage of the heat generated during welding is lost to the FSSW tool and the surrounding environment during welding. Experimental observation reports that 90% of the total heat generated is transferred to the workpiece [Nandan].

The other thermal boundary conditions are defined as 20 W/(m<sup>2</sup>K) for exposed surfaces and 50 W/(m<sup>2</sup>K) for metal-metal contact. An emissivity of 0.2 was applied for the aluminum workpiece surfaces. The volumetric mesh of the 1 mm thick workpiece consisted of 6891 triangular elements, 856 quadrilateral elements, 469 edge elements and 10 vertex elements. The volumetric mesh of the 2 mm thick workpiece consisted of 7110 triangular elements, 856 quadrilateral elements, 470 edge elements and 10 vertex elements. The thermal boundary conditions as well as the mesh used for the workpiece in the simulation can be seen in Figure 78.

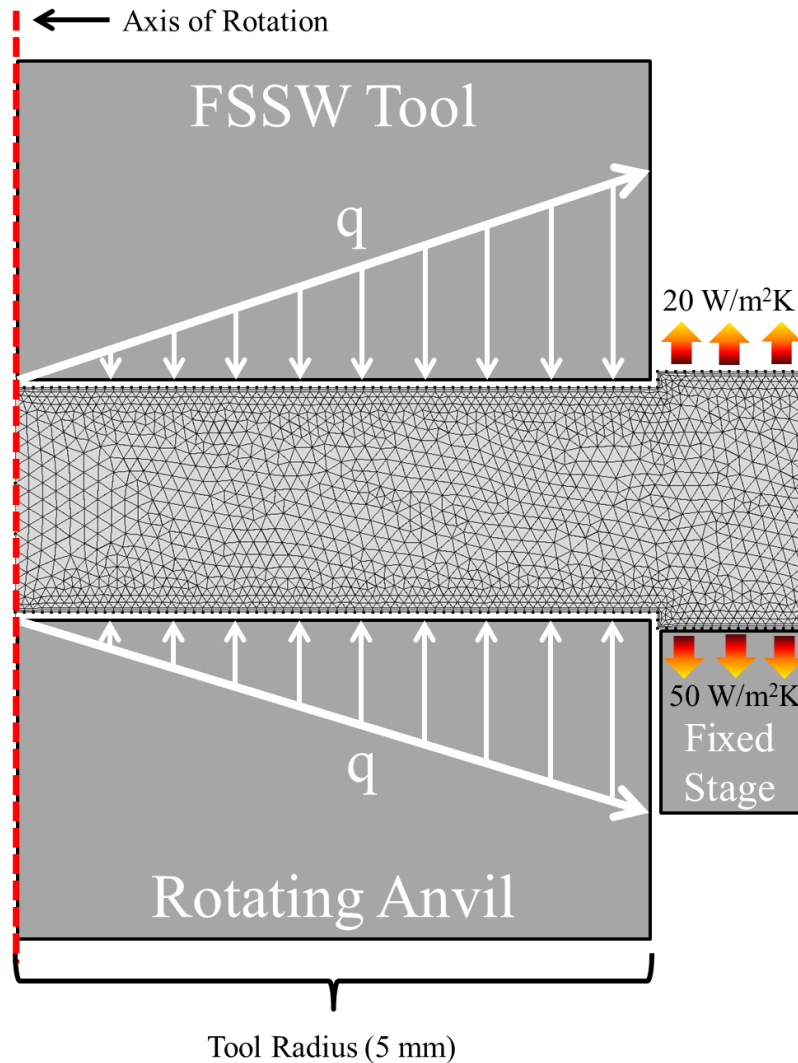
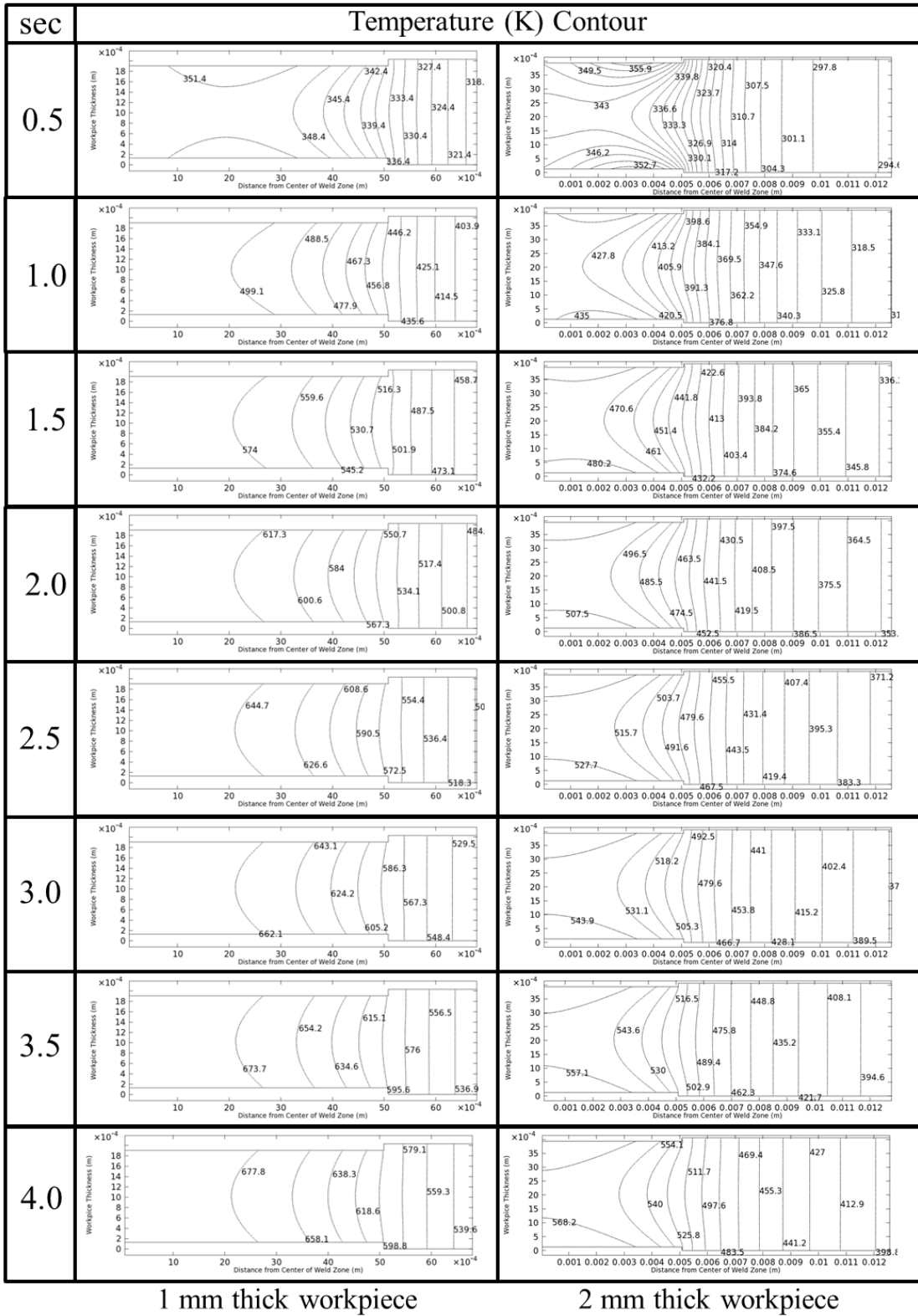


Figure 78: Thermal boundary conditions and mesh used for the workpiece in the FSSW simulation.



1 mm thick workpiece

2 mm thick workpiece

Figure 79: Temperature field within the workpiece during FSSW with a rotating anvil for 1 mm and 2 mm thick workpieces. Temperatures are reported in °K.

The temperature field within the workpiece during FSSW with a rotating anvil can be seen for both workpiece thicknesses in Figure 79. The temperatures within the weld zone are predicted to be approximately 15% hotter than the temperatures measured during single-sided FSSW operations at similar process parameters. The temperature contours within the weld zone for the 2 mm thick workpiece are cooler and are on the order of the temperatures measured in previous single-sided FSSW experiments. The thicker workpiece may require a longer dwell period in order for the weld zone to more fully develop.

#### *Material Flow Model*

To simulate stirring during welding the viscosity of the flow needs to be defined. The viscosity of the weld material was modeled using the Carreau viscosity model (Equation 6.2). The Carreau viscosity model is an alternative method for approximating the non-linear viscosity of the weld material fitting very well with the more prevalent method of defining the viscosity as a function of the strain-rate and shear stress [Lammlein].

$$\mu = \mu_{\infty} + (\mu_0 - \mu_{\infty}) \left[ 1 + \left\{ \dot{\gamma} \lambda \exp\left(\frac{T_0}{T}\right) \right\}^2 \right]^{(n-1)/2} \quad (6.2)$$

Where  $\mu_{\infty}$  is the infinite shear viscosity,  $\mu_0$  is the zero shear viscosity,  $\gamma$  is the local shear strain-rate,  $\lambda$  is the time constant,  $T_0$  is the reference temperature,  $T$  is the local temperature and  $n$  is the power law index. Values for the Carreau model were derived

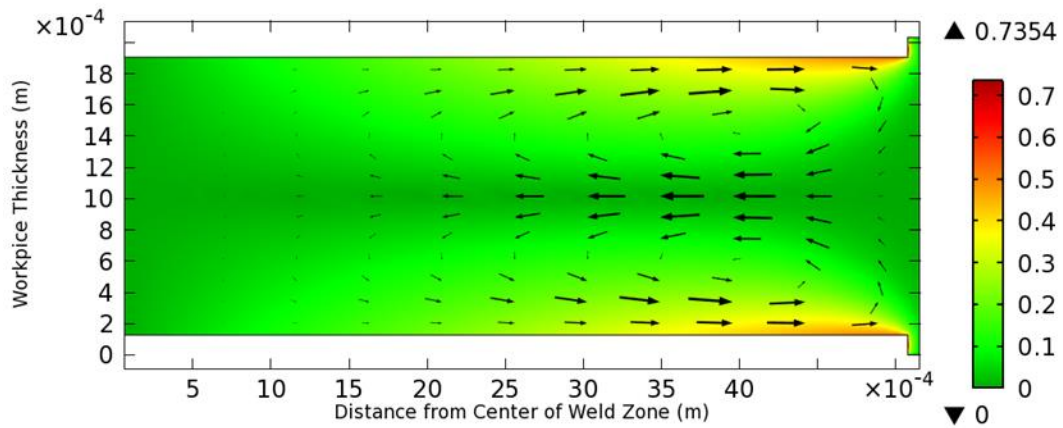


from analytical experiments in Al 6061-T6;  $\mu_{\infty} = 0$ ,  $\mu_0 = 1e8m2/s$ ,  $\lambda = 10$ ,  $n = 0.2$ ,  $T_0 = 293$  K [Atharifar]. This viscosity model is defined throughout the workpiece in the simulation. Temperature dependent functions (linear interpolation) of density, thermal conductivity, and specific heat were used and implemented in COMSOL using the values in Table 8.

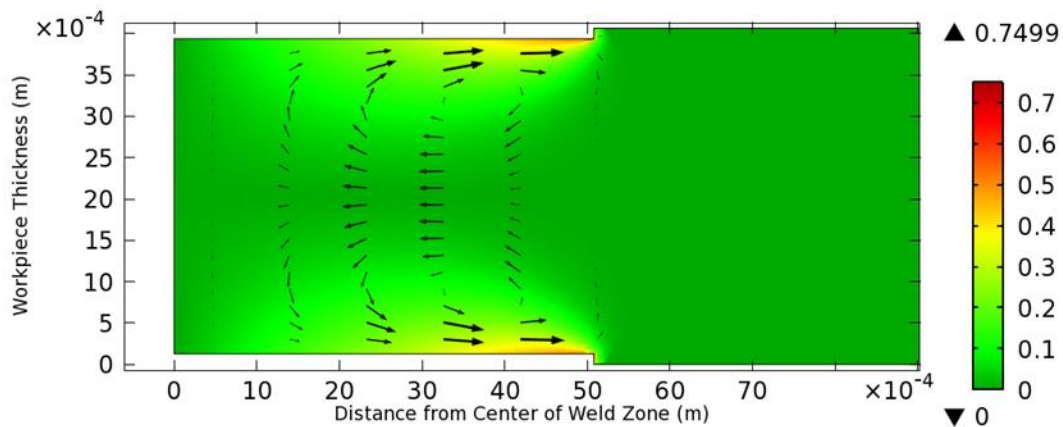
Table 8: Temperature dependent material properties of Al 6061 T6

Material Properties (Al 6061)	Temperature	
	293°K	1073 °K
Density (kg/m <sup>3</sup> )	2705	2372
Thermal Conductivity (W/m°K)	195	92
Specific Heat (J/kg°K)	870	1170

The interface between the welding tool and workpiece (boundary condition) was simulated to rotate in the clockwise direction (out of the page) while the interface between the rotating anvil and workpiece (boundary condition) is simulated to rotate in the counter clockwise direction (into the page) with respect to the top surface of the workpiece (Figure 2). The rotation rate of the tool and anvil are defined along the same boundaries as the heat input.



(a)



(b)

Figure 80: Cross section view of the velocity contours and arrow surface of the RAFSSW process when joining a) 1 mm and b) 2 mm thick workpieces of Al 6061 T6. A rotation rate of 1000 rpm is used. The contour is taken at the end of the 3 second dwell period, immediately before the tool is retracted.

The model contours for material velocity within the weld zone for the a) 1 mm and b) 2 mm thick workpiece (a total weldment thickness of 2 mm and 4 mm respectively) can be seen in Figure 80. In both cases it can be seen that there is material flow along the joint interface of the workpieces. There is less stirring of material flow directly beneath the center of the welding tool (as well as above the center of the rotating anvil) due to the

lower local tangential velocity. The predicted shape of the weld zone for both cases is symmetric about the welding tool's rotational axis and mirrors itself across the original joint line.

Figure 80 also shows the direction and proportional magnitude of the material flow via an arrow surface superimposed over the velocity contour. The material is predicted to flow from beneath the center of the welding tool's shoulder outward toward the shoulder's edge of the welding tool then downward and back toward the center of the weld zone. The material being pushed down by the welding tool meets along the interface with the material being pushed upwards by the rotating anvil. The occurrence of weld flash during spot welding may be caused by the direction of material flow predicted by the model. Because the material is accelerating toward the outer edge of the shoulder some of this material may be expelled from the weld zone and result in the formation of weld flash. A larger contoured shoulder with scrolling may be used as a means to mitigate the formation of weld flash. The inclusion of the rotating anvil increases stirring and results in a larger spot weld cross section.

### *Results*

Using Fluent to model the RAFSSW process is something that the software package was not intended to do. Approximating the plastically deformed metal as a highly-viscous fluid greatly increases the programs sensitivity to initial conditions, boundary conditions, and any changes made to the model during the iterations. The temperature and velocity gradients within the weld zone are very steep which also contributes to the instability of the program.

The first case modeled in Fluent was using the RAFSSW process to join 0.040” thick plate of Al 6061-T6 in a lap joint configuration. A rotation rate of 1000 RPM was used for both the tool and the anvil. The tool and anvil were rotated in the opposite direction with respect to the weldment. This plate thickness is typically the upper limit of plate thickness that can be joined for pinless FSSW tools. A flat shouldered tool with a diameter of 0.5 inches is used.

Figure 80 presents the model contours for velocity and temperature for the 1<sup>st</sup> case. In Figure 80.a it can be seen that there is substantial material flow at the interface between the top and bottom Al sheets. The lack of flow directly beneath the tool suggests that there may be insufficient mixing at this location. Figure 80.b shows that the temperature is sufficient for plastic deformation directly beneath the tool but defects (such as a hooking defect) may occur at the interface between the weld zone and base material.

## Experimental

### *Rotating Anvil Design*

Using the results of the CFD model and experimental data previously collected from creating spot welds using the FSSW process a physical system was designed so that the RAFSSW process could be implemented on the VUWAL FSW machine. The existing FSW machine is a retrofitted Kearney and Trecker CNC milling machine. The first concern was to ensure that the RAFSSW system would be cable of handling the high process forces (8-10kN) and torques (10-50 Nm) experienced during the FSSW process. By examining the torque loads placed on the main spindle motor (20 HP) during the

normal FSSW process a 7.5 HP AC motor was selected to provide power to the rotating anvil. Power will be provided to the rotating anvil via the FSW traverse motor power supply, as the traverse motor is not needed for the spot welding operation. The communication to the FSW weld computer will be established through the traverse motor's variable frequency drive (VFD). Second, the RAFSSW device needs to be designed so that it can be easily mounted and safely operated using the existing VUWAL FSW machine (Figure 81). Finally, the design will need provide the user with the ability to orient the FSSW tool, workpiece, and rotating anvil in the vertical direction.

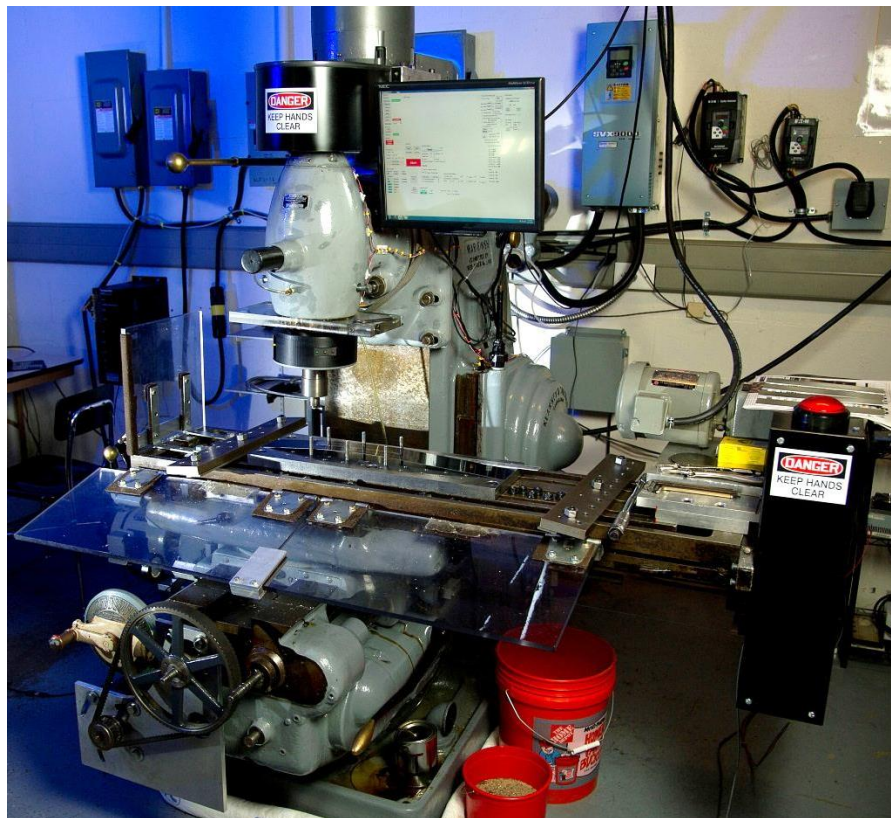


Figure 81: The VUWAL FSW Machine.

There are size restrictions that need to be considered when designing the RAFSSW device since it will be mounted on the worktable of the existing FSW machine. The main consideration is the vertical distance between the tool chuck worktable. The main support anvil for FSW and single sided FSSW will be removed for the RAFSSW process to provide more clearance. A shorter tool chuck is used to allow for additional clearance.

When possible, off-the-shelf components will be used in the design including bearings, pulleys, springs, and travel posts (bolts). The rotating assembly housing, base plate, and sample stage were machined from aluminum. A CAD drawing of the initial RAFSSW device design can be seen in Figure 82. The device will be mounted to the FSW machine's worktable using bolts that pass through the mounting holes in the base plate. The worktable can be moved laterally and horizontally prior to welding to ensure proper alignment of the FSSW tool and rotating anvil. Misalignment between the FSSW tool and rotating anvil can result in process instability and low quality welds. The RAFSSW device will utilize a tool chuck similar to the one used on the existing FSW machine so that different rotating anvil geometries can be experimentally evaluated.

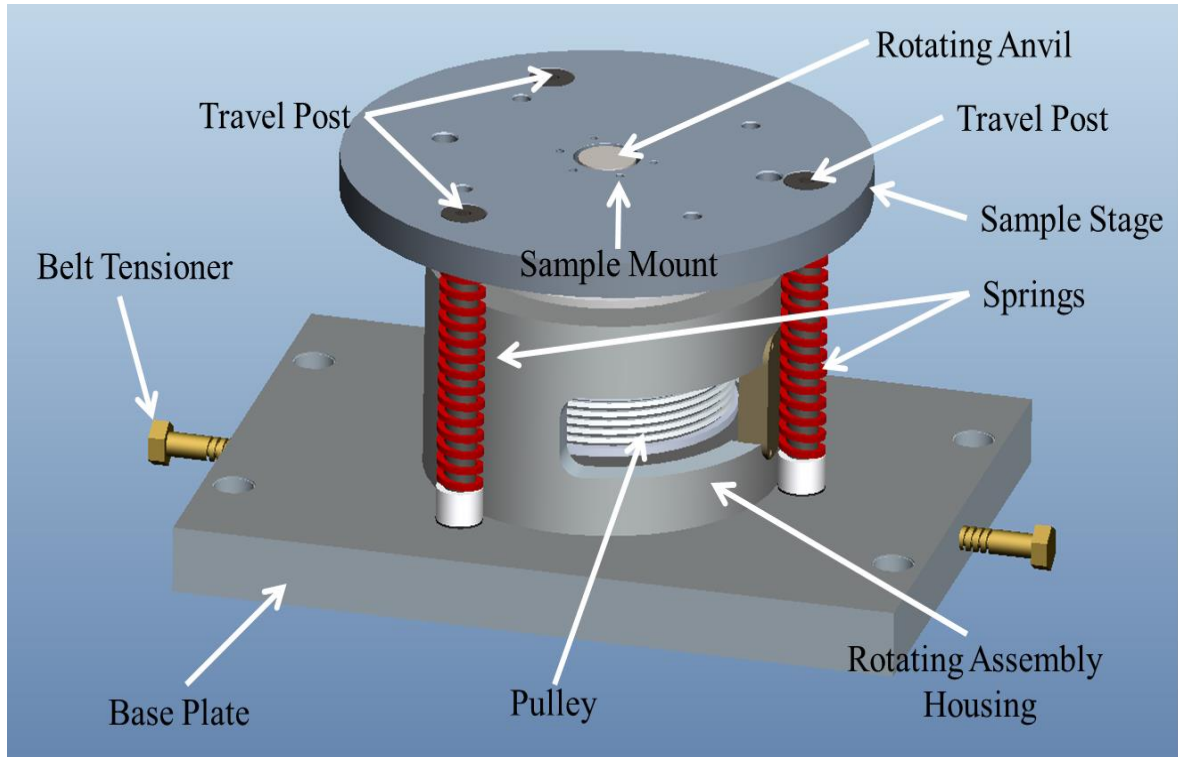


Figure 82: CAD drawing of the preliminary RAFSSW device design.

In order to achieve the appropriate position of the FSSW tool, workpiece, and rotating anvil a “free-floating” stage was implemented in the design (Figure 82). The sample stages motion is guided by three cylindrical travel posts and rests on three 144 lbs. die springs that will be compressed during welding. Prior to welding the top surface of the rotating anvil is beneath the sample stage. The RAFSSW process occurs in the following sequence:

1. The process begins with the workpiece positioned very close (0.005”) to the FSSW tool and rotating anvil but not in contact. The die-springs are not compressed.

2. The worktable begins to rise until a pre-determined load is experienced by the weld machine in the Z direction. The FSSW tool makes contact first, compressing the die springs. At this point the FSSW tool, workpiece and rotating anvil are in contact respectively.
3. The stage lowers to relieve the loading on the machine. The FSSW tool and rotating anvil begin to spin simultaneously. The die springs are less compressed and the FSSW tool is in contact with the workpiece. The rotating anvil is not.
4. The stage rapidly rises until a positional limit (the desired plunge depth) is achieved. The stage then stops motion. The die springs are again compressed.
5. After a predetermined period of time (the dwell time), the stage rapidly lowers until there is no measured load on the machine. The FSSW tool and rotating anvil stop spinning. The FSSW tool is in contact with the workpiece until the die springs are no longer compressed.





Figure 83: The RAFSSW Device. The motor can be seen mounted in front of the welding machine. During welding the worktable and rotating anvil would raise causing the belt to slip.

The first iteration of the RAFSSW device can be seen in Figure 83. During the preliminary use of the device several key issues were identified. The motor for the rotating anvil was attached to a post mounted to the floor in front of the FSW machine. During welding, the worktable and RAFSSW device would rise during welding resulting in belt misalignment (because the motor was not free to move). This alignment issue made it difficult to transfer power to the rotating anvil effectively due to the belt slipping. To address this issue a motor mount was constructed and used to attach the motor to the worktable of the FSW welding machine (Figure 85). During the weld the sample stage would vibrate causing the process to be unstable and difficult to perform. A stabilization arm was created and attached to the sample stage to reduce this vibration during welding. The stabilization arm was a large piece of aluminum attached to a precision hinge

allowing the sample stage to only experience displacements in the Z direction. The additional mass of the stabilization arm also helps to dampen the vibration during welding. The acceleration of the sample stage in the Z direction before and after the stabilization arm can be seen in Figure 84. A large acceleration is experienced during welding without the stabilization arm that is not experienced with it in place.

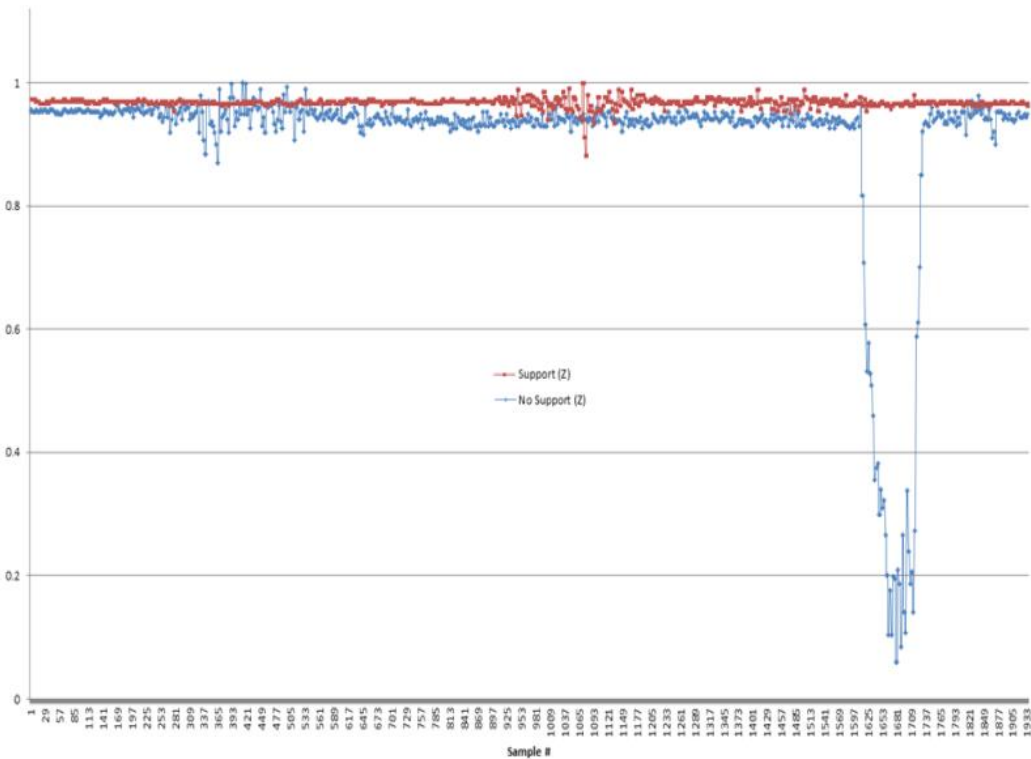


Figure 84: Plot of accelerometer data from the sample stage during welding with (red line) and without (blue line) the stabilization arm.

The present form of the RAFSSW device can be seen in Figure 85. The rotating anvil, motor, and stabilization arm are mounted to the work stage. This arrangement allowed for easy setup and safe operation. The standard belt guard of the FSW machine can now be used during the RAFSSW process, which was not possible with the first design iteration.

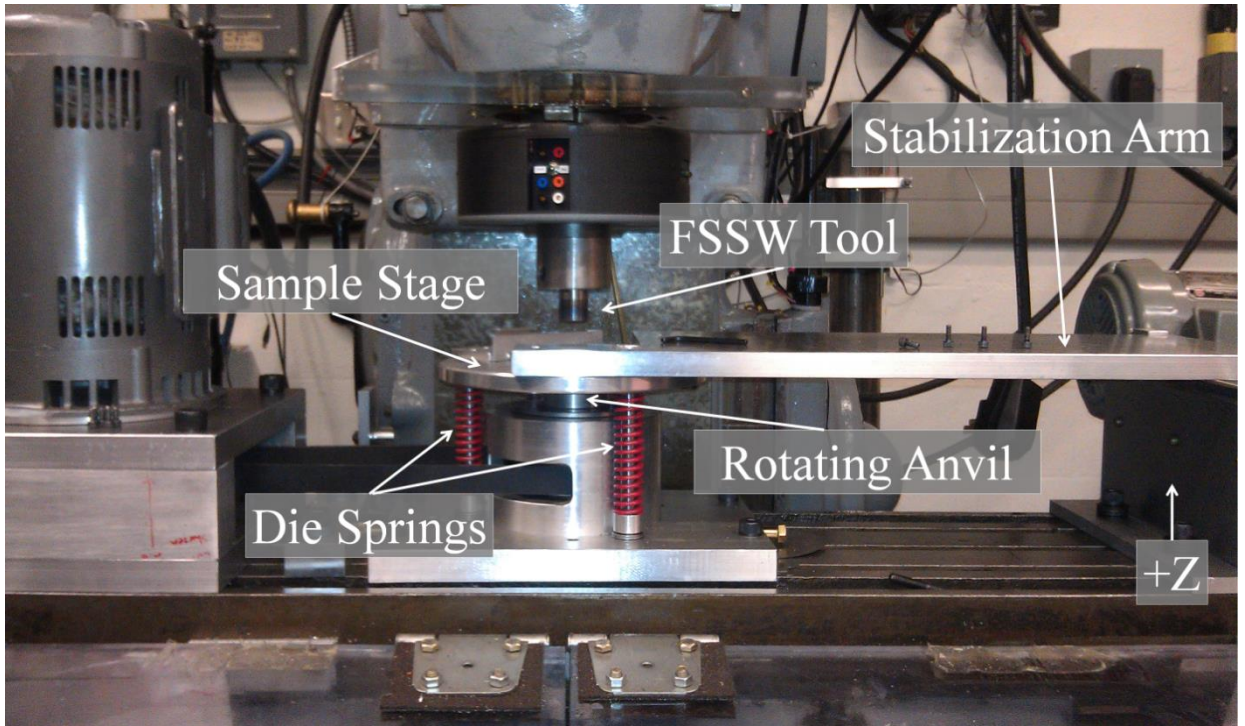


Figure 85: The RAFSSW device. The FSSW tool receives power from the main spindle of the FSW machine. The rotating anvil assembly, stabilization arm and 7.5 HP motor are all mounted to the stage of the FSW machine. The vertical actuation of the RAFSSW device is achieved through a simple combination of the vertical drive of the FSW machine and the floating stage.

A software routine is written that will enable the operator to create spot welds at desired process parameters and monitor the process environment real-time.

#### *Using the RAFSSW Process*

Spot welds were created on 51 x 76 mm samples of 1 and 2 mm thick plate of Al 6061-T6. Parameters for creating the spot welds were selected based on the results of the numerical model. Rotation rates of 750, 1000 and 1500 RPM, dwell times of 0.5 and 1.5 seconds, a plunge rate of 0.3 mm/sec and a plunge depth of 0.2 mm were used to create spot welds. A lap joint configuration was used such that the rolled direction would be

parallel to the loading direction during testing. Rigid fixturing was used to ensure that the samples did not shift during the spot weld process.

The pinless welding tool and rotating anvil are made of O1 tool steel with a maximum overall diameter of 25.4 mm featuring a scrolled, spherically tapered (convex) shoulder of 76.2 mm radius (of curvature) with a 10 mm flat (Figure 86).



Figure 86: The welding tool and rotating anvil. A spherically tapered (convex) shoulder with scrolling and a 10.2 mm flat ground into the end.

## Experimental Results

### *Macrosection Analysis*

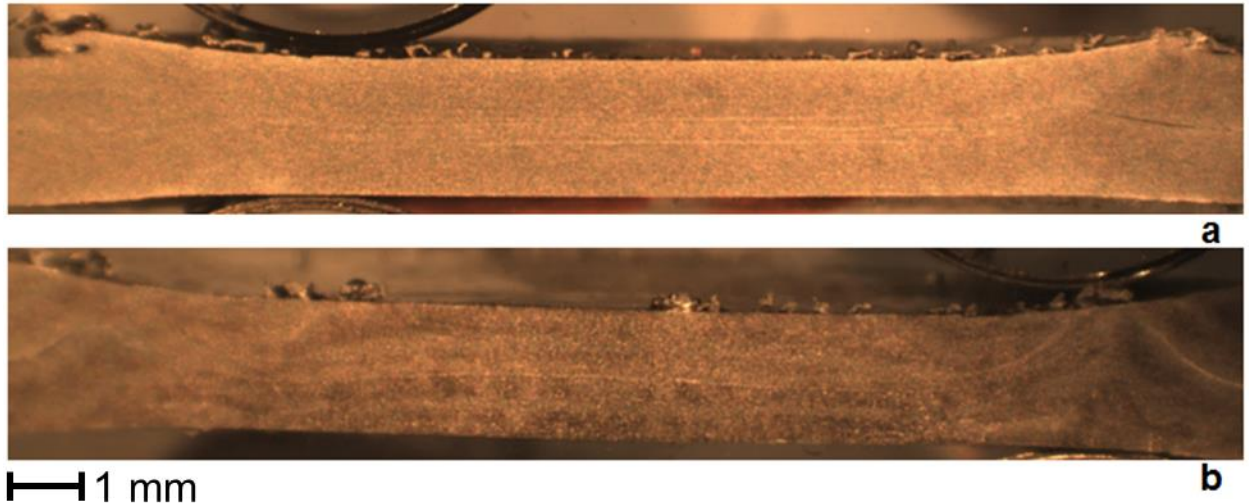


Figure 87: Macrosection image of spot welds made using the RAFSSW process. Spot weld created at a) 750 rpm (welding tool and anvil) and a 0.5 second dwell phase and b) 1500 rpm and a 0.5 dwell time. A hooking defect can be seen on the left and right side of the 1500 rpm spot weld macrosection.

Macrosection analysis was performed on spot welds created on 1 mm thick plate. The analysis was performed to reveal the structure of the weld zones as well as to check for defects. The macrosectioned samples were etched with a 5 ml Hf, 10 ml H<sub>2</sub>SO<sub>4</sub>, and 85ml H<sub>2</sub>O solution. The cross section of a spot weld created at 750 rpm and a 0.5 second dwell period can be seen in Figure 87.a. There are no observable defects in this spot weld. A severe hooking defect was observed on both sides of the spot weld made at 1500 rpm and a 0.5 second dwell period. The hooking defect is an unbonded region and is known to be detrimental to the weld strength. This is a common defect observed in linear FSW, typically on either the advancing or retreating side, when too much heat is generated during welding due to parameter selection. For FSSW, the hooking defect may encircle

the spot weld. Also present are oxide bands in the spot weld made at 1500 rpm, which are more pronounced at higher rotation rates when welding with a pinless tool.

### *Mechanical Strength*

The strength of the spot welds created in 1 mm thick plate by the RAFSSW process were compared to spot welds created by the traditional single-sided FSSW process using a rotation rate of 750 and 1500 rpm and 2 different dwell times; 0.5 and 1.5 seconds.

Results can be seen in Figure 88. For the spot welds made at 750 rpm with a 0.5 second dwell period the resultant strength showed an 18% improvement compared to a single-sided FSSW approach. The spot welds made at 750 rpm with a 1.5 second dwell period saw a 2% increase in joint strength when compared to the traditional single-sided process.

The strength of the spot weld made at 1500 rpm with a 0.5 and 1.5 second dwell period saw a 38% and 35% increase in joint strength respectively when compared to the single-sided process. The observed increase in joint strength can most likely be attributed to the uniformity in the shape of the weld zone, the overall larger cross sectional area of the weld joint, and the increased stirring which helps to break up any oxide layers that may be present along the original joint line interface.

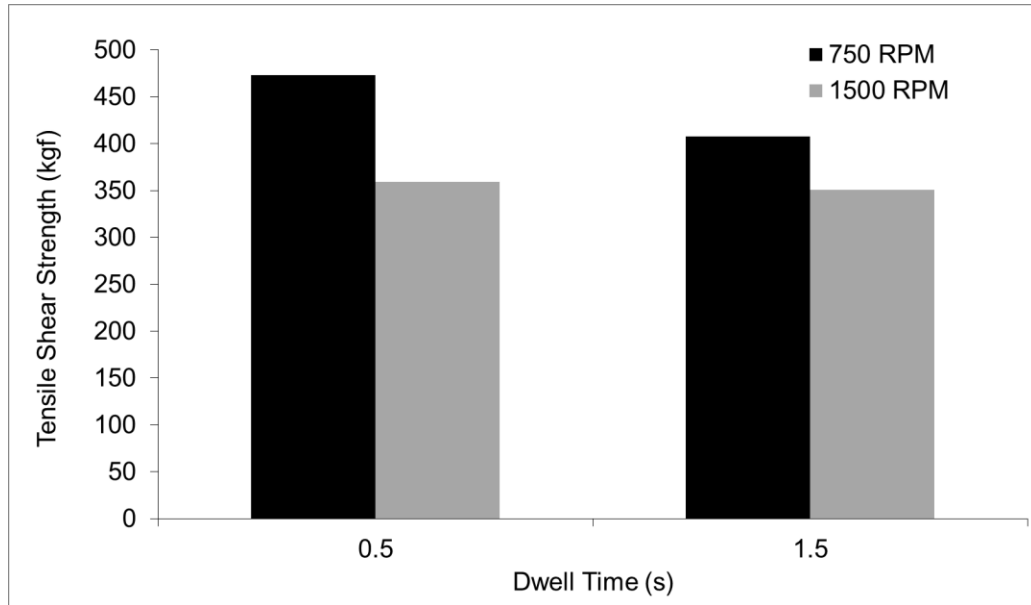


Figure 88: Comparison of joint strengths between spot welds made using the RAFSSW process using 750 and 1500 rpm and two different dwell times in 1 mm thick Al 6061 plate.

Spot welds were made in 2 mm thick plate using the RAFSSW process with rotation rates of 1000 and 1500 rpm. The resulting joint strengths can be seen in Figure 89. No comparison is made to the traditional FSSW process since it was not possible to create reliable spot welds with a pinless tool without the rotating anvil at this plate thickness. Unlike for the 1 mm thick workpieces, longer dwell times resulted in an increase in joint strength. Increasing the dwell time from 0.5 seconds to 1 second resulted in an increase of 19% and 54% in the joint strength respectively. This additional dwell period may provide extra time for the weld zone to better develop in the thicker workpieces, resulting in a stronger weld. An optimal combination of rotation rate and dwell time for mechanical strength may exist. The optimal dwell time may increase as the thickness of the workpiece increases. Selecting a dwell period that is too short or long may be detrimental to the strength of the spot weld. Varying the dwell period directly affects the heat generated during welding. “Cold” welding parameters can result in a lack of

bonding, while “hot” welding parameters may result in the formation of excessive weld flash and hooking defects. Increasing the rotation rate from 1000 to 1500 rpm resulted in a loss in joint strength for all cases investigated.

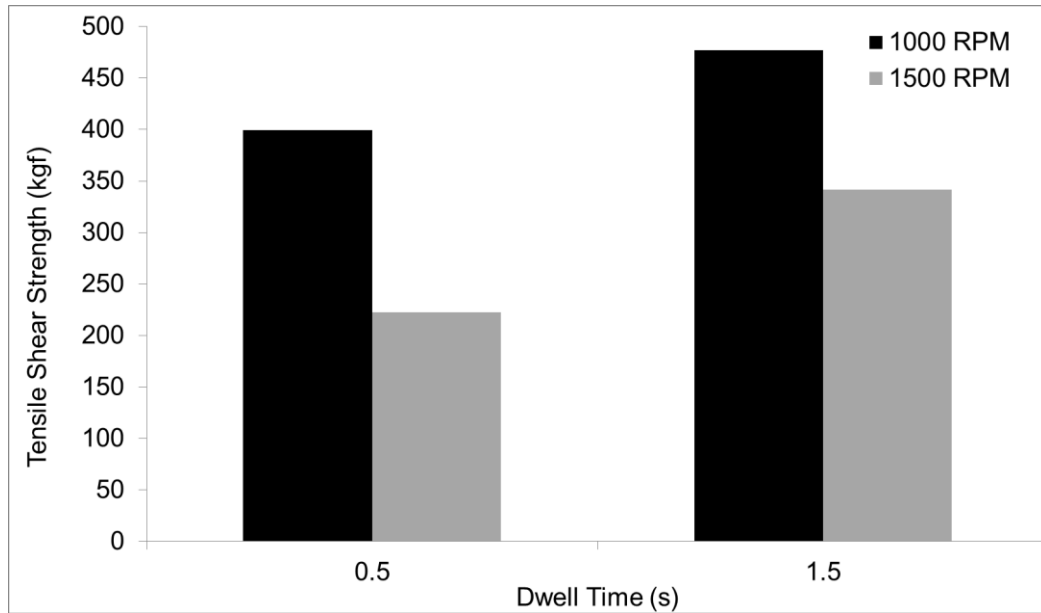


Figure 89: Comparison of joint strengths between spot welds made using the RAFSSW process using 750 and 1500 rpm and two different dwell times in 2 mm thick Al 6061 plate.

### *Process Forces*

Previous FSSW research using a pinless spot welding tool has shown to place a significant axial load of 9.4 kN on the welding machine. The axial load (in the Z direction) is the largest of the process forces acting on the welding tool and requires that a large robotic frame be used to implement the process. The RAFSSW process has been shown to significantly reduce the axial loading on weld machine. Comparing the process forces measured when welding 1 mm thick plate using the standard single-sided process



the axial force was reduced by as much as 62% (an axial force of 4 kN) when using a rotating anvil (Figure 90). This reduction in process forces can be attributed to the increased heat input into the spot welds. By introducing plastic deformation on the underside of the weld the rigidity of the weld zone may also be reduced which could also lend to the reduction in axial forces. Though spot welds are not able to be made in 2 mm thick plate using the single-sided method the axial force is much lower when using the RAFSSW process, approximately 4.7 kN during welding. This reduction in process forces would be beneficial for the application of FSSW via a robotic manipulator.

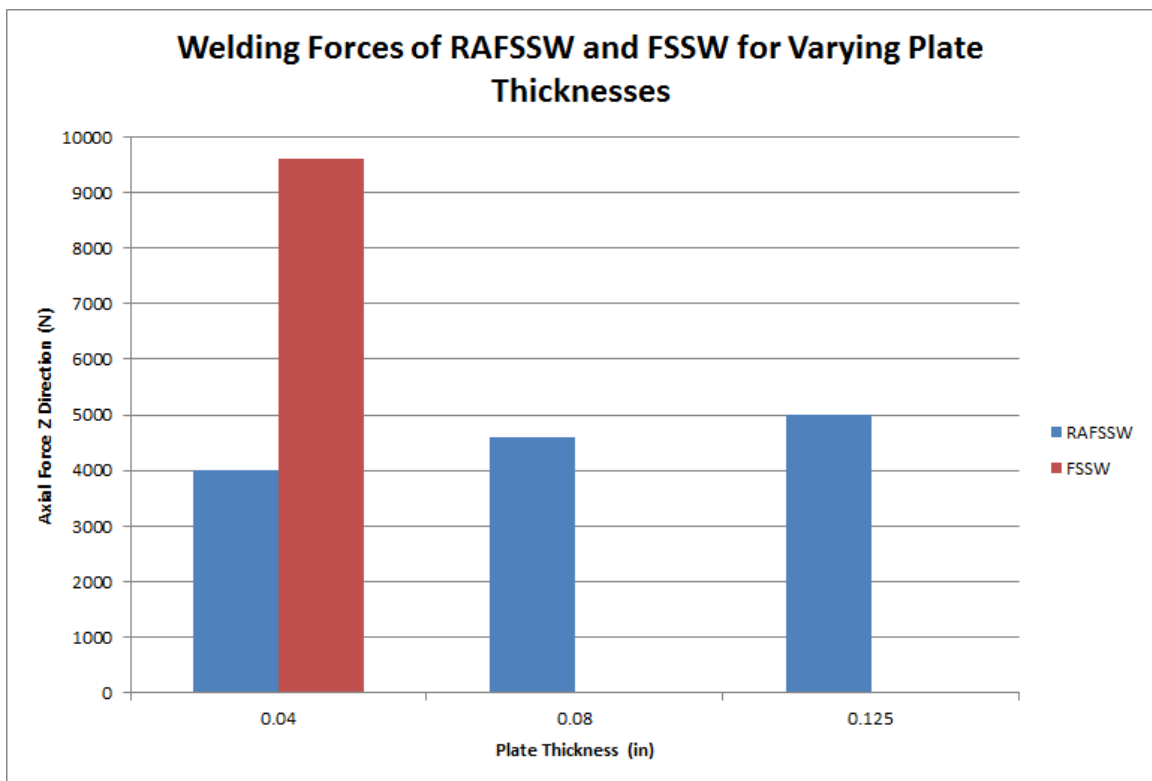


Figure 90: Comparison of welding forces between the traditional FSSW and RAFSSW processes created in the 1 mm (0.04”) thick plate. Axial forces created in 2 mm (0.08”) and 3 mm (0.125”) using the RAFSSW are also presented.

## Conclusions

The 2 dimensional axisymmetric CFD model of the RAFSSW process provided valuable insight that lead to the design of the RAFSSW device. The material is predicted to flow outward toward the edge of the shoulder along the interface between the welding tool and rotating anvil. The material then flows down toward the joint interface. At the joint interface the material stirred by the welding tool and rotating anvil meet and move inward toward the center of the weld zone. The outward direction of material beneath the shoulder and rotating anvil may lead to the formation of weld flash. As such, a contoured shoulder with scrolling was used in the experimental design as a means to reduce the formation of weld flash along the perimeter of the weld.

As in single-sided FSSW, excessive heating is detrimental to the quality of the spot weld. Due to the increased heat input by the rotating anvil the dwell time should be shortened such that spot weld is not over heated.

In the case of the 1 mm plate the application of the rotating anvil improved the strength of the spot weld for both the low and high rotation rate. The longer dwell time for both rotation rates resulted in a loss of strength.

The rotating anvil made it possible to create quality spot welds in the 2 mm thick Al plate. For the thicker plate, increasing the dwell time resulted in an increase in the strength of the spot weld. Because of the additional plate thickness it may require more time for the weld zone to develop. It has been shown that the RAFSSW process is a technology that is capable of creating solid state spot welds in thin metal plate typical for automotive manufacturing applications. The RAFSSW method has been demonstrated to:

- Create stronger spot welds than the traditional process by 150%.
- Create quality spot welds in 1 mm and 2 mm thick Al 6061 plate
- Reduce cycle times by up to 90% without losing joint strength.
- Reduce axial forces experienced by the weld machine by as much as 62%

## CHAPTER VII

### ENERGY INPUT DURING FRICTION STIR SPOT WELDING

Chase D. Cox, Brian T. Gibson, Alvin M. Strauss, George E. Cook

#### Abstract

Friction stir spot welding is often performed on thin plates of an aluminum alloy. This chapter presents the results on how the number of tool rotations affects the quality of the resulting spot weld. Different combinations of rotation rate and dwell time are investigated. A linear relationship was found to exist between the number of tool rotations completed during the spot weld and the resulting tensile shear strength. Spot welds that only completed 10 rotations were 177% stronger than those created at 50 tool rotations. The energy generated during the welding operation was quantified and also found to have a linear relationship with tensile shear strength. A modified open-loop position control system is proposed that monitors and limits the energy generated during friction stir spot welding by adjusting the dwell time.

#### Introduction

Rising fuel costs have placed a demand on automobile manufactures to produce vehicles with better fuel economy. One approach to achieve this goal is to replace structural and cosmetic components in the vehicle made of steel with lighter aluminum alloys. However traditional spot welding processes can prove problematic when joining metals like

aluminum. Friction Stir Spot Welding (FSSW) is a solid-state joining process capable of joining light-weight metals with high thermal conductivity such as aluminum, making it an attractive process for manufacturers. In FSSW, the joint is created by plunging a rotating tool into a weldment until the tool's shoulder reaches a desired penetration depth. It will remain at this depth for a specified length of time, at which point the tool is retracted. Unlike fusion welding, FSSW does not melt the parent material, require consumables such as filler rod, shielding gas, or welding sticks, and uses 99% less energy to create the weld [Feldman]. For these reasons FSSW can be considered a "green technology". Technologies like self-piercing rivets can afford manufacturers some of the same advantages of FSSW but adds to the overall complexity and weight of the design and increases overhead for production.

Several parameter studies have been performed in FSSW in order to quantify the effects they have on the quality of the spot weld. Karthikeyan et al. investigated the effects rotation speed, plunge speed, plunge depth, and dwell time have on the strength of the spot weld. They concluded that the plunge rate was the most critical factor in determining weld quality, followed by plunge depth, dwell time, and tool rotation speed [Karthikeyan]. The inclusion of a pin in the welding tool design makes the plunge rate an important process parameter. The additional time required to plunge the rotating welding tool into the workpiece can generate too much heat such that the quality of the weld is negatively affected before the spot weld is even formed. In this study a pinless FSSW welding tool will be used. Tozaki et al. found that increasing the rotation rate from 1000 rpm to 2000 rpm was detrimental to the quality of the spot weld. Tozaki also reports that for a given rotation rate there exists an optimal dwell time for creating a quality spot weld

[Tozaki]. The combination of rotation rate with dwell time can instead be considered in terms of tool rotations. Previous work found that welding at higher rotation rates (1500-2000 rpm) and long dwell periods (4-6 seconds) resulted in a weld zone that was too hot and prone to defect formation [Cox].

It is the primary objective of this work to understand how many tool rotations it takes to create a friction stir spot weld in an aluminum alloy. Understanding this relationship could be a critical step for the advancement of FSSW in manufacturing. The secondary objective of this work is to quantify the energy generated during welding for the purpose of identifying a process parameter that may be related to weld quality.

## Experimental

Table 9: Experimental Welding Parameters

<b>RPM</b>	<b>Dwell Time (sec)</b>	<b>Tool Turns</b>	<b>Plunge Rate (mm/sec)</b>	<b>Plunge Depth (mm)</b>
<i>800</i>	<i>0.75</i>	<i>10</i>	<i>0.21</i>	<i>0.2</i>
<i>1200</i>	<i>0.5</i>	<i>10</i>	<i>0.21</i>	<i>0.2</i>
<i>1200</i>	<i>1</i>	<i>20</i>	<i>0.21</i>	<i>0.2</i>
<i>1600</i>	<i>0.75</i>	<i>20</i>	<i>0.21</i>	<i>0.2</i>
<i>1800</i>	<i>1</i>	<i>30</i>	<i>0.21</i>	<i>0.2</i>
<i>1200</i>	<i>1.5</i>	<i>30</i>	<i>0.21</i>	<i>0.2</i>
<i>1600</i>	<i>1.5</i>	<i>40</i>	<i>0.21</i>	<i>0.2</i>
<i>1200</i>	<i>2</i>	<i>40</i>	<i>0.21</i>	<i>0.2</i>
<i>1500</i>	<i>2</i>	<i>50</i>	<i>0.21</i>	<i>0.2</i>

Spot welds are made using 1 mm x 50 mm x 76.2 mm sheets of Al 6061 T6. The spot welding parameters are listed in Table 9. Combinations of rotation rate and dwell time were selected such that spot welds would be made with 10, 20, 30, 40, and 50 turns of the

welding tool. A constant plunge depth and plunge rate of 0.2 mm and 0.21 mm/sec respectively were used for each spot weld.

One identified drawback of this process is that the tooling leaves a keyhole (the size of its dynamic volume) in the weld during retraction that requires removal via either post-processing or costly, highly specialized tool design. As such, pinless tool designs have been identified in the literature as a low-cost alternative in this situation [Backavos 2009, 2010]. In this work, a pinless FSSW tool is used. The spot welding tool is made from O1 tool steel and is then hardened. The welding tool has a maximum overall diameter of 25.4 mm (1 inch) and features a scrolled, spherically tapered (convex) shoulder of 76.2 mm radius with a 10.2 mm flat (Figure 91). During spot welding the workpiece is rigidly mounted to a backing anvil.



Figure 91: Pinless FSSW tool with a spherically tapered shoulder.

The spot welding experiments are conducted using a modified Milwaukee Model K milling machine which is retrofitted with advanced motors and instrumentation. The weld control computer executes the FSSW routine by simultaneously sending the welding parameters to both the vertical drive and spindle motors. The control computer interfaces with the vertical drive motor via a Compumotor KH Brushless Servo Drive and with the

spindle motor via a Cutler-Hammer SVX9000 variable frequency drive. As the vertical servomotor begins to raise the welding stage, the control system monitors the vertical position of the spot welding sample. At the same time the spindle begins to rotate. Once the spot welding tool reaches the desired plunge depth within the weld sample the vertical motion of the table is halted. After the specified number of tool turns is completed, the welding stage is lowered and the spindle rotation is stopped (Figure 92). During spot welding the spindle torque and axial force are monitored via a custom built wireless force dynamometer. The quality of the resulting spot welds is evaluated using tensile shear tests.

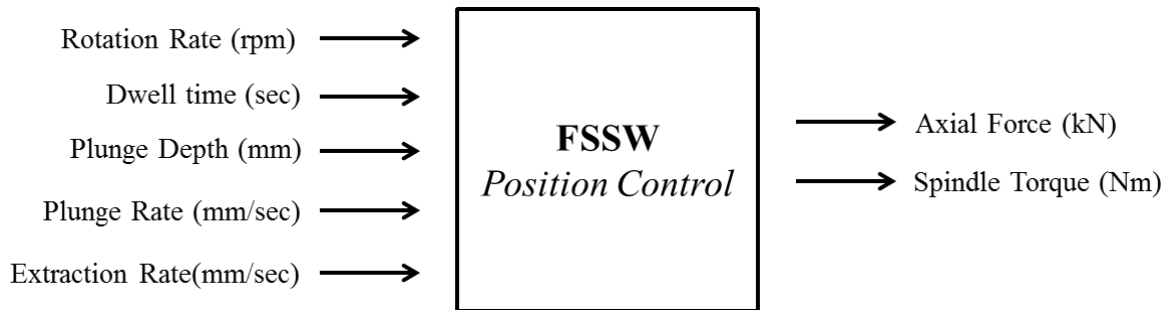


Figure 92: Open-loop position control system used for this experiment. The rotation rate, dwell time, plunge depth, plunge and extraction rates are inputs. The plunge depth and dwell time are the limits in this system. The resulting axial force and spindle torque are monitored during welding.

### Results

The experimental response variables weld energy (kJ), maximum axial force (kN), maximum spindle torque (Nm), and peak failure load (kgf) can be seen in Table 10 for each of the spot welds in the study. For analysis, each of the different number of tool turn combinations (20, 30, 40, etc.) response variables are averaged with the exception being the spot welds made with 10 tool turns. The spindle motor did not perform as desired at



800 RPM. However, spot welds were created at this parameter and will be used later in the discussion section.

Table 10: Experimental spot welding results.

<b>RPM</b>	<b>Dwell (sec)</b>	<b># Turns</b>	<b>Energy (kJ)</b>	<b>Max Axial Force (kN)</b>	<b>Max Torque (Nm)</b>	<b>Peak Load (kgf)</b>
800	0.75	10	4.13	12.96	33.09	462.71
800	0.75	10	4.78	12.08	36.94	364.75
800	0.75	10	5.25	12.38	40.68	443.56
1200	0.5	10	5.96	11.10	34.09	542.74
1200	0.5	10	6.41	10.90	37.25	562.47
1200	0.5	10	6.53	10.88	40.37	554.61
1200	1	20	7.76	10.60	35.02	519.65
1200	1	20	7.81	11.09	34.76	501.87
1200	1	20	8.39	10.95	37.21	519.29
1600	0.75	20	7.95	10.80	25.26	468.58
1600	0.75	20	8.05	10.37	28.36	416.82
1600	0.75	20	8.09	10.76	28.36	438.68
1200	1.5	30	8.18	10.18	31.21	476.17
1200	1.5	30	9.19	10.62	34.09	485.60
1200	1.5	30	9.72	11.10	35.77	486.18
1800	1	30	8.17	10.53	28.36	384.36
1800	1	30	9.21	10.99	24.18	380.27
1800	1	30	9.33	10.67	24.89	394.86
1200	2	40	9.86	11.29	31.93	432.76
1200	2	40	11.47	10.42	36.68	407.80
1200	2	40	11.60	10.98	36.20	420.86
1600	1.5	40	10.42	10.28	26.09	325.05
1600	1.5	40	10.71	10.96	25.47	356.44
1600	1.5	40	10.86	10.25	27.63	314.40
1500	2	50	11.88	9.90	29.93	358.97
1500	2	50	11.96	10.94	28.60	281.76
1500	2	50	12.10	10.18	28.36	298.73

### *Axial Force*

During the spot welding process the welding tool experiences a large axial load due to the mechanical interaction with the workpiece. This axial force is known to be largely dependent on the plunge depth used during welding [Cox]. The pre-welding temperature of the workpiece, geometry of the welding tool, rotation rate, and plunge rate can also affect the maximum axial force during welding. For all of the spot welds in this study a plunge depth of 0.2 mm was used. As a result, the average axial load for the study was  $10.1 \text{ kN} \pm 0.5 \text{ kN}$ . The average of the maximum axial force for each of the tool turns can be seen in Figure 93. The error bars in Figure 93 represent the standard deviation.

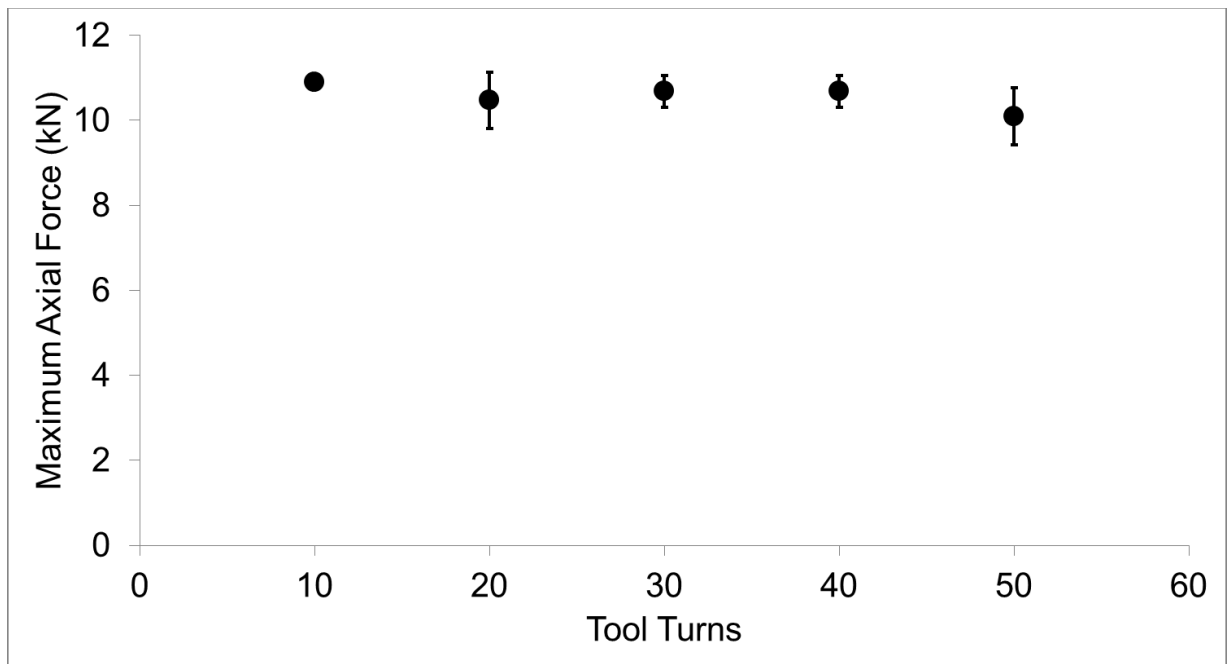


Figure 93: Axial force during FSSW for different numbers of tool turns. The average axial force is  $10.1 \text{ kN} \pm 0.5 \text{ kN}$ . For this experiment, an open-loop position control scheme was used. Error bars represent standard deviation.

### *Spindle Torque*

Like with the axial force, the spindle torque measured during FSSW is a result of the welding tool's interaction with the workpiece. The spindle torque is largely dependent on the spindle speed, but can also be affected by dwell time, workpiece temperature, tool geometry, etc. Higher rotation rates generate more weld energy which results in a hotter weld environment. This hotter weld environment softens the workpiece making it easier for the welding tool to stir the material. The maximum torque value is measured when the tool reaches the desired plunge depth. During the dwell phase the torque can be seen to decrease until the tool is retracted, never reaching a steady-state condition (Figure 94). There was no observed relationship between maximum spindle torque and the number of tool turns however. The average of the maximum measured spindle torque is observed to decrease with an increase in the rotation rate.

### *Spot Weld Energy*

The weld power can be calculated from spindle torque through the relationship shown in Equation 7.1.

$$\text{Weld Power} = \Omega M \quad (7.1)$$

Where  $\Omega$  is the rotation rate (rad/sec) and  $M$  represents the spindle torque (Nm). The spindle VFD used in this experiment is capable of reporting the motor power output. However, using this signal would not account for any mechanical losses within the

drivetrain. The weld power method is more accurate as it includes any mechanical losses between the motor shaft and spot welding tool.

In linear friction stir welding, a steady state condition can be reached during joining and as such a spindle torque can be specified for control and/or quality purposes [Longhurst]. By maintaining a desired spindle torque the user can control the process to help ensure a quality weld is created by maintaining a constant thermomechanical environment [Prater]. Because of the transient nature of FSSW it is not possible to reach a constant torque value for a similar control or quality assessment application. Equation 7.1 defines the power being generated during welding at any instant during spot welding. Defining the weld power for a spot weld during the dwell phase is difficult due to the fact that the torque acting on the tool is not constant during welding. If this signal can provide any valuable information on the process it will need to account for any variation in the signal during welding. One such approach is to account for the total energy generated during spot welding. Monitoring the total energy during spot welding will provide information on the thermomechanical environment within the weld zone.

To do this, we first monitor the spindle torque from the instant the rotating tool first makes contact with the workpiece until the tool retracts from the workpiece after the dwell phase (Figure 92). If we then multiply the spindle torque vs. weld time curve by the rotation rate (in rad/sec) we obtain a curve that now represents weld power vs. weld time. Integrating the weld power vs. weld time curve provides the total energy output during spot welding (Equation 7.2) (Figure 92) [Zimmer].

$$Weld\ Energy = \int_{Tool\ Contact}^{Tool\ Retraction} Weld\ Power\ dt \quad (7.2)$$

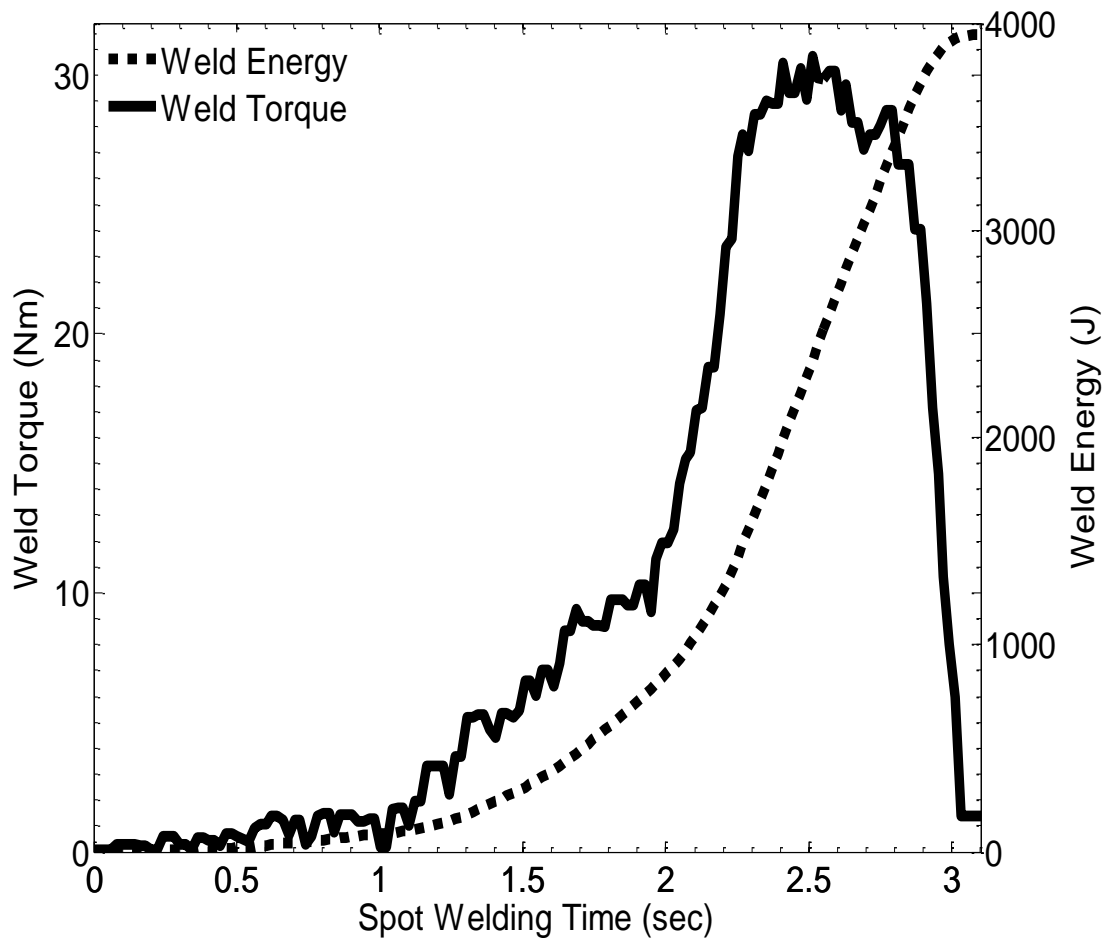


Figure 94: Spindle torque (Nm) and energy (J) during spot welding. 1200 RPM, 0.5 sec dwell, 10 tool turns.

The computed weld energy for each of the different number of tool turns is plotted in Figure 95. A strong linear relationship was found to exist between the number of tool turns and the energy measured during the spot welding process. For each number of tool turns different combinations of rotation rates and dwell times were used. Higher rotation rates paired with shorter dwell times are found to input a comparable amount of energy during spot welding as lower rotation rates paired with longer dwell times. The larger standard deviation seen for the spot welds made at 30 tool turns could be a result of the

larger difference between the two rotation rates used; 600 RPM. The 20 and 40 tool turn rotation rates only had a difference of 400 RPM. The error bars in Figure 95 represent standard deviation.

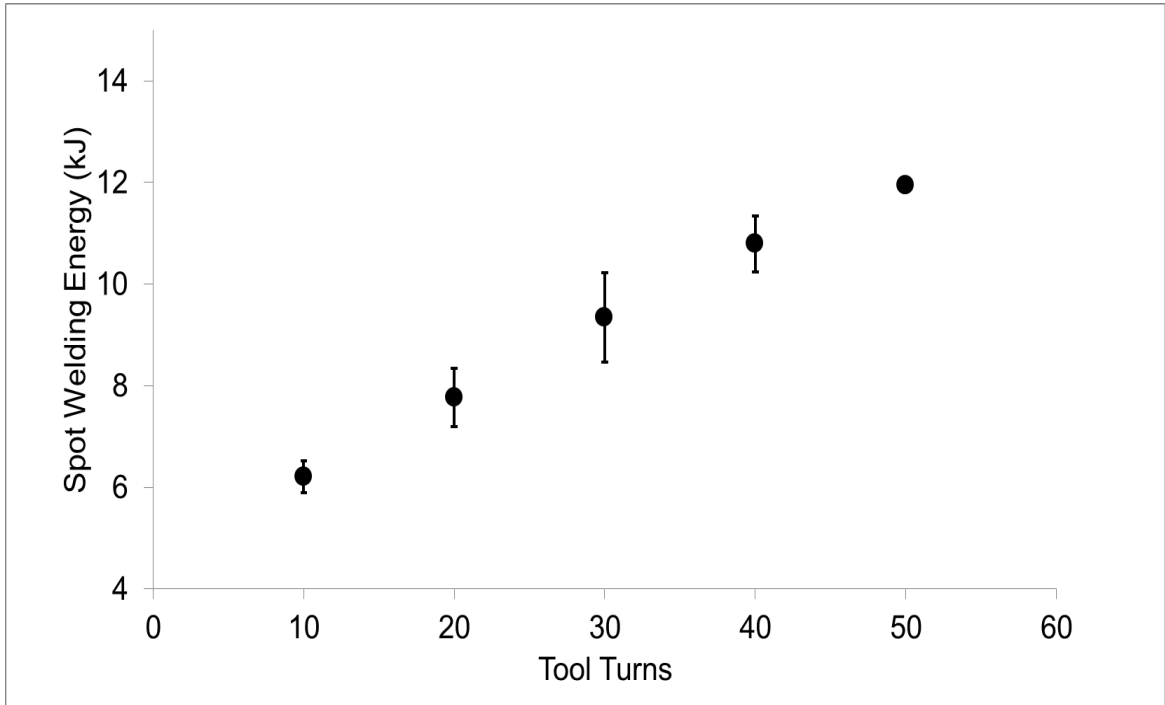


Figure 95: Total spot welding energy generated during FSSW. Error bars represent standard deviation.

### *Tensile Shear Strength*

The resulting tensile shear strength is plotted in Figure 96. A linear relationship was also observed between the number of tool turns and the resulting tensile shear strength of the spot welds. Like with the energy input during welding, higher rotation rates paired with shorter dwell times are found to result in spot welds with tensile shear strengths similar to welding at lower rotation rates paired with longer dwell times. Previous FSSW work has suggested that creating spot welds at higher rotation rates is detrimental to the quality of

the weld. However in this experiment it was found that the number of tool turns during welding, and not necessarily the rotation rate, is responsible for the quality of the weld. Welding at higher rotation rates may simply require a shorter dwell phase. The error bars in Figure 96 represent standard deviation.

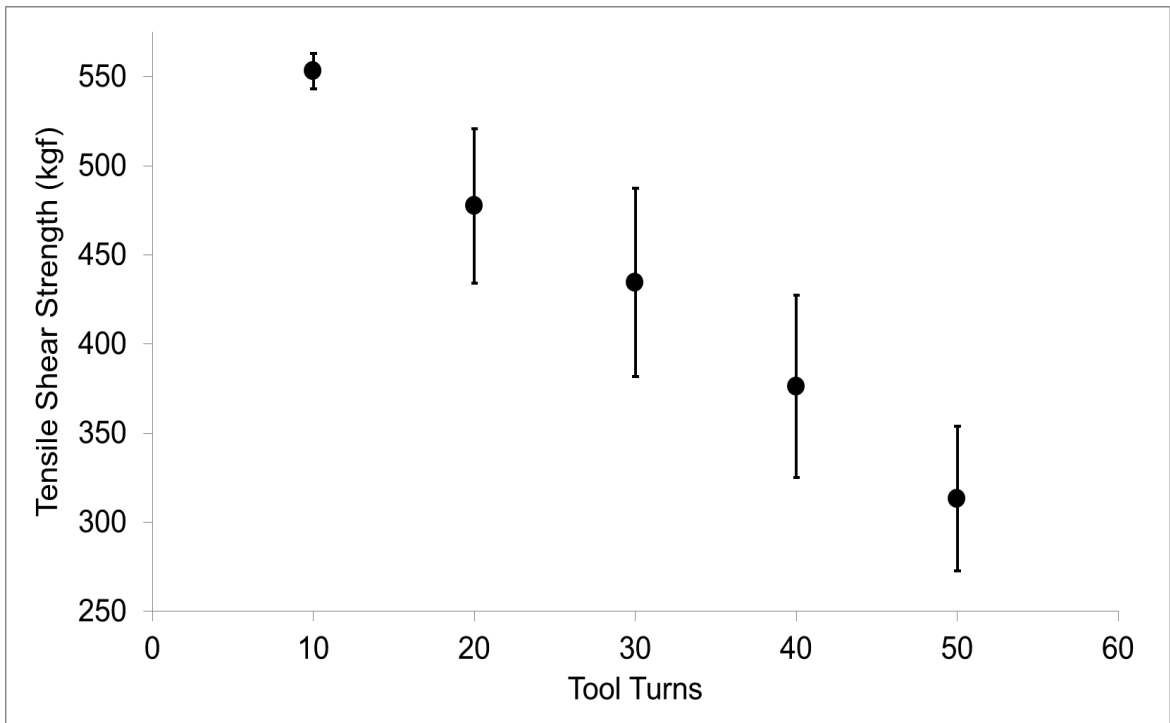


Figure 96: Spot Weld Strength. Error bars represent standard deviation.

### Discussion

Each rotation of the spot welding tool generates some amount of energy. As the welding tool completes additional rotations, more energy is generated and the workpiece experiences more heating and deformation. It is not known in this experiment how much of the energy generated is transferred to the workpiece during welding. Some of the energy generated is lost through the spindle and to the environment via conduction and

convection. However these losses are assumed to be identical for each of the welding experiments presented. In Figure 95 it can be seen that for each tool turn 0.15 kJ of energy is generated. Equation 7.3 defines the linear best fit for this data ( $R^2 = 0.997$ ).

$$\text{Weld Energy (kJ)} = 0.15 * \text{Number of Tool Turns} + 4.86 \quad (7.3)$$

Figure 97 compares spot weld energy and tensile shear strength. The error bars in Figure 97 represent standard deviation for both spot weld energy (x-axis) and tensile shear strength (y-axis). Spot welds created with more weld energy were found to be significantly weaker. Creating a spot weld with 6.3 kJ (10 tool turns, 1200 RPM) resulted in an average joint strength of 553.7 kgf. Whereas spot welds made with less energy 4.2 kJ (10 tool turns, 800 RPM) resulted in an average joint strength of 423.68 kgf. The spindle motor was significantly underpowered at 800 RPM and was not able to maintain a constant rotation rate during the spot welding operation. An optimal welding energy input condition may exist between 4.2 kJ and 6.3 kJ for 2 mm thick sheet of Al 6061 T6. The welding machine is at its lower operational limit at 1200 RPM for FSSW. Additionally, the welding stage cannot be actuated in such a manner as to reduce the time of the dwell phase to less than 0.5 seconds.



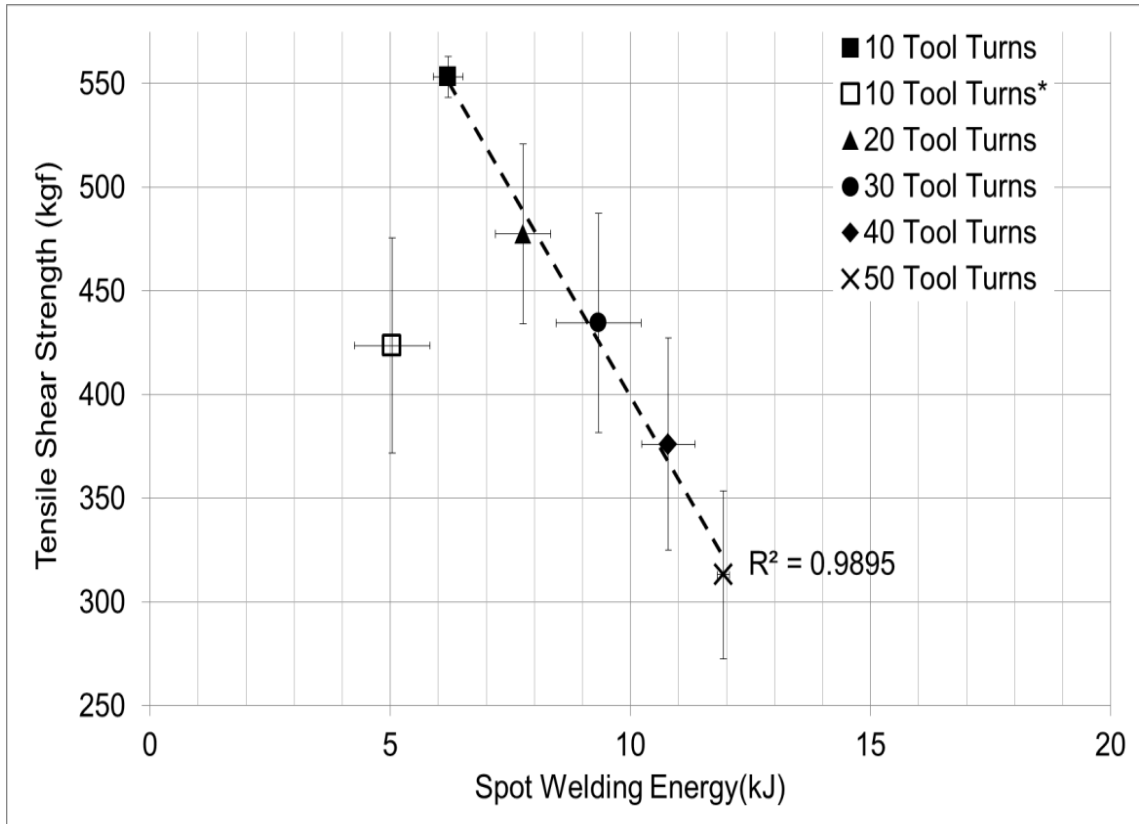


Figure 97: Spot Weld Tensile Shear Strength vs. Spot Welding Energy. Error bars represent standard deviation.

Higher spot welding energies result in a hotter welding environment. Excessive heat generation during FSSW can lead to defects within the weld zone that can be detrimental to the quality of the weld. As such, the selection of rotation rate and dwell time are paramount for weld quality. If an FSSW tool with a probe is used the selection of the plunge speed, which can be limiting, also becomes a critical parameter as it can have a dramatic effect on the heat generated during spot welding. Monitoring the weld energy during the process may help to avoid overheating during welding.

The FSSW process is exclusively implemented using robotic and requires automation. Axial force can be and is used as a means for feedback control in FSSW as it is a good indicator of the welding tool's contact condition with the workpiece. However for the

case of FSSW presented here, it provided no quantifiable information regarding the quality of the resulting spot weld. Therefore the use of axial force could only be used to ensure proper positional alignment and would not necessarily account for any variations in the process that may affect weld quality. Likewise, spindle torque is also a popular parameter for the purpose of feedback control in FSW. Like with the axial force, the spindle torque by itself was not found to provide any indication of weld quality. However, using the spindle torque to calculate the spot welding energy was found to have a strong linear relationship with weld quality. This relationship may be used by engineers to develop an open-loop control system for FSSW similar to what is done for resistive spot welding. The effect of workpiece temperature before welding and tool wear, among other things, on quality is not yet documented and should be fully understood if an open-loop control system is developed such as the one seen in Figure 98. By monitoring the weld energy generated during FSSW it may be possible to monitor the weld quality *in situ*.

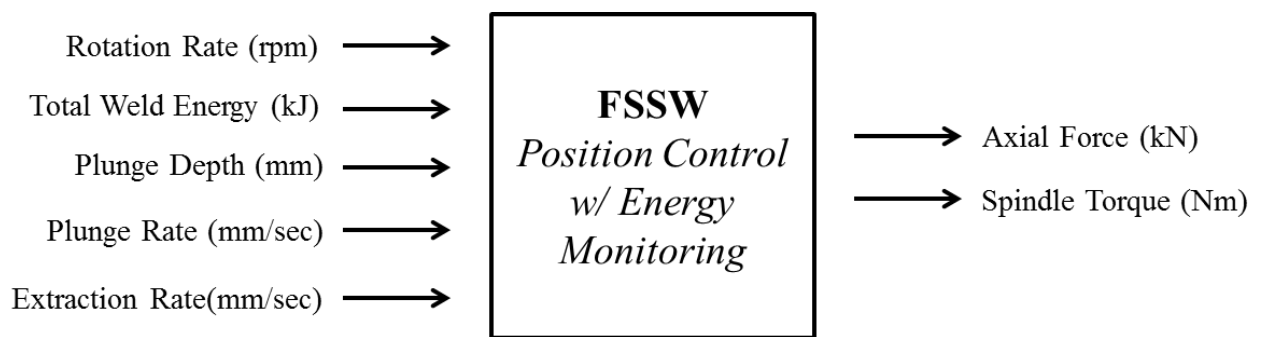


Figure 98: Proposed FSSW open-loop control system with energy monitoring. Like with traditional position control, the rotation rate, plunge depth, plunge and extraction rate are still input into the system. Instead of inputting a dwell time, total weld energy is specified. The plunge depth and total weld energy are now the limits on the system. Once the specified weld energy is generated, the welding tool would retract.

## Conclusions

From the results, it is found that a strong linear relationship exists between the energy generated during welding and the resulting tensile shear strength of the spot weld. Spot welds created at lower energies, above some threshold energy level, were significantly stronger than those created at higher energies. For 2 mm thick Al 6061 plate an optimal spot welding energy may exist between 4.2 kJ and 6.3 kJ. Using higher rotation rates in FSSW requires that they be combined with an appropriate dwell time to ensure a quality spot weld is created.

Monitoring the energy generated during welding may be used to develop an open-loop control system for FSSW. This system would work in a manner similar to FSSW position control (Figure 92) but would monitor the weld energy generated in lieu of specifying a dwell time. When some pre-determined weld energy limit is reached, the spot welding tool would retract. The future work of this project will be to develop an energy monitoring control system for FSSW. This control system has great potential for the application of FSSW in manufacturing.

## ROTATING ANVIL APPLICATIONS FOR FRICTION STIR SPOT WELDING

### Abstract

The rotating anvil for Friction Stir Spot Welding is investigated. First, the operation of the welding process is improved by implementing an open-loop force control system. Selecting axial force as the control variable resulted in a more repeatable process and improved the cycle time. Non-matched rotation rates between the welding tool and anvil are also investigated. There were no observed operational issues related to the difference in rotation rates but increasing the difference resulted in more energy input into the weld which weakened the weld joints. The rotating anvil is then used to create spot welds in a triple-lap joint using an aluminum-aluminum-aluminum and an aluminum-steel-aluminum joint configuration. The all-aluminum triple-lap joint resulted in a mechanically sound weld. The aluminum-steel-aluminum joint configuration was not as strong as the all-aluminum joint due to a lack of mixing between the aluminum plates with the steel plate. The strength of the aluminum-steel-aluminum configuration is greatly improved with the inclusion of a through hole in the steel sheet. The through hole allows metal from the weld zone in both the top and bottom plates to extrude into the volume of the through hole and forge together forming a solid weld locking the three plates together. Finally, a method of overlapping spot welds made using the RAFSSW process is presented as a viable alternative to fixed-gap bobbin tools for thin plate.

## Introduction

Automotive manufacturers continue to face issues related to creating light weight vehicles in an effort to improve fuel economy. Using lighter materials in the design of the structure such as aluminum in lieu of steel is one approach manufactures can take to reduce the weight of their vehicles. However traditional joining processes such as resistance spot welding are difficult to implement on metals like aluminum due to their higher thermal conductivity. Using technologies like self-piercing rivets affords manufacturers some of the same advantages of FSSW but adds to the overall complexity and weight of the design and increases the overhead for production.

Friction stir welding (FSW) was invented by Wayne Thomas at The Welding Institute (UK) in 1991. As a solid-state joining process capable of joining light-weight metals with lower melting points, FSW quickly received the attention of many researchers around the world. Friction Stir Spot Welding (FSSW) is a more recent application of the FSW process. The initial development of FSSW was performed by Sumitomo Light Metal Industries, LTD., Mazda, Kawasaki Heavy Industries, LTD., and Norsk Hydro. In 2003, Mazda implemented FSSW in the assembly of the rear door panel of their RX-8, the first noted application of the process [Mishra].

In FSSW, the joint is created by plunging a rotating tool into a weldment until the welding tool's shoulder reaches a desired penetration depth. It will remain at this plunge depth for a specified length of time, at which point the tool is retracted. Unlike fusion welding, FSSW does not melt the parent material, require consumables such as filler rod, shielding gas, or welding sticks, and uses 99% less energy to create the weld [Feldman]. For these reasons FSSW can be considered a "green technology". The FSSW process can

be characterized by three main parameters: rotation rate, plunge depth, and dwell time. Compared to the multitude of parameters involved in resistance spot welding, FSSW presents the operator with a simpler, more controllable process.

A pinless tool is capable of creating a quality spot weld in thin plate of Al 6061-T6 without the undesirable keyhole. Previous work also shown that implementing a rotating anvil for FSSW has the potential to present manufacturers with several advantages over the traditional FSSW process including increased joint strength, the ability to weld thicker workpieces, and a significant reduction in the process forces and torques acting on the welding frame.

In this chapter the application of the rotating anvil for FSSW is explored. The objective is to better understand and improve the process. An open-loop force control system for RAFSSW is created and evaluated for its potential to improve the process. The effect non-matched rotation rates between the welding tool and rotating anvil have on the joint strength and quality of the resulting spot welds is discussed.

The application of a rotating anvil can also be used to create weld joints that were not previously possible using FSSW including a triple-lap joint. The triple-lap joint consists of the three sheets in lieu of the standard two sheets and is beginning to see more application in the automotive industry. Acura has presented an alternative hemming method to join an aluminum-steel-aluminum triple-lap joint for the purpose of reducing the weight of their vehicles. The RAFSSW process will be evaluated for its ability to create quality spot welds in an aluminum-aluminum-aluminum and aluminum-steel-aluminum joint in this configuration. A variation of the aluminum-steel-aluminum triple-

lap joint with a through hole cut in the steel sheet is presented. In addition to the triple-lap joint an overlapping Friction Stir Spot Stich welding approach is presented.

## Experimental

Friction stir spot welds are made using the RAFSSW process on the VUWAL welding machine. The welding machine is a World War II era Kearney and Trecker vertical milling machine that has been retrofitted for FSW/FSSW. The rotating anvil was designed and built by members of VUWAL. The spot welds are made using different combinations of 0.040 and 0.080 inch thick plates of Al-6061-T6 and 0.060 inch thick plates of low carbon steel. The workpieces are sheared into 2 x 3 inch coupons for welding. Before welding the workpieces are scrubbed with a Scotch-Brite pad to remove any oxide layers and cleaned with a 50/50 mixture of methyl ethyl ketone (MEK) and toluene. Rigid fixturing is used to ensure that the weld samples do not shift relative to the work table at any point during welding. The pinless welding tool and rotating anvil are made of O1 tool steel with a maximum overall diameter of 1 inch featuring a scrolled, spherically tapered (convex) shoulder of 3 inch radius (of curvature) with a 0.4 inch flat (See Chapter VI).

## Results and Discussion

### *Force Control*

The FSSW research presented in this work thus far has utilized an open-loop position control system. This position control system works by first establishing a zero-point

defined by the vertical location of the welding tool when it makes sufficient contact (measurable axial load e.g. 200 N) with the workpiece. This position is recorded by the system and the plunge depth is added to this to ensure proper tool penetration into the workpiece during welding. Obtaining the zero-point location for the welding tool is required for each spot weld due to unknown variation in workpiece thickness ( $\pm 0.004$  inch). Each zero-point location is measured multiple times to ensure an accurate measurement. The acquisition of the zero-point for each spot weld adds time (in excess of several minutes) to the welding operation. This type of control system is typically used due to its ease of use and operation [Tozaki]. However using this position control system for the RAFSSW process was burdensome and sometimes unreliable due to the mechanical system (spring support) that is used to implement the rotating anvil. The position control system works by monitoring the vertical orientation of the tool during the plunge stage of the spot welding process. When the vertical orientation matches the desired plunge depth the vertical motion of the plunge stage is halted and the weld is created.

The variation in the axial force and weld height can be seen in Figures 99 and 100 respectively for three spot welds made using the rotating anvil in Chapter V. The axial force can be seen to have a standard deviation of  $\pm 544.7$  N for these spot welds made at identical welding parameters. This variation in the axial force is related to the reliability of the welding system position monitoring system. The variation in the weld height can be seen to overshoot the desired weld position by as much as 28% (0.0022 inch). This distance can be significant when the plunge depth is specified to be 0.008 inch and the thickness of the top sheet is 0.040 inch (5.5% of the thickness) (Figure 100). This



overshooting of the desired weld height is a result of both the motor that controls the vertical motion of the weld table and the temperature of the workpiece during welding. Inaccuracy in the measurement of the zero-point location can also result in poor control over the desired penetration depth. The issue with the control system may not be completely in the open-loop architecture itself but rather with the selected controlling variable, position.

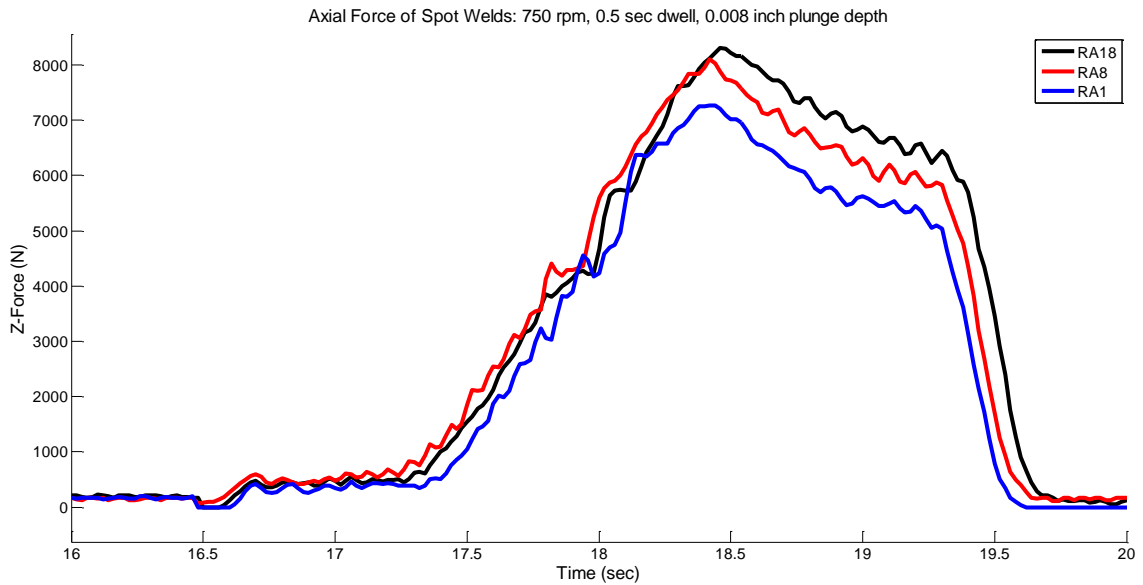


Figure 99: Axial force during RAFSSW with position control. The desired plunge depth is 0.008 inch. The maximum axial force of RA1 is 6080 N, of RA8 is 6710 N, and of RA18 is 7140 N.

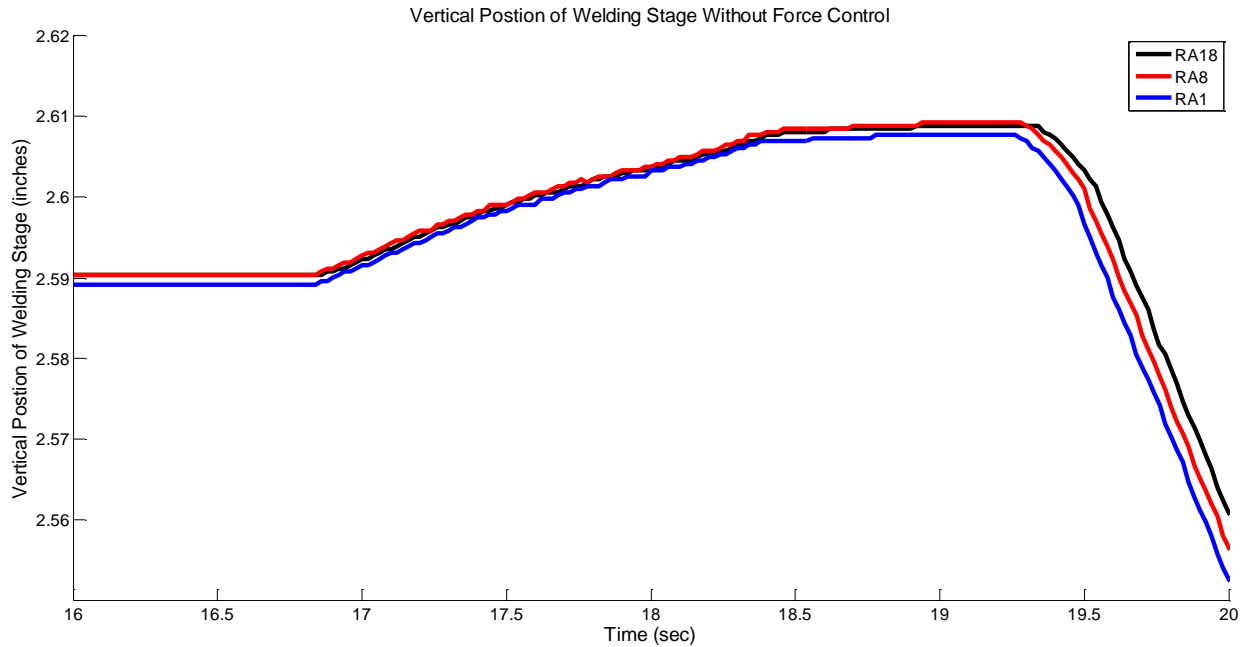


Figure 100: Vertical position of welding stage during a friction stir spot weld (rotating anvil) without force control. RA1 overshoot the desired plunge depth by 0.0018 in (23%), RA8 by 0.0022 in (28%), and RA18 by 0.0018 in (23%)

As an alternative to monitoring the position of the welding tool, the axial force acting on the welding frame may be used as the control variable. The force control system used in this experiment will also be an open-loop control system. In this case however, during the plunge stage of the welding process the axial force acting on the welding frame will be monitored. When the desired cut-off force is measured the plunge stage will be halted and the spot weld will be made. Previous research on single-sided FSSW has shown a strong linear dependence of axial force on the plunge depth during welding (Figure 101) i.e. controlling the axial force effectively controls the plunge depth during welding. The main advantage of using axial force as the controlling variable is that it will not require that a zero-point location be obtained before each spot weld which greatly improves the cycle time of the process.

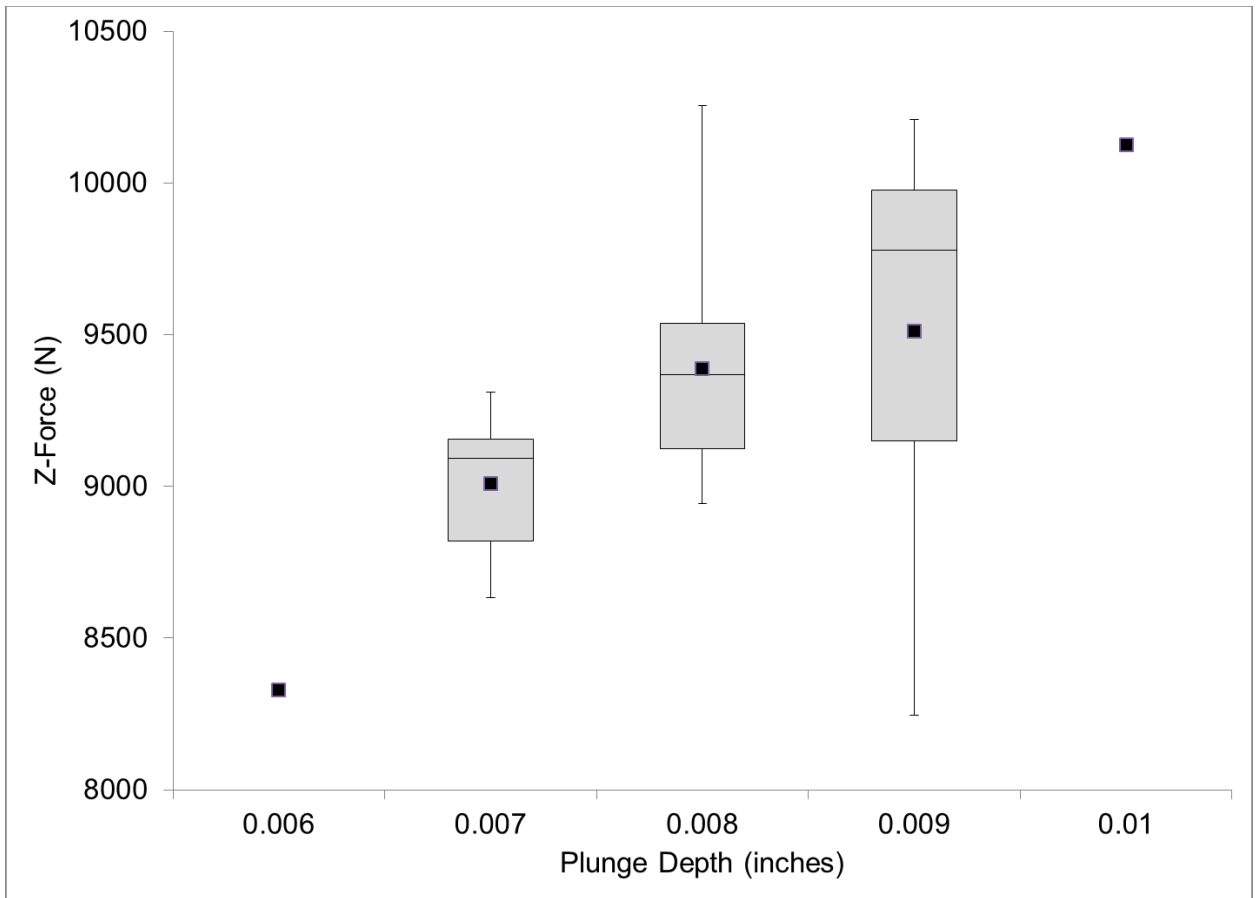


Figure 101: Z-Force vs. Plunge Depth. An increase in the plunge depth resulted in a linear increase in the axial force acting on the welding frame. The weld data for this plot is from the experiments performed in Chapter IV.

The variation in the axial force and weld height can be seen in Figures 102 and 103 respectively for the spot welds made using the open-loop force control system. The axial force can be seen to have a standard deviation of  $\pm 136.6$  N for these spot welds made at identical parameters. The run-to-run variation in axial force is significantly improved by using the axial force as the controlling variable. There is no variation in the vertical position of the welding table for spot welds RAFC8 and RAFC9. The vertical position data for spot weld RAFC5 is not reported in Figure 103 as its position data relative to the

weld study was compromised by a necessary reset of the power to the welding machine between experimental runs. The improvement in the run-to-run variation can largely be credited to the elimination of the need to reliably obtain an auto-zero point before each spot weld. If the location of the zero-point could be more reliably measured an open-loop position control system may be more accurate, but it would still require a separate measurement before each spot weld is created.

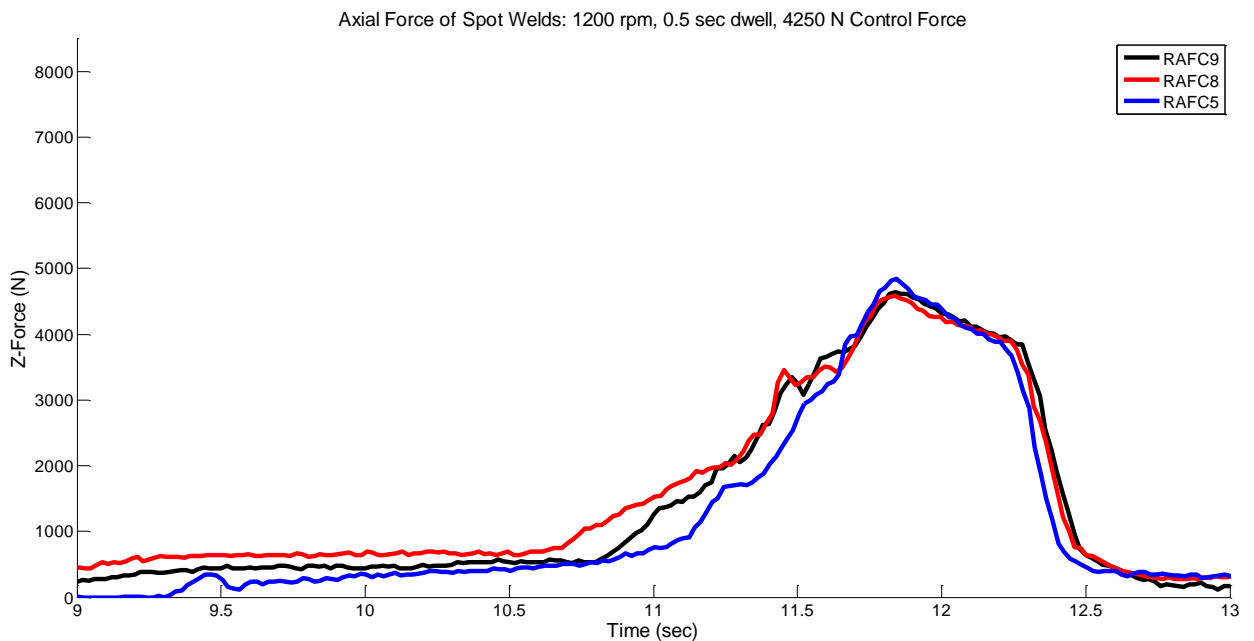


Figure 102: Axial force during RAFSSW with force control. The cut-off force is 4250 N. The maximum axial force of RAFC5 is 4645 N, of RAFC8 is 4581 N, and of RAFC9 is 4843 N. RAFC5 exceeded the cut-off force by 9%, RAFC8 by 8%, and RAFC9 14%.

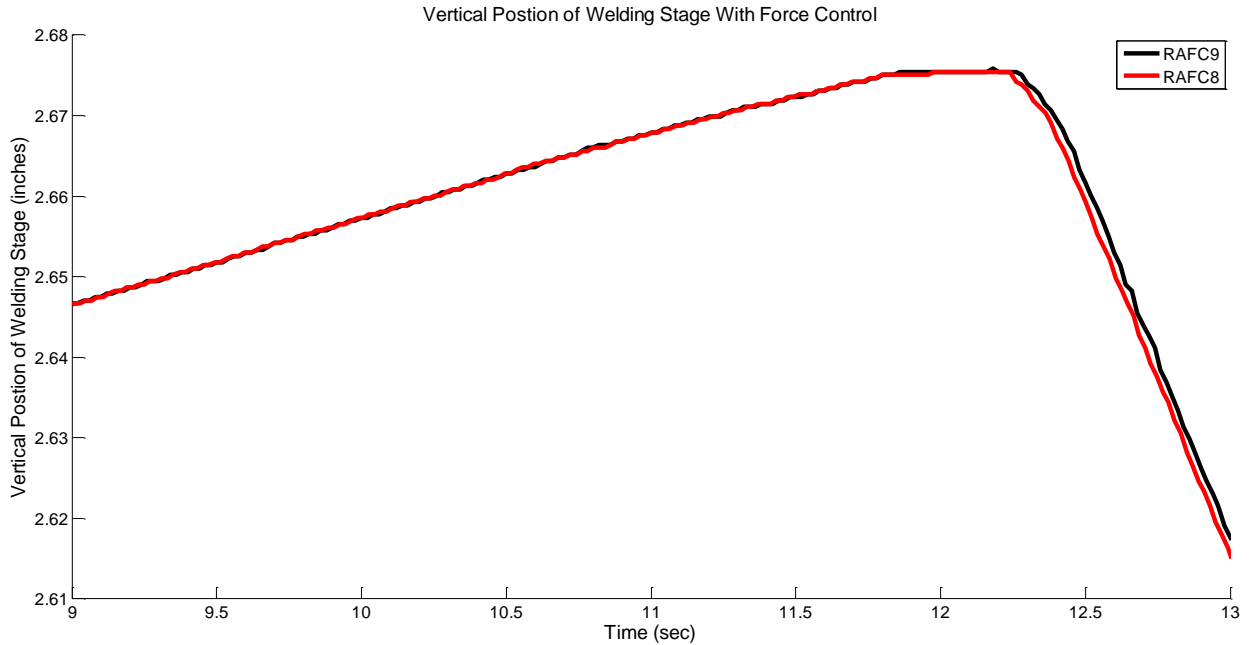


Figure 103: Vertical position of welding stage during a friction stir spot weld (rotating anvil) with force control.

During the plunge stage of the spot welding process the vertical position of the workpiece or axial load on the welding frame is constantly monitored for the respective open-loop control system being implemented. Within the welding code is an “if statement” that, when the desired weld height / axial load is reached, sends a command message to the vertical control motor to stop motion. Because the vertical motor requires some time to receive the command and then stop (not instantaneous) the weld table is able to continue on its original path due to the inertia of the welding table. This results in both the welding tool and rotating anvil penetrating deeper into the workpiece than desired. This effect can be exacerbated by the temperature of the workpiece. As the workpiece heats up it loses some of its mechanical strength (becoming softer) allowing the welding tool and rotating anvil to penetrate even further into the workpiece. This type of overshoot could possibly

be mitigated by implementing a feedback control system using either position or axial load as the feedback signal. Feedback control may be difficult to implement due to the short time scale and transient nature of the spot welding process.

#### *Non-Matched Rotation Rates*

The initial work on double-sided spot welding has only considered matched, or identical, rotation rates for the FSSW tool and rotating anvil. Here, the effect of non-matched rotation rates on the energy input and tensile shear strength of the resulting spot welds is investigated. A baseline matched rotation rate of 1200 rpm is used for the analysis. The anvil will be rotated at 1200, 1500, and 1800 rpm while the welding tool will have a constant rotation rate of 1200 rpm for each case in this experiment. The experimental results can be seen in Table 11.

Table 11: Experimental results for the non-matched rotation rates for the FSSW tool and rotating anvil.

Rotation Rate (rpm)		Dwell Time	Welding Energy (kJ)			Strength (kgf)
FSSW Tool	Anvil		FSSW Tool	Anvil	Total Energy (kJ)	
1200	1200	0.5 (sec)	6.07	2.24	8.32	262.20
1200	1500	0.5 (sec)	7.17	3.63	10.8	223.83
1200	1800	0.5 (sec)	8.59	5.12	13.71	194.34

The effect the non-matched rotation rate of the anvil has on the tensile shear strength can be seen in Figure 104. The rotation rate of the anvil is found to be inversely proportional to the tensile shear strength of the spot weld. The effect the non-matched rotation rate has on the spot weld energy can be seen in Figure 105. The rotation rate of the anvil is found to be proportional to the spot weld energy during welding. The spot welding energy is calculated by multiplying the measured weld torque signal rate by the spindle speed

(rad/sec) and then integrating that signal. Each data point in the resulting integrated signal is then summed to provide the total weld energy. The tensile strength is inversely proportional to the calculated weld energy (Figure 106). Previous work has shown that too much energy is detrimental to weld strength and can lead to over mixing and defect formation along the joint line.

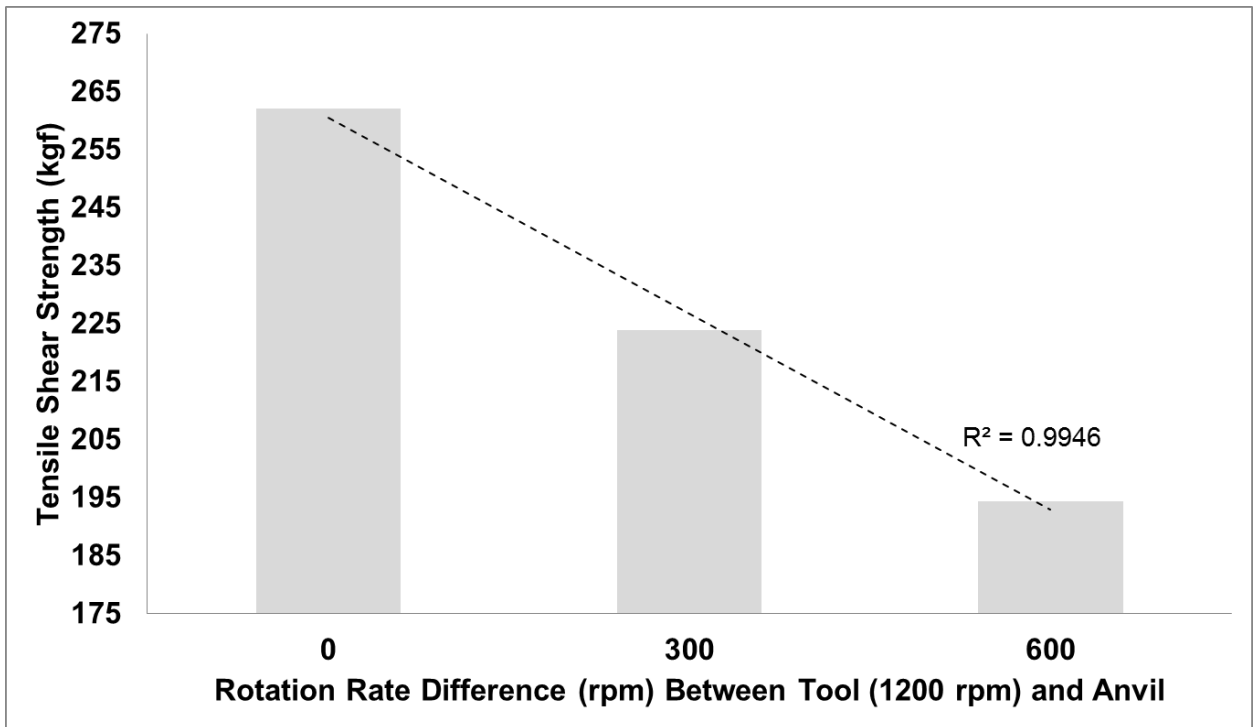


Figure 104: Tensile shear strength of spot welds made using non-matched rotation rates between the FSSW tool and rotating anvil. The rotation rate of the FSSW tool for all cases was 1200 rpm. The rotating anvil had rotation rates of 1200 (0 rpm difference), 1500 (300 rpm difference), and 1800 (600 rpm difference).

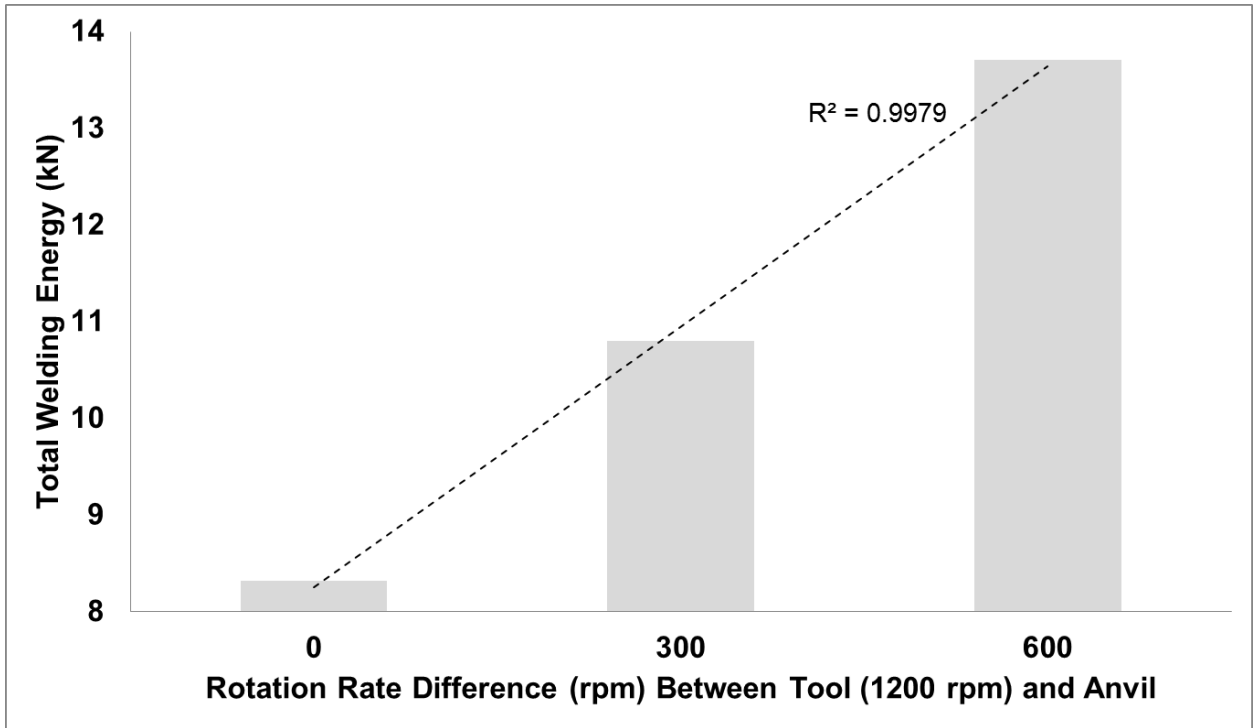


Figure 105: Total spot weld energy of spot welds made using non-matched rotation rates between the FSSW tool and rotating anvil. The rotation rate of the FSSW tool for all cases was 1200 rpm. The rotating anvil had rotation rates of 1200 (0 rpm difference), 1500 (300 rpm difference), and 1800 (600 rpm difference).



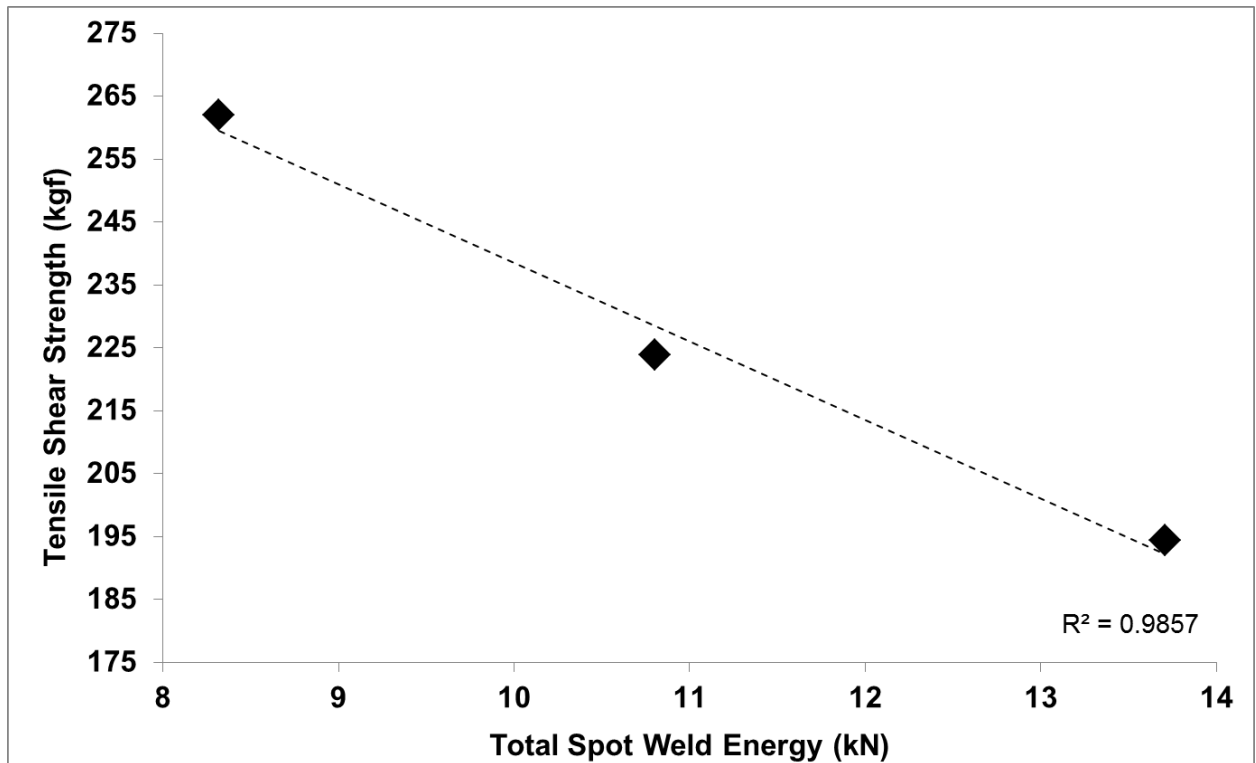


Figure 106: Tensile shear strength (kgf) vs. total spot weld energy (kN). Increase in weld energy results in a decrease in joint strength.

The difference in the energy generated by the FSSW tool and rotating anvil is significant. For the matched case the rotating anvil input 36% as much energy as the welding tool. Increasing the rotation rate of the anvil by 300 and 600 rpm increased this percentage to 50% and 60% respectively. This difference may be a result of the welding operation itself. Because the welding tool engages the workpiece first it encounters cold (room temperature) metal. Previous work has shown the welding torque acting on the tool is inversely proportional to the temperature of the workpiece (low temperature == higher torque) [Sinclair]. When the rotating anvil makes contact with the workpiece it may be as much as 100°C hotter than room temperature depending on the selected process parameters. Additionally, the welding tool is used to compress the springs that support

the workpiece so that the rotating anvil can make contact with the workpiece. This step of the operation increases the welding tool's contact time with the workpiece. When the spot weld is complete, the welding tool retracts but still remains in contact with the workpiece until the support springs are relieved, furthering the tool's contact time with the workpiece. In this welding operation's current state, it is estimated that the rotating anvil would need to be rotated 238% faster (2848 rpm) in order to match the energy input of welding tool assuming the trend observed holds true for greater differences in rotation rate. It is not yet known if matching the energy input between the FSSW tool and rotating anvil is required for ensuring weld quality.

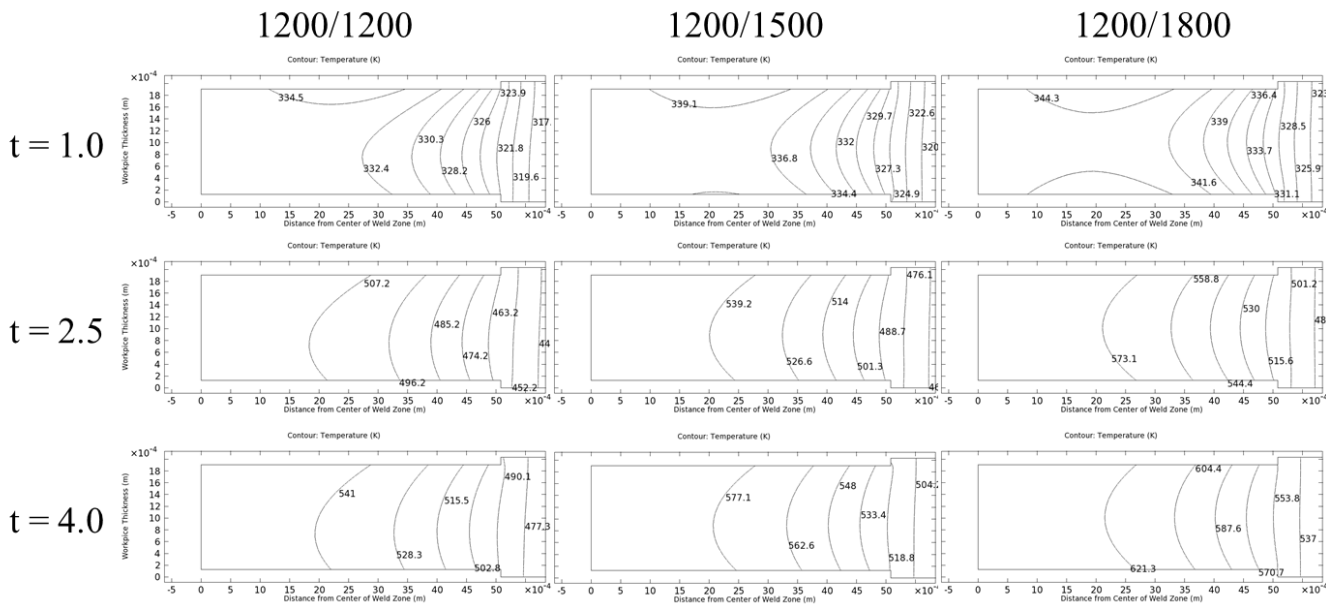


Figure 107: Numerical simulation results of the double-sided FSSW process showing the temperature contours within the workpiece during welding using non-matched rotation rates.

The numerical simulation created in Chapter V is used here to investigate the temperature contours within the workpiece during welding. In Chapter V it is assumed that the

welding tool and rotating anvil have identical power inputs. To calculate the power input using the weld power method the maximum measured torque during spot welding is multiplied by the spindle speed (rad/sec). For the matched case (1200/1200 rpm) the maximum weld torque for the welding tool and rotating anvil are 20.39 Nm and 10.91 Nm resulting in a power input of 2562.3 W and 1371.0 W respectively. For the non-matched case of 1200/1500 rpm the maximum weld torque for the weld tool and rotating anvil were 20.07 Nm and 12.11 Nm resulting in a power input of 2522.1 W and 1902.2 W respectively. For the non-matched case of 1200/1800 rpm the maximum weld torque for the weld tool and rotating anvil were 19.94 Nm and 13.42 Nm resulting in a power input of 2505.7 W and 2529.6 W respectively. These weld power calculations are defined along the appropriate boundary within the simulation. The effect this has on the temperature contour within the workpiece can be seen in Figure 107. It can be seen that the temperature contour for the 1200/1200 rpm and 1200/1500 rpm case are not symmetric through the thickness of the workpiece as originally thought. The 1200/1800 rpm case resulted in a symmetric temperature contour throughout the workpiece and is indistinguishable from the appearance of the results presented in Chapter V.

From a welding machine operator's perspective, spinning the anvil at a non-matched rotation rate did not affect the performance of the welding machine. No instability was observed with the spot welding device. Because the maximum torque acting on the welding tool is greater than the torque acting on the rotating anvil there is a net torque acting on the welding frame. For an articulated robotic application any net torque acting on the frame would need to be considered as it could affect the compliancy of the robot. Actuating the position of the welding tool and rotating anvil independently

of the workpiece may allow for a more symmetrical loading of the welding system. This may also help with balancing the energy generated by the welding tool and rotating anvil.

### *Triple-Lap Joint Welding*

The rotating anvil process has the capability of joining three metal sheets in a lap joint configuration. This configuration would be impossible using a pinless tool with single-sided FSSW without making multiple spot welds. The “triple-lap” joint is beginning to see application in the automotive industry today. For example, Acura is creating an Al-Steel-Al joint for the purpose of weight reduction with a 2-fold hemming process called “3D Lock Seam”. The previous iteration (original) of this joint was Steel-Steel-Steel and was created with a resistance spot weld (Figure 108). Resistance spot welding is not able to create a joint in the Al-Steel-Al configuration due to the 1) dissimilar joint and 2) higher thermal conductivity of aluminum. By replacing steel components on the door paneling of the 2014 Acura RLX they hope to improve fuel economy by means of a weight reduction of around 17% per door and better handling dynamics. There are plans to roll this technology out to the more popular Honda line of automobiles in the near future [Vijayenthiran].

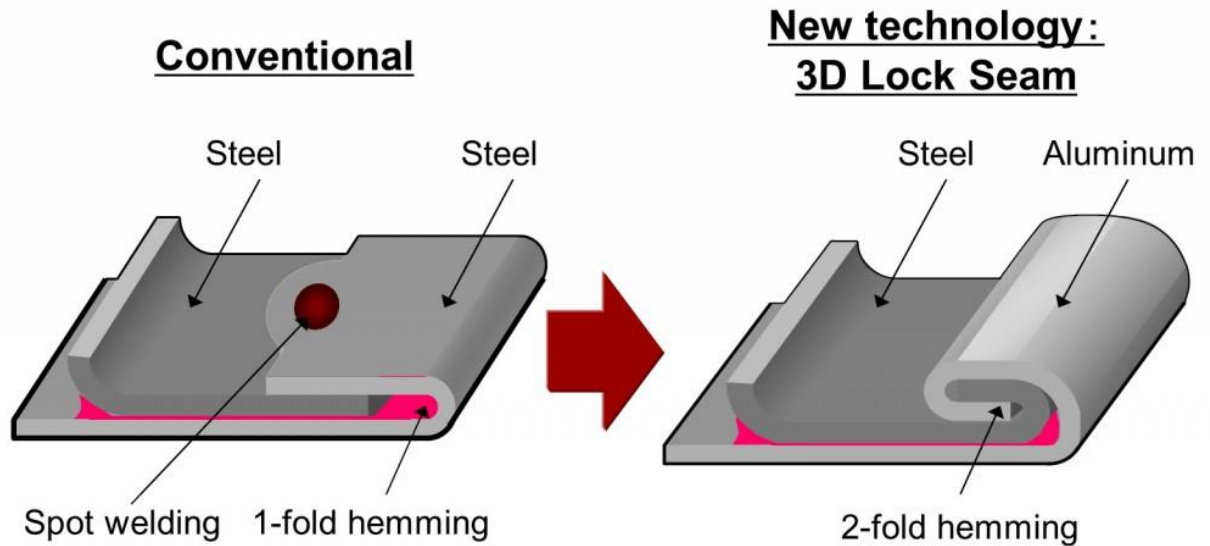


Figure 108: Acura's "3D Lock Seam" technology created to join Al-Steel-Al in a triple-lap joint configuration.

The proposed triple-lap joint will be performed using the RAFSSW process using an all-aluminum joint (Al-Al-Al) and an aluminum-steel-aluminum joint to replicate the configuration being implemented on the 2014 Acura RLX. For this experiment, for the aluminum plates Al 6061-T6 will be used and for the steel plate general low-carbon steel will be used. For the Al-Al-Al case the top and bottom sheets of aluminum are 0.040" thick while the middle aluminum sheet is 0.080" thick. For the Al-Steel-Al case the top and bottom sheets of aluminum are 0.040" thick while the middle sheet of low-carbon steel is 0.060" thick (Figure 109). For the spot welds in this experiment both the welding tool and rotating anvil have a rotation rate of 1200 rpm, a plunge rate of 0.5 inches per minute and a 1 sec dwell time period. An open-loop force control method is used with a cutoff axial force of 4500 N. All three of the sheets for the workpiece are scrubbed with a Scotch-Brite pad to remove any surface oxide layers or any other possible contaminant.

The sheets are cleaned with a 50/50 solution of MEK (methyl ethyl ketone) and toluene prior to welding.



Figure 109: Triple-lap joint configuration used for the Al-Al-Al and Al-Steel-Al spot welds.

The tensile shear strength of the resulting all-aluminum triple-lap joint was 633.87 kgf. An additional spot weld made at identical welding parameters was cross-sectioned and etched using Keller's reagent for further analysis (Figure 110). Both the top and bottom plate can be seen to be welded to the thicker middle sheet. The material within the weld zone of the middle plate is mechanically displaced enough to form an interlocking bond with the top and bottom sheet (Figure 111). The stir zones created by the welding tool and rotating anvil are separate and distinct zones. The weld zone does not completely penetrate the triple-lap joint.

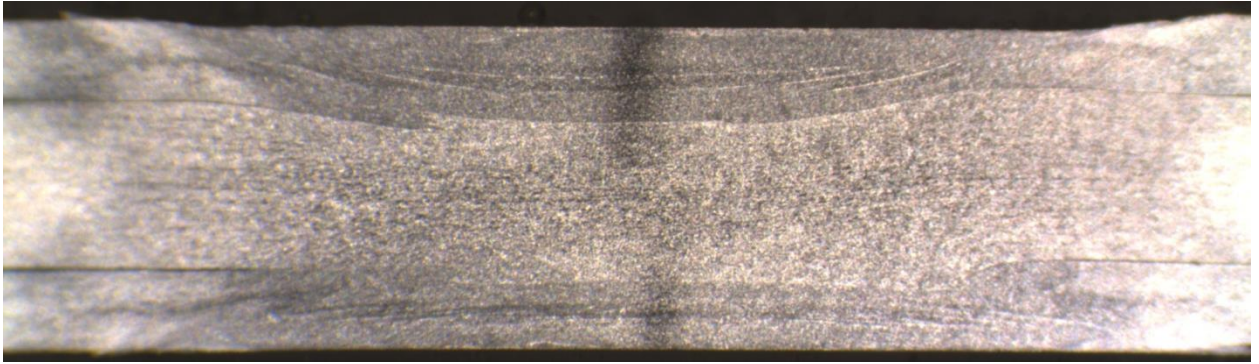


Figure 110: Macrosection of an Al-Al-Al triple lap spot weld made using RAFSSW.

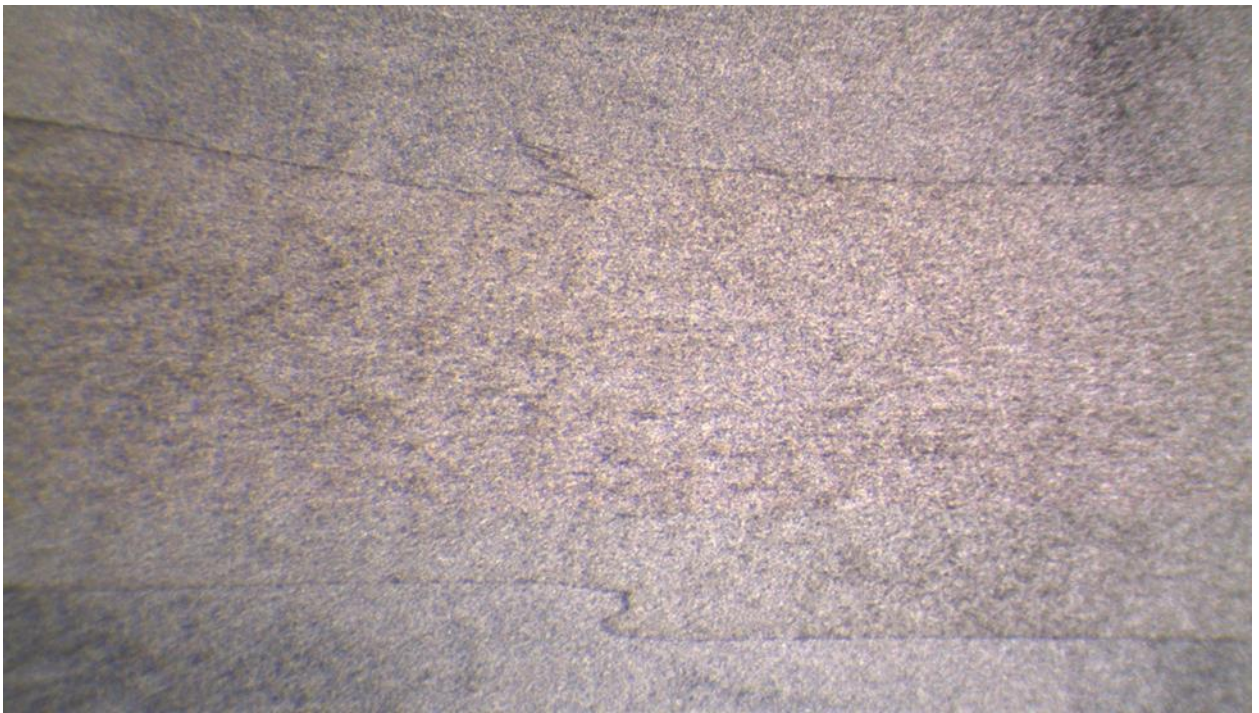


Figure 111: Interlocking of the top and bottom plate with the thicker middle plate of an Al-Al-Al triple-lap joint made using the RAFSSSW process.

The tensile shear strength of the resulting Al-Steel-Al triple-lap joint was 324.16 kgf. Like with the all-aluminum joint, an additional spot weld made at identical welding parameters was cross-sectioned for inspection (Figure 112). Unlike the all-aluminum joint, there does not appear to be any mechanical interaction (mixing) between the top

and bottom aluminum sheet with the middle steel sheet. The stir zone only appears to extend through the aluminum sheets. If the steel *is* mechanically affected by the welding process it may only be on the surface of the weld interface. The rotation of the weld zone in the aluminum combined with the axial force and elevated welding temperatures within the weld zone may be enough to form a clean surface on the steel sheet allowing the welded aluminum to create the bond [Tran]. A similar spot welding process using an FSSW tool with a pin (that does not penetrate the steel sheet) is currently being used by the Mazda Motor Corporation to join a 6XXX series aluminum alloy to steel in a traditional lap joint configuration. A closer view of the weld interface shows that there is no mechanical interlocking between the sheets (Figure 113).

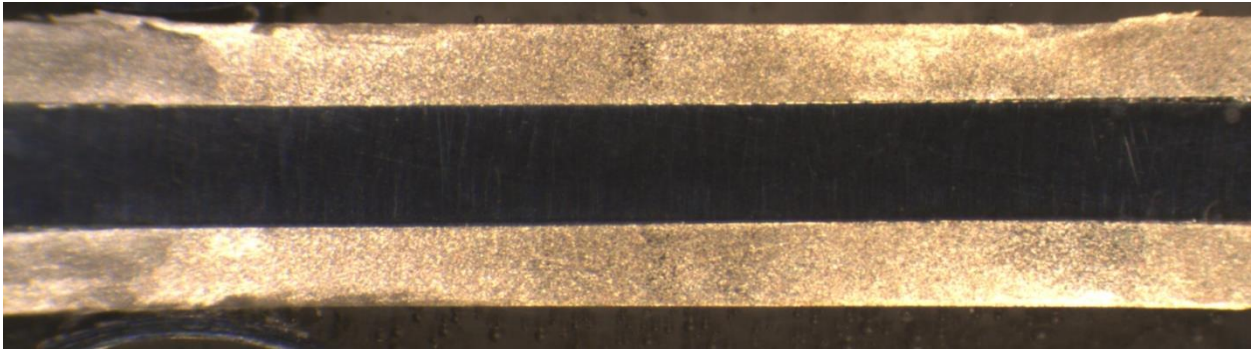


Figure 112: Al-Steel-Al triple lap spot weld with RAFSSW



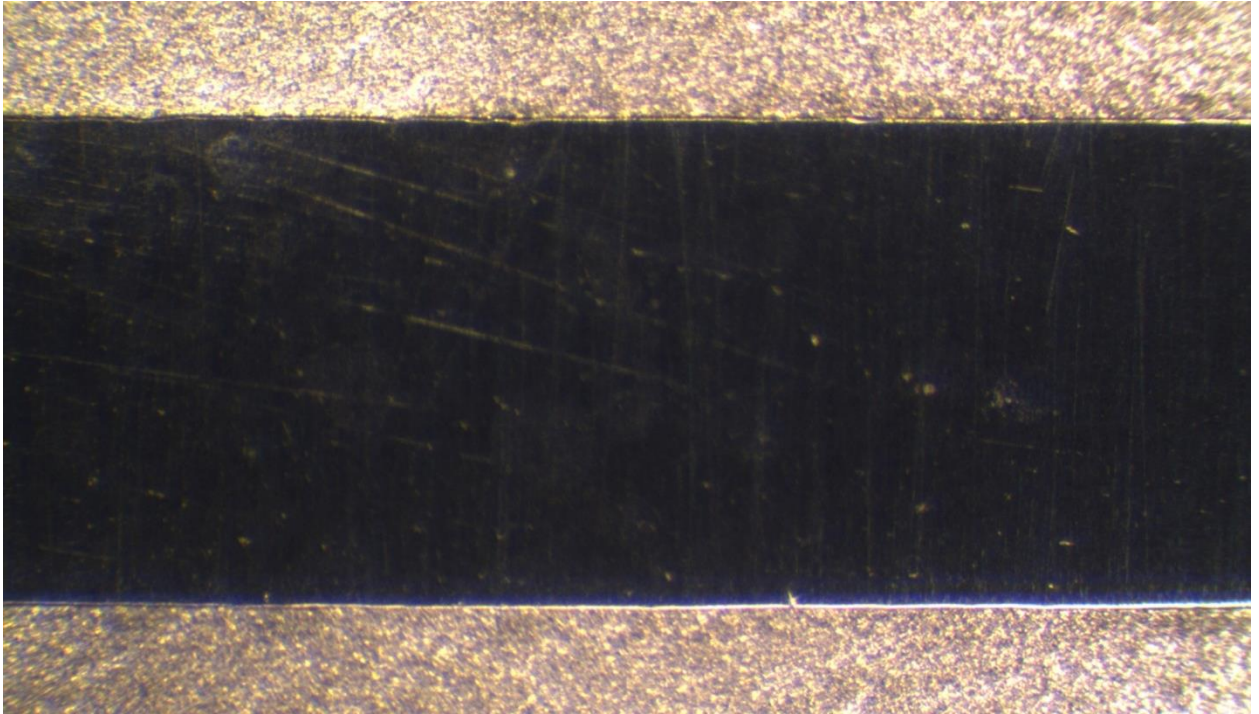


Figure 113: No mixing or mechanical interlocking was observed for the Al-Steel-Al RAFSSW joint.

The middle sheet in the triple-lap joint acts a “substrate” of sorts for which the top and bottom sheets are welded to. For the observed case where the weld zones created by the welding tool and rotating anvil don’t intersect the middle sheet could potentially be any thickness required by the application.

For comparison, a spot weld made using the RAFSSW process on 0.080 in thick workpieces (an identical total workpiece thickness of 0.16 in) using only two plates had a tensile shear strength of only 54.20 kgf. In both cases (triple-lap and 0.080 in thick plates) the process is not yet optimized. However the results can be used to help understand the interaction of the weld zones. At the selected parameters the RAFSSW process did not create a quality spot weld in the 0.080 in thick workpiece because of the increased depth of the joint interface. Meaning at the selected welding parameters there is not sufficient

material displacement, weld zone temperatures, forging load, etc. required to create a quality weld joint at the great of depth. Even though the total weld joint thickness is identical, the strength of the triple-lap joint is significantly stronger due to the fact that the joint interface is only 0.040 inches below the surface of the welding tool / workpiece interface where the resulting weld zone is sufficient for creating a quality joint.

For both the Al-Al-Al and Al-Steel-Al joints the results of the process may be improved by increasing the cutoff force used for the control system. A higher axial load would result in deeper tool and anvil penetration creating a physically larger spot weld. This would perhaps benefit the Al-Steel-Al joint more if in fact the joint is created by bonding the aluminum to a “clean” steel surface as reported by Tran et al [Tran].

#### *Al-Steel-Al With Through Hole*

The application of a pinless tool to join aluminum to steel using FSSW is not reported in the literature, perhaps in part due to its inability to displace the steel sheet into the aluminum sheet creating an interlocking weld joint. Bozzi et al reported excellent spot weld joint strength (458 kgf) joining aluminum to steel using an FSSW tool with a pin that did penetrate into the steel sheet. The improved joint strength can be attributed to the displacement of the steel sheet into the aluminum sheet forming the interlocking joint (Figure 114). However this approach leaves the manufacturer with a keyhole that may need to be removed or filled post weld depending on the application. Additionally, because the welding tool penetrates the steel sheet the material used to construct the tool needs to be tougher to avoid issues with tool wear [Prater]. The welding tool used by Bozzi et al. to join the aluminum to steel was made of a tungsten rhenium alloy. Using a

pinless FSSW tool to join aluminum to steel would benefit the manufacturer by 1) eliminating the unwanted keyhole and 2) allow the FSSW welding to be constructed of easier to machine and less expensive tool steel because of the fact that the welding tool never makes contact with the steel.

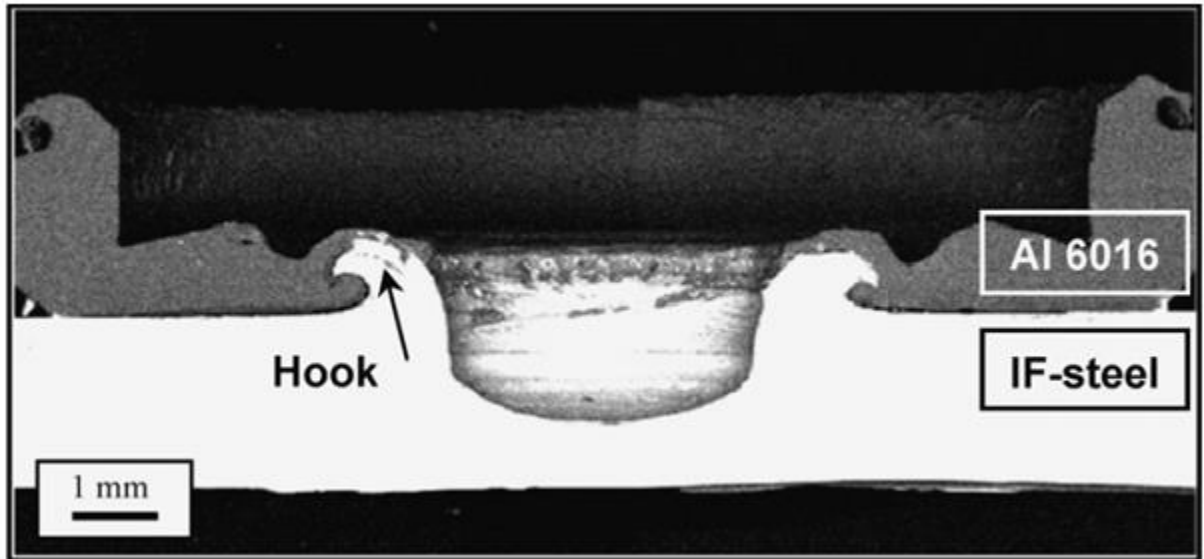


Figure 114: Cross section of an aluminum to steel FSSW spot weld using a tool that penetrates into the steel sheet [Bozzi]

The concept of a creating a “through hole” in the steel sheet was inspired in part by a combination of the friction stir forming (FSF) process and an unintended experimental result. In FSF a non-consumable tool of the same type as that used in FSW is pressed along a workpiece which has been placed on a die. As the tool moves, the friction stir process occurs and the workpiece flows into the die under the workpiece as a result of plastic flow. The shape of the die is transferred to the workpiece, or the workpiece and the die are mechanically fastened by the “anchor effect” [Nishihara]. The unintended experimental result occurred when the FSSW process (single-sided) was performed on a

0.125 inch thick piece of aluminum (6061-T6) for a temperature measurement using a pinless tool. The aluminum sheet was unintentionally positioned in such a way that placed the weld zone directly over a threaded hole in the anvil. When the weld was complete the workpiece appeared to be “stuck” to the anvil. Upon further investigation it was found that the plastically deformed aluminum had extruded into the threaded hole creating an aluminum “screw” extrusion (Figure 115). The result was that the aluminum plate had to be “unscrewed” from the support anvil.

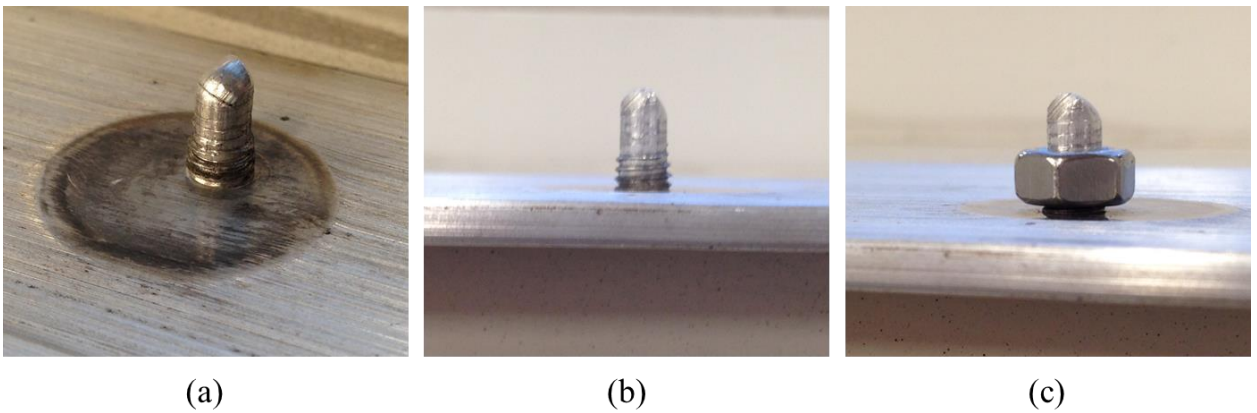


Figure 115: Aluminum plastically deformed into the threaded hole. a) top view of extruded weld zone material b) side view of threads c) side view with a standard nut attached to the threads.

A drawing of the proposed through hole method can be seen in Figure 116. The concept is that during the RAFSSW process the plastically deformed metal within the stir zone of the top and bottom aluminum sheets will flow into the through hole and forge together creating a solid-state aluminum joint that effectively locks the aluminum plates into the steel via the through hole. The resulting joint will join the three sheets (Al-Steel-Al) in a manner similar to a mechanical fastener such as a rivet. The potential advantages of this

process over mechanical fasteners are a reduction in vehicle weight, production overhead (no rivets), and process time.

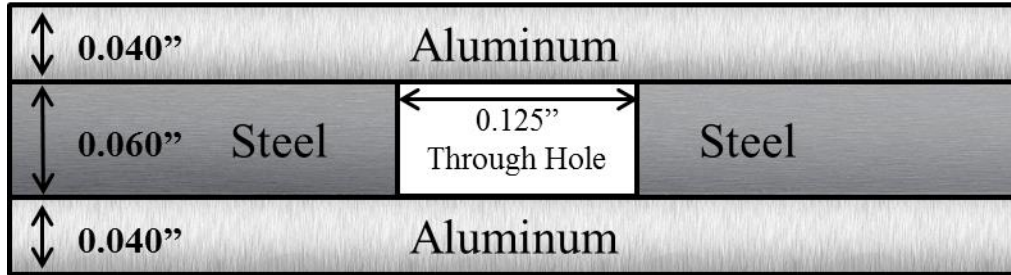


Figure 116: The proposed through hole method. A 0.125 inch hole is punched in the steel directly in line with the RAFSSW weld zone. The size, location, and orientation may be altered.

The experimental through hole joint will be performed using the RAFSSW process. Al 6061-T6 will be used for the top and bottom aluminum plates and low-carbon steel for the middle steel plate. The top and bottom sheets of aluminum are 0.040” thick while the middle sheet of low-carbon steel is 0.060” thick. For the spot welds in this experiment both the welding tool and rotating anvil have a rotation rate of 1200 rpm and a plunge rate of 0.5 inches per minute. Prior to welding all three of the sheets for the workpiece are scrubbed with a Scotch-Brite pad to remove any surface oxide layers or any other possible contaminant. The sheets are cleaned with a 50/50 solution of MEK (methyl ethyl ketone) and toluene before welding. An open-loop force control system is used.

The diameter of the through hole is selected by comparing the volume of the through hole (the void to be filled) to the volume of the weld zone of the top and bottom plates (the material to be extruded). If the hole is too large then it will not be possible for the extruded aluminum to fill the void. The volume of both the through hole and weld zones are assumed to be cylindrical. The diameter of the weld zone is taken to be 0.4

inches (the diameter of the flat of the weld tool) with a height of 0.004 inches (the thickness of the aluminum workpieces). The diameter of the through hole is varied for the calculation between 0.031 – 0.50 inches with a height of 0.06 inches (the thickness of the steel plate). A comparison of the through hole volume to the volume of the available material to be extruded can be seen in Figure 117. For this experiment a through hole diameter of 0.125 inches is selected (7.32% of the volume of the available weld zone material).

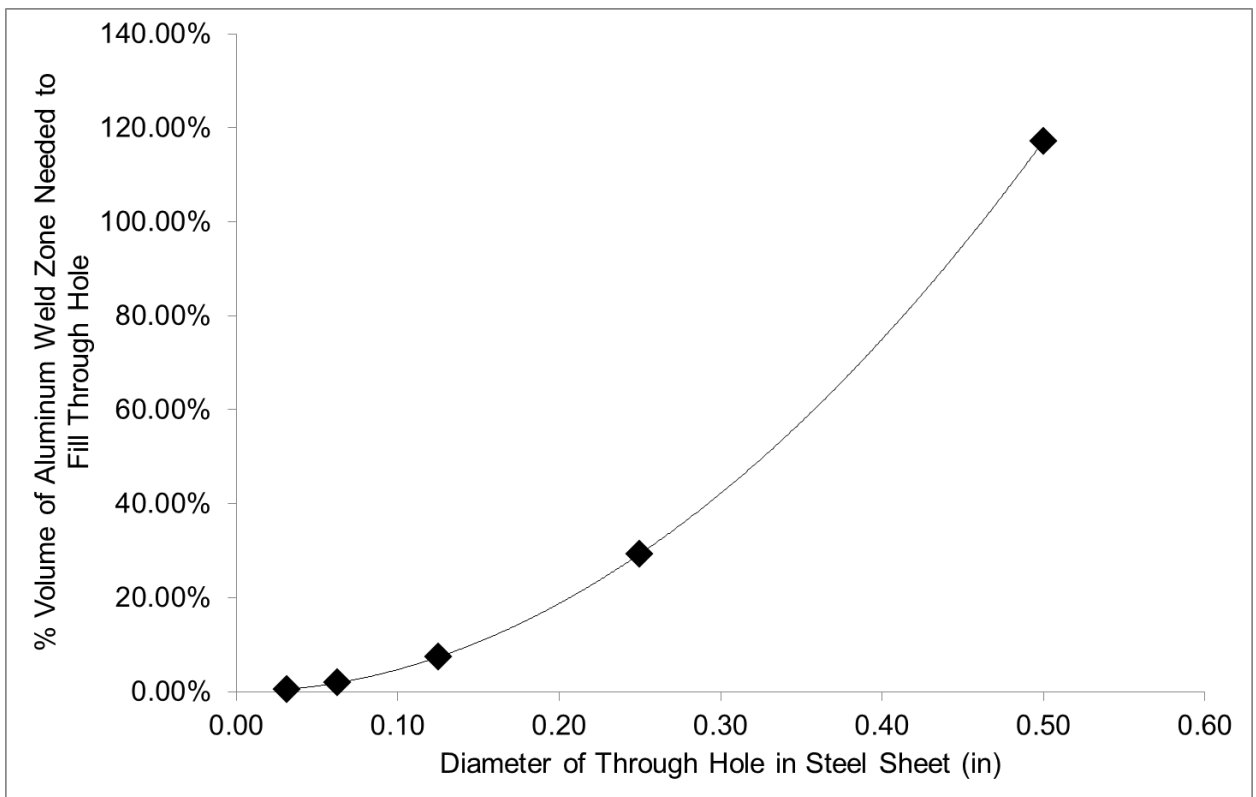


Figure 117: % Volume of the available material to be extruded into the through hole according to the selected diameter of the through hole.

Two cases are considered for the inclusion of a through hole. To obtain a baseline comparison of strength and weld appearance, the Al-Steel-Al triple-lap spot weld from

the previous section is used. For the first case the 0.125 inch through hole is centered along the axis of the welding tool and rotating anvil. The second case investigates the effect of offsetting the through hole 0.125 inches off of the axis of the welding tool and anvil. For both cases a dwell time of 1 sec and a control force of 4250 N are used. The tensile shear strength of these through hole spot welds can be seen in Figure 118. At the selected parameters the inclusion of the through hole resulted in a decrease in strength by 29% and 67% for the centered hole and offset hole respectively. Macrosection analysis of the spot weld reveals that the reduction in strength is caused by a lack of material filling the volume of the through hole (Figure 119). The extruded material within the through hole is insufficient for the solid state weld to form between the top and bottom plates. The decrease in joint strength may be a result of a decrease ( $\approx 20\%$ ) in the available bonding surface between the aluminum and steel sheets. Increasing the dwell time to 1.5 seconds resulted in an increase of joint strength by 11% (Figure 118). The material from within the weld zones is observed to have extruded into the through hole.

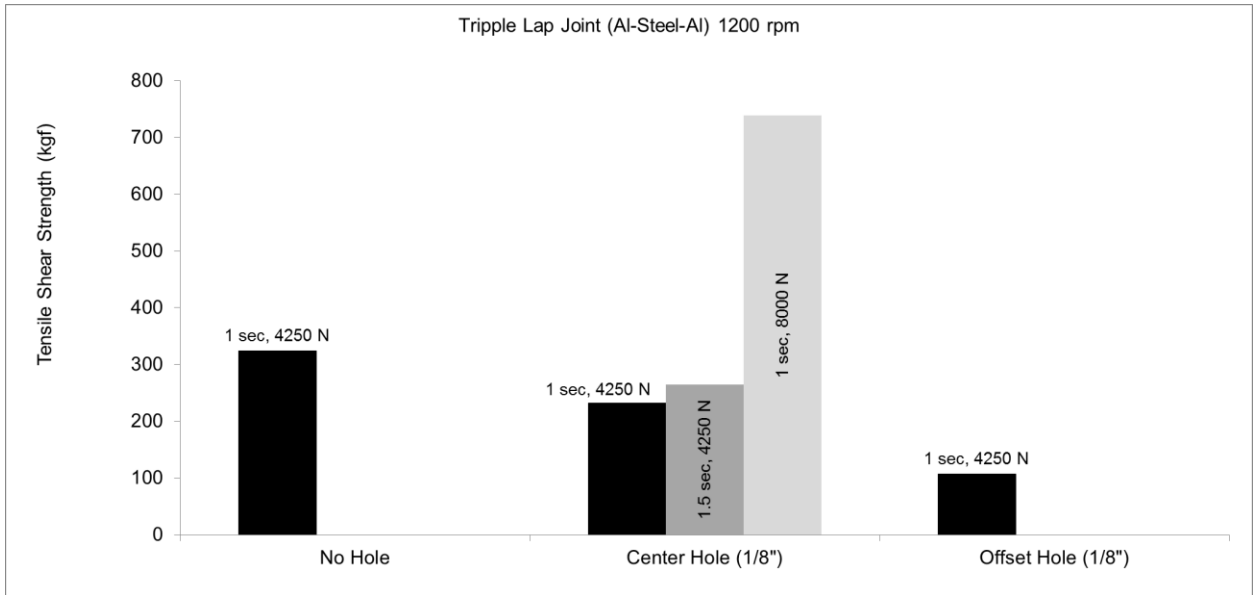


Figure 118: Tensile shear strength of spot welds made using the through hole with the RAFSSW process. Three cases are presented; no hole, center hole, and an offset hole. The dwell time and control force for each case are listed above (or within) their respective case. For all cases the welding tool and anvil had a rotation rate of 1200 rpm.

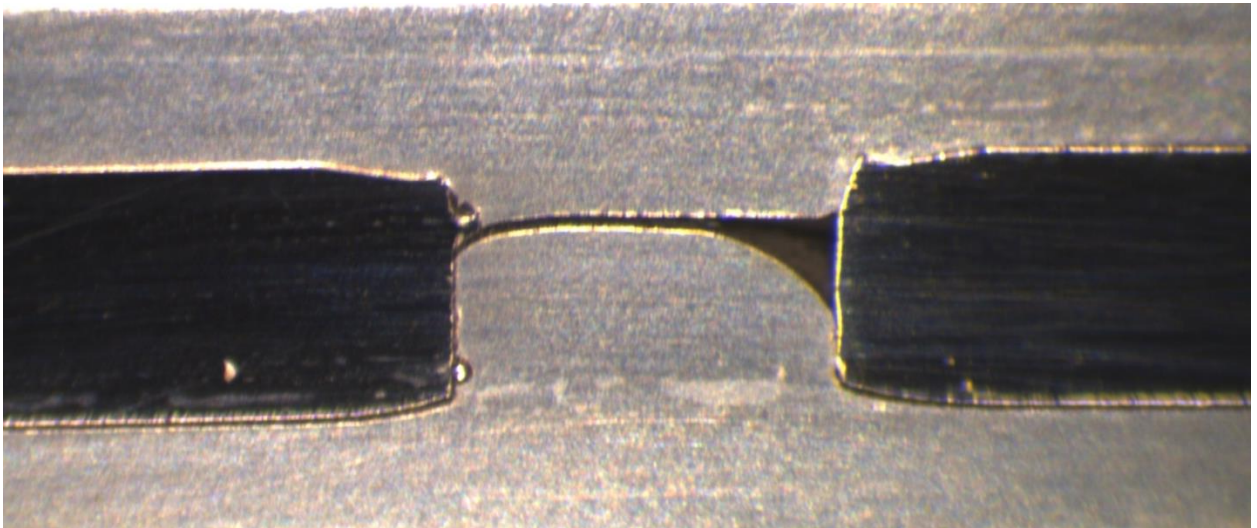


Figure 119: Al-Steel-Al with a through hole. 1200 rpm, 1 sec, 4250 N control force. The extruded material has not completely filled the volume of the through hole. No weld joint is formed.



Based upon the observations of the initial experiments the cutoff control force was increased to 8000 N in an attempt to better fill the void of the through hole and create a solid state bond between the aluminum plates. Increasing the axial force will result in more material being displaced, higher temperatures within the weld zone, and a larger forging force. Spot welds were made with a centered through hole with a welding tool/anvil rotation rate of 1200 rpm, a 1 sec dwell period and a control force of 8000 N. The resulting tensile shear strength of the spot weld was 739.24 kgf, 228% stronger than the triple-lap joint without a through hole. The macrosection of this spot weld reveals that, again, the volume of the through hole was not completely filled. The material extruded by the top and bottom plates did converge within the weld zone resulting in a welded joint (Figure 120). The length of the welded joint was approximately 0.04 inches long. Volumetric voids can be seen on both sides of the spot weld near the outer edge of the through hole.

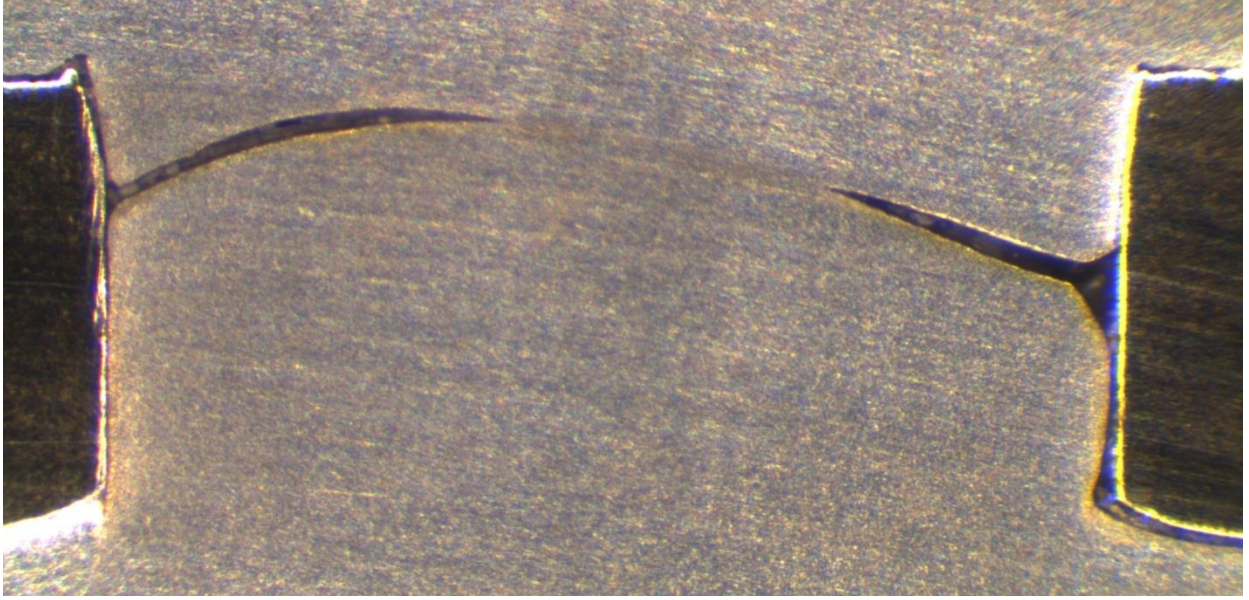


Figure 120: Al-Steel-Al with a through hole. 1200 rpm, 1 sec, 8000 N control force. The extruded material from the top and bottom sheet has not completely filled the volume of the through hole. A weld joint was formed within the through hole however.

In a final attempt to fill the volume of the through hole the dwell time was increased to 5 seconds. The spot weld was made using a centered through hole with a welding tool/anvil rotation rate of 1200 rpm, a 5 sec dwell period and a control force of 8000 N. The macrosection of the spot weld revealed that the volume of the through hole has been completely filled (Figure 121). There is no tensile shear strength data of this spot weld to report. Deformation of the steel sheet along the top edge of the through hole in the steel sheet is observed in the macrosection. This deformation may be a result of the increased axial load and lengthened dwell period.



Figure 121: Al-Steel-Al with through hole. 1200 rpm, 5 sec, 8000 N control force. The extruded material from the top and bottom sheets has completely filled the volume of the through hole. There is no observable joint line.

The concept of using a through hole has been shown to be a successful method for joining aluminum to steel in a triple-lap joint configuration. With the proper selection of process parameters it is possible to create a solid-state joint between the aluminum joints within the volume of the through hole in the steel plate. The extruded material interacts within the through hole and forges together forming the joint. The resulting weld acts as a mechanical fastener to join the three plates together.

The next stages of this research will look into the effect dwell time and axial load have on the formation of the strength of the weld. The size and shape of the through hole, as well as inclusions of features such as threads, could also impact the process and should be investigated. The effect the volumetric ratio presented in Figure 117 has on joint strength should be investigated and could be expanded to thicker steel and aluminum plates once the parameter space of the welding process is better characterized.

### *Spot Stich Welding*

Friction Stir Spot Stich Welding (FSSSW) is an application of the RAFSSW process in which multiple overlapping spot welds are created on the same workpiece. The overlapping spot welds can be used to create a continuous welded area similar to a conventional weld made using linear FSW (Figure 122). For thin aluminum plate this spot welding process may be a reasonable alternative to using a fixed-gap style bobbin tool for double sided FSW. Fixed-gap bobbin tools are difficult to manufacture, prone to failure, and require complex geometries to insure a quality weld is created. Using the RAFSSW process to create a series of overlapping spot welds may eliminate these issues.

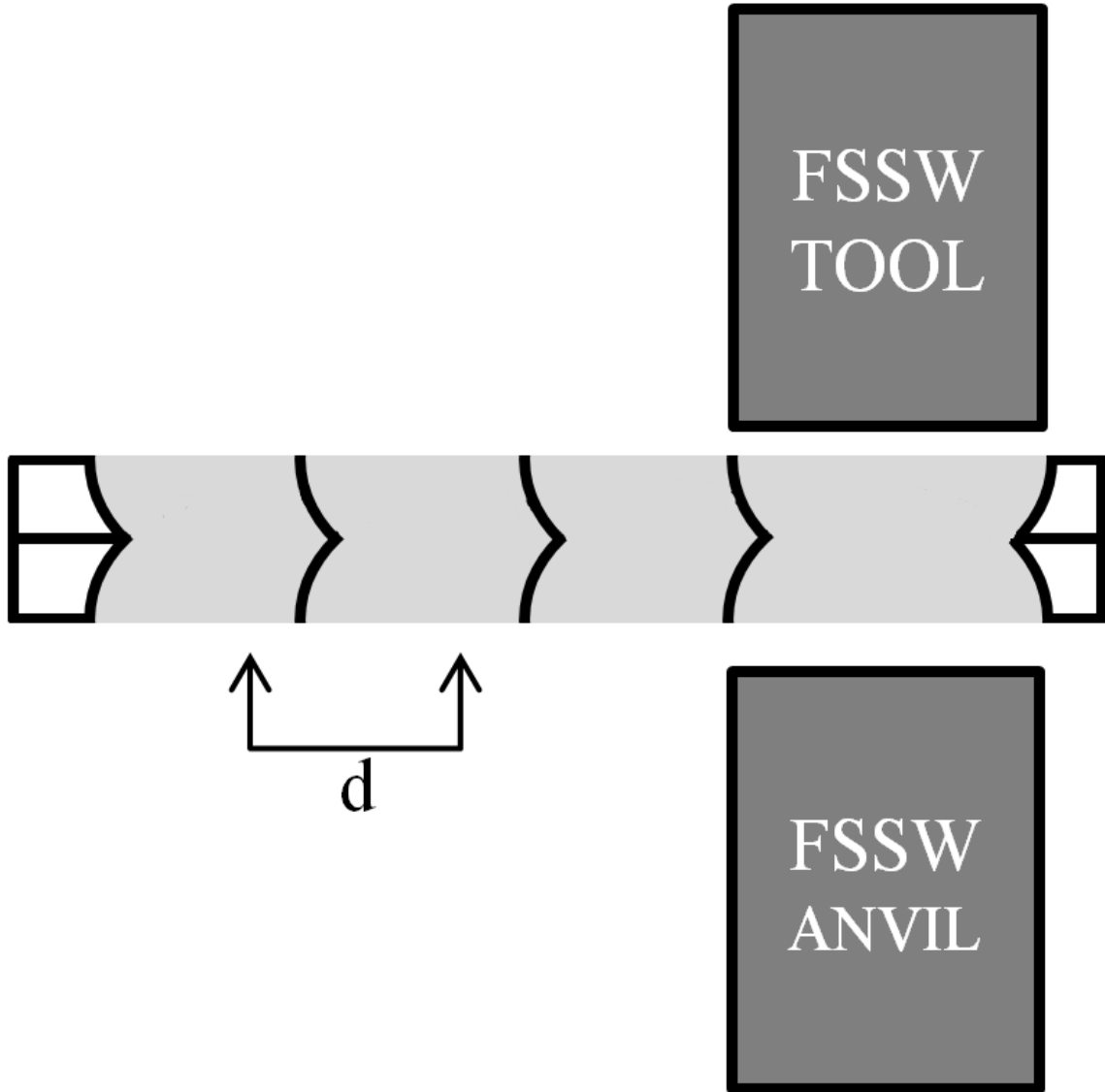


Figure 122: The Friction Stir Spot Stitch welding process.  $d$  is the spacing between each FSSW spot weld.

A series of spot welds was created using the RAFSSW process on two 0.040 inch thick plates of Al 6061-T6 in a traditional lap joint configuration. The welding tool and rotating anvil had a rotation rate of 1200 rpm, a dwell time of 0.5 seconds, a plunge rate of 0.5 inches per minute, and a control force of 4500 N. The distance between each spot weld ( $d$ ) was 0.325 inches. The resulting stitch spot weld was macrosectioned and etched

using Keller's reagent for inspection (Figure 123). In Figure 123 three overlapping spot welds can be seen. The original joint line is no longer present. The series of spot welds creates a continuous weld zone.

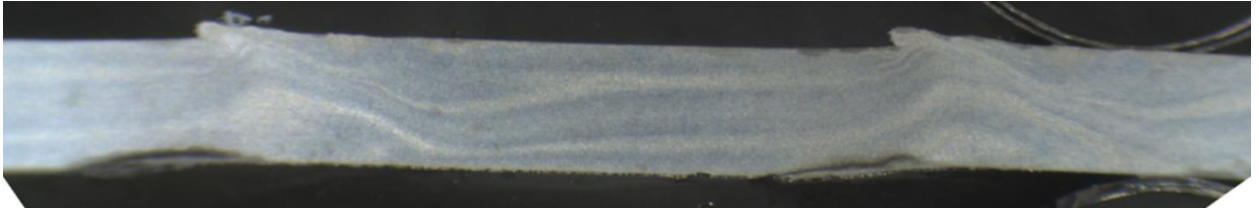


Figure 123: A series of overlapping spot welds created using the RAFSSW process.

The effect the distance between the spot welds has on the strength of the resulting strength should be investigated. The distance should be such that “d” is less than the diameter of the welding tool being used. If the distance between the spot welds is larger than the diameter of the tool the spot welds would not overlap. This case may still be of use depending on the application of the weld joint.

### Conclusions

The use of an open-loop force control system resulted in a more repeatable and faster spot welding operation. Increasing the difference in rotation rate between the welding tool and anvil resulted in an increase in the energy input into the weld which decreased the joint strength of the resulting spot welds. The RAFSSW process was capable of creating spot welds in the triple-lap joint configuration for an all-aluminum and aluminum-steel-aluminum joint configuration. The inclusion of a through hole greatly improved the strength of the weld joint. Lastly, the RAFSSW process is capable of a

creating a series of spot welds that overlap resulting in a continuous length of weld along a joint line. This process may be an alternative to traditional double sided linear FSW.

## CHAPTER VIII

### DISCUSSION OF RESULTS

#### Overview

The focus of this dissertation has been to gain a better understanding of the FSSW process through numerical simulation and experimental observation. The knowledge gained from this work will be of benefit to both researchers and manufacturers as the application of the FSSW process becomes more prevalent in the automotive industry. A direct result of these efforts has been the creation of a novel variation of the FSSW process; the rotating anvil. Here, the results of this research are discussed.

#### Tool Geometry

The research presented on the welding tool's pin length confirmed that a pinless tool could be used to create quality spot welds in thin aluminum plate. It was found that the inclusion of a tool pin that did not penetrate the bottom sheet of the lapped joint was detrimental to the quality of the weld. While it had been known that there existed an optimal pin length for welding lap joints there had been no discussion in the literature of a lower bound for pin length. The size and shape of the shoulder were found to not only contribute to the heat generated during welding but also to the size and shape of the weld zone. The FSSW tool should only include a pin if needed.

Using a spherically tapered shoulder with scrolling improved the tool's sensitivity to position during welding as well as reduced the formation of unwanted weld flash. The spherical taper of the shoulder resulted in a linear response in the axial load and torque



acting on the welding machine depending on the plunge depth during welding i.e. larger plunge depths result in higher axial loading and spindle torque. This is an intended function of the tool's design.

There was no observed tool wear during any of the experiments presented in this dissertation. Wear was not expected to be an issue when welding aluminum with a heat treated FSSW tool made of tool steel. However one might expect tool wear to be an issue when welding aluminum to steel with the same tool material. Because the tool is pinless it never comes into contact with the steel, thereby avoiding the steel-on-steel contact all together.

#### Spot Welding Parameters

The effect process parameters have on the quality of the spot weld was investigated using design of experiments and ANOVA. Among the numerous welding parameters considered, the rotation rate and dwell time were identified as being the most significant parameters affecting the quality of the spot weld. Short dwell times (< 2 sec) and slower rotation rates (< 1200 rpm) were found to result in the strongest spot welds.

The terms rotation rate and dwell time are commonly used in linear FSW. The discussion on FSW in the literature typically focuses on the steady state portion of the process and tends to pay little attention to the initial plunge and retraction stages. Because FSSW is a transient process it is suggested in this work that the discussion of the process would be better served to consider FSSW in terms of tool rotations (rotation rate (rpm)/60 sec \* dwell time (sec)). The selection of welding parameters directly affects the heat generated during welding which was determined to be the primary factor affecting weld

quality. Excessive heat generation during welding resulted in defects along the perimeter of the spot weld that adversely affected the weld quality.

The geometry of the FSSW tool also affects the heat generated during welding. The inclusion of a pin on the FSSW tool increases the cycle time during the plunge stage of the welding process which can drastically increase the amount of heat that being generated during welding. The plunge rate can be increased to help mitigate this affect but an upper limit exists due to the resulting axial forces higher plunge rates place on the welding machine. If the plunge rate is too fast (and the axial load too large) the welding tool or welding machine (robot) could incur serious damage.

A method for calculating the energy generated during the spot welding process is presented in this dissertation. The energy generated during FSSW was found to be inversely proportional to the strength of the resulting spot weld. It is hoped that this observed relationship will be of benefit to the FSSW community for quality assessment and/or process control applications.

### Rotating Anvil

The development of a rotating anvil for FSSW is presented in this dissertation. The rotating anvil, as discussed in Chapter VI, offers many advantages over conventional single-sided FSSW. In addition to lowering the process forces, shortening the cycle time, and improving the joint strength, the rotating anvil also resulted in the ability to create triple-lap joints with a pinless tool. This joint configuration is not possible with single-sided FSSW (with a pinless tool).

Additionally, the inclusion of a through hole in the steel sheet when welding in a triple-lap joint configuration resulted in a significant improvement in the strength of the spot weld. This process is a combination of the friction stir forming and friction stir spot welding process.

The rotating anvil also serves to benefit robotic applications of FSSW. The FSSW process is typically implemented via c-frame type “end effector” in the automotive industry. By rotating the anvil, the torque acting on the robotic arm can be reduced or eliminated, improving the operation of the welding process.

### Numerical Modeling

The use of numeric models is presented throughout this dissertation. The computational fluid dynamic models are used to predict the temperatures within the workpiece and the size and shape of the weld zone. The models were created using either ANSYS FLUENT or COMSOL. The models were able to accurately predict the temperatures measured during FSSW. The predicted size and shape of the weld zones did a good job of matching the observed geometry of the weld zones. The models also provide an insight into the rate at which the material within the weld zone is “stirring” which aids in understanding the relationship between tool turns, the heat generated during the welding process, and the observation of joint-line defects in certain spot welds.

## CHAPTER IX

### RECOMMENDATIONS FOR FUTURE WORK

#### Friction Stir Spot Welding

The successful use of a pinless tool as a method for eliminating the keyhole has been presented in the dissertation. The effect process parameters and tool geometry have on weld quality has been investigated using both experimental and numerical experiments. The next steps of this research should focus on process improvements and applying the process to more joint configurations. In all cases, the proposed future work could be applied to both single sided FSSW and FSSW with the rotating anvil.

#### Tool Rotation Feedback

The effect that the heat generated during welding has on spot weld quality has been presented in this dissertation. Apart from a user specified rotation rate, the current state of the FSSW machine at Vanderbilt does not provide any feedback on the actual spindle speed during welding. Any acceleration of the spindle (speed up or slow down) is not captured. Knowing the real-time speed of the spindle would provide a more accurate estimation of the weld power and energy being generated during welding. This would also aid in specifying the heat input boundary condition of the numerical models.

#### FSSW Tool Turn Limit

The current state of the FSSW machine restricts the minimum number of tool turns that can be executed during a friction stir spot weld. The limit exists due to a combination of the spindle motor and vertical stage motor. Creating a spot weld at a rotation rate of less

than 750 rpm places too large of a load on the spindle motor which tends to stall the motor out. The present transmission ratio between the motor shaft and welding machine spindle is approximately 3:4 with respect to diameter. In order to increase the power output of the spindle motor it needs to operate at a higher rpm. Decreasing the transmission ratio would allow the spindle motor to operate at a higher rpm (improving power output) without increasing the rotation rate of the FSSW spindle. It may be possible to rotate the FSSW tool at lower rotation rates without stalling the motor if the proper transmission ratio is used.

The other limiting factor is the vertical stage motor. In its present state the vertical actuation of the system requires 0.5 seconds to respond. This limit may be more difficult to overcome as the delay occurs as a result of the communication between the weld computer code and welding machine.

Currently spot welds can be made in as few as  $\approx 6.25$  turns of the welding tool. By lowering the tool rotation rate by 130 rpm, the number of tool turns can be decreased by 1. Even without making improvements to the 0.5 second dwell limit the number of tool turns could be reduced by a significant amount.

#### FSSW of Butt Joints

Presently the only weld joint considered for FSSW has been the lap joint. Unlike other traditional spot joining methods (resistance spot welding, rivets, etc.) FSSW with a pinless tool could be used to create single spot welds in the butt joint configuration. The methods used in Chapter V (for both single and double sided FSSW) could be used to characterize the process for the new joint configuration. If a series of overlapping spot

welds (stitched) were created along a butt joint instead, the RAFSSW process could potentially be used as an alternative to the bobbin tool used to create double sided friction stir welds.

#### FSSW with Sealant

Friction stir welding with sealants is currently under investigation by Gibson et al. at VUWAL. Their results have demonstrated that FSW (linear) can be performed with a sealant applied to the faying surfaces of the weld joint. The application of sealant in FSSW has the potential to be of great interest to automotive manufacturers. A preliminary spot weld has been made at VUWAL using sealant with a pinless FSSW tool. A small amount of sealant (Pelseal 2077) was applied directly in the area of the lap joint that was to be spot welded. The preliminary spot welds were made at the following parameters: 1000 rpm, 1 sec dwell, 0.010 inch plunge depth, and 0.4 inch per minute plunge rate. The resulting spot welds had an average strength of 454.9 kgf. Post weld evaluation revealed that the sealant had been displaced by the welding process such that there was no sealant observed within the weld zone. The effect the sealant layer has on the mechanical strength of the weld, energy input, and temperature within the workpiece should be investigated.

#### FSSW with “Energy” Control

The automated spot welding system currently in place utilizes either the position of the welding tool relative to the workpiece or the axial load acting on the welding frame as the input for the open-loop control system. In the present open-loop control system(s) the

plunging stage is halted when the desired state of the system is reached. In Chapter VII it is reported that the weld energy is strongly related to the strength of the corresponding spot weld. An additional open-loop control system could be added that monitors the energy generated during spot welding. This control system would stop the dwell stage and retract the welding tool when the desired “energy” state of the system is reached. By using a series of controllers the spot weld could be initiated using the existing system and stopped using the new “energy” control system. This would present an approach that has not yet been presented in the literature.

## CHAPTER X

### CONCLUSIONS

Friction stir spot welding presents automotive manufacturers with a process that is capable of joining light-weight aluminum alloys. The desire to eliminate the keyhole, a product of the process, was the main motivation of this dissertation. Using a pinless tool was found to offer a simple, low-cost, option capable of creating spot welds without the keyhole. The research presented in this dissertation greatly expands upon what was a limited understanding of the friction stir spot welding process (with a pinless tool especially.) The result of this work is a more fundamental understanding of the welding process, its parameters, and how they interact to affect the quality of the spot weld.

Relating the weld energy during spot welding to joint strength is one of the most exciting results of this dissertation. The weld energy is the only process response identified in this work to be a good indicator of weld quality. The potential to monitor the welding process in real-time and discern information regarding the quality of that weld would be of great interest to manufacturers.

The development of the rotating anvil is also believed to be of great value to automotive manufactures interested in using FSSW in the assembly of their automobiles. In addition to process advantages (lower forces and cycle times, and thicker workpieces) the rotating anvil can also save manufacturers money by allowing them to use smaller robotic manipulators as a result of the lower process forces incurred during welding.



## REFERENCES

- Aljoaba, S.Z., Jawahir, I.S., Dillon Jr., O.W., Ali, M.H., Khraisheh, M.K. "Modeling of Friction Stir Processing Using 3D CFD Analysis." *Int. J. Material Forming* 2 (2009)
- Arora, A., DeBroy, T., Bhadeshia, H.K.D.H., "Back-of-the-envelope calculations in friction stir welding – velocities, peak temperature, torque, and hardness." *Acta Materialia* 59 (2011) 2020-2028
- Arul, S.G., Pan, T., Lin, P.-C., Pan, J., Feng, Z., Santella, M.L. "Microstructures and Failure Mechanisms of Spot Friction Welds in Lap-Shear Specimens of Aluminum 5754 Sheets", *Society of Automotive Engineers, Inc.* (2005) #2005-01-1256
- Arul, S.G., Miller, S.F., Kruger, G.H., Pan, T.-Y., Mallick, P.K., Shih, A.J., "Experimental study of joint performance in spot friction welding of 6111-T4 aluminium alloy." *Sci. and Technol. of Welding and Joining* 13.7 (2008) 629-637.
- Atharifar, H., Lin, D., Kovacevic, R. "Numerical and Experimental Investigations on the Loads Carried by the Tool During Friction Stir Welding." *J. Materials Engineering and Performance* 18.4 (2008) 339-350
- Awang, M., Mucino, V.H., Feng, Z., David, S.A. "Thermo-Mechanical Modeling of Friction Stir Spot Welding (FSSW) Process: Use of an Explicit Adaptive Meshing Scheme." *SAE International* (2005) #2005-01-1251
- Badarinarayan, H., Yang, Q., Zhu, S. "Effect of tool geometry on static strength of friction stir spot-welded aluminum alloy." *Int. J. Machine Tools and Manufacture* 49 (2009) 142-148

- Badarinarayan, H., Shi, Y., Okamoto, K. "Effect of tool geometry on hook formation and static strength of friction stir spot welded aluminum 5754-O sheets." *Int. J. Machine Tools and Manufacture* 49 (2009) 814-823
- Bakavos, D., Prangnell, P.B. "Effect of reduced or zero pin length and anvil insulation on friction stir spot welding thin gauge 6111 automotive sheet." *Sci. and Technol. of Welding and Joining* 14.5 (2009) 443-456
- Bakavos, D., Chen, Y., Babout, L., Prangnell, P., "Material interactions in a novel pinless tool approach for friction stir spot welding thin aluminum sheet." *Metallurgical and Material Transactions* 42A (2011) 1266-1282
- Bilici, M.K., Yukler, A.I. "Influence of tool geometry and process parameters on macrostructure and static strength in friction stir spot welded polyethylene sheets." *Materials and Design* 33 (2012) 145-152
- Bozzi, S., Helbert-Etter, A.L., Baudin, T., Criqui, B., Kerbiguet, J.G. "Intermetallic compounds in Al 6016/IF-steel friction stir spot welds." *Materials Science and Engineering A* 527 (2010) 4505-4509
- Burford, D.A., Tweedy, B.M., Widener, C.A. "Influence of shoulder configuration and geometric features on FSW track properties." 6<sup>th</sup> International Symposium on Friction Stir Welding, Saint-Sauveur, Nr Montreal, Canada, October 10-13, 2006
- Cao, X., Jahazi, M. "Effect of Tool Rotational Speed and Probe Length on Lap Joint Quality of a Friction Stir Welded Magnesium Alloy." *Materials and Design* 32 (2011) 1-11
- Cederqvist, L., Reynolds, P. "Factors affecting the properties of friction stir welded aluminum lap joints." *Welding Journal* (2001) 281-287
- Chao, Y. J., "Failure mode of spot welds: interfacial versus pullout." *Inst. Of Materials, Minerals and Mining* 8.2 (2003) 133-137

- Colegrove, P.A., Shercliff, H.R. "3-Dimensional CFD modelling of flow round a threaded friction stir welding tool profile." *J. Materials Processing Technology* 169 (2005) 320-327
- Colligan, K. "Material Flow Behavior During Friction Stir Welding of Aluminum." *Welding Journal*, Welding Research Supplement (1999) 229-237
- Cook, G.E., Crawford, R., Clark, D.E., Strauss, A.M. "Robotic friction stir welding." *Industrial Robot: An International Journal* 31.1 (2004) 55-63
- Cox, C.D., Gibson, B.T., Strauss, A.M., Cook, G.E. "Effect of Pin Length and Rotation Rate on the Tensile Strength of a Friction Stir Spot-Welded Al Alloy: A Contribution to Automated Production." *Materials and Manufacturing Processes* 27.4 (2012) 472-478
- Crawford, R. "A Mechanistic Study of the Friction Stir Welding Process." PhD Dissertation, Vanderbilt University, 2006
- Dillet, Romain. "Apple Unveils Totally Redesigned 27" And 21.5" iMac: Thinner, SSD/HD Fusion Drive, Starting At \$1299." Tech Crunch. October 23, 2012. Web. 15
- Feldman, K., G. Kohn, and A. Stern. "Friction Stir Spot Welding." 25 Apr. 2013 <[http://www.engineers.org.il/\\_Uploads/3294feldman160107.pdf](http://www.engineers.org.il/_Uploads/3294feldman160107.pdf)>
- Ferro, P., Bonollo, F. "A semianalytical Thermal Model for Friction Stir Welding." *Metallurgical and Materials Transactions A* 41A (2009) 440-449
- FLUENT Software. "FLUENT 6.3 User's Guide: 8.4.5 Viscosity for Non-Newtonian Fluids." 2006 <<http://cdlab2.fluid.tuwien.ac.at/LEHRE/TURB/Fluent.Inc/fluent6.3.26/help/html/ug/node340.htm>>

- Fujimoto, M., H. Okada, K. Kamimuki. "Applications II: Application study on refill FSSW on aerospace industries." 9th International Friction Stir Welding Symposium. Huntsville, AL. 2012
- Gibson, B.T. "Custom Low-Cost Force Measurement Methods in Friction Stir Welding." M.S. Thesis, Vanderbilt University, 2010
- B.T. Gibson, G.E. Cook, T. Prater, W.R. Longhurst, A.M. Strauss, C.D. Cox. "Adaptive torque control of friction stir welding for the purpose of estimating tool wear." *Proceedings of the Institution of Mechanical Engineers, Part B: Journal of Engineering Manufacture* 225. 8 (2011) 1293-1303
- Hamilton, C., Dymek, S., Sommers, A. "A thermal model of friction stir welding in aluminum alloys." *Int. J. Machine Tools and Manufacture* 48 (2008) 1120-1130
- Heurtier, P., Jones, M.J., Desrayaud, C., Driver, J.H., Montheillet, F., Allehaux, D. "Mechanical and thermal modelling of Friction Stir Welding." *J. Materials Processing Technology* 171 (2006) 348-357
- Honda Worldwide, "Honda Develops New Technology to Weld Together Steel and Aluminum and Achieves World's First Application to the Frame of a Mass-production Vehicle." September 6, 2012 Web
- Karthikeyan, R., Balasubramanian, V. "Predictions of the optimized friction stir spot welding process parameters for joining AA2024 aluminum alloy using RSM." *International Journal of Advanced Manufacturing Technology* 51 (2010) 173-183
- Khandkar, M.Z.H., Khan, J.A., Reynolds, A.P. "Prediction of temperature distribution and thermal history during friction stir welding: input torque based model." *Sci. and Technol. of Welding and Joining* 8.3 (2003) 165-174

- Kim, D., Badarinarayan, H., Ryu, I., Kim, J.H., Jim, C., Okamoto, K., Wagoner, R.H., Chung, K. "Numerical Simulation of Friction Stir Spot Welding Process for Aluminum Alloys." *Met. Mater. Int.* 16.2 (2010) 323-332
- Kumar, K., Kalyan, C., Kailas, S.V., Srivatsan, T.S. "An Investigation of Friction During Friction Stir Welding of Metallic Materials." *Materials and Manufacturing Processes* 24 (2009) 438-445
- Kumar, K., and S. V. Kailas. "Positional Dependence of Material Flow in Friction Stir Welding: Analysis of Joint Line Remnant and Its Relevance to Dissimilar Metal Welding." *Sci. and Technol. of Welding and Joining* 15.4 (2010) 305-311
- Lammlein, D.H., DeLapp, D.R., Fleming, P.A., Strauss, A.M., Cook, G.E. "The application of shoulderless conical tools in friction stir welding: An experimental and theoretical study." *Materials and Design* 30 (2009) 4012-4022
- Lammlein, D.H. "Friction Stir Welding of Spheres, Cylinders, And T-Joints: Design, Experiment, Modelling, and Analysis." PhD Dissertation, Vanderbilt University, 2010
- Lammlein, D.H., Gibson, B.T., DeLapp, D.R., Cox, C.D., Strauss, A.M., Cook, G.E. "The friction stir welding of small-diameter pipe: an experimental and numerical proof of concept for automation and manufacturing." *Proc. IMechE Part B: J. Engineering Manufacture* 226.3 (2011) 383-398
- Lathabai, S., Painter, M. J., Cantin, G.M.D., Tyagi, V.K., "Friction Spot Joining of an Extruded Al-Mg-Si Alloy." *Scripta Materialia* 55 (2006) 899-902
- Longhurst, W.R., Strauss, A.M., Cook, G.E., Fleming, P.A. "Torque control of friction stir welding for manufacturing and automation." *Int. J. Adv. Manuf. Technol.* 51 (2010) 905-913
- Mijajlovic, M., Milcic, D. "Analytical Model for Estimating the Amount of Heat Generated During Friction Stir Welding: Application of plates Made of Aluminium Alloy 2024 T351." *InTech* 2012

Mishra, R.S., Ma, Z.Y. "Friction stir welding and processing." *Materials Science and Engineering R* 50 (2005) 1-78

Mishra, R.S., Mahoney, M.W., "Friction Stir Spot Welding." *Friction Stir Welding and Processing*. Materials Park, OH: ASM International, (2007). 235-72

Nandan, R., Roy, DeBroy, T. "Numerical Simulation of Three-Dimensional Heat Transfer and Plastic Flow During Friction Stir Welding." *Metallurgical and Materials Transactions A* 37A (2006) 1247-1259

Nandan, R., Roy, G.G., Lienert, T.J., DeBroy, T. "Three-dimensional heat and material flow during frictions stir welding of mild steel." *Acta Materialia* 55 (2007) 883-895

Nandan, R., Prabu, B., De, A., DeBroy, T. "Improving Reliability of Heat Transfer and Materials Flow Calculations during Friction Stir Welding of Dissimilar Aluminum Alloys." *Welding Journal* 86 (2007) 313-322

Nandan, R., DeBroy, T., Bhadeshia, H.K.D.H. "Recent advances in friction-stir welding – Process, weldment structure and properties." *Progress in Materials Science* 53 (2008) 980-1023

Nunes, A.C., Bernstein, E.L., McClure, J.C. "A Rotating Plug Model for Friction Stir Welding." 81<sup>st</sup> American Welding Society Convention, Chicago, IL. (2000)

Nunes, A.C. "Innovations in Materials Manufacturing, Fabrication, and Environmental Safety: Chapter 6, Friction Stir Welding" Boca Raton, FL: CRC P. (2011) 137-165

Nunes, A.C, McClure, J, "The Plunge Phase of Friction Stir Welding." Personal Communication (2012)

Perivilli, S., Peddieson, J., Cui, J. "Simplified Two-Dimensional Analytical Model for Friction Stir Welding Heat Transfer." *J. Heat Transfer* 130 (2008) 1-9

- Pew, J.W., Nelson, T.W., Sorenson, C.D. "Torque based weld power model for friction stir welding." *Sci. and Technol. of Welding and Joining* 12.4 (2007) 341-347
- Prater, T.J., Cox, C.D., Gibson, B.T., Strauss, A.M., Cook, G.E. "Dimensional Analysis and a Potential Classification Algorithm for Prediction of Wear in Friction Stir Welding of Metal Matrix Composites." *Proceedings of the Institution of Mechanical Engineers, Part C, Journal of Mechanical Engineering Science* 226.11 (2012) 2759-2769
- Querin, J.A., Schneider, J.A. "Developing an Alternative Heat Indexing Equation for FSW." *Welding Journal* 91 (2012) 76-82
- Rai, R., De, A., Bhadeshia, H.K.D.H., DebRoy, T. "Review: friction stir welding tools." *Sci. and Technol. of Welding and Joining* 16.4 (2011) 325-342
- Reynolds, A.P., Tang, W., Khandkar, Z., Khan, J.A., Lindner, K. "Relationships between weld parameters, hardness distribution and temperature history in alloy 7050 friction stir welds." *Sci. and Technol. Welding and Joining* 10.2 (2005) 190-199
- Romine, P. L. Investigation of Machine Design for Friction Stir Welding. Tech. no. 205205. Research Reports - 1996 NASA/ASEE Summer Faculty Fellowship Program. 1996
- Roy, G.G., Nandan, R., DeBroy, T. "Dimensionless correlation to estimate peak temperature during friction stir welding." *Sci. and Technol. of Welding and Joining* 11 (2006) 606-608
- Schmidt, H., Hattel, J., Wert, J. "An analytical model for heat generation in friction stir welding." *Modelling Simul. Mater. Sci. Eng.* 12 (2004) 143-157
- Schneider, J., Nunes, A.C. "Characterization of Plastic Flow and Resulting Microtextures in a Friction Stir Weld." *Metallurgical and Materials Transactions B* 35B (2004) 777-783

- Schneider, J., Beshears, R., Nunes, A.C. "Interfacial sticking and slipping in the friction stir welding process." *Materials Science and Engineering A* 435-436 (2006) 297-304
- Sheppard, T., Jackson, A. "Constitutive equations for use in prediction of flow stress during extrusion of aluminium alloys." *Materials Science and Technology* 13 (1997) 203-209
- Shibayanagi, T., Gerlich, A., Kashihara, K., North, T., "Textures in Single-Crystal Aluminum Friction Stir Spot Welds." *Metallurgical and Mater. Transactions A* 40A (2009) 920-931
- Song, M., Kovacevic, R. "Numerical and experimental study of the heat transfer process in friction stir welding." *Proc. Institution of Mechanical Engineers, Part B: J Engineering Manufacture* 217 (2003) 73-85
- Tello, K.E., Gerlich, A.P., Mendez, P.F. "Constants for hot deformation constitutive models for recent experimental data." *Sci. and Technol. of Welding and Joining* 15.3 (2010) 260-266
- Threadgill, P.L. "Terminology in friction stir welding." *Sci. and Technol. of Welding and Joining* 12.4 (2007) 357-360
- Tozaki, Y., Uematsu, Y., Tojaki, K. "Effect of tool geometry on microstructure and static strength in friction stir spot welded aluminium alloys." *International Journal of Machine and Tools and Manufacture* 47 (2007) 2230-2236
- Tozaki, Y., Uematsu, Y., Tokaji, K., "Effect of processing parameters on static strength of dissimilar friction stir spot welds between different aluminium alloys." *Fatigue Fract. Engng. Mater. Struct.* 30 (2007) 143-148.
- Tozaki, Y., Uematsu, Y., Tojaki, K. "A newly developed tool without probe for friction stir spot welding its performance." *Journal of Materials and Processing Technology* 210 (2010) 844-851



- Tran, V.-X., Pan, J. “Fatigue behavior of dissimilar spot friction welds in a lap-shear and cross-tension specimens of aluminum and steel sheets.” *International Journal of Fatigue* 32 (2010) 1167-1179
- Ulysse, P. “Three-dimensional modeling of the friction stir-welding process.” *International Journal of Machine Tools and Manufacture* 42 (2002) 1549-1557
- Vijayenthiran, V. “New Welding Technique Helps Acura Integrate Aluminum in Its Cars.” Jan. 10, 2014. < [http://www.motorauthority.com/news/1082391\\_new-welding-technique-helps-acura-integrate-more-aluminum-in-its-cars](http://www.motorauthority.com/news/1082391_new-welding-technique-helps-acura-integrate-more-aluminum-in-its-cars)>
- Yuan, W., Mishra, R.S., Webb, S., Chen, Y.L., Carlson, B., Herling, D.R., Grant, G.J. “Effect of tool design and process parameters on properties of Al alloy 6016 friction stir spot welds.” *Journal of Materials Processing Technology* 211 (2011) 972-977
- Zimmer, S., Langlois, L., Laye, J., et al. “Experimental investigation of the influence of the FSW plunge processing parameters on the maximum generated force and torque.” *International Journal of Advanced Manufacturing Technology* 47 (2010) 201-215

## APPENDIX

### A. Design of A Pinless FSSW Tool

#### Development of a Novel FSSW Tool

##### Motivation

- Axial force not indicative of position / quality
- Standard tools generates excessive weld flash

##### Torque Model

The Nunes model of friction stir welding predicts the weld torque and can be seen in Equation A.1 below. It predicts that the welding torque is the summation of the product of shear flow stress occurring at the shear interface boundary that surrounds the tool and the distance to the axis of rotation.

$$Torque = \int_r^R 2\pi r^2 \sigma dr + 2\pi r^2 t \sigma + \int_0^r 2\pi r^2 \sigma dr \quad (A.1)$$

Where  $\sigma$  is the shear flow stress (psi),  $R$  is the radius of the shoulder (inch),  $r$  is the radius of the tool pin (inch), and  $t$  is the length of the pin (inch). In order to complete the computation it is necessary to define the geometry of the spot welding tool. The tool is a pinless and consists of two parts: 1) a 0.4 inch diameter flat that spherically tapers (convex) out to a 2) 1 inch diameter shank. The “domed” portion of the shoulder has a

height of 0.05 inches and an arc radius of 3.0 inches. The flat is created by grinding down the “dome” until a 0.4 inch diameter surface is created.

The Nune’s expression can be simplified for the pinless tool design:

$$Torque = \int_0^r 2\pi r^2 \sigma dr \quad (A.2)$$

The Nunes’ model assumes that a traditional FSSW tool is being modeled and therefore adjustments must be made to the formulation. Considering convex shoulder, the area of a surface of revolution is given by Equation A.2.

$$S = \int 2\pi r ds \quad \text{where} \quad ds = \sqrt{1 + \left(\frac{dr}{dz}\right)^2} dz \quad (A.3)$$

To compute the torque on the tool it is necessary to not only consider the area but also the radial distance and shear flow stress acting on the tool resulting in:

$$Torque (T) = \int_0^{PD} 2\pi r^2 \sigma \sqrt{1 + \left(\frac{dr}{dz}\right)^2} dz \quad (A.4)$$

The equation for an arc that defines the domed surface of the pinless tool is:

$$r^2 + z^2 = 9 \quad \text{or} \quad r = \sqrt{9 - z^2} \quad (A.5)$$

Differentiating Equation A.5 with respect to z produces:

$$\frac{dr}{dz} = \frac{-z}{\sqrt{9-z^2}} \quad (\text{A.6})$$

The origin of the coordinate system of the tool is located 3 inches above the shoulder.

The relationship of the plunge depth and  $z$  is:

$$z = -3 + PD \quad (\text{A.7})$$

Combining Equations A.5, A.6, and A.7 produces:

$$Torque = \int_{-3}^{-3+PD} 2\pi\sigma\sqrt{9-z^2} \sqrt{\frac{9}{9-z^2}} dz \quad (\text{A.8})$$

Simplifying Equation A.8:

$$Torque = 6\pi\sigma \int_{-3}^{-3+PD} \sqrt{9-z^2} dz \quad (\text{A.9})$$

To evaluate the integral make the following substitutions

$$z = 3 \sin(u) \text{ and } dz = 3 \cos(u) du \quad (\text{A.10})$$

Combining Equations A.9 and A.10

$$Torque = 54\pi\sigma \int_{-3}^{-3+PD} \cos^2(u) du \quad (\text{A.11})$$

Redefining the limits of integration in terms of  $u$ :

$$Torque = 54\pi\sigma \int_{-\frac{\pi}{2}}^{\sin^{-1}\left(\frac{-3+PD}{3}\right)} \cos^2(u) du \quad (A.12)$$

Rewriting  $\cos^2(u)$ :

$$\cos^2(u) = \frac{1}{2} + \frac{1}{2}\cos 2(u) \quad (A.13)$$

Combining Equations A.12 and A.13, and solving

$$Torque = 27\pi\sigma \left( \sin^{-1}\left(\frac{-3+PD}{3}\right) + \left( \frac{1}{2}\sin 2\left(\sin^{-1}\left(\frac{-3+PD}{3}\right)\right) \right) + \frac{\pi}{2} \right) \quad (A.14)$$

Equation A.14 estimates the torque experienced by a spherically tapered shoulder during welding. For this case however, we will need to modify Equation A.14 to account for the machined flat on the end of the tool. We can use Equation A.5 to adjust the limits of the integration in Equation A.12 to account for the flat; a radius of 0.20 inches.

$$Torque = 27\pi\sigma \left( \sin^{-1}\left(\frac{-2.9933+PD}{3}\right) + \left( \frac{1}{2}\sin 2\left(\sin^{-1}\left(\frac{-2.9933+PD}{3}\right)\right) \right) + 1.5708 \right) \quad (A.15)$$

We still need to account for the torque contribution by the flat of the tool. This can be expressed as:

$$Torque = \int_0^{r_{flat}} 2\pi r^2 \sigma dr = \frac{2\pi r^3}{3} \sigma \quad (A.16)$$

The total torque experienced by the tool can be expressed as:

$$Torque = 27\pi\sigma \left( \sin^{-1} \left( \frac{-2.9933+PD}{3} \right) + \left( \frac{1}{2} \sin 2 \left( \sin^{-1} \left( \frac{-2.9933+PD}{3} \right) \right) \right) + 1.5708 \right) + 0.0168\sigma \quad (A.17)$$

Equation A.17 is used to calculate the welding torque in this research. Estimates of  $\sigma$  are made based on temperature measurements made during FSSW. Figure 124 shows a comparison between experimentally measured torques and calculated values of torque for various plunge depths.

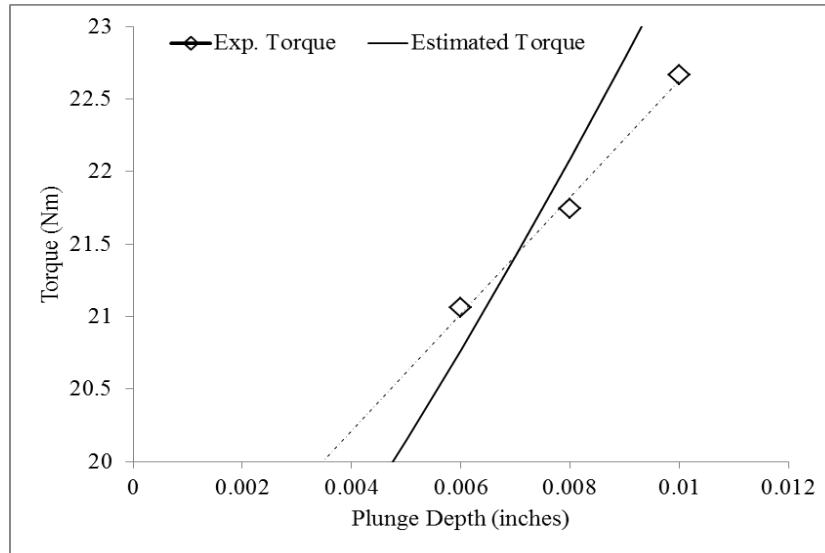


Figure 124: Estimated torque vs. experimental torque for various plunge depths.

B. Patent Application for Double Sided Friction Stir Spot Welding Method

<b>Electronic Acknowledgement Receipt</b>	
<b>EFS ID:</b>	13001234
<b>Application Number:</b>	61659042
<b>International Application Number:</b>	
<b>Confirmation Number:</b>	5784
<b>Title of Invention:</b>	DOUBLE SIDED FRICTION STIR SPOT WELDING METHOD
<b>First Named Inventor/Applicant Name:</b>	Chase D. Cox
<b>Customer Number:</b>	78102
<b>Filer:</b>	Eduardo Jose Quinones/Stephanie Dominguez
<b>Filer Authorized By:</b>	Eduardo Jose Quinones
<b>Attorney Docket Number:</b>	20004.0066
<b>Receipt Date:</b>	13-JUN-2012
<b>Filing Date:</b>	
<b>Time Stamp:</b>	13:11:25
<b>Application Type:</b>	Provisional

**Payment information:**

Submitted with Payment	yes
Payment Type	Credit Card
Payment was successfully received in RAM	\$ 125
RAM confirmation Number	10846
Deposit Account	141437
Authorized User	NELSON,GREGORY
The Director of the USPTO is hereby authorized to charge indicated fees and credit any overpayment as follows: Charge any Additional Fees required under 37 C.F.R. Section 1.16 (National application filing, search, and examination fees) Charge any Additional Fees required under 37 C.F.R. Section 1.17 (Patent application and reexamination processing fees)	



Charge any Additional Fees required under 37 C.F.R. Section 1.19 (Document supply fees)					
Charge any Additional Fees required under 37 C.F.R. Section 1.20 (Post Issuance fees)					
Charge any Additional Fees required under 37 C.F.R. Section 1.21 (Miscellaneous fees and charges)					
<b>File Listing:</b>					
Document Number	Document Description	File Name	File Size(Bytes)/ Message Digest	Multi Part /.zip	Pages (if appl.)
1		Application_20004_0066_.pdf	310951 9b0c56d3ca11259e0c0c677c1b447e309e a31c6	yes	6
<b>Multipart Description/PDF files in .zip description</b>					
<b>Document Description</b>			<b>Start</b>	<b>End</b>	
Abstract			1	1	
Specification			2	3	
Claims			4	6	
<b>Warnings:</b>					
<b>Information:</b>					
2	Drawings-other than black and white line drawings	Drawings_20004_0066_.pdf	655997 97ca7745e7520aed75a3e5e3e9f0921d2 0c468	no	4
<b>Warnings:</b>					
<b>Information:</b>					
3	Provisional Cover Sheet (SB16)	ProvisionalSB.pdf	2071853 8e78707e58980e0231697b0292c5c9c098 2257b	no	3
<b>Warnings:</b>					
<b>Information:</b>					
4	Application Data Sheet	ADS.pdf	1421472 d52042b60ea1c5771307ea12b47a23bc508 c8e1e	no	5
<b>Warnings:</b>					
<b>Information:</b>					
5	Fee Worksheet (SB06)	fee-info.pdf	29938 d878a23bc463f50a0c3548962ff16719405 004	no	2
<b>Warnings:</b>					
<b>Information:</b>					
<b>Total Files Size (in bytes):</b>			4490211		

This Acknowledgement Receipt evidences receipt on the noted date by the USPTO of the indicated documents, characterized by the applicant, and including page counts, where applicable. It serves as evidence of receipt similar to a Post Card, as described in MPEP 503.

**New Applications Under 35 U.S.C. 111**

If a new application is being filed and the application includes the necessary components for a filing date (see 37 CFR 1.53(b)-(d) and MPEP 506), a Filing Receipt (37 CFR 1.54) will be issued in due course and the date shown on this Acknowledgement Receipt will establish the filing date of the application.

**National Stage of an International Application under 35 U.S.C. 371**

If a timely submission to enter the national stage of an international application is compliant with the conditions of 35 U.S.C. 371 and other applicable requirements a Form PCT/DO/EO/903 indicating acceptance of the application as a national stage submission under 35 U.S.C. 371 will be issued in addition to the Filing Receipt, in due course.

**New International Application Filed with the USPTO as a Receiving Office**

If a new international application is being filed and the international application includes the necessary components for an international filing date (see PCT Article 11 and MPEP 1810), a Notification of the International Application Number and of the International Filing Date (Form PCT/RO/105) will be issued in due course, subject to prescriptions concerning national security, and the date shown on this Acknowledgement Receipt will establish the international filing date of the application.

Electronic Patent Application Fee Transmittal				
<b>Application Number:</b>				
<b>Filing Date:</b>				
<b>Title of Invention:</b>		DOUBLE SIDED FRICTION STIR SPOT WELDING METHOD		
<b>First Named Inventor/Applicant Name:</b>		Chase D. Cox		
<b>Filer:</b>		Eduardo Jose Quinones/Stephanie Dominguez		
<b>Attorney Docket Number:</b>		20004.0066		
Filed as Small Entity				
<b>Provisional Filing Fees</b>				
Description	Fee Code	Quantity	Amount	Sub-Total in USD(\$)
<b>Basic Filing:</b>				
Provisional Application filing fee	2005	1	125	125
<b>Pages:</b>				
<b>Claims:</b>				
<b>Miscellaneous-Filing:</b>				
<b>Petition:</b>				
<b>Patent-Appeals-and-Interference:</b>				
<b>Post-Allowance-and-Post-Issuance:</b>				
<b>Extension-of-Time:</b>				

Description	Fee Code	Quantity	Amount	Sub-Total in USD(\$)
<b>Miscellaneous:</b>				
<b>Total in USD (\$)</b>				<b>125</b>

Under the Paperwork Reduction Act of 1995, no persons are required to respond to a collection of information unless it contains a valid OMB control number.

<b>Application Data Sheet 37 CFR 1.76</b>		Attorney Docket Number	20004.0066
		Application Number	
Title of Invention	DOUBLE SIDED FRICTION STIR SPOT WELDING METHOD		
The application data sheet is part of the provisional or nonprovisional application for which it is being submitted. The following form contains the bibliographic data arranged in a format specified by the United States Patent and Trademark Office as outlined in 37 CFR 1.76. This document may be completed electronically and submitted to the Office in electronic format using the Electronic Filing System (EFS) or the document may be printed and included in a paper filed application.			

### Secrecy Order 37 CFR 5.2

Portions or all of the application associated with this Application Data Sheet may fall under a Secrecy Order pursuant to 37 CFR 5.2 (Paper filers only. Applications that fall under Secrecy Order may not be filed electronically.)

### Applicant Information:

<b>Applicant 1</b>					
<b>Applicant Authority</b>		<input checked="" type="radio"/> Inventor		<input type="radio"/> Legal Representative under 35 U.S.C. 117	
				<input type="radio"/> Party of Interest under 35 U.S.C. 118	
<b>Prefix</b>	<b>Given Name</b>	<b>Middle Name</b>	<b>Family Name</b>	<b>Suffix</b>	
	Chase	D.	Cox		
<b>Residence Information (Select One)</b>					
		<input checked="" type="radio"/> US Residency		<input type="radio"/> Non US Residency	
				<input type="radio"/> Active US Military Service	
<b>City</b>	Nashville	<b>State/Province</b>	TN	<b>Country of Residence</b>	US
<b>Citizenship under 37 CFR 1.41(b)</b>		US			
<b>Mailing Address of Applicant:</b>					
<b>Address 1</b>	2400 Highland Ave.,				
<b>Address 2</b>	101 Olin Hall				
<b>City</b>	Nashville	<b>State/Province</b>	TN		
<b>Postal Code</b>	37212	<b>Country</b>	US		
<b>Applicant 2</b>					
<b>Applicant Authority</b>		<input checked="" type="radio"/> Inventor		<input type="radio"/> Legal Representative under 35 U.S.C. 117	
				<input type="radio"/> Party of Interest under 35 U.S.C. 118	
<b>Prefix</b>	<b>Given Name</b>	<b>Middle Name</b>	<b>Family Name</b>	<b>Suffix</b>	
	David		DeLapp		
<b>Residence Information (Select One)</b>					
		<input checked="" type="radio"/> US Residency		<input type="radio"/> Non US Residency	
				<input type="radio"/> Active US Military Service	
<b>City</b>	Nashville	<b>State/Province</b>	TN	<b>Country of Residence</b>	US
<b>Citizenship under 37 CFR 1.41(b)</b>		US			
<b>Mailing Address of Applicant:</b>					
<b>Address 1</b>	400 24th Ave.,				
<b>Address 2</b>	South 267 Jacobs Hall				
<b>City</b>	Nashville	<b>State/Province</b>	TN		
<b>Postal Code</b>	37235	<b>Country</b>	US		
<b>Applicant 3</b>					
<b>Applicant Authority</b>		<input checked="" type="radio"/> Inventor		<input type="radio"/> Legal Representative under 35 U.S.C. 117	
				<input type="radio"/> Party of Interest under 35 U.S.C. 118	
<b>Prefix</b>	<b>Given Name</b>	<b>Middle Name</b>	<b>Family Name</b>	<b>Suffix</b>	
	Alvin	M.	Strauss		
<b>Residence Information (Select One)</b>					
		<input checked="" type="radio"/> US Residency		<input type="radio"/> Non US Residency	
				<input type="radio"/> Active US Military Service	
<b>City</b>	Nashville	<b>State/Province</b>	TN	<b>Country of Residence</b>	US

Under the Paperwork Reduction Act of 1995, no persons are required to respond to a collection of information unless it contains a valid OMB control number.

<b>Application Data Sheet 37 CFR 1.76</b>		Attorney Docket Number	20004.0066	
		Application Number		
Title of Invention	DOUBLE SIDED FRICTION STIR SPOT WELDING METHOD			
Citizenship under 37 CFR 1.41(b)	US			
<b>Mailing Address of Applicant:</b>				
Address 1	2400 Highland Ave.,			
Address 2	101 Olin Hall			
City	Nashville	State/Province	TN	
Postal Code	37212	Country	US	
<b>Applicant 4</b>				
Applicant Authority	<input checked="" type="radio"/> Inventor	<input type="radio"/> Legal Representative under 35 U.S.C. 117	<input type="radio"/> Party of Interest under 35 U.S.C. 118	
Prefix	Given Name	Middle Name	Family Name	Suffix
	George	E.	Cook	
Residence Information (Select One)	<input checked="" type="radio"/> US Residency <input type="radio"/> Non US Residency <input type="radio"/> Active US Military Service			
City	Nashville	State/Province	TN	Country of Residence
				US
Citizenship under 37 CFR 1.41(b)	US			
<b>Mailing Address of Applicant:</b>				
Address 1	Box 1826 Sta B			
Address 2				
City	Nashville	State/Province	TN	
Postal Code	37235	Country	US	
All Inventors Must Be Listed - Additional Inventor Information blocks may be generated within this form by selecting the <b>Add</b> button. <span style="float: right;"><input type="button" value="Add"/></span>				

**Correspondence Information:**

Enter either Customer Number or complete the Correspondence Information section below. For further information see 37 CFR 1.33(a).	
<input type="checkbox"/> An Address is being provided for the correspondence information of this application.	
Customer Number	78102
Email Address	<input type="button" value="Add Email"/> <input type="button" value="Remove Email"/>

**Application Information:**

Title of the Invention	DOUBLE SIDED FRICTION STIR SPOT WELDING METHOD		
Attorney Docket Number	20004.0066	Small Entity Status Claimed	<input checked="" type="checkbox"/>
Application Type	Provisional		
Subject Matter	Utility		
Suggested Class (if any)		Sub Class (if any)	
Suggested Technology Center (if any)			
Total Number of Drawing Sheets (if any)	4	Suggested Figure for Publication (if any)	

Under the Paperwork Reduction Act of 1995, no persons are required to respond to a collection of information unless it contains a valid OMB control number.

<b>Application Data Sheet 37 CFR 1.76</b>	Attorney Docket Number	20004.0066
	Application Number	
Title of Invention	DOUBLE SIDED FRICTION STIR SPOT WELDING METHOD	

**Publication Information:**

<input type="checkbox"/> Request Early Publication (Fee required at time of Request 37 CFR 1.219)
<input type="checkbox"/> <b>Request Not to Publish.</b> I hereby request that the attached application not be published under 35 U.S.C. 122(b) and certify that the invention disclosed in the attached application <b>has not and will not</b> be the subject of an application filed in another country, or under a multilateral international agreement, that requires publication at eighteen months after filing.

**Representative Information:**

Representative information should be provided for all practitioners having a power of attorney in the application. Providing this information in the Application Data Sheet does not constitute a power of attorney in the application (see 37 CFR 1.32). Enter either Customer Number or complete the Representative Name section below. If both sections are completed the Customer Number will be used for the Representative Information during processing.			
Please Select One:	<input checked="" type="radio"/> Customer Number	<input type="radio"/> US Patent Practitioner	<input type="radio"/> Limited Recognition (37 CFR 11.9)
Customer Number	78102		

**Domestic Benefit/National Stage Information:**

This section allows for the applicant to either claim benefit under 35 U.S.C. 119(e), 120, 121, or 365(c) or indicate National Stage entry from a PCT application. Providing this information in the application data sheet constitutes the specific reference required by 35 U.S.C. 119(e) or 120, and 37 CFR 1.78(a)(2) or CFR 1.78(a)(4), and need not otherwise be made part of the specification.			
Prior Application Status	Expired	<a href="#">Remove</a>	
Application Number	Continuity Type	Prior Application Number	Filing Date (YYYY-MM-DD)
	non provisional of	61494935	2011-06-09
Additional Domestic Benefit/National Stage Data may be generated within this form by selecting the <b>Add</b> button.			

**Foreign Priority Information:**

This section allows for the applicant to claim benefit of foreign priority and to identify any prior foreign application for which priority is not claimed. Providing this information in the application data sheet constitutes the claim for priority as required by 35 U.S.C. 119(b) and 37 CFR 1.55(a).			
			<a href="#">Remove</a>
Application Number	Country <sup>1</sup>	Parent Filing Date (YYYY-MM-DD)	Priority Claimed
			<input checked="" type="radio"/> Yes <input type="radio"/> No
Additional Foreign Priority Data may be generated within this form by selecting the <b>Add</b> button.			

**Assignee Information:**

Providing this information in the application data sheet does not substitute for compliance with any requirement of part 3 of Title 37 of the CFR to have an assignment recorded in the Office.
<b>Assignee 1</b>

Under the Paperwork Reduction Act of 1995, no persons are required to respond to a collection of information unless it contains a valid OMB control number.

<b>Application Data Sheet 37 CFR 1.76</b>		Attorney Docket Number	20004.0066	
		Application Number		
Title of Invention	DOUBLE SIDED FRICTION STIR SPOT WELDING METHOD			

If the Assignee is an Organization check here. <input checked="" type="checkbox"/>			
Organization Name	Vanderbilt University		
<b>Mailing Address Information:</b>			
Address 1	305 Kirland Hall		
Address 2	2201 West End Avenue		
City	Nashville	State/Province	TN
Country	US	Postal Code	37240
Phone Number		Fax Number	
Email Address			
Additional Assignee Data may be generated within this form by selecting the <b>Add</b> button.			

**Signature:**

A signature of the applicant or representative is required in accordance with 37 CFR 1.33 and 10.18. Please see 37 CFR 1.4(d) for the form of the signature.					
Signature	/Eduardo J. Quinones/		Date (YYYY-MM-DD)	2012-06-13	
First Name	Eduardo	Last Name	Quinones	Registration Number	58575

This collection of information is required by 37 CFR 1.76. The information is required to obtain or retain a benefit by the public which is to file (and by the USPTO to process) an application. Confidentiality is governed by 35 U.S.C. 122 and 37 CFR 1.14. This collection is estimated to take 23 minutes to complete, including gathering, preparing, and submitting the completed application data sheet form to the USPTO. Time will vary depending upon the individual case. Any comments on the amount of time you require to complete this form and/or suggestions for reducing this burden, should be sent to the Chief Information Officer, U.S. Patent and Trademark Office, U.S. Department of Commerce, P.O. Box 1450, Alexandria, VA 22313-1450. DO NOT SEND FEES OR COMPLETED FORMS TO THIS ADDRESS. **SEND TO: Commissioner for Patents, P.O. Box 1450, Alexandria, VA 22313-1450.**



## Privacy Act Statement

The Privacy Act of 1974 (P.L. 93-579) requires that you be given certain information in connection with your submission of the attached form related to a patent application or patent. Accordingly, pursuant to the requirements of the Act, please be advised that: (1) the general authority for the collection of this information is 35 U.S.C. 2(b)(2); (2) furnishing of the information solicited is voluntary; and (3) the principal purpose for which the information is used by the U.S. Patent and Trademark Office is to process and/or examine your submission related to a patent application or patent. If you do not furnish the requested information, the U.S. Patent and Trademark Office may not be able to process and/or examine your submission, which may result in termination of proceedings or abandonment of the application or expiration of the patent.

The information provided by you in this form will be subject to the following routine uses:

1. The information on this form will be treated confidentially to the extent allowed under the Freedom of Information Act (5 U.S.C. 552) and the Privacy Act (5 U.S.C. 552a). Records from this system of records may be disclosed to the Department of Justice to determine whether the Freedom of Information Act requires disclosure of these records.
2. A record from this system of records may be disclosed, as a routine use, in the course of presenting evidence to a court, magistrate, or administrative tribunal, including disclosures to opposing counsel in the course of settlement negotiations.
3. A record in this system of records may be disclosed, as a routine use, to a Member of Congress submitting a request involving an individual, to whom the record pertains, when the individual has requested assistance from the Member with respect to the subject matter of the record.
4. A record in this system of records may be disclosed, as a routine use, to a contractor of the Agency having need for the information in order to perform a contract. Recipients of information shall be required to comply with the requirements of the Privacy Act of 1974, as amended, pursuant to 5 U.S.C. 552a(m).
5. A record related to an International Application filed under the Patent Cooperation Treaty in this system of records may be disclosed, as a routine use, to the International Bureau of the World Intellectual Property Organization, pursuant to the Patent Cooperation Treaty.
6. A record in this system of records may be disclosed, as a routine use, to another federal agency for purposes of National Security review (35 U.S.C. 181) and for review pursuant to the Atomic Energy Act (42 U.S.C. 218(c)).
7. A record from this system of records may be disclosed, as a routine use, to the Administrator, General Services, or his/her designee, during an inspection of records conducted by GSA as part of that agency's responsibility to recommend improvements in records management practices and programs, under authority of 44 U.S.C. 2904 and 2906. Such disclosure shall be made in accordance with the GSA regulations governing inspection of records for this purpose, and any other relevant (i.e., GSA or Commerce) directive. Such disclosure shall not be used to make determinations about individuals.
8. A record from this system of records may be disclosed, as a routine use, to the public after either publication of the application pursuant to 35 U.S.C. 122(b) or issuance of a patent pursuant to 35 U.S.C. 151. Further, a record may be disclosed, subject to the limitations of 37 CFR 1.14, as a routine use, to the public if the record was filed in an application which became abandoned or in which the proceedings were terminated and which application is referenced by either a published application, an application open to public inspections or an issued patent.
9. A record from this system of records may be disclosed, as a routine use, to a Federal, State, or local law enforcement agency, if the USPTO becomes aware of a violation or potential violation of law or regulation.

<b>Provisional Application for Patent Cover Sheet</b>					
This is a request for filing a PROVISIONAL APPLICATION FOR PATENT under 37 CFR 1.53(c)					
<b>Inventor(s)</b>					
Inventor 1					<input type="button" value="Remove"/>
Given Name	Middle Name	Family Name	City	State	Country j
Chase	D.	Cox	Nashville	TN	US
Inventor 2					<input type="button" value="Remove"/>
Given Name	Middle Name	Family Name	City	State	Country j
David		DeLapp	Nashville	TN	US
Inventor 3					<input type="button" value="Remove"/>
Given Name	Middle Name	Family Name	City	State	Country j
Alvin	M.	Strauss	Nashville	TN	US
Inventor 4					<input type="button" value="Remove"/>
Given Name	Middle Name	Family Name	City	State	Country j
George	E.	Cook	Nashville	TN	US
All Inventors Must Be Listed – Additional Inventor Information blocks may be generated within this form by selecting the <b>Add</b> button.					<input type="button" value="Add"/>
<b>Title of Invention</b>	DOUBLE SIDED FRICTION STIR SPOT WELDING METHOD				
Attorney Docket Number (if applicable)	20004.0066				
<b>Correspondence Address</b>					
Direct all correspondence to (select one):					
<input checked="" type="radio"/> The address corresponding to Customer Number			<input type="radio"/> Firm or Individual Name		
Customer Number	78102				

The invention was made by an agency of the United States Government or under a contract with an agency of the United States Government.	
<input type="radio"/> No.	
<input checked="" type="radio"/> Yes, the name of the U.S. Government agency and the Government contract number are:	
NASA Share Services Center NNXIOAM45H	

Under the Paperwork Reduction Act of 1995, no persons are required to respond to a collection of information unless it displays a valid OMB control number

<b>Entity Status</b>					
Applicant claims small entity status under 37 CFR 1.27					
<input checked="" type="radio"/> Yes, applicant qualifies for small entity status under 37 CFR 1.27 <input type="radio"/> No					
<b>Warning</b>					
Petitioner/applicant is cautioned to avoid submitting personal information in documents filed in a patent application that may contribute to identity theft. Personal information such as social security numbers, bank account numbers, or credit card numbers (other than a check or credit card authorization form PTO-2038 submitted for payment purposes) is never required by the USPTO to support a petition or an application. If this type of personal information is included in documents submitted to the USPTO, petitioners/applicants should consider redacting such personal information from the documents before submitting them to USPTO. Petitioner/applicant is advised that the record of a patent application is available to the public after publication of the application (unless a non-publication request in compliance with 37 CFR 1.213(a) is made in the application) or issuance of a patent. Furthermore, the record from an abandoned application may also be available to the public if the application is referenced in a published application or an issued patent (see 37 CFR 1.14). Checks and credit card authorization forms PTO-2038 submitted for payment purposes are not retained in the application file and therefore are not publicly available.					
<b>Signature</b>					
Please see 37 CFR 1.4(d) for the form of the signature.					
Signature	/Eduardo J. Quinones/			Date (YYYY-MM-DD)	2012-06-13
First Name	Eduardo	Last Name	Quinones	Registration Number (if appropriate)	58575
This collection of information is required by 37 CFR 1.51. The information is required to obtain or retain a benefit by the public which is to file (and by the USPTO to process) an application. Confidentiality is governed by 35 U.S.C. 122 and 37 CFR 1.11 and 1.14. This collection is estimated to take 8 hours to complete, including gathering, preparing, and submitting the completed application form to the USPTO. Time will vary depending upon the individual case. Any comments on the amount of time you require to complete this form and/or suggestions for reducing this burden, should be sent to the Chief Information Officer, U.S. Patent and Trademark Office, U.S. Department of Commerce, P.O. Box 1450, Alexandria, VA 22313-1450. <b>DO NOT SEND FEES OR COMPLETED FORMS TO THIS ADDRESS. This form can only be used when in conjunction with EFS-Web. If this form is mailed to the USPTO, it may cause delays in handling the provisional application.</b>					

## Privacy Act Statement

**The Privacy Act of 1974 (P.L. 93-579)** requires that you be given certain information in connection with your submission of the attached form related to a patent application or patent. Accordingly, pursuant to the requirements of the Act, please be advised that: (1) the general authority for the collection of this information is 35 U.S.C. 2(b)(2); (2) furnishing of the information solicited is voluntary; and (3) the principal purpose for which the information is used by the U.S. Patent and Trademark Office is to process and/or examine your submission related to a patent application or patent. If you do not furnish the requested information, the U.S. Patent and Trademark Office may not be able to process and/or examine your submission, which may result in termination of proceedings or abandonment of the application or expiration of the patent.

The information provided by you in this form will be subject to the following routine uses:

1. The information on this form will be treated confidentially to the extent allowed under the Freedom of Information Act (5 U.S.C. 552) and the Privacy Act (5 U.S.C. 552a). Records from this system of records may be disclosed to the Department of Justice to determine whether disclosure of these records is required by the Freedom of Information Act.
2. A record from this system of records may be disclosed, as a routine use, in the course of presenting evidence to a court, magistrate, or administrative tribunal, including disclosures to opposing counsel in the course of settlement negotiations.
3. A record in this system of records may be disclosed, as a routine use, to a Member of Congress submitting a request involving an individual, to whom the record pertains, when the individual has requested assistance from the Member with respect to the subject matter of the record.
4. A record in this system of records may be disclosed, as a routine use, to a contractor of the Agency having need for the information in order to perform a contract. Recipients of information shall be required to comply with the requirements of the Privacy Act of 1974, as amended, pursuant to 5 U.S.C. 552a(m).
5. A record related to an International Application filed under the Patent Cooperation Treaty in this system of records may be disclosed, as a routine use, to the International Bureau of the World Intellectual Property Organization, pursuant to the Patent Cooperation Treaty.
6. A record in this system of records may be disclosed, as a routine use, to a n other federal agency for purposes of National Security review (35 U.S.C. 181) and for review pursuant to the Atomic Energy Act (42 U.S.C. 218(c)).
7. A record from this system of records may be disclosed, as a routine use, to the Administrator, General Services, or his/her designee, during an inspection of records conducted by GSA as part of that agency's responsibility to recommend improvements in records management practices and programs, under authority of 44 U.S.C. 2904 and 2906. Such disclosure shall be made in accordance with the GSA regulations governing inspection of records for this purpose, and any other relevant (i.e., GSA or Commerce) directive. Such disclosure shall not be used to make determinations about individuals.
8. A record from this system of records may be disclosed, as a routine use, to the public after either publication of the application pursuant to 35 U.S.C. 122(b) or issuance of a patent pursuant to 35 U.S.C. 151. Further, a record may be disclosed, subject to the limitations of 37 CFR 1.14, as a routine use, to the public if the record was filed in an application which became abandoned or in which the proceedings were terminated and which application is referenced by either a published application, an application open to public inspection or an issued patent.
9. A record from this system of records may be disclosed, as a routine use, to a Federal, State, or local law enforcement agency, if the USPTO becomes aware of a violation or potential violation of law or regulation.

May 26<sup>th</sup>, 2011

Double Sided Friction Stir Welding Method

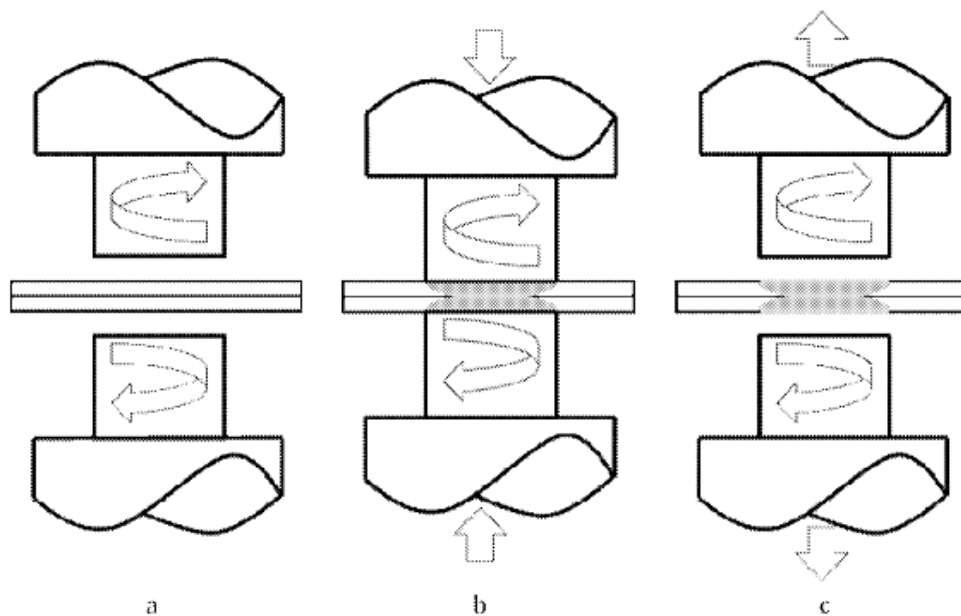
Vanderbilt University Welding Automation Laboratory

Chase D. Cox, David R. DeLapp, Brian T. Gibson, Alvin M. Strauss, George E. Cook

**Abstract**

Double sided friction stir spot welds have been successfully made using the method developed at Vanderbilt University. This technology is novel because no such method or device currently exists in the literature or patents. Further, this technology provides several advantages over existing process such as the elimination of the “key-hole”, quicker cycle times and increased joint strengths. This document outlines the principals of the technology, the theoretical design and implementation of the device, and preliminary experimental results.

**Double Sided Friction Stir Spot Welding Method**



*Figure 1 Method for Friction Stir Spot Welding Using a Pin-less Tool and double sided FSSW. a) The pin-less tool and anvil both rotate (clockwise & anti-clockwise) relative to the top of the weldment b) The pin-less tool and anvil make contact with the weldment and apply a welding load. The pin-less tool*

*and anvil remain in contact with the weldment while rotating for some period of time c) The pin-less tool and anvil retract from the surface leaving the weldment joined.*

The method presented for Friction Stir Spot Welding (FSSW) using a counter rotating anvil and pin-less tool is a novel application of the process. A drawing of the double sided FSSW method can be seen in Figure 1. The double sided FSSW method uses an anvil of dimensions similar to the pin-less tool. Conventional friction stir spot welds are made using traditional Friction Stir Welding (FSW) tools which may include threads, flutes, non-symmetric geometries etc. FSW tools typically consist of both a pin and a shoulder. The tool used in the double sided FSSW method is pin-less and may have scrolling on the shoulder. The advantages of using the double sided FSSW method are:

1. The elimination of the “key-hole” left in the weld zone. The tooling used in traditional FSSW leaves a hole in the material that is of the same volume as that of the pin (plunged within the material) used to make the weld. This reduces the amount of material contained within the weld zone. The lack of material within the weld zone leads to a weaker weld and a cosmetic flaw that may need to be addressed in a manufacturing application.
2. This method can be used to join similar metals, dissimilar metals, metal matrix composites, similar polymers, dissimilar polymers.
3. Increased joint strength. Welding from both sides (top and bottom) of the weldment geometry will increase the area of contact between the weldment and weld nugget. Increasing this contact area of the weld will increase the joint strength of the weld.
4. The application of the welding force from both sides of the weldment will largely reduce the reaction force experienced by the FSSW apparatus.
5. The application of the welding torque from both sides of the weldment will largely reduce the reaction torque experienced by the FSSW apparatus.
6. The method can be used to perform seam welds by stitching together overlapping spot welds.
7. The method can be used to traditional lap welds on thin plate. This process would have a result similar to that of a bobbin tool but without the need to drill a starting hole.
8. The method can be used to fill the “key-hole” left by the conventional FSW process.

9. The use of concentric cylinders to apply the clamping force during welding (see Figure 4). Clamps would make contact with the weldment prior to the engagement of the rotating tools and would retract after the weld is completed.
10. The use of a rolling-contact clamping apparatus to facilitate seam and lap welding.
11. The application to place sensors, valves, gauges etc. to existing hardware without the use of epoxy, drilling and tapping, or redesign.
12. The design of a hollow friction stir spot welding tool for the purpose of attaching sensors, valves, gauges etc. to existing hardware.
13. The method of monitoring process signals (force, torque, current, temperature, vibration, acoustic emission) for quality and process control.
14. The use of a spherically shaped tool profile for FSSW.

Potential applications of the double sided FSSW method range from stand alone FSSW machines, hand-held FSSW, automated robotic FSSW, etc. The reduction in forces and torques associated with the double sided FSSW method greatly increases the potential for the process to be utilized in applications that otherwise could not be implemented e.g. manual operation, extended range of allowable robotic link compliancy. The double sided FSSW method also has application in the manufacturing industry (automotive, aerospace, etc.) and reparative work.

## Claims

What is claimed is:

1. A welding assembly for joining workpieces, comprising:

a first friction stir weld (FSW) tool having a first shaft and a first motor for axially rotating the first shaft, an end of the first shaft defining a first shoulder area;

a second FSW tool having a second shaft and a second motor for axially rotating the second shaft, an end of the second shaft defining a second shoulder area, the second shoulder area facing the first shoulder area, and the second rotating shaft being substantially parallel to the first rotating shaft; and

at least one linear actuator for adjusting a position at least one of the first FSW tool or the second FSW tool so that the first shoulder area and the second shoulder area apply axially opposing forces to the workpieces to be joined when the first shaft and the second shaft are rotating.

2. The welding assembly of claim 1, wherein the first motor and the second motor are configured to provide counter-rotation of the first shaft and the second shaft.

3. The welding assembly of claim 1, wherein the first motor and the second motor are configured to provide different rotation speeds for the first shaft and the second shaft.

4. The welding assembly of claim 1, wherein the first shoulder area and the second shoulder area are the same.

5. The welding assembly of claim 1, wherein the first shaft and the second shaft have a same axis of rotation.

6. The welding assembly of claim 1, wherein at least one of the first shaft or the second shaft further comprises a pin extending from the a corresponding shoulder area.

7. The welding assembly of claim 1, wherein the first FSW tool comprises a first clamping tool and the second FSW comprises a second clamping tool, the first and second clamping tools configured to apply a clamping force to the workpieces to be joined.

8. The welding assembly of claim 7, wherein at least one of the first and second clamping tools comprises:  
a cylinder concentrically arranged with respect to a corresponding shaft; and



a second linear actuator for applying an axial force using the cylinder independently of the corresponding shaft.

9. A method for joining workpieces, using a welding assembly comprising a first friction stir weld (FSW) tool having a first shaft and a first motor for axially rotating the first shaft, an end of the first shaft defining a first shoulder area, a second FSW tool having a second shaft and a second motor for axially rotating the second shaft, an end of the second shaft defining a second shoulder area facing the first shoulder area, and the second axially rotating shaft being substantially parallel to the first axially rotating shaft, and at least one linear actuator for adjusting a position at least one of the first FSW tool or the second FSW tool, the method comprising:

positioning the workpieces to be joined between the first and second shoulder areas;

rotating the first and second shafts;

adjusting the at least one linear actuator to a processing position so that the first shoulder area and the second shoulder area apply axially opposing forces to the workpieces to be joined when the first shaft and the second shaft are rotating; and

after a welding time is complete, adjusting the at least one linear actuator to a retracted position so that the first shoulder area and the second shoulder area do not apply axially opposing forces to the workpieces to be joined when the first shaft and the second shaft are rotating.

10. The method of claim 9, wherein the rotating comprises configuring the first motor and the second motor to provide counter-rotation of the first shaft and the second shaft.

11. The method of claim 9, wherein the rotating comprises configuring the first motor and the second motor to provide different rotation speeds for the first shaft and the second shaft.

12. The method of claim 9, further comprising selecting the first shoulder area and the second shoulder area to be same.

13. The method of claim 9, further comprising selecting the first shaft and the second shaft to have a same axis of rotation.

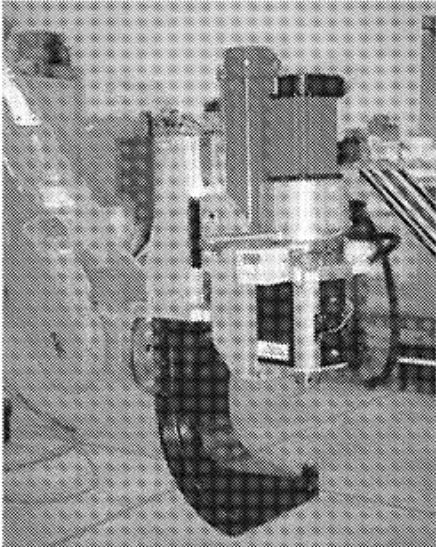
14. The method of claim 9, further comprising selecting at least one of the first shaft or the second shaft further to comprise a pin extending from the a corresponding shoulder area.

15. The method of claim 9, wherein the first FSW tool comprises a first clamping tool and the second FSW comprises a second clamping tool, and wherein the method further comprises:

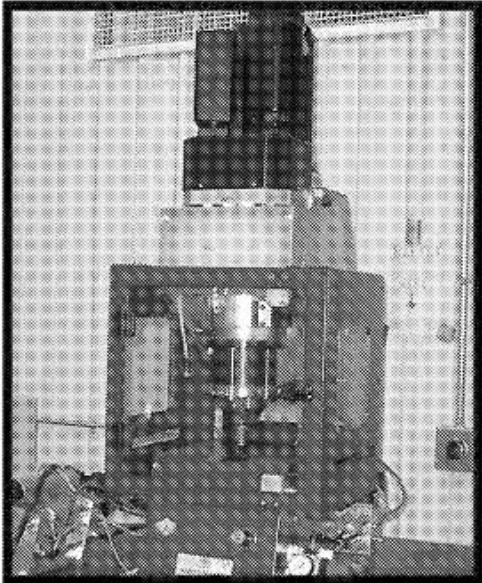
prior to the adjusting of the at least one linear actuator to the processing position, configuring the first and second clamping tools to apply a clamping force to the workpieces to be joined.

16. The method of claim 15, further comprising selecting at least one of the first and second clamping tools to comprise a cylinder concentrically arranged with respect to a corresponding shaft and a second linear actuator for applying an axial force using the cylinder independently of the corresponding shaft, and wherein the method further comprises.

**Examples of Existing FSSW machines:**



*Figure 2: Single Sided FSSW machine using a C-frame design (The Welding Institute)*



*Figure 3: Stand-alone FSSW machine (RIFTEK)*

#### CAD Drawing of Double Sided FSSW Device:

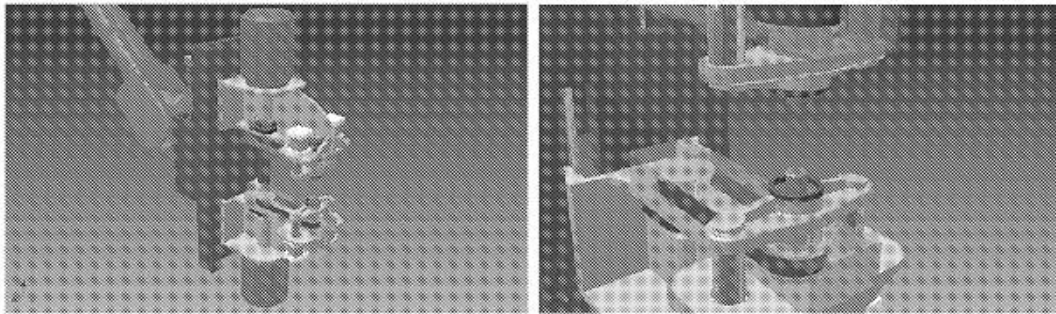


Figure 4: (left) conceptual design of the double sided FSSW device. (right) close up of the top and bottom tool alignment with clamping mechanism.

Figure 4 shows what the implementation of the double sided FSSW device might look like. The picture includes the top and bottom FSSW tools, two motors to provide the necessary rotation and the mechanism used to provide the linear actuation needed to create the welding force. The device is shown as being attached to an articulated robot; a similar approach currently used by both conventional resistance spot welding and single sided FSSW.

#### Experimental Double Sided FSSW Device Design

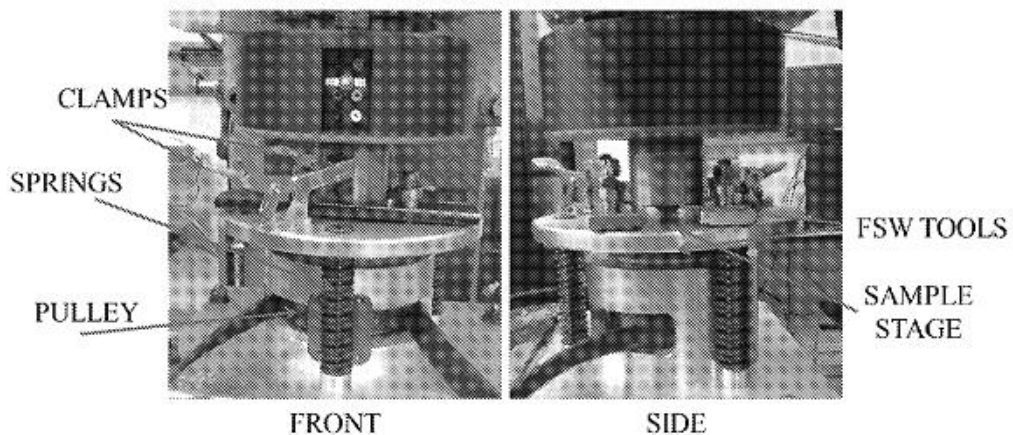
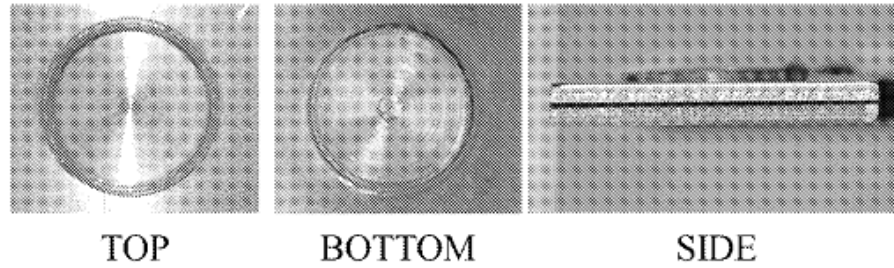


Figure 5: Double Sided FSSW device. This device contains the bottom FSSW tool, provides rotation and rigidly clamps the sample during welding.

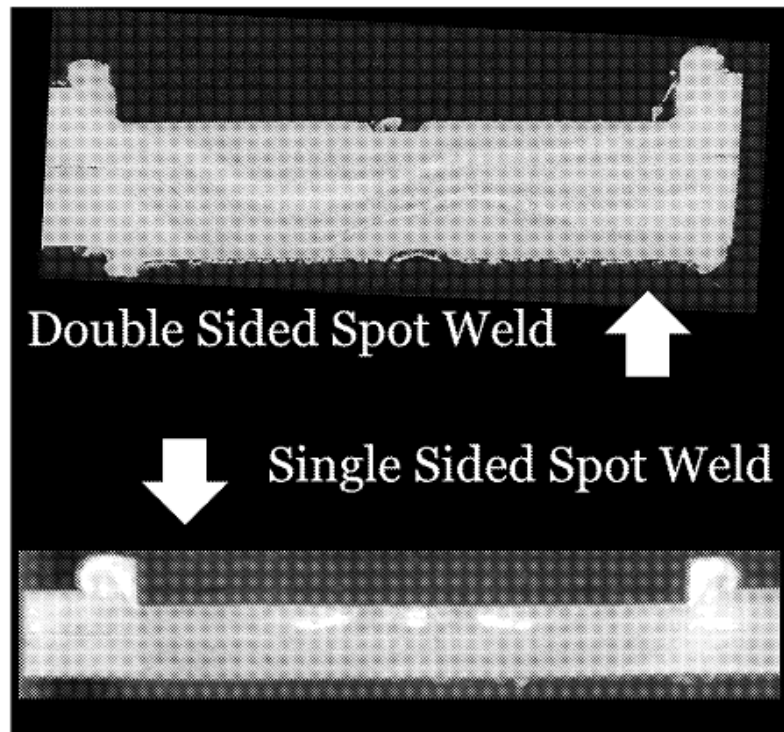
The device used to implement the double sided FSSW method can be seen in Figure 5. The device was rigidly mounted to the anvil of a converted FSW machine. The existing FSW machine was used to rotate the top tool and provide necessary welding force to create the spot weld. An external motor was used to provide the bottom tool rotation.

#### **Preliminary Experimental Results**



*Figure 6: Images of the top, bottom, and side of the spot weld created by the double sided FSSW method are shown. The side view shows that there are two plates being joined.*

These double sided FSSW welds were created in the Vanderbilt University Welding Automation Laboratory. 2 mm thick Al 6061-T6 sheets were joined using the double sided FSSW method in a lap joint configuration. The top and bottom tool were rotated clockwise and counterclockwise respectively at 1400 rpm. A dwell time of 5 seconds was used. These welds were created using the double sided FSSW device.



*Figure 7: comparison of a double sided friction stir spot weld to a single sided friction stir spot weld. (top) the spot weld was created using 2 mm thick plate (2x). (bottom) the spot weld was created on 1 mm thick plate (2x).*

The macrosection image of the double sided spot weld revealed a unique weld zone structure. This weld zone looks significantly different than that of a single sided friction stir spot weld created with an identical FSSW tool. The observed “banding” within the weld zone of the double sided weld is most likely a result of a mechanical effect created by the counter rotating tools. A computational fluid dynamic model will be created to provide insight into the observed material flow pattern.